Ab-Initio Approach to Hypernuclei

Vom Fachbereich Physik der Technischen Universität Darmstadt
zur Erlangung des Grades eines

Doktors der Naturwissenschaften (Dr. rer. nat.)

genehmigte Dissertation von

Roland Wirth, M.Sc.
aus Berlin-Lichtenberg

Darmstadt 2018

D17

Ab-Initio Approach to Hypernuclei
Ein Ab-Initio Zugang zu Hyperkernen

Abstract

Studying systems with strangeness provides a unique opportunity to deepen our understanding of the strong interaction. The purpose of this work is the development of an *ab initio* framework that is suitable for addressing finite (single-Λ) hypernuclei. Such a framework connects models of the hyperon-nucleon (YN) interaction, which are ill constrained due to lack of scattering data, to observables of p-shell hypernuclei. Thus, it not only enables predictions of quantities that have not been measured, but can also be used to improve the interaction model itself.

The many-body method we employ here is the Importance-Truncated No-Core Shell Model (IT-NCSM), which has been successfully used in light nuclei. We implement an extended IT-NCSM in which particles of differing rest mass can be treated without approximation. Also, the coupled-channel problem arising from the low mass difference between the Λ and Σ hyperons is fully included.

A crucial part of the framework is the Similarity Renormalization Group (SRG) transformation of the Hamiltonian, which accelerates model-space convergence of the IT-NCSM so that ground-state and hyperon-separation energies can be extracted reliably. As a tradeoff, the SRG transformation induces many-body terms beyond those present in the initial Hamiltonian. We show that it is necessary to include the induced hyperon-nucleon-nucleon (YNN) terms in order to get precise values for energy observables. We present in detail the procedure with which the induced terms can be calculated, and discuss technical issues of its practical implementation.

With a Hamiltonian built from chiral effective field theory interactions including nucleon-nucleon, three-nucleon, and YN interactions, we survey absolute energies and spectra of light hypernuclei; first with a bare YN interaction, then with an evolved interaction along with the induced three-body terms. We find remarkable agreement with experimental data, despite using a leading-order hyperon-nucleon interaction. We also study binding energies and neutron-separation energies along the neutron-rich helium and lithium isotopic chains and their daughter hyperisotopes. Contrary to the naive expectation, we find that the neutron drip line for the hyperisotopes is the same as for their nucleonic parents. Finally, we turn to double-Λ hypernuclei and investigate core-polarization effects in $_{\Lambda\Lambda}^{6}\text{He}$, concluding that the hyperon-hyperon interaction has to be very weak.

We also consider medium-mass hypernuclei with closed-shell parents, presenting applications of the Hartree-Fock (HF) method, second-order many-body perturbation theory (MBPT), and Brueckner-Bethe-Goldstone theory to these systems, paving the way for a full *ab initio* treatment. We find that, for closed-shell nuclei, the Brueckner-Hartree-Fock (BHF) approximation is less suitable for SRG-evolved interactions than perturbative approaches. Also, the correlations included in BHF and second-order MBPT have only a small effect on hyperon-separation energies, which are almost completely determined by the HF ground-state energies.

The induced YNN terms are generated by integrating out the Σ hyperons from the low-lying eigenstates of the Hamiltonian via suppressing the Λ-Σ conversion terms of the YN interaction.

Without the induced terms, the separation energies do not saturate with particle number; only their inclusion make the calculation results follow the experimental trend. From these findings, we propose a solution to the hyperon puzzle in neutron-star physics for approaches employing a scheme with only Λ hyperons by showing that the strong repulsive ΛNN interaction required to solve the puzzle is generated naturally by integrating out Σ hyperons.

Zusammenfassung

Systeme mit Strangeness zu untersuchen ist eine einmalige Gelegenheit unser Verständnis der starken Wechselwirkung zu vertiefen. Zweck dieser Arbeit ist die Entwicklung eines *ab initio* Framework für endliche einfache Hyperkerne, d.h. Hyperkerne mit einem Hyperon. Dieses Framework verbindet Wechselwirkungsmodelle für die Hyperon-Nukleon (YN) Wechselwirkung, deren Parameter mangels ausreichender Streudaten nur ungenau bestimmt werden können, mit Observablen von p-Schalen-Hyperkernen. Dadurch ermöglicht ein solches Framework nicht nur die Vorhersage von Größen, die noch nicht gemessen sind, sondern kann auch dazu verwendet werden, das Wechselwirkungsmodell selbst zu verbessern.

Die Vielteilchenmethode, die wir hier verwenden, ist das Importance-Trunkierte No-Core Schalenmodell (IT-NCSM), welches mit Erfolg zur Beschreibung von leichten Kernen eingesetzt wird. Wir implementieren ein erweitertes IT-NCSM, in dem Teilchen unterschiedlicher Ruhemasse ohne Näherung behandelt werden können. Zudem berücksichtigen wir das Mehrkanalproblem voll, das durch den geringen Massenunterschied zwischen Λ und Σ Hyperonen entsteht.

Ein entscheidender Teil des Frameworks ist die Similarity-Renormalization-Group (SRG) Transformation des Hamiltonians, die die Modellraumkonvergenz des IT-NCSM beschleunigt, sodass wir Absolutenergien und Hyperon-Separationsenergien zuverlässig aus den Rechnungsergebnissen extrahieren können. Im Tausch für die beschleunigte Konvergenz induziert die SRG Transformation Vielteilchenkräfte, die über die im anfänglichen Hamiltonian vorhandenen hinausgehen. Wir zeigen, dass es nötig ist, die induzierten Hyperon-Nukleon-Nukleon (YNN) Terme explizit in die Rechnung einzubeziehen, um präzise Werte für Energie-Observablen zu erhalten. Dafür beschreiben wir detailliert eine Prozedur, mit der die induzierten Terme berechnet werden können, und diskutieren technische Fragen, die bei der praktischen Implementierung auftreten.

Mit einem Hamiltonian bestehend aus Nukleon-Nukleon-, Drei-Nukleon- und Hyperon-Nukleon-Wechselwirkungen machen wir eine Übersichtsstudie über die Absolutenergien und Spektren leichter Hyperkerne; erst mit der initialen, dann mit der evolvierten YN-Wechselwirkung mit den zugehörigen induzierten Dreiteilchentermen. Hierbei entstammen die initialen Wechselwirkungen einer chiralen effektiven Feldtheorie. Wir beobachten eine bemerkenswerte Übereinstimmung der Ergebnisse mit experimentellen Daten, obwohl wir nur die führende Ordnung der YN-Wechselwirkung verwenden. Wir untersuchen außerdem die Bindungsenergien und Neutronen-Separationsenergien entlang der neutronenreichen Helium und Lithium Isotopenketten und deren Tochter-Hyperisotopen. Entgegen der naiven Erwartung bleibt die Neutronen-Dripline der Hyperisotopenkette gegenüber der der normalen Isotopenkette unverändert. Schließlich wenden wir uns Doppel-Hyperkernen zu und studieren Polarisationseffekte in $^{6}_{\Lambda\Lambda}$He. Aus den Ergebnissen schließen wir, dass die Hyperon-Hyperon-Wechselwirkung in diesem Kern sehr schwach sein muss.

Wir betrachten auch mittelschwere Hyperkerne, deren Mutterisotopen abgeschlossene Schalen haben, und zeigen Anwendungen der Hartree-Fock (HF) Methode, von zweiter Ordnung Störungstheorie, und von Brueckner-Bethe-Goldstone-Theorie für diese Systeme. Damit ebnen wir den Weg für eine volle *ab initio* Behandlung dieser Hyperkerne. Die Ergebnisse unserer Rechnungen zeigen, dass bei Kernen mit Schalenabschluss und SRG-evolvierten Wechselwirkungen die Brueckner-Hartree-Fock (BHF) Approximation weniger geeignet ist als perturbative Ansätze. Außerdem haben die Korrelationen, die in BHF und zweiter Ordnung Störungstheorie berücksichtigt werden, nur einen sehr kleinen Effekt auf die Hyperon-Separationsenergien der entsprechenden Tochterkerne; sie sind größtenteils durch die HF-Erwartungswerte bestimmt.

Die induzierten YNN-Terme werden dadurch generiert, dass die Σ Hyperonen aus dem niedrigliegenden Spektrum des Hamiltonian ausintegriert werden. Dies geschieht durch Unterdrückung der Λ-Σ-Konversion in der YN-Wechselwirkung. Ohne die induzierten Terme saturieren die Separationsenergien nicht mit zunehmender Teilchenzahl. Nur durch deren Berücksichtigung folgen die Ergebnisse der Rechnungen dem experimentellen Trend. Im Licht dieser Beobachtungen schlagen wir eine Lösung für das Hyperonen-Puzzle in der Neutronenstern-Physik vor: Für Zugänge, die ein Schema mit nur Λ Hyperonen verwenden, können wir zeigen, dass die zur Lösung des Puzzles nötigen stark repulsiven ΛNN-Wechselwirkungsterme natürlicherweise durch das Ausintegrieren der Σ Hyperonen generiert wird.

Contents

List of Figures

List of Tables

1. Introduction

Quantum Chromodynamics (QCD), the theory of the strong interaction acting inside atomic nuclei, describes interactions between quarks and gluons. There are six quark types (flavors), of which only the lightest two, the up and down quarks, make up the proton and neutron, and thus all atomic nuclei. Using energetic particles, however, one can replace one of the up and down quarks inside a proton or neutron (nucleon) with a strange quark—the lightest of the other flavors—and create a hyperon. If the hyperon happens to be bound in an atomic nucleus, because the original nucleon was or because the hyperon was captured by a nucleus, the system becomes a hypernucleus.

The lightest hyperons are the Λ^0 and $\Sigma^{\pm,0}$ baryons, which contain one strange quark. One obtains the $\Xi^{0,-}$ hyperons by substituting an additional strange quark. All these hyperons have spin 1/2 and behave like fermions. Due to them containing strange quarks, they are distinguishable from the nucleons. The number of strange quarks defines the *strangeness* of a hyperon (traditionally defined with a minus sign), so that the Λ and Σ hyperons have strangeness $\mathcal{S} = -1$ while the Ξ hyperons have $\mathcal{S} = -2$.

The up and down quarks are much lighter than the strange quark so that hyperons decay quickly via weak processes. The typical lifetime of a strange hyperon is 10^{-10} s. Although this time scale is short compared to the the typical lifetime of a weakly-decaying nucleus, it is orders of magnitude longer than the time scales of strong and electromagnetic processes. Thus, hypernuclear energy levels are well defined and electromagnetic transitions between them can be measured.

The first experimental detection of a hypernucleus goes back to Danysz and Pniewski [DP53] in a balloon-flown emulsion stack, in which the hypernucleus was produced by a cosmic ray. Since then, a multitude of experiments have been conducted using kaon beams, which already carry strangeness, or pion and electron beams, where a strange-antistrange pair is created in the production reaction. The early experiments used bubble chambers or emulsion stacks as target, where the tracks of the produced particles can be used to infer properties of the produced hypernuclei [TAA+01; Dav05]. More recent spectrometer experiments can measure hypernuclear ground and excited states with high resolution via their decay [ENS+15] or reaction products [SFI+05; CUA+09; NMO+13]. Also, direct measurement of the gamma rays produced by the deexcitation of the hypernucleus after production provides excitation spectra with high precision [TTA+00; TTA+01; AAC+02; HT06].

Hypernuclei challenge our understanding of the strong interaction: The interaction among hyperons and nucleons cannot currently be computed realistically from the interactions among the quarks themselves, which are described by QCD. This is rooted in the complex internal structure of these objects and in QCD exhibiting *confinement*, which prevents single quarks and gluons from being observed. Efforts employing lattice QCD to generate synthetic scattering data [BBL+07] or to compute the potential directly [NAD+17] are underway but currently

1. Introduction

limited by unphysical quark masses or insufficient statistics.

With chiral effective field theory (χEFT), we have a systematic symmetry-based connection between QCD and the hyperon-nucleon and nucleonic interactions in the form of a low-momentum expansion with parameters fitted to experimental data [EHM09; ME11]. Together with recent developments in unitary transformations that accelerate convergence with respect to the size of the model space, this sparked a tremendous development of *ab initio* many-body methods, i.e., methods that provide systematically improvable solutions to the quantum many-body problem, for nonstrange nuclei [HLK17].

The hyperon-nucleon interaction is not well-known because scattering experiments, which are the experimental foundation on which all models of the nucleon-nucleon and hyperon-nucleon interactions are built, are intrinsically challenging due to the short hyperon lifetime. On the other hand, there is a wealth of data on hypernuclear observables from over 50 years of experiments. The χEFT-based potentials provide an accurate description of light nuclei, so the hyperon-nucleon interaction is the main source of uncertainty. *Ab initio* methods provide a systematic link between the ill-constrained interaction and the precise hypernuclear data. We can use this link to better constrain the hyperon-nucleon interaction and provide predictions for observables that have not been measured or are not experimentally accessible.

There are many different approaches for a theoretical description of hypernuclei, like cluster models [Hiy12; MBI$^+$85], mean-field models [CLS00; GDS12; GVH$^+$93], the Brueckner-Hartree-Fock method [VPR$^+$01], and the microscopic shell model [GSD71; Mil07]. These are not *ab initio* approaches because they are not systematically improvable. The *ab initio* methods available for hypernuclei are few-body methods like Faddeev-Yakubovsky calculations [Nog13] or methods based on an expansion of the wavefunction in (correlated) Gaussians [HKM$^+$01; NAS02]. For heavier systems, Quantum Monte-Carlo approaches have been devised [LGP13; LPG14], which target only ground states, work in a scheme without Σ hyperons, and are restricted to very simple NN and YN interactions.

The goal of this work is the development of an *ab initio* many-body method suitable for *p*-shell hypernuclei that can use general baryon-baryon interactions, compute excited states, and treat observables like radii or electromagnetic moments and transition strengths. To this end, we extend the No-Core Shell Model (see [BNV13] for a review), which is a successful *ab initio* method for *p*-shell nuclei.

This work is organized as follows: Chapter 2 defines the general structure of the Hamiltonian used in the subsequent investigations, summarizes the properties of the hyperon-nucleon interaction, and gives a short overview of interaction models and baryon-baryon interactions from χEFT. In chapter 3, we introduce the Similarity Renormalization Group, which we use to unitarily transform the Hamiltonian into a form that is more amenable to the many-body method. The many-body method itself, the No-Core Shell Model, is described in chapter 4, where we also present calculations for a set of hypernuclei up to the mid *p* shell, and show that hyperon-nucleon-nucleon interaction terms induced by the Similarity Renormalization Group transformation are important and have to be included in the calculation. Their inclusion is detailed in chapter 5, where we show the transformation of the interaction in three-body space and their transformation into a form that can be used in many-body calculations. We conclude this chapter with a comparison of the calculations with and without the induced terms, a survey of light neutron-rich hypernuclei, and an exploration of the doubly-strange hypernucleus $^{6}_{\Lambda\Lambda}$He.

In chapter 6, we go beyond the *p* shell towards medium-mass hypernuclei and present two very simple many-body methods whose computational demand scales much softer with particle number than the No-Core Shell Model: perturbation theory, and Brueckner-Bethe-Goldstone theory. With these two methods, we explore hypernuclei with closed-shell nucleonic cores up to the tin region. The final chapter, chapter 7, considers the effect of our findings regarding the induced many-body terms on our understanding of the structure of neutron stars. Here, we propose an explanation for the so-called hyperon puzzle.

2. Hypernuclear Hamiltonian

Starting point of our investigations is an intrinsic Hamiltonian for the A-body system,

$$H = \Delta M + T_{\text{int}} + V_{2B} + V_{3B} + \cdots \,, \tag{2.1}$$

which contains two-body, three-body, and, in principle, higher many-body interaction terms. Since (hyper-) nuclei are self-bound systems and the problem is Galilei invariant, we use an intrinsic Hamiltonian with the intrinsic kinetic energy $T_{\text{int}} = T - T_{\text{c.m.}}$, where

$$T \equiv \sum_{i=1}^{A} \frac{\vec{p}_i^2}{2m_i} \quad \text{and} \quad T_{\text{c.m.}} \equiv \frac{\vec{P}^2}{2M} \tag{2.2}$$

are the kinetic energies of the individual particles and of the center of mass (c.m.), respectively. Here, the $\vec{p}_i$ and m_i denote the momentum and mass operators of particle i, while

$$\vec{P} = \sum_{i=1}^{A} \vec{p}_i \tag{2.3}$$

is the c.m. momentum. The operator

$$\Delta M \equiv M - M_0 \quad \text{with} \quad M = \sum_{i=1}^{A} m_i \tag{2.4}$$

accounts for the different rest energies of the particles, which are shown in table 2.1. The offset $M_0 \equiv \mathcal{Q} m_p + (A - \mathcal{Q} + \mathcal{S}) m_n - \mathcal{S} m_\Lambda$ sets the zero point of the energy to the rest mass of a system of noninteracting protons, neutrons and Λ hyperons with the correct quantum numbers. It depends on the particle number A, and the total charge $\mathcal{Q}$ and strangeness $\mathcal{S}$ of the system under consideration.

We write the intrinsic kinetic energy in a manifestly Galilei-invariant way,

$$
\begin{aligned}
T_{\text{int}} = T - T_{\text{c.m.}} &= \sum_{i=1}^{A} \frac{\vec{p}_i^2}{2m_i} - \frac{\vec{P}^2}{2M} \\
&= \sum_{i=1}^{A} \frac{1}{2m_i} \left(\vec{p}_i^2 - 2\frac{m_i}{M} \vec{p}_i \cdot \vec{P} + \frac{m_i^2}{M^2} \vec{P}^2 \right) + \frac{1}{M} \sum_{i=1}^{A} \vec{p}_i \cdot \vec{P} - \sum_{i=1}^{A} \frac{m_i}{2M^2} \vec{P}^2 - \frac{\vec{P}^2}{2M} \\
&= \sum_{i=1}^{A} \frac{\left(\vec{p}_i - \frac{m_i}{M} \vec{P} \right)^2}{2m_i} + \frac{\vec{P}^2}{M} - \frac{M}{2M^2} \vec{P}^2 - \frac{\vec{P}^2}{2M} = \sum_{i=1}^{A} \frac{\left(\vec{p}_i - \frac{m_i}{M} \vec{P} \right)^2}{2m_i} \,,
\end{aligned} \tag{2.5}
$$

Particle	Mass m [MeV]	Charge [e]	Isospin t	Isospin Projection τ	Strangeness $\mathcal{S}$
n	939.565 346	0	1/2	−1/2	0
p	938.272 013	+1	1/2	+1/2	0
Λ	1115.683	0	0	0	−1
Σ^-	1197.449	−1	1	−1	−1
Σ^0	1192.642	0	1	0	−1
Σ^+	1189.37	+1	1	+1	−1

Table 2.1.: Properties of nucleons and singly-strange hyperons. Data from [Nak⁺10].

where we used the definition of $\vec{P}$ and M in the second and third terms. Consisting only of scalar products of momenta, this expression is invariant under rotations and translations. If we apply a boost by a velocity $\vec{v}$ to the system, all momenta $\vec{p}_i$ get shifted to $\vec{p}_i' \equiv \vec{p}_i + m_i \vec{v}$, leading to a shift of $\vec{P}' = \vec{P} + M\vec{v}$ for the center-of-mass momentum. Thus, $\vec{p}_i' - (m_i/M)\vec{P}' = \vec{p}_i - (m_i/M)\vec{P}$ and the intrinsic kinetic energy is unchanged.

The interaction terms can be further separated according to the types of interacting particles. We split the two-body interaction into a nucleon-nucleon (NN) interaction V_{NN}, a hyperon-nucleon (YN) interaction V_{YN}, and a hyperon-hyperon (YY) interaction V_{YY}. In analogy, the three body terms separate into 3N, YNN, YYN, and 3Y terms. In the following, we consider only systems with at most one hyperon, so we can remove the YY, YYN, and 3Y terms, which do not contribute. We also neglect four- and higher many-body terms, which are small in the nucleonic sector [Sch18], and YNN terms in this initial Hamiltonian. However, we will see that YNN terms are generated by the transformation described in chapter 3, and have to be accounted for.

2.1. Nucleonic Interactions

Since baryons are composed of quarks and gluons, interactions among them are, in principle, determined by Quantum Chromodynamics (QCD), the theory of the strong interaction. At low energies, QCD interactions are strong and the theory exhibits confinement so that no individual quarks and gluons can be observed. Instead, they are confined into hadrons. These features preclude a perturbative treatment in terms of the fundamental degrees of freedom of the theory, which makes deriving baryon-baryon interactions from QCD an extremely challenging task.

Hence, for a long time, the NN interaction was modeled using physical insight from experimental data on the deuteron and scattering, and general symmetry considerations. This lead to the development of realistic interaction models like the family of Argonne potentials [WSS95] or the CD-Bonn potential [Mac01], which reproduce the available scattering data with $\chi^2 \sim 1$ per datum. For describing systems of more than two particles, three-body interactions are added.

A drawback of these models is that there is no systematic way in which they can be improved. Also, the two- and three-body interactions are not necessarily consistent with each other. Chiral effective field theory, introduced by the works of Weinberg [Wei79; Wei91], solves these

problems. Chiral effective field theory is a low-energy description of QCD, rooted in its symmetries, with nucleons and pions as degrees of freedom. Together with a power counting that determines the importance of interaction terms, it provides a systematic low-momentum expansion of the interaction, where three- and higher many-body interactions appear naturally. It is an effective theory, so new parameters may enter the expansion at each order in the expansion. These parameters, the low-energy constants (LEC), control the short-range behavior of the theory and have to be determined by fitting to experiment or by other means. All many-body terms are rooted in the same effective field theory, so they share LECs. The leading 3N interaction, for example, has only two parameters that are not determined from the two-body sector. To date, the two-body interaction has been derived up to next-to-next-to-next-to-next-to-leading order (N^{4}LO) [EMN17; EKM15]. The 3N terms, which first appear at N^{2}LO have been worked out up to N^{3}LO; so have the leading four-body terms at N^{3}LO [EHM09; ME11].

In this work, we restrict ourselves to a single nucleonic Hamiltonian with an N^{3}LO nucleon-nucleon [EM03] and a local three-nucleon interaction at N^{2}LO [Nav07]. This Hamiltonian has been extensively tested in nucleonic calculations and reproduces experimental data on *p*-shell nuclei well.

2.2. The Hyperon-Nucleon Interaction

There are some differences between the NN and the YN interaction. First, hyperons and nucleons are distinguishable particles so there can be antisymmetric spin-orbit interaction terms, like terms proportional to $(\vec{s}_1 - \vec{s}_2) \cdot \vec{L}$, which are absent in the NN interaction. These terms are forbidden for identical particles because they are not invariant under permutation of particles. Antisymmetric spin-orbit terms facilitate transitions between $S = 0$ and $S = 1$ states in partial waves with $J = L$.

Also, the spectrum of hyperons (cf. table 2.1) features a small gap of 77 MeV between the Λ and the Σ isotriplet; much smaller than, e.g., the gap between the nucleons and the Δ resonance, which is 293 MeV. This small gap implies that we cannot ignore the Σ degrees of freedom but have to consider terms that convert a $|\Lambda N\rangle$ state to a $|\Sigma N\rangle$ state. The Λ-Σ conversion plays an important role in the binding of hypernuclei, and in explaining the spectra of the *s*-shell systems $^4_\Lambda$H and $^4_\Lambda$He [GAC$^+$94; HKM$^+$01; NAS02; NKG02].

The YN interaction is weaker than the NN interaction. There is no YN two-body bound state analogous to the deuteron. The lightest bound hypernucleus is the hypertriton $^3_\Lambda$H, which is extremely weakly bound with a hyperon separation energy $B_\Lambda = 0.13(5)$ MeV [Dav05].

Like the NN interaction, the YN interaction is not fundamentally known, although it should be derivable from QCD. Therefore, one has to resort to modeling the interaction and fitting the parameters of the model to the available data. Since YN scattering is inherently difficult due to the short lifetime of the hyperons, experimental data is very scarce, and the YN interaction is much less constrained than the NN interaction.

For a long time, the main tool for developing YN interaction models was the meson-exchange picture, where the baryons interact by emitting and absorbing single scalar, pseudoscalar, and vector mesons. Some newer models go beyond the one-meson exchange approximation and incorporate the correlated exchange of two mesons. This has lead to families of potentials that

successfully describe the available scattering data and some of the data on s-shell hypernuclei, e.g., the Nijmegen [MRS89; RSY99; RY06] and Jülich potentials [RHK$^+$96; HM05]. Recently, there have been attempts at computing YN scattering observables [BBL$^+$07] or a YN potential [Nem09; NAD$^+$17] directly from Lattice QCD, but the former used unphysical quark masses, and the latter still suffer from statistical uncertainties.

One can also extend the idea of chiral effective field theory to more general baryon-baryon interactions by considering flavor SU(3) symmetry: This chiral effective field theory includes the octet baryons and pseudoscalar mesons
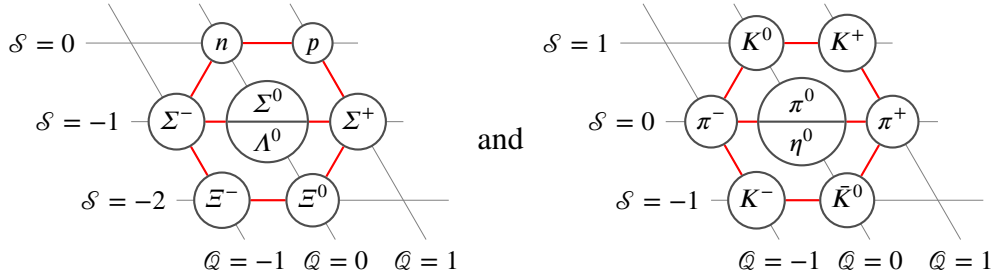
as degrees of freedom. Compared to the SU(2) symmetry that is associated with isospin in the nucleonic sector, the SU(3) is more strongly broken due to the higher mass of the strange quark. Still, the symmetry provides the basis for a systematic expansion even if it is broken and reduces the number of free parameters that have to be fitted to experiment. This is crucial for the YN interaction where data is scarce.

Hyperon-nucleon potentials are available at LO [PHM06] and NLO [HPK$^+$13]. There is also an NLO potential for the $\mathcal{S} = -2$ sector [HMP16]. In this work, we use the LO interaction because there are only five LECs at this order. These can be constrained by YN scattering data only, in contrast to the NLO potentials, which need to use NN data to fit the additional LECs. This mixing of data sources is necessary to fix the P-wave LECs, which are impossible to constrain from the YN data set, which consists mostly of total cross sections. However, the S-wave LECs determined from NN data are incompatible with those determined from the YN data set [HPK$^+$13], so the validity of the P-wave LECs might be uncertain. Thus, we take the LO potential and investigate its predictions for the structure of hypernuclei, solely based on YN data. However, the methods we present in the following only need matrix elements of the interaction, so other interactions can be easily tested in the future.

3. Similarity Renormalization Group

The baryon-baryon interaction contains significant short-range and tensor correlations that manifest as large matrix elements coupling low- and high-momentum states. This coupling has to be included into the model space of the many-body method in order to get converged energies and wavefunctions. This inclusion is, however, computationally very expensive so that convergence cannot be reached for all but the lightest systems.

Alternatively, one can transform the Hamiltonian to a form that is more amenable to the many-body calculation. The transformation itself should leave all observables invariant, which is guaranteed if the transformation is unitary. Examples of transformations of the Hamiltonian are the $V_{\mathrm{low}k}$ [BKS03], Okubo-Lee-Suzuki [Ôku54; LS80], Unitary Correlation Operator Method [FNR$^+$98] and Similarity Renormalization Group (SRG) approaches [GW93; Weg94; BFP07]. The SRG, on which we will focus in the following, is conceptually simple and very powerful.

3.1. Formalism

The SRG is derived from a general unitary transformation of the Hamiltonian

$$\boldsymbol{H}(\alpha) \equiv \boldsymbol{U}^{\dagger}(\alpha)\boldsymbol{H}(0)\boldsymbol{U}(\alpha) \tag{3.1}$$

that depends on a continuous flow parameter α. Differentiating, we get

$$\frac{\mathrm{d}\boldsymbol{H}(\alpha)}{\mathrm{d}\alpha} = \frac{\mathrm{d}\boldsymbol{U}^{\dagger}(\alpha)}{\mathrm{d}\alpha}\boldsymbol{H}(0)\boldsymbol{U}(\alpha) + \boldsymbol{U}^{\dagger}(\alpha)\boldsymbol{H}(0)\frac{\mathrm{d}\boldsymbol{U}(\alpha)}{\mathrm{d}\alpha}. \tag{3.2}$$

The transformation $\boldsymbol{U}(\alpha)$ is unitary, thus $\boldsymbol{U}^{\dagger}(\alpha)\boldsymbol{U}(\alpha) = \boldsymbol{U}(\alpha)\boldsymbol{U}^{\dagger}(\alpha) = \boldsymbol{1}$ and

$$0 = \frac{\mathrm{d}\boldsymbol{1}}{\mathrm{d}\alpha} = \frac{\mathrm{d}\boldsymbol{U}^{\dagger}(\alpha)}{\mathrm{d}\alpha}\boldsymbol{U}(\alpha) + \boldsymbol{U}^{\dagger}(\alpha)\frac{\mathrm{d}\boldsymbol{U}(\alpha)}{\mathrm{d}\alpha}. \tag{3.3}$$

With this, the derivative of the Hamiltonian is

$$\begin{aligned}
\frac{\mathrm{d}\boldsymbol{H}(\alpha)}{\mathrm{d}\alpha} &= \frac{\mathrm{d}\boldsymbol{U}^{\dagger}(\alpha)}{\mathrm{d}\alpha}\boldsymbol{U}(\alpha)\boldsymbol{U}^{\dagger}(\alpha)\boldsymbol{H}(0)\boldsymbol{U}(\alpha) + \boldsymbol{U}^{\dagger}(\alpha)\boldsymbol{H}(0)\boldsymbol{U}(\alpha)\boldsymbol{U}^{\dagger}(\alpha)\frac{\mathrm{d}\boldsymbol{U}(\alpha)}{\mathrm{d}\alpha} \\
&= \frac{\mathrm{d}\boldsymbol{U}^{\dagger}(\alpha)}{\mathrm{d}\alpha}\boldsymbol{U}(\alpha)\boldsymbol{U}^{\dagger}(\alpha)\boldsymbol{H}(0)\boldsymbol{U}(\alpha) - \boldsymbol{U}^{\dagger}(\alpha)\boldsymbol{H}(0)\boldsymbol{U}(\alpha)\frac{\mathrm{d}\boldsymbol{U}^{\dagger}(\alpha)}{\mathrm{d}\alpha}\boldsymbol{U}(\alpha) \\
&= [\boldsymbol{\eta}(\alpha), \boldsymbol{H}(\alpha)], \tag{3.4}
\end{aligned}$$

where the generator

$$\boldsymbol{\eta}(\alpha) \equiv \frac{\mathrm{d}\boldsymbol{U}^{\dagger}(\alpha)}{\mathrm{d}\alpha}\boldsymbol{U}(\alpha) = -\boldsymbol{U}^{\dagger}(\alpha)\frac{\mathrm{d}\boldsymbol{U}(\alpha)}{\mathrm{d}\alpha} \tag{3.5}$$

is an arbitrary anti-Hermitian operator defining the transformation.

While the eigenenergies of the Hamiltonian remain invariant under the SRG transformation, the eigenstates change. Consider the Schrödinger equation

$$\boldsymbol{H}(0) \, |\Psi_i(0)\rangle = E_i \, |\Psi_i(0)\rangle . \qquad (3.6)$$

Inserting identities and multiplying by $\boldsymbol{U}^\dagger(\alpha)$, we get

$$\boldsymbol{U}^\dagger(\alpha)\boldsymbol{H}(0)\boldsymbol{U}(\alpha)\boldsymbol{U}^\dagger(\alpha) \, |\Psi_i(0)\rangle = \boldsymbol{H}(\alpha)\boldsymbol{U}^\dagger(\alpha) \, |\Psi_i(0)\rangle = E\boldsymbol{U}^\dagger(\alpha) \, |\Psi_i(0)\rangle . \qquad (3.7)$$

The eigenstates of the initial and evolved Hamiltonian are therefore related by $|\Psi_i(\alpha)\rangle = \boldsymbol{U}^\dagger(\alpha) \, |\Psi_i(0)\rangle$. For observables to remain invariant, we have to demand that

$$\langle\Psi_i(0)|\boldsymbol{O}(0)|\Psi_j(0)\rangle = \langle\Psi_i(\alpha)|\boldsymbol{O}(\alpha)|\Psi_j(\alpha)\rangle = \langle\Psi_i(0)|\boldsymbol{U}(\alpha)\boldsymbol{O}(\alpha)\boldsymbol{U}^\dagger(\alpha)|\Psi_j(0)\rangle \qquad (3.8)$$

for an arbitrary observable $\boldsymbol{O}$. Hence, observables transform like the Hamiltonian,

$$\boldsymbol{O}(\alpha) = \boldsymbol{U}^\dagger(\alpha)\boldsymbol{O}(0)\boldsymbol{U}(\alpha), \qquad (3.9)$$

and obey the same flow equation (3.4). In general, the generator depends on the Hamiltonian so that both flow equations have to be solved simultaneously. If multiple observables are to be evolved, this becomes inefficient, and one can instead solve a differential equation for the transformation $\boldsymbol{U}(\alpha)$ itself, which is derived from (3.5):

$$\frac{\mathrm{d}\boldsymbol{U}(\alpha)}{\mathrm{d}\alpha} = -\boldsymbol{U}(\alpha)\boldsymbol{\eta}(\alpha). \qquad (3.10)$$

The generator governs the behavior of the Heisenberg-like flow equation (3.4). It is commonly chosen such that the desired behavior of the transformation corresponds to a trivial fixpoint of the generator. In the initial formulation for the many-body problem by Wegner [Weg94],[1] the generator is chosen as $\boldsymbol{\eta} = [\boldsymbol{H}_d(\alpha), \boldsymbol{H}(\alpha)]$, where $\boldsymbol{H}_d(\alpha)$ contains only the diagonal of $\boldsymbol{H}(\alpha)$, so the generator vanishes once $\boldsymbol{H}(\alpha) = \boldsymbol{H}_d(\alpha)$. This drives the Hamiltonian to diagonal form in the basis chosen for $\boldsymbol{H}_d(\alpha)$. Other choices for $\boldsymbol{H}_d(\alpha)$ are used to make the Hamiltonian block diagonal and using a different form for $\boldsymbol{\eta}$ can improve the speed of suppression of the offdiagonal matrix elements [Whi02].

Since we want to decouple low and high momenta, the kinetic energy is an obvious starting point for constructing a generator. Indeed, the conventional choice for nuclear-physics applications is [BFP07]

$$\boldsymbol{\eta}(\alpha) = m_N^2[\boldsymbol{T}_{\mathrm{int}}, \boldsymbol{H}(\alpha)], \qquad (3.11)$$

with the nucleon mass m_N fixing the units of the flow parameter. This choice drives the Hamiltonian to diagonal form in momentum space and to band-diagonal form in HO basis. With this choice, it is also convenient to define a flow-parameter-dependent potential $\boldsymbol{V}(\alpha)$ such that

$$\boldsymbol{H}(\alpha) \equiv \boldsymbol{\Delta M} + \boldsymbol{T}_{\mathrm{int}} + \boldsymbol{V}(\alpha). \qquad (3.12)$$

---

[1]Głazek and Wilson [GW93] independently proposed the method in a quantum-field-theory context and coined the name.

This absorbs SRG corrections to the kinetic energy and the mass term into the interaction.

The commutator structure of (3.4), as an operator differential equation, reveals a common feature of unitary transformations: if we evaluate a commutator $[\boldsymbol{A}, \boldsymbol{B}]$ of an m-body operator $\boldsymbol{A}$ with an n-body operator $\boldsymbol{B}$ in second quantization, the result is an operator with up to $(m + n - 1)$-body terms. Thus, if $\boldsymbol{\eta}$ is not a pure one-body operator, the flow equation induces interactions with particle rank beyond that of the initial Hamiltonian and, in general, up to the A-body level for an A-body system. Including all these terms is not feasible and we have to truncate the induced interaction terms at some lower particle rank. This breaks the unitarity of the transformation so that observables develop a flow-parameter dependence, which can be used to assess the importance of the neglected terms. For the YN interaction, this is done in section 4.7.

Equation (3.4) is an operator equation, but in order solve it numerically we have to choose a basis and turn it into a matrix ordinary differential equation (ODE). Since they are Galilei invariant, neither $\boldsymbol{T}_{\text{int}}$ nor $\boldsymbol{H}(\alpha)$ can have one-body parts and the first nontrivial evolution takes place in the two-body system. We can also exploit the symmetries of the Hamiltonian by working in a basis with good total angular momentum J defined with respect to the relative coordinate between the two particles. In the following, we thus consider the SRG evolution of a baryon-baryon interaction in a two-body relative-momentum and HO basis.

3.2. Evolution in Two-Body Momentum Space

A general basis for the two-body system is given by the set of states

$$|\vec{P}\rangle \otimes |[qL, (s_a s_b)S]JM, \chi_a \chi_b\rangle_n \tag{3.13}$$

with c.m. momentum $\vec{P}$, relative momentum q, orbital angular momentum L and spins s_a, s_b coupled to S, coupled to total angular momentum J with projection M. The collective quantum numbers $\chi_i = \{s_i t_i \tau_i \mathscr{S}_i\}$ denote a particle species with spin s_i, isospin t_i with projection τ_i and strangeness $\mathscr{S}_i$. The subscript n indicates a nonantisymmetric state. The overlap of two states is given by

$$\langle \vec{P}'|\vec{P}\rangle_n \langle [q'L', (s'_a s'_b)S']J'M', \chi'_a \chi'_b|[qL, (s_a s_b)S]JM, \chi_a \chi_b\rangle_n =$$
$$\delta^{\chi_a \chi_b}_{\chi'_a \chi'_b} \delta^{LSJM}_{L'S'J'M'} \delta^{(3)}(\vec{P}' - \vec{P})\frac{\delta(q' - q')}{q'q}, \tag{3.14}$$

which implies that the identity operator in relative space is

$$\mathbf{1} = \sum_{\substack{LSJM \\ \chi_a \chi_b}} \int \mathrm{d}q\, q^2\, |[qL, (s_a s_b)S]JM, \chi_a \chi_b\rangle_{n\,n}\langle [qL, (s_a s_b)S]JM, \chi_a \chi_b|. \tag{3.15}$$

Since we are dealing with fermions, we can restrict the basis to the antisymmetric subspace of normalized relative states given by

$$|[qL, (s_a s_b)S]JM, \chi_a \chi_b\rangle = \sqrt{2}(1 + \delta^{\chi_a}_{\chi_b})^{1/2} \mathscr{A}_{12}\, |[qL, (s_a s_b)S]JM, \chi_a \chi_b\rangle_n, \tag{3.16}$$

where

$$\mathcal{A}_{12} = \frac{1}{2}(1 - P_{12}) \tag{3.17}$$

is the antisymmetrizer in the two-body system, and P_{12} permutes the particles. The action of P_{12} on a nonantisymmetric state is

$$P_{12} \, |[qL, (s_a s_b)S]JM, \chi_a\chi_b\rangle_n = (-1)^{L+S-s_a-s_b} \, |[qL, (s_b s_a)S]JM, \chi_b\chi_a\rangle_n, \tag{3.18}$$

where the phase factor arises from an exchange of the coupling order in the spin Clebsch-Gordan coefficient and from the inversion of the argument of a spherical harmonic. States with identical particles are eigenstates of P_{12} with eigenvalue $(-1)^{L+S+1}$, because $2s_a$ is odd. They are also eigenstates of the antisymmetrizer, which is a polynomial of P_{12} and maps states with $L + S$ even (odd) to themselves (zero).

The antisymmetric basis states are eigenstates of the total angular momentum J^2, charge $\mathcal{Q}$ and strangeness $\mathcal{S}$. Charge and strangeness are connected by the Gell-Mann–Nishijima formula [Gel56]

$$\mathcal{Q} = M_T + \frac{1}{2}(A + \mathcal{S}) \tag{3.19}$$

Thus, the Hamiltonian splits into blocks of J, $\mathcal{S}$, and $\mathcal{Q}$ (or M_T), which can be evolved separately. Each block may consist of several partial waves $\nu = \{[L, (s_a s_b)S]J, \chi_a\chi_b\}$ of particles with the same total charge and strangeness, coupled by tensor or antisymmetric spin-orbit interactions. The Hamiltonian is also independent of the c.m. state so we can omit it in the following considerations.

Writing the momentum-space matrix elements of the interaction as

$$V_{\nu\nu'}(q, q'; \alpha) \equiv \langle [qL, (s_a s_b)S]J|V(\alpha)|[q'L', (s_a's_b')S']J\rangle, \tag{3.20}$$

where we omit the total angular momentum projection M for brevity because the interaction matrix elements are independent of it, we can evaluate the flow equation (3.4) with the generator given in (3.11) in two-body space,

$$\frac{dV_{\nu\nu'}(q, q'; \alpha)}{d\alpha} = m_N^2 \langle q\nu|[[T_{\text{int}}, V(\alpha)], H(\alpha)]|q'\nu'\rangle, \tag{3.21}$$

where we used that T_{int} and ΔM commute. The shift M_0 from ΔM drops out from all following formulae, so we omit it for brevity and work with the full mass operator M instead. In the two-body system, the intrinsic and relative kinetic energies coincide, and we can use the eigenvalue relations

$$T_{\text{int}} \, |q\nu\rangle = \frac{q^2}{2\mu_\nu} \, |q\nu\rangle, \tag{3.22}$$

$$M \, |q\nu\rangle = M_\nu \, |q\nu\rangle, \tag{3.23}$$

with total and reduced mass M_ν and μ_ν to expand the commutators:

$$\frac{dV_{\nu\nu'}(q, q'; \alpha)}{d\alpha} = m_N^2 \langle q\nu|[T_{\text{int}}V(\alpha) - V(\alpha)T_{\text{int}}, T_{\text{int}} + M + V(\alpha)]|q'\nu'\rangle$$
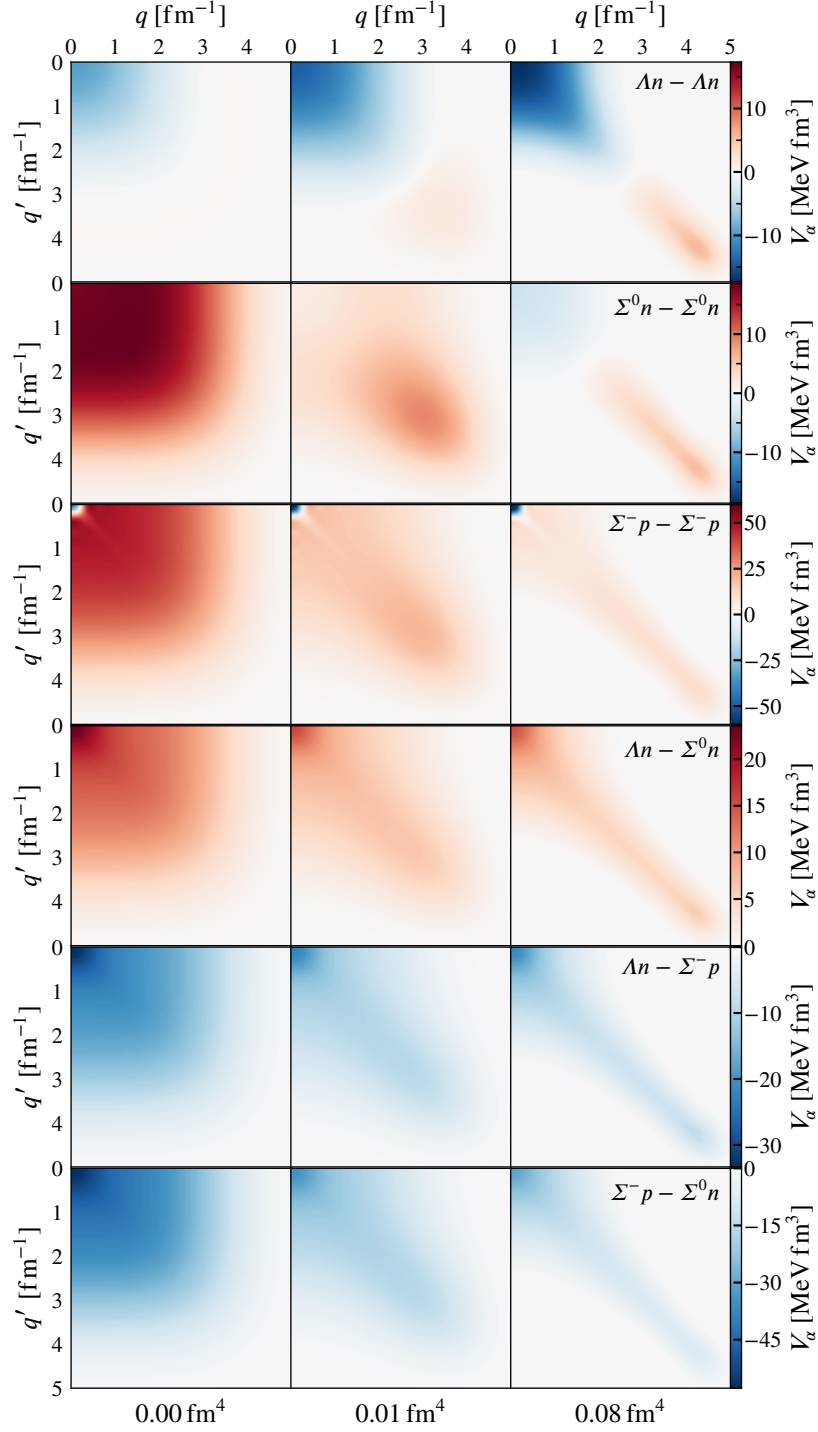
Figure 3.1.: Momentum-space matrix elements of the LO YN interaction with cutoff $\Lambda_Y = 700$ MeV/c for different flow parameters. Shown are the diagonal and conversion potentials in the $\mathcal{Q} = 0$, $^1S_0$ block for the bare interaction (left column), a slightly evolved interaction ($\alpha = 0.01$ fm^4, middle column), and the interaction at the flow parameter that is commonly used in many-body calculations ($\alpha = 0.08$ fm^4, right column).

$$
\begin{aligned}
&= m_N^2 \langle q\nu| \left(\boldsymbol{T}_{\text{int}} \boldsymbol{V}(\alpha)(\boldsymbol{T}_{\text{int}} + \boldsymbol{M}) - \boldsymbol{V}(\alpha)\boldsymbol{T}_{\text{int}}(\boldsymbol{T}_{\text{int}} + \boldsymbol{M}) + \text{h.c.} \right) \\
&\qquad + \boldsymbol{V}(\alpha)\boldsymbol{V}(\alpha)\boldsymbol{T}_{\text{int}} + \boldsymbol{T}_{\text{int}}\boldsymbol{V}(\alpha)\boldsymbol{V}(\alpha) - 2\boldsymbol{V}(\alpha)\boldsymbol{T}_{\text{int}}\boldsymbol{V}(\alpha) \, |q'\nu'\rangle \\
&= -m_N^2 \left(\frac{q^2}{2\mu_\nu} - \frac{q'^2}{2\mu_{\nu'}} \right) \left(\frac{q^2}{2\mu_\nu} - \frac{q'^2}{2\mu_{\nu'}} + M_\nu - M_{\nu'} \right) V_{\nu\nu'}(q, q'; \alpha) \\
&\quad + m_N^2 \sum_{\nu''} \int \mathrm{d}q'' \, q''^2 \left(\frac{q^2}{2\mu_\nu} - 2\frac{q''^2}{2\mu_{\nu''}} + \frac{q'^2}{2\mu_{\nu'}} \right) V_{\nu\nu''}(q, q''; \alpha) V_{\nu''\nu'}(q'', q'; \alpha).
\end{aligned}
$$
$$(3.24)$$

To perform a numerical solution of this integro-differential equation, we need to discretize the integral. Since the chiral potentials are very smooth and are already regulated in momentum space, we find that a simple equidistant grid with $0.1\,\text{fm}^{-1}$ spacing and a maximum momentum of $7\,\text{fm}^{-1}$ suffices to capture and evolve the interaction. The discretization turns (3.24) into a system of coupled ODEs, which can also be cast into matrix form and solved via standard numerical methods.

The process is illustrated for the $\mathcal{Q} = 0$, ${}^1S_0$ block of the LO YN interaction in fig. 3.1. Each row shows the (particle diagonal or particle conversion) potential at three points during the evolution: the initial potential, at a low flow parameter, and at the end of the flow. One can clearly see the flow driving the potential towards a diagonal form. Simultaneously, the Λn interaction becomes more attractive at low momenta while developing a repulsive component at higher momenta. Being offdiagonal, the transition potentials get slowly suppressed during the flow.

3.3. Evolution in Harmonic-Oscillator Basis

The evolution in HO basis is more straight forward than in momentum space because the identity operator needs no additional scaling factors. Also, the basis is already discrete, so the integrals on right-hand side of the ODE become ordinary sums and no additional discretization has to be done. An expansion of the commutators in (3.4) provides no further insight because the kinetic energy is not diagonal in this basis. Thus, we compute matrix representations of the intrinsic kinetic energy and the Hamiltonian up to a maximum HO energy $E_{2\text{max}}$,

$$
\mathrm{T}_{n\nu,n'\nu'} = \frac{1}{2}\Omega \times
\begin{cases}
2n + L + \frac{3}{2} & : n = n' \\
\sqrt{n'\left(n + L + \frac{3}{2}\right)} & : n = n' - 1 \\
\sqrt{n\left(n' + L + \frac{3}{2}\right)} & : n = n' + 1
\end{cases}
\tag{3.25}
$$

$$
\mathrm{M}_{n\nu,n'\nu'} = M_\nu \delta_{n'\nu'}^{n\nu}
\tag{3.26}
$$

$$
\mathrm{V}_{n\nu,n'\nu'} = \langle n\nu| \boldsymbol{V}(\alpha) |n'\nu'\rangle
\tag{3.27}
$$

$$
\mathrm{H}_{n\nu,n'\nu'}(\alpha) = \mathrm{M}_{n\nu,n'\nu'} + \mathrm{T}_{n\nu,n'\nu'} + \mathrm{V}_{n\nu,n'\nu'},
\tag{3.28}
$$

where n, n' are radial quantum numbers and the upright symbols denote matrices, and solve the flow equation for $\mathrm{H}(\alpha)$ by directly evaluating the resulting matrix commutators:

$$
\frac{\partial \mathrm{H}(\alpha)}{\partial \alpha} = [[\mathrm{T}, \mathrm{H}(\alpha)], \mathrm{H}(\alpha)]
\tag{3.29}
$$

After the SRG evolution, we recover the evolved interaction by subtracting the kinetic energy from the evolved Hamiltonian,

$$V_{n\nu,n'\nu'}(\alpha) = H_{n\nu,n'\nu'}(\alpha) - M_{n\nu,n'\nu'} - T_{n\nu,n'\nu'}. \qquad (3.30)$$

The initial interaction matrix elements are commonly given in momentum-space representation, and we need to convert them into HO basis before the evolution. Even if the evolution is done in momentum space, we still have to perform this basis conversion because most many-body methods either work in HO basis directly or use this basis as a starting point of the calculation. The conversion

$$V_{n\nu,n'\nu'}(\alpha) = \int \mathrm{d}q \int \mathrm{d}q' \, q^2 q'^2 \, \langle n\nu|q\nu\rangle \, \langle q\nu|V(\alpha)|q'\nu'\rangle \, \langle q'\nu'|n'\nu'\rangle \qquad (3.31)$$

is a double integral over momenta with the momentum-space representation of the HO wavefunction

$$\langle q\nu|n\nu\rangle = (-1)^n \sqrt{\frac{2n! b_\nu^3}{\Gamma\left(n + L + \frac{1}{2}\right)}} e^{-\frac{1}{2}(b_\nu q)^2} (b_\nu q)^L L_n^{(L+1/2)}\left((b_\nu q)^2\right), \qquad (3.32)$$

where $b_\nu \equiv (\mu_\nu \Omega)^{-1/2}$ is the oscillator length for the relative coordinate, Γ is Euler's gamma function, and $L_n^{(\alpha)}$ is an associated Laguerre polynomial. For simplicity, we discretize these integrals on the same grid that is used for the momentum-space evolution.

3.4. Stability of the Trivial Fixed Point

We constructed the SRG generator such that the flow equation has a trivial fixed point when the Hamiltonian is diagonal in momentum space. This fixed point actually designates a whole operator subspace because we can permute the diagonal elements of the Hamiltonian without causing nonvanishing matrix elements of the generator. A different question is whether the flow equation actually converges to the fixed point for large values of the flow parameter. A necessary condition for this is that the fixed point is stable.

Consider again the flow equation in momentum space (3.24). We assume that the Hamiltonian is diagonal in momentum space and create a small perturbation ϵ in an offdiagonal matrix element $\langle q_0 \nu_0 | V(\alpha) | q_0' \nu_0' \rangle$. Under these assumptions, the interaction may be written as

$$V_{\nu\nu'}(q, q'; \alpha) = \delta_{\nu'}^{\nu} \frac{\delta(q - q')}{qq'} V_{q\nu}(\alpha) + \left(\delta_{\nu_0}^{\nu} \delta_{\nu_0'}^{\nu'} \delta(q - q_0) \delta(q' - q_0') + \text{h.c.} \right) \epsilon(\alpha) \qquad (3.33)$$

with diagonal elements $V_{q\nu}$. We insert this ansatz into the flow equation and equate coefficients on both sides to get a flow equation for the perturbation:

$$\frac{\mathrm{d}\epsilon(\alpha)}{\mathrm{d}\alpha} = -m_N^2 \left(\frac{q_0^2}{2\mu_{\nu_0}} - \frac{q_0'^2}{2\mu_{\nu_0'}} \right) \left(\frac{q_0^2}{2\mu_{\nu_0}} - \frac{q_0'^2}{2\mu_{\nu_0'}} + M_{\nu_0} - M_{\nu_0'} \right) \epsilon(\alpha)$$

$$+ m_N^2 \left(\frac{q_0'^2}{2\mu_{\nu_0'}} - \frac{q_0^2}{2\mu_{\nu_0}} \right) \left(V_{q_0\nu_0}(\alpha) - V_{q_0'\nu_0'}(\alpha) \right) \epsilon(\alpha)$$
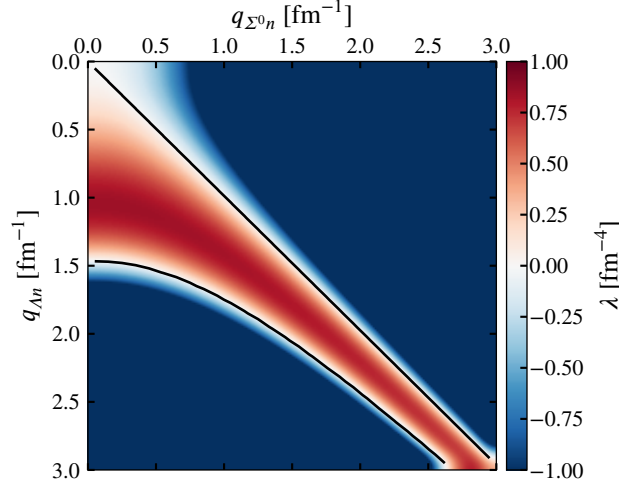
Figure 3.2.: The coefficient λ of the perturbation $\epsilon(\alpha)$ in the flow equation (3.35), for matrix elements between Λn and $\Sigma^0 n$ states. The contours denote the curve given by $d\epsilon/d\alpha = 0$. In the red-colored regions the perturbation is enhanced with incresing flow parameter, while it is suppressed in the blue-colored ones.

$$
= -m_N^2 \left(\frac{q_0^2}{2\mu_{\nu_0}} - \frac{q_0'^2}{2\mu_{\nu_0'}} \right) \left(\frac{q_0^2}{2\mu_{\nu_0}} - \frac{q_0'^2}{2\mu_{\nu_0'}} + M_{\nu_0} - M_{\nu_0'} + V_{q_0\nu_0}(\alpha) - V_{q_0'\nu_0'}(\alpha) \right) \epsilon(\alpha)
$$

$$
= -m_N^2 \left(\frac{q_0^2}{2\mu_{\nu_0}} - \frac{q_0'^2}{2\mu_{\nu_0'}} \right) \left(E_{q_0\nu_0}(\alpha) - E_{q_0'\nu_0'}(\alpha) \right) \epsilon(\alpha), \tag{3.34}
$$

where we identified eigenvalues of the Hamiltonian $E_{q\nu}(\alpha) = q^2/(2\mu_\nu) + M_\nu + V_{q\nu}(\alpha)$ in the last step. If the product of the kinetic energy differences and the total energy differences becomes negative, the perturbation is not suppressed but enhanced; the fixed point is unstable against such perturbations while it is stable against perturbations where the product stays positive.

If we assume that the diagonal elements of the interaction are only weakly dependent on q and the partial wave ν so that we can neglect the difference $V_{q_0\nu_0}(\alpha) - V_{q_0'\nu_0'}(\alpha)$, we can identify the mass term as the origin of the instability: The ODE (3.34) simplifies to

$$
\frac{d\epsilon(\alpha)}{d\alpha} = \lambda \epsilon(\alpha) \tag{3.35}
$$

with

$$
\lambda = -m_N^2 \left(\frac{q_0^2}{2\mu_{\nu_0}} - \frac{q_0'^2}{2\mu_{\nu_0'}} \right) \left(\frac{q_0^2}{2\mu_{\nu_0}} - \frac{q_0'^2}{2\mu_{\nu_0'}} + M_{\nu_0} - M_{\nu_0'} \right) \equiv -m_N^2 \delta T (\delta T + \delta M), \tag{3.36}
$$

which has the solution $\epsilon(\alpha) = \epsilon(0) \exp(\lambda\alpha)$. For hyperons, $\delta M \approx 77\,\text{MeV}$ in the Λ-Σ-converting parts of the interaction, so there is a region of low-momentum matrix elements where $\delta T < 0$ but $\delta T + \delta M > 0$ and small perturbations are enhanced. This is illustrated for the case of Λn-$\Sigma^0 n$ conversion in fig. 3.2, where we show the coefficient in the plane of

Λn and $\Sigma^0 n$ relative momenta $q_{\Lambda n}$ and $q_{\Sigma^0 n}$. In the lower triangle where $q_{\Lambda n} > q_{\Sigma^0 n}$, there is a region where the coefficient becomes positive, enhancing the perturbation with increasing flow parameter. The largest coefficients are of the order of $\lambda = 1\,\mathrm{fm}^{-4}$, so the flow amplifies the perturbation by a factor of e^α.

The flow can be stabilized by using $\boldsymbol{T}_{\mathrm{int}} + \boldsymbol{M}$ instead of just $\boldsymbol{T}_{\mathrm{int}}$ inside the generator. The additional term makes the coefficient a square with a negative sign, which suppresses all offdiagonal matrix elements independent of position. In practice, however, we ignore the stability issues: First, because the enhancement is small for the flow-parameter range that we are interested in. And, second, because the additional mass term in the generator will suppress the Λ-Σ conversion terms faster and induce stronger many-body terms (see section 4.7).

4. No-Core Shell Model

With the SRG-evolved interaction in place, the final ingredient needed to calculate observables of hypernuclei is a means of solving the quantum many-body problem. Our method of choice is the No-Core Shell Model (NCSM) because it is both powerful and conceptually simple. The NCSM is based on an expansion of the eigenstates of the many-body Hamiltonian in terms of HO states [BNV13]. It comes in two complementary formulations. The first formulation describes the system under consideration in terms of Jacobi relative coordinates, with respect to which the HO wavefunctions are defined, and uses an angular-momentum-coupled basis that fully exploits the Galilean invariance of the Hamiltonian. The symmetry-adapted basis dramatically reduces the dimension of the model spaces for a given truncation and thus enables us to consider larger basis-truncation parameters than would be possible without exploiting the symmetries. However, the basis states have to be explicitly antisymmetrized, which becomes computationally more and more difficult with increasing number of particles, and matrix elements of the Hamiltonian have to be embedded into the many-body basis via a computationally demanding procedure. This limits the range of applicability to $A \lesssim 7$ [NKB00; LMN16].

The second formulation, which we consider in the following, uses Slater determinants of HO states defined with respect to single-particle coordinates. The Slater-determinant basis does not have good angular momentum and contains c.m. degrees of freedom, which increase the model-space dimension compared to the Jacobi-coordinate formulation. Antisymmetrization of basis states, however, is trivial and computation of many-body matrix elements is inexpensive.

In both formulations, we compute a matrix representation of the Hamiltonian in the respective basis and use the Lanczos algorithm to extract a few of the lowest-energy eigenvalues and eigenstates. The eigenstates can be used to compute observables like radii or electromagnetic moments and transition rates. We first published the extension of both NCSM formulations for hypernuclei in [WGN$^+$14]. The details of the calculations are published in [WGN$^+$18].

4.1. Model Space

The NCSM model space is built from HO Slater determinants

$$|a_1, a_2, \ldots, a_A\rangle, \tag{4.1}$$

with single-particle states $a_i = \{n_i(l_i s_i)j_i m_i, \chi_i\}$. We truncate this infinite basis by limiting the total number of HO excitation quanta

$$\sum_{i=1}^{A}(2n_i + l_i) \leq N_{\max} + N_0 \tag{4.2}$$

with N_0 the number of quanta in the lowest Pauli-allowed state.

Due to rotational invariance and parity conservation of the Hamiltonian, we can impose additional constraints on the basis states that lower the model-space dimension: Rotational invariance implies that each eigenenergy of the Hamiltonian is $(2J + 1)$-fold degenerate, for total angular momentum J, and the eigenspace is spanned by states with different total angular-momentum projection $M = \sum_i m_i$. Parity conservation splits the Hilbert space into two sectors with positive and negative parity. Hence, we can selectively compute eigenstates with a definite projection M and parity in order to remove the degeneracy and reduce the dimension of the model space. The selection of a particular M gives rise to the name "*m* scheme" for this type of basis.

The untruncated *m*-scheme basis can accommodate any state with $J \geq |M|$, so that we can exclude low-spin states from the model space by choosing a larger value for the projection. However, we are most commonly targeting the whole low-lying spectrum and use $M = 0$ ($M = 1/2$) for even-A (odd-A) systems.

The parity of a basis state is given by $(-1)^{l_1 + \cdots + l_A}$. Since the single-particle energy is given by $e_i = 2n_i + l_i$, Slater determinants with an even total energy quantum number have positive parity while those with odd total energy have negative parity. Thus, a basis with definite parity only acquires new basis states every two steps in $N_{\max}$. Whether even $N_{\max}$ values correspond to positive or negative parity is determined by the parity of the lowest Pauli-allowed state. We call the parity of this state "natural parity", the opposite parity is called "unnatural".

The model space $\mathcal{M}(N_{\max})$ for a given value of $N_{\max}$ includes the model spaces for all smaller values,

$$\mathcal{M}(N_{\max} = 0) \subseteq \mathcal{M}(N_{\max} = 2) \subseteq \cdots \subseteq \mathcal{M}(N_{\max}) \subseteq \mathcal{M}(N_{\max} + 2) \subseteq \cdots \subseteq \mathcal{H}, \qquad (4.3)$$

where $\mathcal{H}$ is the many-body Hilbert space.[1] Since solving the eigenvalue equation in the model space $\mathcal{M}(N_{\max})$ for the ground state is equivalent to minimizing the energy functional

$$E[|\Psi\rangle] = \frac{\langle \Psi | H | \Psi \rangle}{\langle \Psi | \Psi \rangle} \qquad (4.4)$$

over this space, we get a monotonically-decreasing sequence of ground-state energies

$$E_0(N_{\max} = 0) \geq E_0(N_{\max} = 2) \geq \cdots \geq E_{\mathrm{gs}}. \qquad (4.5)$$

This variational principle ensures that the ground-state energy in each model space is an upper bound for the true ground-state energy E_{gs} that gets tighter with increasing $N_{\max}$. We thus have to perform a sequence of calculations, increasing $N_{\max}$ until the energies converge or until a reliable extrapolation is possible, in order to get the eigenenergies of the Hamiltonian.

Since the YN interaction couples pairs of particles with the same charge and strangeness, we have to include Slater determinants with different particle content into the basis. For example, the model space for the hypertriton $^3_\Lambda\mathrm{H}$ contains states of the types $|pn\Lambda\rangle$, $|pn\Sigma^0\rangle$, $|pp\Sigma^-\rangle$, and $|nn\Sigma^+\rangle$. These additional particle contents increase the model space dimension dramatically.

---

[1] The same argument can be made for the unnatural-parity model spaces with $N_{\max} = 1, 3, \ldots$.
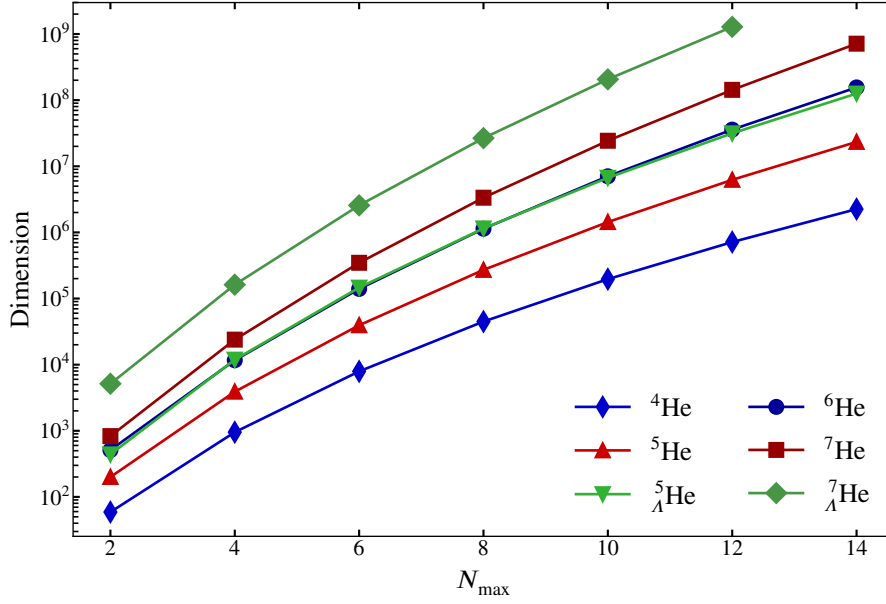
Figure 4.1.: Dimension of the NCSM model space for natural parity and $M = \{0, 1/2\}$ as function of N_{max} for the two hypernuclei $^5_\Lambda$He and $^7_\Lambda$He, compared to their nucleonic parents and the nuclei obtained by replacing the hyperon with a neutron.

A comparison of model-space dimensions for two hypernuclei and related nuclei is shown in fig. 4.1. Comparing the curves for ^{4}He, ^{5}He, and $^5_\Lambda$He, we see an N_{max}-dependent factor between the model-space dimensions. At $N_{\text{max}} = 14$, the model space for ^{4}He contains 2.3×10^6 states, which is one order of magnitude below the model space for ^{5}He, having a dimension of 2.3×10^7. The model space for the hypernucleus $^5_\Lambda$He has 1.3×10^8 basis states, adding another order of magnitude. For ^{6}He, the effect is similar: The spaces at $N_{\text{max}} = 12$ have dimensions 3.6×10^7, 1.4×10^8, and 1.3×10^9. Here, adding a hyperon increases the model space about nine times as much as adding another nucleon. Overall, the dimension of the model space grows rapidly with both N_{max} and A, which limits applications of the NCSM to light systems.

4.2. Matrix Elements

Having defined a finite model space, we next compute a matrix representation of the Hamiltonian in the *m*-scheme basis. The basis states being Slater determinants, we can use Slater-Condon rules to evaluate many-body matrix elements. For a two-body operator

$$\boldsymbol{O} = \sum_{i<j} \boldsymbol{o}_{ij}, \tag{4.6}$$

where $\boldsymbol{o}_{ij}$ acts on particles i and j, we can divide the nonvanishing many-body matrix elements into three classes, depending on the number of differing single-particle states d between the bra

and ket determinant:

$$d = 0 : \qquad \langle a_1 \cdots a_A | \boldsymbol{O} | a_1 \cdots a_A \rangle = \frac{1}{2!} \sum_{i,j=1}^{A} \langle a_i a_j | \boldsymbol{o} | a_i a_j \rangle , \qquad (4.7\text{a})$$

$$d = 1 : \qquad \langle a_1 \cdots a_{A-1} a_A | \boldsymbol{O} | a_1 \cdots a_{A-1} a'_A \rangle = \sum_{i=1}^{A-1} \langle a_i a_A | \boldsymbol{o} | a_i a'_A \rangle , \qquad (4.7\text{b})$$

$$d = 2 : \qquad \langle a_1 \cdots a_{A-2} a_{A-1} a_A | \boldsymbol{O} | a_1 \cdots a_{A-2} a'_{A-1} a'_A \rangle = \langle a_{A-1} a_A | \boldsymbol{o} | a'_{A-1} a'_A \rangle . \qquad (4.7\text{c})$$

Here, $\boldsymbol{o}$ denotes the two-body operator not embedded into the A-body space. Matrix elements for one- and three-body operators are computed in an analogous fashion. The Slater determinants shown are in maximum-matching order, where only the last d states differ between bra and ket and the others are identical. Since exchanging two states only adds a phase factor -1, we can evaluate many-body matrix elements between states in this order by sorting the determinants accordingly and tracking the resulting phase. Matrix elements with three or more differing states vanish because an n-body operator can connect at most n pairs of differing states.

This property is another advantage of a Slater determinant basis: the resulting many-body matrix is inherently very sparse. Moreover, we can predict the locations of potential nonzero matrix elements by looking at the respective bra and ket states.[2] All other matrix elements vanish automatically and need not be computed.

4.2.1. Conversion to Single-Particle Coordinates

To evaluate the many-body matrix elements of a two-body operator like the YN interaction or the intrinsic kinetic energy, we need two-body matrix elements with respect to single-particle states, but the interaction and intrinsic kinetic energy are given in terms of HO matrix elements with respect to the relative coordinate of the two particles. Thus, we have to transform between these two sets of coordinates. Three-body interactions need a similar transformation, which is considered in chapter 5.

The transformation is a computation-intensive task so we want to save the resulting matrix elements. However, storing m-scheme matrix elements is not very efficient because the basis does not exploit rotational invariance to the full extent. Therefore, we store the matrix elements in an intermediate basis where the single-particle states are coupled to good total angular momentum, $|(\bar{a}\bar{b})JM\rangle$, where the symbols $\bar{a} = a \setminus \{m_a\}$ collect the quantum numbers of the single-particle states. The bar over the symbol denotes omission of the total angular-momentum projection m_a.

Just like in chapter 3, we need antisymmetrized states, which we get by applying the antisymmetrizer to a product state,

$$\mathscr{A}_{12} |(\bar{a}\bar{b})JM\rangle_p = \tfrac{1}{2} \big(|(\bar{a}\bar{b})JM\rangle - (-1)^{j_a + j_b - J} |(\bar{b}\bar{a})JM\rangle \big), \qquad (4.8)$$

and the normalized antisymmetrized state is

$$|(\bar{a}\bar{b})JM\rangle = \sqrt{2} \mathscr{N} \mathscr{A}_{12} |(\bar{a}\bar{b})JM\rangle_p \qquad (4.9)$$

---

[2]One can lower the effort further by grouping the states according to their orbital occupation and exclude matrix elements between groups of states if the occupations differ by more than n [SNY⁺08].

with $\mathcal{N} = (1 + \delta_{b}^{\bar{a}})^{-1/2}$ a normalization coefficient.

The transformation between the coordinate systems itself is effected by HO brackets (see appendix A.4). These depend on a parameter d that defines the orthogonal transformation between the two sets of coordinates. In order to make the transformation between the relative and single-particle coordinates orthogonal, we define scaled versions of the single-particle coordinates $\vec{r}_i$,

$$\vec{x}_i \equiv \sqrt{\frac{m_i}{m_N}}\vec{r}_i. \tag{4.10}$$

The nucleon mass m_N is an arbitrary scale chosen so that the scaled and unscaled coordinates coincide for nucleons. Additionally, we define the two-body Jacobi coordinates

$$\vec{\xi}_0 \equiv \frac{1}{\sqrt{M_2}}(\sqrt{m_1}\vec{x}_1 + \sqrt{m_2}\vec{x}_2) = \sqrt{\frac{M_2}{m_N}}\vec{R} \tag{4.11a}$$

$$\vec{\xi}_1 \equiv \sqrt{\frac{m_1 m_2}{M_2}}\left(\frac{1}{\sqrt{m_1}}\vec{x}_1 - \frac{1}{\sqrt{m_2}}\vec{x}_2\right) = \sqrt{\frac{\mu_{12}}{m_N}}\vec{r} \tag{4.11b}$$

that are proportional to the c.m. coordinate $\vec{R}$ and to the relative coordinate $\vec{r}$, respectively. The symbol $M_2 = m_1 + m_2$ denotes the total mass of the two particles.

From this definition, we can read off $d = m_a/m_b$, i.e., the mass ratio of the two particles. The transformation works as follows[3]: first, the coupling scheme is changed from jj type to LS type coupling using a 9j symbol. Then, the HO bracket can be inserted to transform between the coordinate systems, introducing sums over relative and c.m. radial and orbital quantum numbers $N\Lambda, n\lambda$. The next step changes the coupling order from $[(\Lambda\lambda)LS]J$ to $[\Lambda(\lambda S)j]J$ using a 6j symbol. In the final step, the c.m. and relative angular momenta are decoupled via a Clebsch-Gordan coefficient. The final result, which expresses a state in the J-coupled basis in terms of relative and c.m. HO states, reads

$$|(\bar{a}\bar{b})JM\rangle = \mathcal{N}(1 + \delta_{\chi_b}^{\chi_a})^{\frac{1}{2}} \sum_{j} \sum_{\substack{N\Lambda \\ n\lambda}} \sum_{LS} \sum_{m_\Lambda m_j} (-1)^{\Lambda+\lambda+S+J}\hat{L}^2\hat{S}\hat{j}\hat{j}_a\hat{j}_b$$

$$\times \begin{Bmatrix} l_a & s_a & j_a \\ l_b & s_b & j_b \\ L & S & J \end{Bmatrix} \begin{Bmatrix} \Lambda & \lambda & L \\ S & J & j \end{Bmatrix} \begin{pmatrix} \Lambda & j \\ m_\Lambda & m_j \end{pmatrix} \begin{vmatrix} J \\ M \end{vmatrix} \langle\!\langle N\Lambda, n\lambda \mid n_1 l_1, n_2 l_2 : L \rangle\!\rangle_d$$

$$\times |N\Lambda m_\Lambda\rangle |[n\lambda, (s_a s_b)S]jm_j, \chi_a\chi_b\rangle, \tag{4.12}$$

where we introduced shorthands $\hat{j} \equiv \sqrt{2j+1}$ for the angular momentum multiplicities. We apply the same transformation to the bra state to compute a matrix element of a two-body operator o:

$$\langle(\bar{a}'\bar{b}')JM|o|(\bar{a}\bar{b})JM\rangle =$$

---

[3]The step-by-step derivation can be found in [Wir13].

$$\mathcal{N}\mathcal{N}'(1 + \delta^{\chi_a}_{\chi_b})^{\frac{1}{2}}(1 + \delta^{\chi'_a}_{\chi'_b})^{\frac{1}{2}} \sum_{j} \sum_{N\Lambda} \sum_{\substack{n\lambda \\ n'\lambda'}} \sum_{\substack{LS \\ L'S'}} (-1)^{S+S'} \hat{L}^2 \hat{L}'^2 \hat{S}\hat{S}'\hat{j}^2 \hat{j}_a \hat{j}'_a \hat{j}_b \hat{j}'_b$$

$$\times \begin{Bmatrix} l_a & s_a & j_a \\ l_b & s_b & j_b \\ L & S & J \end{Bmatrix} \begin{Bmatrix} l'_a & s'_a & j'_a \\ l'_b & s'_b & j'_b \\ L' & S' & J \end{Bmatrix} \begin{Bmatrix} \Lambda & \lambda & L \\ S & J & j \end{Bmatrix} \begin{Bmatrix} \Lambda & \lambda' & L' \\ S' & J & j \end{Bmatrix}$$

$$\times \langle\!\langle N\Lambda, n\lambda \mid n_a l_a, n_b l_b : L \rangle\!\rangle_d \langle\!\langle N\Lambda, n'\lambda' \mid n'_a l'_a, n'_b l'_b : L' \rangle\!\rangle_{d'}$$

$$\times \langle [n'\lambda', (s'_a s'_b)S']j, \chi'_a \chi'_b | o | [n\lambda, (s_a s_b)S]j, \chi_a \chi_b \rangle, \tag{4.13}$$

where $d' = m'_a/m'_b$ is the mass ratio of the primed particles. Here, we exploited that the operator does not act on the c.m. coordinate.

We can recover *m*-scheme matrix elements from these matrix elements by removing the *J*-coupling:

$$\langle \bar{a}'m'_a, \bar{b}'m'_b | o | \bar{a}m_a, \bar{b}m_b \rangle = \sum_{JM} \begin{pmatrix} j'_a & j'_b \\ m'_a & m'_b \end{pmatrix} \begin{vmatrix} J \\ M \end{pmatrix} \begin{pmatrix} j_a & j_b \\ m_a & m_b \end{pmatrix} \begin{vmatrix} J \\ M \end{pmatrix} \mathcal{N}^{-1}\mathcal{N}'^{-1} \langle (\bar{a}'\bar{b}')JM | o | (\bar{a}\bar{b})JM \rangle. \tag{4.14}$$

The normalization factors $\mathcal{N}$ are often omitted in actual calculations because they appear as a prefactor in the transformation (4.13) and their inverse multiplies the coupled matrix element during decoupling so that they have no net effect.

Equation (4.13) is only valid for rotation-invariant operators, i.e., operators of spherical tensor rank zero; formulae for reduced matrix elements of nonzero-rank tensors are similar, but require additional recoupling steps. By virtue of the Wigner-Eckart theorem [VMK88],

$$\langle \alpha'j'm' | o^K_Q | \alpha j m \rangle = (-1)^{2K} \begin{pmatrix} j & K \\ m & Q \end{pmatrix} \begin{vmatrix} j' \\ m' \end{pmatrix} \frac{1}{\hat{j}'} \langle \alpha'j' \| o^K \| \alpha j \rangle, \tag{4.15}$$

we can express a general matrix element of a rank-*K* spherical tensor operator o^K_Q in terms of reduced matrix elements $\langle \alpha'j' \| o^K \| \alpha j \rangle$, which are independent of the projection quantum numbers. Here, α denotes the remaining quantum numbers of the state. For the transformation, we have to express a matrix element between c.m. and relative states coupled to good total angular momentum *J* in terms of the reduced matrix elements of o^K with respect to relative states. For this, we use [VMK88, eq. 13.(40)], which yields

$$\langle \{N'\Lambda', n'[\lambda', (s'_a s'_b)S']j'\}J'M' | o^K_Q | \{N\Lambda, n[\lambda, (s_a s_b)S]j\}JM \rangle = \delta^{N\Lambda}_{N'\Lambda'}(-1)^{J'-\Lambda'-j-K}\hat{j}$$

$$\times \begin{pmatrix} J & K \\ M & Q \end{pmatrix} \begin{vmatrix} J' \\ M' \end{pmatrix} \begin{Bmatrix} j & \Lambda & J \\ J' & K & j' \end{Bmatrix} \langle n'[\lambda', (s'_a s'_b)S']j' \| o^K \| n[\lambda, (s_a s_b)S]j \rangle. \tag{4.16}$$

Finally, we have to reduce the resulting matrix element to remove the dependence on the projection quantum numbers. This is done via the inversion of the Wigner-Eckart theorem,

$$\langle \alpha'j' \| o^K \| \alpha j \rangle = \frac{(-1)^{2K}}{\hat{j}'} \sum_{mm'Q} \begin{pmatrix} j & K \\ m & Q \end{pmatrix} \begin{vmatrix} j' \\ m' \end{pmatrix} \langle \alpha'j'm' | o^K_Q | \alpha j m \rangle. \tag{4.17}$$

Using (4.12) together with these two relations, we arrive at

$$
\begin{aligned}
\langle (\bar{a}'\bar{b}')J \| o^K \| (\bar{a}\bar{b})J \rangle = {}& \mathcal{N}\mathcal{N}'(1 + \delta_{\chi_b}^{\chi_a})^{\frac{1}{2}}(1 + \delta_{\chi_b'}^{\chi_a'})^{\frac{1}{2}} \\
& \times \sum_{jj'} \sum_{\substack{N\Lambda \\ n'\lambda'}} \sum_{\substack{n\lambda \\ L'S'}} \sum_{LS} (-1)^{\lambda+\lambda'+S+S'+J'-\Lambda-j+K} \hat{L}^2 \hat{L}'^2 \hat{S}\hat{S}' \hat{j}\hat{j}' \, \hat{j}_a\hat{j}_a'\hat{j}_b\hat{j}_b' \hat{J}\hat{J}' \\
& \times \begin{Bmatrix} l_a & s_a & j_a \\ l_b & s_b & j_b \\ L & S & J \end{Bmatrix} \begin{Bmatrix} l_a' & s_a' & j_a' \\ l_b' & s_b' & j_b' \\ L' & S' & J' \end{Bmatrix} \begin{Bmatrix} \Lambda & \lambda & L \\ S & J & j \end{Bmatrix} \begin{Bmatrix} \Lambda & \lambda' & L' \\ S' & J' & j' \end{Bmatrix} \begin{Bmatrix} j & \Lambda & J \\ J' & K & j' \end{Bmatrix} \\
& \times \langle\!\langle N\Lambda, n\lambda \mid n_a l_a, n_b l_b : L \rangle\!\rangle_d \langle\!\langle N\Lambda, n'\lambda' \mid n_a'l_a', n_b'l_b' : L' \rangle\!\rangle_{d'} \\
& \times \langle n'[\lambda', (s_a's_b')S']j' \| o^K \| n[\lambda, (s_as_b)S]j \rangle.
\end{aligned} \tag{4.18}
$$

We can recover the respective *m*-scheme matrix elements by applying the Wigner-Eckart theorem and decoupling the result,

$$
\begin{aligned}
\langle \bar{a}'m_a', \bar{b}'m_b' | o^K | \bar{a}m_a, \bar{b}m_b \rangle = {}& \sum_{\substack{JM \\ J'M'}} \frac{(-1)^{2K}}{\hat{j}'} \begin{pmatrix} j_a' & j_b' \\ m_a' & m_b' \end{pmatrix}\!\begin{vmatrix} J' \\ M' \end{vmatrix} \begin{pmatrix} J & K \\ M & Q \end{pmatrix}\!\begin{vmatrix} J' \\ M' \end{vmatrix} \begin{pmatrix} j_a & j_b \\ m_a & m_b \end{pmatrix}\!\begin{vmatrix} J \\ M \end{vmatrix} \\
& \times \mathcal{N}^{-1}\mathcal{N}'^{-1} \langle (\bar{a}'\bar{b}')J' \| o^K \| (\bar{a}\bar{b})J \rangle.
\end{aligned} \tag{4.19}
$$

4.2.2. Matrix Elements of Intrinsic Observables

Observables that depend on the positions or momenta of particles relative to the c.m. of the system acquire a dependence on the total rest mass M_A of all particles and matrix elements have to be adapted to the system under consideration. To give an example, the intrinsic kinetic energy (cf. chapter 2)

$$
T_{\text{int}} = \sum_{i=1}^{A} \frac{\left(\vec{p}_i - \frac{m_i}{M_A}\vec{P} \right)^2}{2m_i} \tag{4.20}
$$

depends on the total mass and can be rewritten as a sum over relative two-body kinetic energies:

$$
T_{\text{int}} = \sum_{i<j} \frac{m_i + m_j}{M_A} T_{ij,\text{rel}}, \tag{4.21}
$$

where $T_{ij,\text{rel}} = q_{ij}^2/(2\mu_{ij})$ is the relative kinetic energy between particles i and j. Technically, these operators are A-body operators because they depend on the inverse of the total mass M_A but we can use that the Slater determinants are eigenstates of this operator to evaluate the inverse. Then, T_{int} can be exactly mapped to the generic two-body operator (4.6). Relative kinetic energy matrix elements can be computed in relative coordinates via (3.25) and transformed via the procedure described in the previous section. Formulae for other operators like radii have been derived in [Wir13] and are reproduced in appendix B for completeness.

Electromagnetic operators are also defined with respect to the c.m. of the system. The electric transition operators, for example, are given by

$$
\mathscr{E}(\lambda, \mu) \equiv \sum_{i=1}^{A} e_i \rho_i^\lambda Y_{\lambda\mu}(\vec{\rho}_i), \tag{4.22}
$$

where the $\vec{\rho}_i \equiv \vec{r}_i - \vec{R}$ are the particle coordinates in the c.m. frame, e_i is the charge operator for the ith particle, and $Y_{\lambda\mu}(\vec{r})$ denotes a spherical harmonic. To evaluate matrix elements of these operators, we can rewrite them in terms of operators of low particle rank. This is simple, e.g., for the electric dipole operator: using the explicit representation of the spherical harmonics Y_{1m} in cartesian coordinates, we see that the intrinsic dipole operator is the plain single-particle operator with a shifted charge:

$$\mathscr{E}(1, \mu) = \sum_{i=1}^{A} \left(e_i - \mathcal{Q}\frac{m_i}{M} \right) r_i Y_{1\mu}(\vec{r}_i). \tag{4.23}$$

The quadrupole becomes

$$\mathscr{E}(2, \mu) = \sum_{i<j}^{A} \left(\frac{e_i m_j + e_j m_i}{M} - \mathcal{Q}\frac{m_i m_j}{M^2} \right) r_{ij}^2 Y_{2\mu}(\vec{r}_{ij}), \tag{4.24}$$

with $\vec{r}_{ij} = \vec{r}_i - \vec{r}_j$.

These expressions become quite cumbersome, but in the NCSM, we do not need to use explicitly translation-invariant operators: We can express the single-particle transition operator in terms of irreducible tensor products of spherical harmonics with respect to coordinates in the c.m. frame and the c.m. coordinate [VMK88, eq. 5.5.(3)]:

$$\sum_{i=1}^{A} e_i r_i^{\lambda} Y_{\lambda\mu}(\vec{r}_i) = \sum_{i=1}^{A} e_i r_i^{\lambda} Y_{\lambda\mu}(\vec{\rho}_i + \vec{R})$$

$$= \sum_{l=0}^{\lambda} \sqrt{\frac{4\pi(2l + 1)(2\lambda - 2l + 1)}{2\lambda + 1}} R^{\lambda - l} \sum_{i=1}^{A} e_i \rho_i^l \{Y_l(\vec{\rho}_i) \otimes Y_{\lambda - l}(\vec{R})\}_{\lambda\mu}. \tag{4.25}$$

We take matrix elements of the transition operator between states $|(NL, \Psi j)JM\rangle$ consisting of a c.m. state $|NL\rangle$ and an intrinsic state $|\Psi j\rangle$ with good angular momentum. We also assume that the c.m. states on the bra and ket side are identical and that $L = 0$, which implies $J = j$ and $J' = j'$. The first component of the irreducible tensor product acts only on the intrinsic state, while the second acts only on the c.m. state. Also, the tensor product is linear, so we can include the sum over i and the factor $e_i \rho_i^l$ into the first component, recovering $\mathscr{E}(l)$. The matrix element evaluates to

$$\langle (N0, \Psi'J')J'M'|\{\mathscr{E}(l) \otimes Y_{\lambda - l}(\vec{R})\}_{\lambda\mu}|(N0, \Psi J)JM\rangle$$

$$= \hat{\lambda}\hat{J} \left(\begin{matrix} J & \lambda \\ M & \mu \end{matrix} \middle| \begin{matrix} J' \\ M' \end{matrix} \right) \begin{Bmatrix} (\lambda - l) & l & \lambda \\ 0 & J' & J' \\ 0 & J & J \end{Bmatrix} \langle \Psi'J' \| \mathscr{E}(l) \| \Psi J \rangle \langle N0 \| Y_{\lambda - l}(\vec{R}) \| N0 \rangle, \tag{4.26}$$

and it follows from the properties of the 9j symbol that the matrix element vanishes unless $\lambda = l$. In that case, the reduced matrix element becomes $\langle N0 \| Y_0(\vec{R}) \| N0 \rangle = (4\pi)^{-1/2}$, the 9j symbol assumes a simple value, and we get

$$\langle (N0, \Psi'J')J'M'|\{\mathscr{E}(l) \otimes Y_{\lambda - l}(\vec{R})\}_{\lambda\mu}|(N0, \Psi J)JM\rangle$$

$$= \frac{\hat{\lambda}\hat{J}}{\sqrt{4\pi}\hat{J}\hat{J}'} \left(\begin{matrix} J & \lambda \\ M & \mu \end{matrix} \middle| \begin{matrix} J' \\ M' \end{matrix} \right) \langle \Psi'J' \| \mathscr{E}(l) \| \Psi J \rangle$$

$$= \frac{1}{\sqrt{4\pi}} \langle \Psi' J' M' | \mathscr{E}(l) | \Psi J M \rangle, \tag{4.27}$$

where we used the Wigner-Eckart theorem to unreduce the matrix element. Substituting these results back into (4.25), we arrive at

$$\langle (N0, \Psi' J') J' M' | \sum_{i=1}^{A} r_i^\lambda Y_{\lambda\mu}(\vec{r}_i) | (N0, \Psi J) J M \rangle = \langle \Psi' J' M' | \mathscr{E}(l) | \Psi J M \rangle. \tag{4.28}$$

Hence, matrix elements of the simple single-particle transition operator with respect to states with c.m. degrees of freedom are identical to those of the intrinsic transition operator with respect to the corresponding intrinsic states, provided that the bra and ket states have the same c.m. state with $L = 0$. In the next section, we show that the c.m. degrees of freedom of NCSM eigenstates can be forced into such a state.

4.3. Center-of-Mass Degrees of Freedom

Since we use single-particle coordinates to define our basis states, the calculation includes c.m. degrees of freedom. These are redundant, but decouple from the intrinsic degrees of freedom in an NCSM calculation. The HO basis is unique with respect to the transformation between different sets of coordinates: the HO brackets, which mediate the transformation, conserve the total HO energy. In consequence, the set of states given with respect to one system of coordinates that comprise the expansion of a HO state given in another system is finite. For example, we can exactly expand any HO state with total energy quantum number E, given in relative coordinates, in a set of Slater determinants with the same total energy and vice versa. Since the state in relative coordinates can be factorized into a c.m. and intrinsic part, that factorization is also possible for eigenstates of the Hamiltonian if we include all basis states up to a certain maximum energy. Hence, the use of the $N_{\max}$ truncation scheme together with a HO single-particle basis guarantees factorization of the intrinsic and c.m. states at every finite truncation value. Other single-particle bases provide this factorization only in the limit of the full Hilbert space.

While the states factorize, there can be a residual effect of the c.m. state on the intrinsic one due to the model-space truncation: Consider a state $|\psi\rangle = |ELM_L\rangle_{\mathrm{c.m.}} \otimes |\psi\rangle_{\mathrm{intr.}}$ in an $N_{\max}$-truncated space. The maximum total HO energy of this state is $E_{\max} = N_{\max} + N_0$. If the c.m. state is excited to an energy E this excitation takes up HO quanta and the effective model space for the intrinsic state is reduced from $E_{\max}$ to $E_{\max} - E$. Thus, intrinsic states of eigenstates carrying a c.m. excitation correspond to intrinsic states computed at smaller $N_{\max}$ without c.m. excitations. These states consequently appear at a higher energy—the energy they had for $N'_{\max} = N_{\max} - E$. If we sort the spectrum of the Hamilton matrix by the energy of the c.m. excitation, we can extract all results for smaller $N_{\max}$ values from a single calculation. However, the excited c.m. state can carry orbital angular momentum that couples to the total angular momentum of the intrinsic state and creates a multiplet of degenerate states.

Overall, states with c.m. excitations carry no new information and the degeneracy slows down the convergence of the eigenvalue solver. We, therefore, remove them from the low-lying

spectrum of the Hamiltonian by adding a Hamiltonian acting on the c.m., which yields the total Hamiltonian

$$\boldsymbol{H}_{\text{tot}} = \boldsymbol{H}_{\text{int}} + \beta \boldsymbol{H}_{\text{c.m.}}, \tag{4.29}$$

where we denote the Hamiltonian that acts on the intrinsic state only by $\boldsymbol{H}_{\text{int}}$ for clarity. The c.m. Hamiltonian is a HO Hamiltonian with the same frequency Ω as the basis, shifted so that the ground state has zero energy:

$$\boldsymbol{H}_{\text{c.m.}} = \frac{\vec{\boldsymbol{P}}^2}{2\boldsymbol{M}} + \frac{1}{2}\boldsymbol{M}\Omega^2\vec{\boldsymbol{R}}^2 - \frac{3}{2}\Omega. \tag{4.30}$$

Like the intrinsic kinetic energy, it can be decomposed into zero-, one- and two-body parts (cf. appendix B.3). The strength is controlled by a parameter β, which we commonly choose as $\beta = 1$ to shift excitations by 2Ω (excitations have increments of two due to parity) while avoiding numerical instabilities.

4.4. Solution of the Eigenvalue Problem

After computing the large sparse matrix of the Hamiltonian $\boldsymbol{H}_{\text{tot}}$ in the *m*-scheme basis, we have to compute its eigenvalues and eigenvectors. Commonly used direct methods like the QR algorithm are unsuitable because they do not exploit the sparsity of the matrix and compute all eigenpairs, whereas our focus lies on the low-lying states. Also, storing a full many-body matrix simply requires too much computer memory for all but the smallest problems.

   Hence, we employ a sophisticated version of the Lanczos algorithm [Lan50], as it is implemented in the ARPACK library [LSY97]. The Lanczos algorithm is an iterative method that is ideally suited for computing a small set of extremal eigenpairs of a symmetric sparse matrix A, because the only operation involving the large sparse matrix is a matrix-vector multiplication, whose runtime is linear in the number of nonzero matrix elements, and because the extremal eigenpairs converge fastest.

   The basic idea of the algorithm is the construction of an orthogonal basis of the Krylov subspace

$$\mathscr{K}_n(\text{A}, \vec{v}_1) = \text{span}\{\vec{v}_1, \text{A}\vec{v}_1, \dots, \text{A}^{n-1}\vec{v}_1\} \tag{4.31}$$

for an arbitrary pivot vector $\vec{v}_1$. The construction is such that the matrix A is tridiagonal in this basis and all matrix elements are computed during the basis construction. The projection of the matrix A onto the *n*-dimensional Krylov subspace $\mathscr{K}_n$ provides approximations to the eigenvalues and eigenvectors of the matrix. The error of these approximations with respect to the true eigenvectors is in the direction of the next basis vector that would be added to form the subspace $\mathscr{K}_{n+1}$. Thus, the Lanczos method provides a sequence of approximations to the eigenpairs of A that are improved systematically by increasing the dimension *n* of the subspace. The lowest and highest eigenpairs of the matrix commonly converge very fast so that *n* can be much smaller than the linear dimension of the matrix. Typically, $n \sim 100$ suffices to get the low-lying eigenvalues with an accuracy of 10^{-4} MeV.

   In practical implementations, roundoff errors introduced by finite precision arithmetic and memory constraints limit the maximum size of the subspace. The roundoff errors lead to loss of

orthogonality of the Lanczos basis vectors, creating spurious copies of eigenpairs. To address both issues, more sophisticated implementations reorthogonalize the basis vectors and use a restarting mechanism that computes a new pivot vector $\vec{v}_1$ from the results of the current iteration step to construct a new Krylov subspace once the dimension grows beyond a set limit.

4.5. Importance Truncation

The increase of the NCSM model-space dimension with N_{max} and particle number A severely limits its range of applicability. The problem is exacerbated for hypernuclei because model-space dimensions are larger from the outset and exhibit the same scaling.

In order to mitigate the model-space growth and extend the range of applicability of the NCSM we introduce an importance-truncation scheme that was successfully employed for nuclei [Rot09]. Consider the basis expansion of a low-lying eigenstate of the Hamiltonian

$$|\Psi_k\rangle = \sum_\nu c_{k,\nu} |\phi_\nu\rangle \tag{4.32}$$

in terms of Slater determinants $|\phi_\nu\rangle$. This state is most likely dominated by a few low-lying determinants while the expansion coefficients $c_{i,\nu}$ for many high-lying basis states are very small. These states could be omitted from the model space without affecting the resulting energy and other observables very much.

This raises the question of how to determine which states are important for the low-lying spectrum of the Hamiltonian without actually solving the eigenvalue problem. To achieve this, we start from a reference state $|\Psi_{k,\mathrm{ref}}\rangle$ that is an eigenstate from a diagonalization in a smaller reference space $\mathscr{M}_{\mathrm{ref}}$. This state obeys the eigenvalue relation

$$\boldsymbol{P}_{\mathrm{ref}} \boldsymbol{H} \boldsymbol{P}_{\mathrm{ref}} |\Psi_{k,\mathrm{ref}}\rangle = E_{k,\mathrm{ref}} |\Psi_{k,\mathrm{ref}}\rangle \tag{4.33}$$

with projector $\boldsymbol{P}_{\mathrm{ref}}$, and approximates the target state that we want to describe. Perturbation theory gives a simple estimate on how the eigenstate changes when the model space is enlarged: the first-order state correction

$$|\Psi_{k,\mathrm{ref}}^{(1)}\rangle = -\sum_{|\phi\rangle \in \mathscr{M}_\perp} \frac{\langle \Psi_{k,\mathrm{ref}} | \boldsymbol{W} | \phi \rangle}{\langle \phi | \boldsymbol{H}_0 | \phi \rangle - \langle \Psi_{k,\mathrm{ref}} | \boldsymbol{H}_0 | \Psi_{k,\mathrm{ref}} \rangle} |\phi\rangle \,, \tag{4.34}$$

where $\boldsymbol{H}_0$ is the unperturbed Hamiltonian, $\boldsymbol{W}$ is the perturbation, and the sum is over an orthogonal set of states spanning the subspace $\mathscr{M}_\perp$ orthogonal to $|\Psi_{k,\mathrm{ref}}\rangle$.

This estimate is based on a partitioning of the Hamiltonian into an unperturbed part $\boldsymbol{H}_0$ and a perturbation $\boldsymbol{W} = \boldsymbol{H} - \boldsymbol{H}_0$. We define the unperturbed Hamiltonian as

$$\boldsymbol{H}_0 = \sum_l E_{l,\mathrm{ref}} |\Psi_{l,\mathrm{ref}}\rangle \langle \Psi_{l,\mathrm{ref}}| + \sum_{\nu \notin \mathscr{M}_{\mathrm{ref}}} \epsilon_\nu |\phi_\nu\rangle \langle \phi_\nu| \,. \tag{4.35}$$

Since $\langle \Psi_{k,\mathrm{ref}} | \boldsymbol{H} | \Psi_{l,\mathrm{ref}} \rangle = \langle \Psi_{k,\mathrm{ref}} | \boldsymbol{P}_{\mathrm{ref}} \boldsymbol{H} \boldsymbol{P}_{\mathrm{ref}} | \Psi_{l,\mathrm{ref}} \rangle = E_{k,\mathrm{ref}} \delta_l^k$, the reference state does not receive corrections from inside the reference space. Thus, we can restrict the sum in the state correction to a sum over states not in the reference space.

With this partitioning, we write the first-order state correction to the reference state as

$$|\Psi_{k,\text{ref}}^{(1)}\rangle = -\sum_{\nu \notin \mathcal{M}_{\text{ref}}} \frac{\langle \Psi_{k,\text{ref}} | \boldsymbol{H} | \phi_\nu \rangle}{\epsilon_\nu - E_{k,\text{ref}}} |\phi_\nu\rangle \equiv \sum_{\nu \notin \mathcal{M}_{\text{ref}}} \kappa_{k,\nu} |\phi_\nu\rangle. \tag{4.36}$$

The remaining parameters are the ϵ_ν. For simplicity, we set $\epsilon_\nu = E_{k,\text{ref}} + \Omega \sum_i (2n_{\nu(i)} + l_{\nu(i)}) + \Delta M_\nu$, i.e., the sum of HO single-particle energies shifted by the reference energy of the target state and the difference to the reference rest mass M_0. The notation $\nu(i)$ denotes the ith single-particle state in the determinant $|\phi_\nu\rangle$. The partitioning is different for each target state but this choice simplifies the numerical implementation and yields energy denominators that are independent of the reference state.

The quantity $\kappa_{k,\nu}$ is a measure of the importance of a basis state $|\phi_\nu\rangle$ for the description of the target state approximated by $|\Psi_{k,\text{ref}}\rangle$. Given a set of target states, we can hence build an importance-truncated model space by introducing a threshold κ_{min} and only including basis states whose importance measures exceed the threshold, $|\kappa_{k,\nu}| \geq \kappa_{\text{min}}$, for any of the target states.

The reference state itself is given in terms of Slater determinants,

$$|\Psi_{k,\text{ref}}\rangle \equiv \sum_{\mu \in \mathcal{M}_{\text{ref}}} c_{k,\mu}^{\text{ref}} |\phi_\mu\rangle. \tag{4.37}$$

Substituting this into (4.36), we get the importance measure

$$\kappa_{k,\nu} = -\sum_{\mu \in \mathcal{M}_{\text{ref}}} c_{k,\mu}^{\text{ref}} \frac{\langle \phi_\mu | \boldsymbol{H} | \phi_\nu \rangle}{\epsilon_\nu - E_{k,\text{ref}}}, \tag{4.38}$$

and we can calculate the importance measure by computing many-body matrix elements between the candidate basis state and all basis states from the reference space. For a two-body Hamiltonian, the matrix element vanishes unless the candidate state is at most a two-particle-two-hole (2p2h) excitation of the reference basis state, i.e., both determinants differ at most by two single-particle states. We can thus construct the whole importance-truncated model space by considering 1p1h and 2p2h excitations of all reference basis states.

The construction of the importance-truncated space scales with the square of the dimension of the reference space because the basis states enter into the computation of the importance measure and into the generation of candidate states. The computational cost of this process becomes prohibitive for reference space with more than 10^7 basis states. However, the basis expansion of the reference state also has some states with small expansion coefficients that contribute only very little to the importance measure so we can omit them from the computation. By introducing a threshold $|c_{k,\mu}^{\text{ref}}| \geq c_{\text{min}}$ we reduce the dimension of the reference space by an order of magnitude, gaining a large factor in speed of the model-space construction.

The N_{max}-truncated model spaces are related in the same manner as the importance-truncated space and the reference space: we can construct the $N_{\text{max}} + 2$ space by considering 1p1h and 2p2h excitations on the basis states of the N_{max} space. This gives rise to an iterative procedure that, in the limit of vanishing κ_{min}, yields the full N_{max}-truncated space: we start with a full NCSM calculation in a small model space, e.g., $N_{\text{max}} = 4$. The low-lying eigenstates resulting
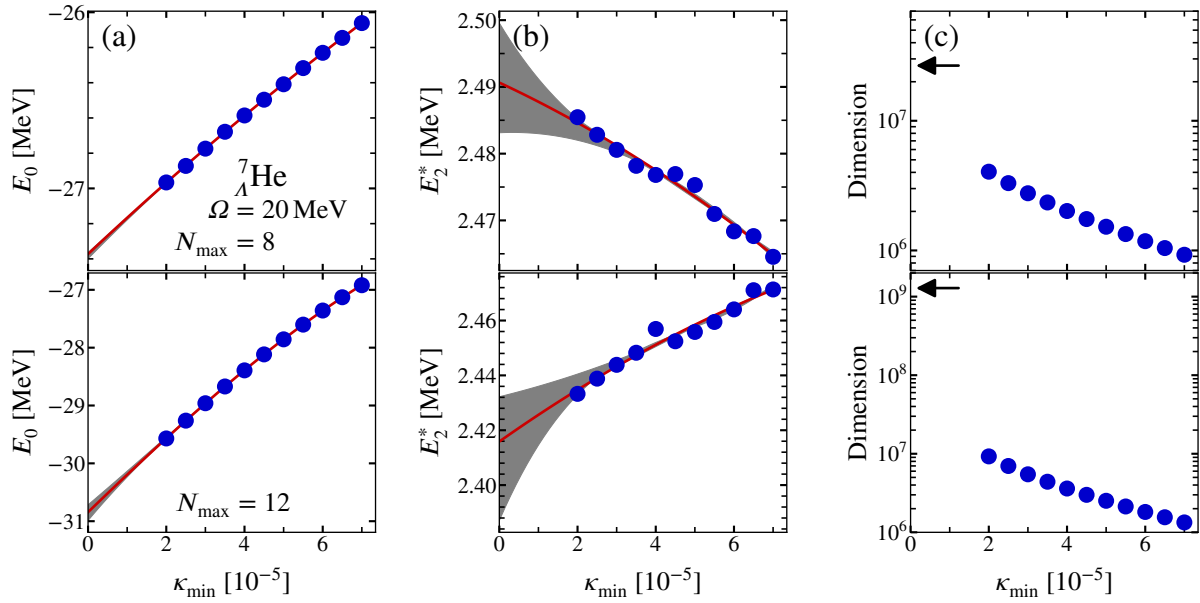
Figure 4.2.: Threshold extrapolation for $^{7}_{\Lambda}$He. Depicted are the extrapolation polynomials and their associated uncertainty bands for (a) the ground-state energy and (b) the excitation energy of the second excited state, for two values of the model-space truncation $N_{max} = 8, 12$. Panel (c) shows a comparison of the dimensions of the importance-truncated model spaces (blue dots) and the full NCSM space (black arrow).

from this calculation define the reference states for the first importance-truncation step during which we construct the importance-truncated $N_{max} = 6$ model space. For the importance truncation, we consider all 1p1h and 2p2h excitations on basis states of the reference space up to a maximum excitation energy $N_{max} = 6$, compute their importance measure, and include those into the new model space that exceed the importance threshold κ_{min}. The diagonalization of the Hamiltonian in this model space provide the reference states for the construction of the $N_{max} = 8$ space. The process is repeated until the desired value of the N_{max} truncation is reached.

The finite threshold κ_{min} has an effect on observables because the expansion coefficients of the excluded states are small but not exactly zero. To approximately account for this effect, we construct importance-truncated spaces for multiple thresholds, fit polynomials to the resulting sequences of observables $O(\kappa_{min})$, and take the limit $\kappa_{min} \to 0$. We estimate the uncertainty of the extrapolation by fitting polynomials of higher and lower degrees, and by leaving out one or two of the smallest threshold values. This creates a family of five extrapolation polynomials that allow us to assess the error. This extrapolation procedure, together with the construction of the importance-truncated model space, constitutes the Importance-Truncated No-Core Shell Model (IT-NCSM).

The extrapolation procedure is illustrated in fig. 4.2 for the hypernucleus $^{7}_{\Lambda}$He. The κ_{min} sequences are smooth and the extrapolation only needs to cover a few percent of the ground-state energy. Meanwhile, the dimension of the importance-truncated model space is two orders of magnitude smaller than the full NCSM model space at $N_{max} = 12$.

4.6. Results for Selected Hypernuclei

With the interaction and the many-body method in place, we calculate the low-lying spectra of light hypernuclei. For the nucleonic sector, we use a 2N interaction at N³LO by Entem and Machleidt [EM03] and a 3N interaction at N²LO by Navrátil [Nav07], both with a cutoff $\Lambda_N = 500$ MeV/c and SRG-evolved to a flow parameter of $\alpha_N = 0.08$ fm⁴. The 3N interaction matrix elements are truncated at a total HO energy of $E_{3max} = 12$. This Hamiltonian provides a good description of p-shell nuclei and the flow-parameter dependence is small for $A \lesssim 12$ [RCL+14]. For the YN sector, we use the LO interaction by Polinder et al. [PHM06] with two cutoffs to assess the cutoff dependence. We defer discussing the SRG evolution in the YN sector to the following section and use the bare YN interaction here. The basis frequency is fixed at $\Omega = 20$ MeV, because this value is close to the optimum for the nucleonic parents considered. The results shown here are also published in refs. [WGN+14; WGN+18].

4.6.1. Showcase: $^{7}_{\Lambda}$Li

The first system we consider is $^{7}_{\Lambda}$Li, one of the best-studied hypernuclei, and its nucleonic parent ^{6}Li, shown in fig. 4.3. The top row of the figure shows the absolute energies of low-lying states in (a) ^{6}Li, and (b) $^{7}_{\Lambda}$Li as a function of the model-space truncation N_{max}. States are colored according to their total angular momentum, and the dashed lines in panel (b) denote results for the YN interaction with $\Lambda_Y = 600$ MeV/c cutoff. The bottom row shows the excitation spectrum.

Figure 4.3.: Absolute and excitation energies of (a) ^{6}Li and (b) its daughter hypernucleus $^7_\Lambda$Li using a bare YN interaction with cutoff $\Lambda_Y = 700$ MeV/c (solid lines) and $\Lambda_Y = 600$ MeV/c (dashed lines). The basis frequency is $\Omega = 20$ MeV and the SRG flow parameter in the nucleonic sector is $\alpha_N = 0.08$ fm^4. Vertical bars denote threshold-extrapolation uncertainties. Experimental values taken from [Dav05; HT06; WAW$^+$12; TCG$^+$02].

The calculation for the parent is well-converged and the calculation describes the experimental data to a few hundred keV. The excitation energy of the 3^+ state is slightly overestimated.

Adding a hyperon to this system changes the states in two ways: The absolute energies are lowered because the YN interaction provides additional attraction that binds the nucleons, and each of the parent's states, except for $J = 0$ states, splits into a doublet. These doublets can qualitatively be explained as the coupling of the hyperon in an $s_{1/2}$ orbit to a state of the parent nucleus. Thus, the splitting among the doublet states is governed by the YN interaction while the separation between the doublets follows the excitation energies of the parent.

Since we are using a bare YN interaction, the absolute energies of the hypernucleus are far from being converged with respect to the model-space size. However, we can already see that there is a sizable cutoff dependence by comparing the absolute energies computed with the 600 MeV/c and the 700 MeV/c cutoff. The lower cutoff provides significantly more binding and overbinds the hypernucleus already at $N_{max} = 12$ by approximately 1 MeV. The calculated energies are variational, so the converged ground-state energy will be even lower.

Convergence of excitation energies is much better. The energies show a significant dependence on the YN interaction cutoff: The lower cutoff shows splittings among the doublet states half as wide as the higher cutoff, which become smaller with increasing N_{max}. To our surprise, we find a reasonable reproduction of the experimental excitation energies for both cutoffs at this level of convergence, considering that the 3^+ excitation in the parent nucleus is slightly too high, which shifts the $5/2^+$ and $7/2^+$ to higher energies.

Next, we investigate the evolution of spectra along an isotopic chain and along the $N = Z$ line. For the former, we study light nuclei from the helium isotopic chain and their daughter hypernuclei. We also present $^9_\Lambda$Be and $^{13}_\Lambda$C as representative symmetric hypernuclei.

4.6.2. The Hyper-Helium Chain

The lightest hypernucleus that we consider from the helium isotopic chain is $^5_\Lambda$He (cf. fig. 4.4). The nucleonic parent is ^{4}He with the first excited state at ~ 20 MeV, so we only show the ground state. While the parent ground state is converged to tens of keV at $N_{max} = 12$, the hypernuclear ground state shows MeV-level changes, and both cutoffs will likely overbind the hypernucleus compared to experiment. The cutoff dependence is similar to the $^7_\Lambda$Li case. The overbinding of the ground state is a common phenomenon for interactions that reproduce the binding energy of the $A = 4$ systems [GH95; GHM16], and the tensor part of the Λ-Σ conversion plays a crucial role for reproducing the $A = 4$ and $A = 5$ systems simultaneously [NAS02]. Some of these tensor structures might be missing from the LO YN interaction.

The next hypernucleus along the isotopic chain, $^6_\Lambda$He, shown in fig. 4.5, is special because its nucleonic core is unstable against neutron emission. Comparing the experimental ground-state energies of $^6_\Lambda$He and $^5_\Lambda$He, we see that the addition of the hyperon to the particle-unstable ^{5}He resonance produces a stable hypernucleus with a ground state that is very close to the neutron-separation threshold. Probably owing to the overbound $^5_\Lambda$He, the LO YN interaction does not show this behavior: both cutoffs put the $^6_\Lambda$He ground state approximately 1 MeV above threshold. The spectra show smaller splittings than in $^7_\Lambda$Li. The splitting of the excited-state doublet is nearly cutoff-independent; the doublet itself behaves similarly to the energy of the $1/2^-$ resonance in ^{5}He, which converges slowly to the ^{4}He + n threshold in this IT-NCSM
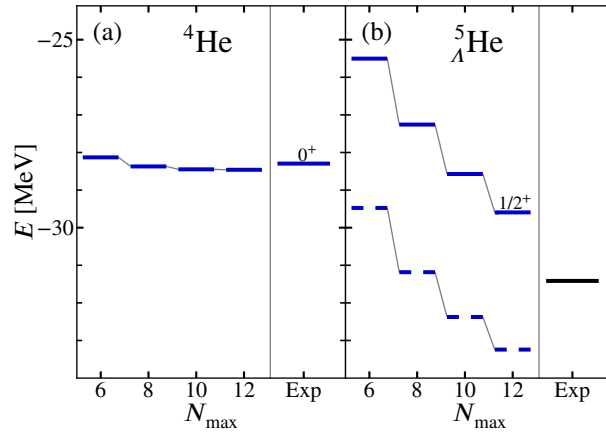
Figure 4.4.: Ground-state energy of (a) ^{4}He and (b) its daughter hypernucleus $^5_\Lambda$He using a bare YN interaction. Notations and parameters like in fig. 4.3. Experimental values taken from [Dav05; HT06; WAW$^+$12; TCG$^+$02].
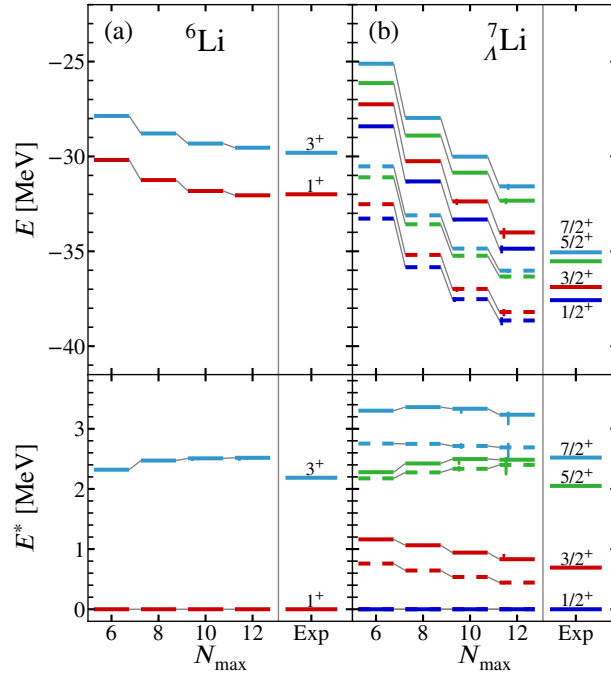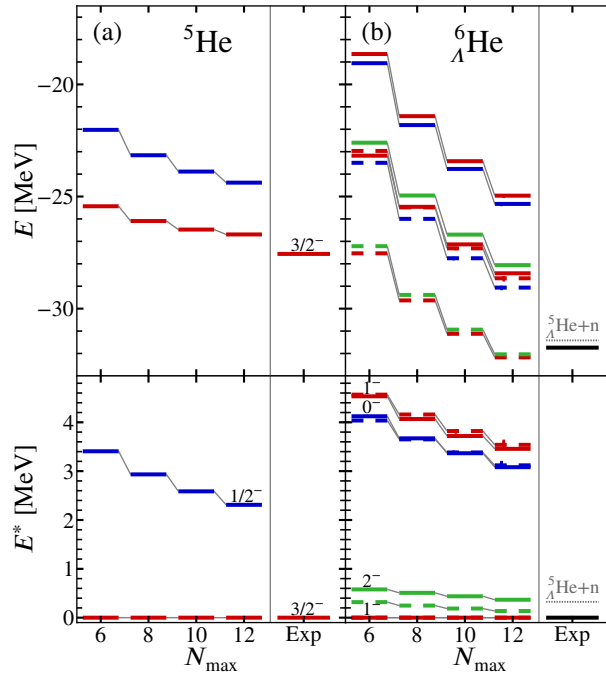

Figure 4.5.: Absolute and excitation energies of (a) ^{5}He and (b) its daughter hypernucleus $^6_\Lambda$He using a bare YN interaction. Notations and parameters like in fig. 4.3, the gray dotted line marks the experimental neutron-separation threshold. Experimental values taken from [Dav05; HT06; WAW$^+$12; TCG$^+$02].
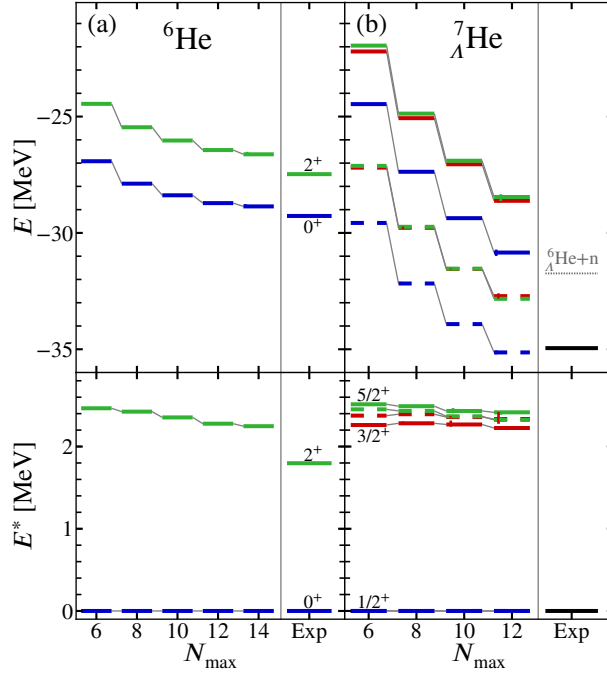
Figure 4.6.: Absolute and excitation energies of (a) ^{6}He and (b) its daughter hypernucleus $^7_\Lambda$He using a bare YN interaction. Notations and parameters like in fig. 4.3. Experimental values taken from [NMO+13; HT06; WAW+12; TCG+02].

calculation. The ground-state doublet splitting is reduced for the lower 600 MeV/c cutoff. Apart from the lack of convergence in the hypernuclear calculation, the proximity to the neglected continuum degrees of freedom introduces additional uncertainties. A calculation including the continuum, like the NCSM with continuum [BNQ13], may even push the ground state below the $^5_\Lambda$He + n threshold.

Continuum effects are less important for $^7_\Lambda$He, shown in fig. 4.6. The ground state is well separated from the nearest threshold both in experiment and in our calculation. The description of the parent nucleus, which is a halo nucleus, is good. This is surprising because the NCSM needs large model spaces to accommodate for the long-range tail of the halo-neutron wave functions. For the hypernucleus, our calculation predicts an excited-state doublet consisting of a $3/2^+$ and a $5/2^+$ state with a splitting of roughly 0.2 MeV.

4.6.3. Symmetric Hypernuclei

We move to the symmetric hypernuclei and consider $^9_\Lambda$Be, shown in fig. 4.7. Like the parent of $^6_\Lambda$He, the parent nucleus ^{8}Be is a resonance; in this case it is a narrow α-α resonance very close to threshold. The additional attraction due to the hyperon stabilizes the hypernucleus and makes not only the ground state, but also the excited-state doublet bound. The absolute energies are still far from convergence, but the excitation energies show very little variation with N_{max}. The excited-state doublet is nearly degenerate and shows an inversion of the spins in experiment, with the $5/2^+$ below the $3/2^+$ [TAA+05], in contrast to $^7_\Lambda$Li, where the upper doublet state has

Figure 4.7.: Absolute and excitation energies of (a) ^{8}Be and (b) its daughter hypernucleus $^{9}_{\Lambda}$Be using a bare YN interaction. Notations and parameters like in fig. 4.3. Experimental values taken from [Dav05; HT06; WAW^{+}12; TKG^{+}04].
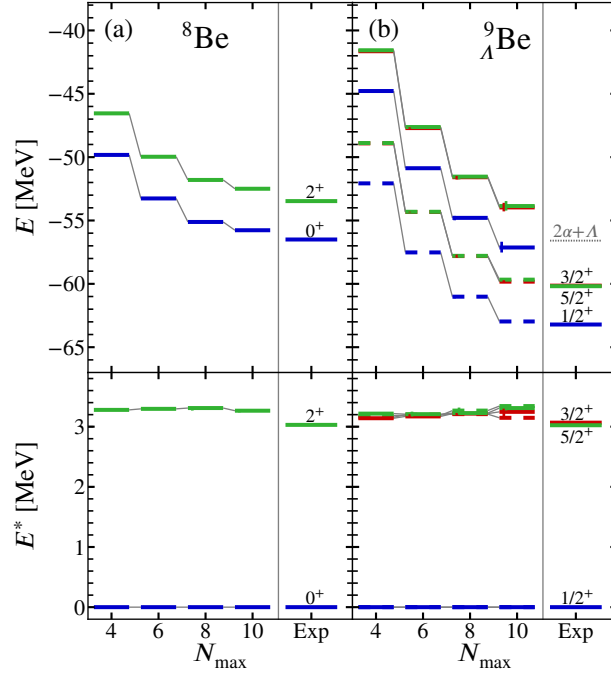
the higher angular momentum. The degeneracy is captured by the calculation.

We conclude our investigation with $^{13}_{\Lambda}$C (cf. fig. 4.8). Here, the calculation for the parent nucleus already shows some overbinding that translates to the hypernucleus. Like in $^{9}_{\Lambda}$Be, the excitation energies of the positive-parity states are nearly independent of the model-space size despite the absolute energies being far from convergence. The low-lying spectrum is similar to $^{7}_{\Lambda}$Li, with a relatively large splitting. The splitting, however, is independent of the interaction cutoff. This doublet is close to the experimental energy of the $3/2^{+}$ state, but if the inversion seen in $^{9}_{\Lambda}$Be carries over to heavier systems, the $3/2^{+}$ should be the upper doublet state.

We also consider the lowest (unnatural) negative-parity states that are associated with the hyperon in a p state, coupled to the 0^{+} ground state of ^{12}C [Mil07]. Experimentally, these also form a nearly degenerate $1/2^{-}$, $3/2^{-}$ doublet with the $3/2^{-}$ as lower state. Our calculation of the excitation energies is not converged at $N_{\text{max}} = 9$, but the excitation energies are above the experimental ones with an upward trend. The rate of convergence of positive- and negative-parity states in the NCSM can be very different, so this effect might simply be caused by slower convergence of the negative-parity states. Also, the doublet splitting is at the MeV-level, whereas the experimental value is only $0.15\,\text{MeV}$. Thus, it is probable that the YN interaction is lacking some p-wave structures, which lead to these discrepancies.

In conclusion, we can access many hypernuclear observables already with calculations using the bare YN interaction. Especially spectra are converged well enough to confront them with experimental data. For most states, we get a very good agreement with experimental data, especially considering that the YN interaction is at leading order of chiral EFT. However, there
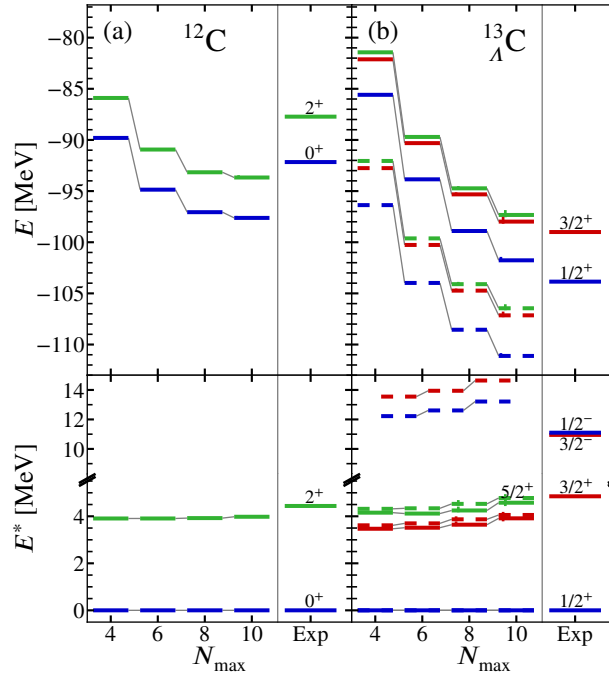
Figure 4.8.: Absolute and excitation energies of (a) ^{12}C and (b) its daughter hypernucleus $^{13}_{\Lambda}$C using a bare YN interaction. For the hypernucleus, we show the positive- and negative parity states (computed with the $\Lambda_Y = 600$ MeV/c cutoff only). Notations and parameters like in fig. 4.3. Experimental values taken from [Dav05; HT06; WAW$^+$12; Ajz90].

are some deficiencies. We see a cutoff dependence of the excitation energies in $^7_\Lambda$Li that lessens when going to more neutron-rich systems. The interaction reproduces the small splitting in the excited-state doublet of $^9_\Lambda$Be, but the splitting of the negative-parity doublet in $^{13}_\Lambda$C is an order of magnitude too large. Also, there are hints that $^5_\Lambda$He is strongly overbound. These deficiencies may be addressed in subleading terms of the YN interaction beyond LO, which provide additional contact terms and a richer operator structure.

4.6.4. Dependence of Hyperon Separation Energies on the 3N Interaction

Calculations for hypernuclei are often done directly for the hyperon separation energy, using nucleonic interactions that are either schematic, or realistic but lacking three-body terms [HKM$^+$01; NAS02; LGP13]. While the ground-state energies themselves are unrealistic, the hyperon separation energy is governed by the YN interaction, and a more realistic treatment is abandoned for conceptual or computational simplicity, assuming that the effect of the nucleonic interactions on the separation energy is small. Indeed, the hyperon separation energies of s-shell hypernuclei are nearly independent of the choice of nucleonic Hamiltonian [NKG02; Nog05].

In the p shell, we find a similar behavior for the bare YN interaction: Figure 4.9(a) shows the hyperon separation energy of $^7_\Lambda$Li with and without a 3N interaction. The difference in the hyperon separation energy is of the order of 0.1 MeV. However, this is not the case for the SRG-evolved interaction, shown in panel (b): There is a clear difference of the order of 0.7 MeV between the two curves with the 3N interaction decreasing the separation energy. This emphasizes the importance of using a realistic nucleonic Hamiltonian for hypernuclear calculations, which not only has the benefit of providing realistic absolute energies but also reduces the uncertainty of hyperon separation energies.

4.7. Induced YNN Terms

While we can access some hypernuclear observables using a bare YN interaction, others like absolute energies or separation energies are too far from convergence to extract a reliable value from the calculation. The rate of convergence with respect to the model-space size of the calculations shown in the previous section is dominated by the bare YN interaction that, through its large offdiagonal matrix elements, couples low- and high-energy Slater determinants. To improve this, we need to perform the SRG transformation also in the YN sector.

If the SRG evolution is performed at the two-body level, we have to consider a possible loss of unitarity of the transformation. Variation of the flow parameter α_Y in the YN sector is a simple tool to assess the size of induced terms. The results of such a variation for $^7_\Lambda$Li are shown in fig. 4.10. At very small flow parameters, the energies of the ground-state doublet drop steeply by approximately 2.5 MeV before saturating at $\alpha_Y \sim 0.08\,\text{fm}^4$. To put this into perspective, the drop amounts to 45 % of the experimental hyperon separation energy of $B_\Lambda = E_0(^6\text{Li}) - E_0(^7_\Lambda\text{Li}) = 5.58\,\text{MeV}$ [Dav05], and still 28 % of the extrapolated separation energy of $B_\Lambda = 8.9(6)\,\text{MeV}$ at $\alpha_Y = 0\,\text{fm}^4$.
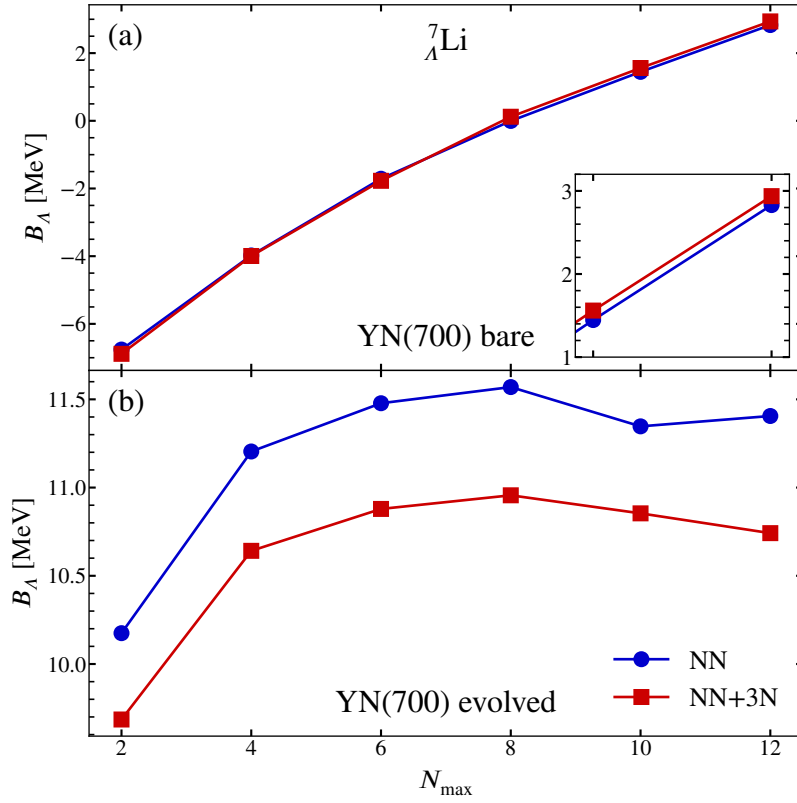
Figure 4.9.: Effect of the 3N interaction on the hyperon separation energy of $^{7}_{\Lambda}$Li. Shown is the hyperon separation energy as a function of N_{max} for a calculation with and without a 3N interaction for (a) the unevolved and (b) the evolved YN interaction. The nucleonic Hamiltonian is SRG-evolved with the standard generator to a flow parameter of $\alpha_N = 0.08\,\mathrm{fm}^4$ in order to improve convergence; the basis frequency is $\Omega = 20\,\mathrm{MeV}$, and the YN interaction cutoff is $\Lambda_Y = 700\,\mathrm{MeV/c}$.
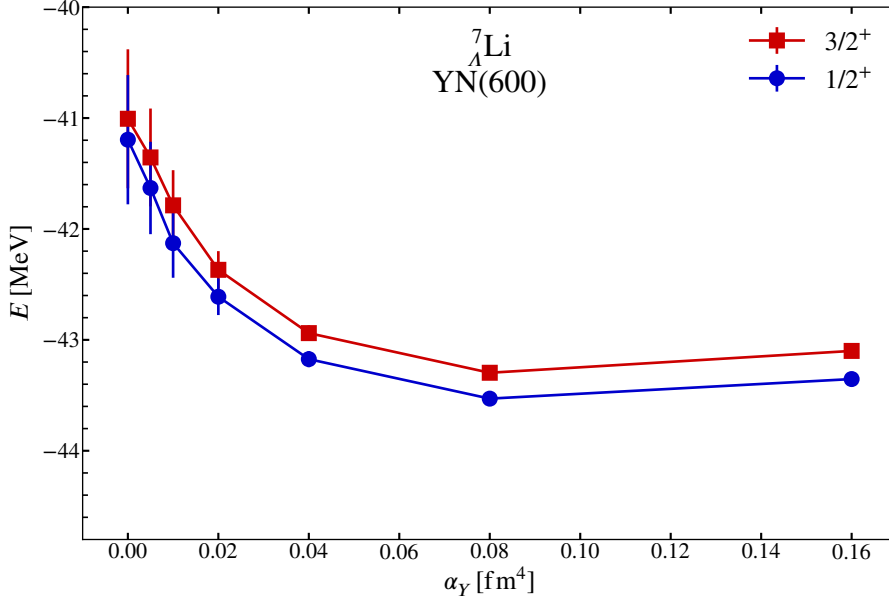
Figure 4.10.: SRG evolution in the YN sector for $^{7}_{\Lambda}$Li. Shown are the extrapolated absolute energies of the ground-state doublet as a function of the SRG flow parameter in the YN sector α_Y. In the nucleonic sector, the flow parameter is fixed at $\alpha_N = 0.08\,\mathrm{fm}^4$ to ensure adequate convergence of the calculations. The basis frequency is $\Omega = 20\,\mathrm{MeV}$, and the interaction cutoff is $\Lambda_Y = 600\,\mathrm{MeV/c}$.

The induced YNN (and beyond) terms are, thus, much stronger than the induced 3N terms, compared to the net effect of the interaction, which is the binding energy of the nucleus for the 3N and the hyperon separation energy for the YNN interaction. Furthermore, the effect of the induced three-body interaction terms naively scales with the number of interacting triples. In ^{6}Li, there are $6!/(3!)^2 = 20$ nucleon triples. There, the induced 3N terms amount to 14 % of the calculated binding energy [RLC$^+$11], or 0.7 % per triple. In $^{7}_{\Lambda}$Li, we have the same number of nucleon triples and $6!/(2!4!) = 15$ YNN triples, so that the overbinding in the extrapolated separation energy amounts to 1.9 % per triple.

The strength of the induced YNN terms necessitates their explicit inclusion into the many-body calculation, but also raises the question of their origin. The most significant difference between the YN and NN interactions is the presence of Λ-Σ conversion terms. Since the Σ hyperons are heavier than the Λ hyperon, the SRG evolution suppresses these conversion terms since the linear term of (3.24) includes a difference of the total masses of the bra and ket particles.

To separate this decoupling from the prediagonalization in momentum space, we devise an SRG generator that only decouples the Λ- from the Σ-containing states. For that, we employ Wegner's prescription

$$\eta(\alpha) = [\boldsymbol{H}_d(\alpha), \boldsymbol{H}(\alpha)] \quad \text{with} \quad \boldsymbol{H}_d(\alpha) = \boldsymbol{H}_{\Lambda\Lambda}(\alpha) + \boldsymbol{H}_{\Sigma\Sigma}(\alpha). \tag{4.39}$$

The operator $\boldsymbol{H}_{\Lambda\Lambda}$ ($\boldsymbol{H}_{\Sigma\Sigma}$) is a projection of the Hamiltonian onto the Λ (Σ) states. This prescription takes the Hamiltonian to a blockdiagonal form in the limit $\alpha \to \infty$, where the Λ-Σ
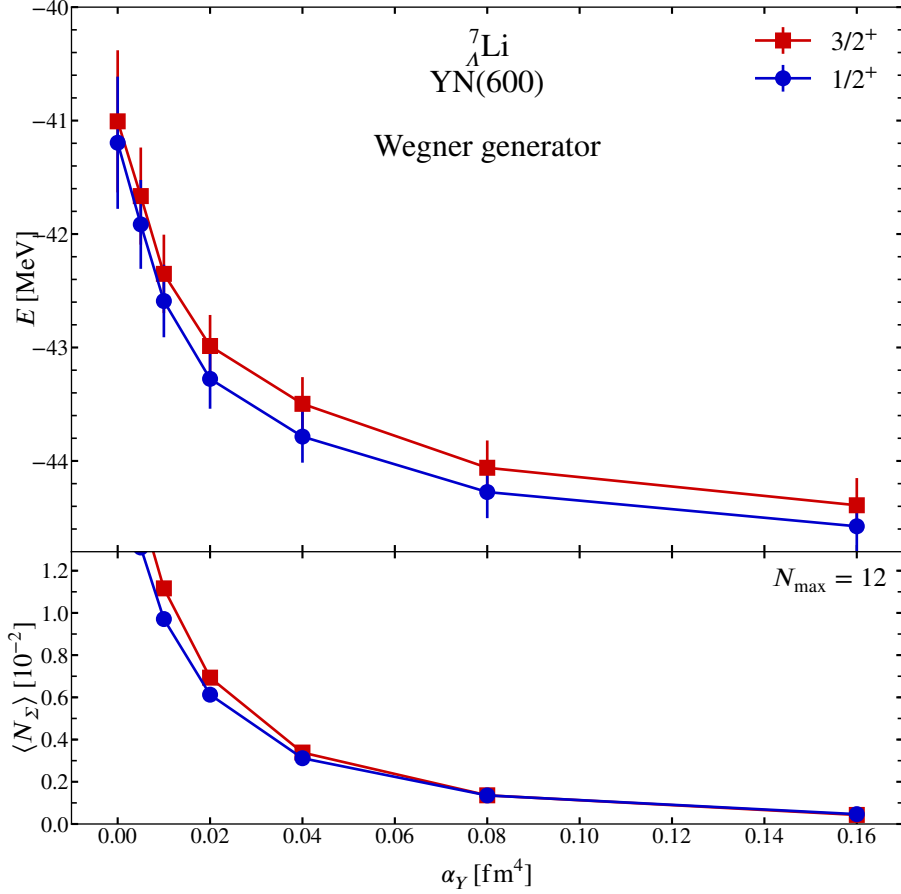
Figure 4.11.: SRG evolution in the YN sector for $^{7}_{\Lambda}$Li using the Wegner generator (4.39). Shown are (a) the extrapolated absolute energies of the ground-state doublet as a function of the SRG flow parameter α_Y, and (b) the expectation value of the Σ number operator $\boldsymbol{N}_\Sigma$. In the nucleonic sector, the flow parameter is fixed at $\alpha_N = 0.08\,\mathrm{fm}^4$ to ensure adequate convergence of the calculations. The basis frequency is $\Omega = 20\,\mathrm{MeV}$, and the interaction cutoff is $\Lambda_Y = 600\,\mathrm{MeV/c}$.

conversion is absent.

We perform the flow-parameter variation for this generator, shown in fig. 4.11, and observe the same behavior as for the standard generator. Simultaneous to the drop of the ground-state energy, the expectation value of the Σ number operator $\boldsymbol{N}_\Sigma = \sum_i \boldsymbol{a}_i^\dagger \boldsymbol{a}_i$, where i runs over Σ single-particle states, decreases from above 1 % to below 0.1 %. Also, the difference in Σ admixture between the two doublet states vanishes.

At the start of the flow, we have the full Λ-Σ coupled-channel problem with significant Σ admixture in low-lying states. The channels are decoupled with increasing flow parameter, so that, for large flow parameters, the low-lying spectrum consists of pure Λ states, which we could describe in a model space without Σ hyperons. At the same time, the SRG transformation generates large repulsive ΛNN terms. The transformation thus unitarily changes the scheme from one with Σ degrees of freedom and no three-body forces to one with only Λ hyperons and

and a strongly-repulsive ΛNN three-body force.

To illustrate this, consider an iterated interaction in a three-body system, e.g., generated in a perturbation series. Disregarding permutations, there are two diagrams that start and end in a ΛNN state, but have a ΣNN intermediate state:
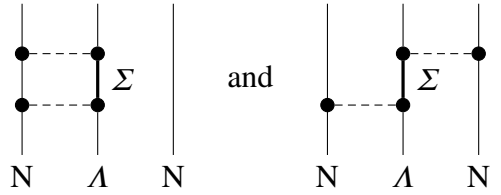
The two interactions are indicated by dashed lines connecting the interacting particles. The thick line marks an intermediate Σ state. In the initial scheme, these diagrams are nothing but iterated two-body interactions. After the SRG evolution, in the Λ-only scheme, they do not exist anymore because there are no Σ intermediate states, but their effect on observables is still present because the transformation between the schemes is unitary. The first diagram can be absorbed into a two-body interaction, but the second can change the states of three particles and is thus a genuine three-body interaction term in the Λ-only scheme. Capturing these terms is the subject of the next chapter.

At first, these results might seem contrary to the findings of, e.g., [NKG02], who get an increase in the ground-state energy when removing the Σ hyperons in a phaseshift-preserving way. The Faddeev-Yakubovsky calculation in that work uses a t matrix that encodes the full two-body scattering. The t matrix is calculated with full Λ-Σ conversion and then projected onto the Λ subspace. While this procedure preserves the Λ-N scattering observables, the projection cuts away nonzero offshell matrix elements of the t matrix, which enter the Faddeev-Yakubovsky calculation. With the interaction transformed by (4.39) the t matrix is blockdiagonal from the outset, and no information is lost during the projection.

5. Explicit Treatment of Induced YNN Interactions

Since the SRG evolution of the initial YN interaction induces strong YNN terms we need to treat these explicitly. This is achieved by performing the evolution in a space spanned by three-body states of two nucleons and one hyperon.

In the following, we derive the tools necessary for carrying out the SRG evolution in a three-body Jacobi HO basis. This basis allows for an explicit elimination of the center-of-mass degree of freedom which gives us access to the model-space sizes that are necessary to achieve convergence of the SRG evolution.

After the evolution we have to disentangle the induced irreducible three-body parts from the evolved two-body terms. Then, we can convert the irreducible three-body matrix elements to a JT-coupled three-body basis in terms of single-particle coordinates that is suitable for IT-NCSM calculations.

We start out in section 5.1 by defining three sets of coordinates—the Jacobi coordinates—that decouple the center of mass of the three-body system from its relative degrees of freedom. In section 5.2, we define the basis sets that are used in the following computations. In the next step, in section 5.3, we perform the explicit antisymmetrization of the Jacobi HO basis. The last step of the computation is the transformation to a JT-coupled basis given in terms of single-particle coordinates. For that we derive the so-called T coefficients in section 5.4 and put the pieces together in section 5.5. Finally, we consider the initial matrix elements and the model space in which the evolution is carried out in section 5.6 and its computational implications in section 5.7. Throughout this chapter, we follow [Cal10; Bin10] and generalize their results for the 3N system to the hypernuclear case.

5.1. Jacobi coordinates for the YNN system

We start with A particles of masses m_i at locations described by position vectors $\vec{r}_i$. In terms of these variables, the Jacobi coordinates $\vec{\rho}_n$ are defined via the relations

$$\vec{\rho}_0 \equiv \frac{1}{M_A} \sum_{k=1}^{A} m_k \vec{r}_k \tag{5.1}$$

$$\vec{\rho}_n \equiv \left(\frac{1}{M_n} \sum_{k=1}^{n} m_k \vec{r}_k \right) - \vec{r}_{n+1}, \quad n = 1, 2, \ldots, A-1 \tag{5.2}$$
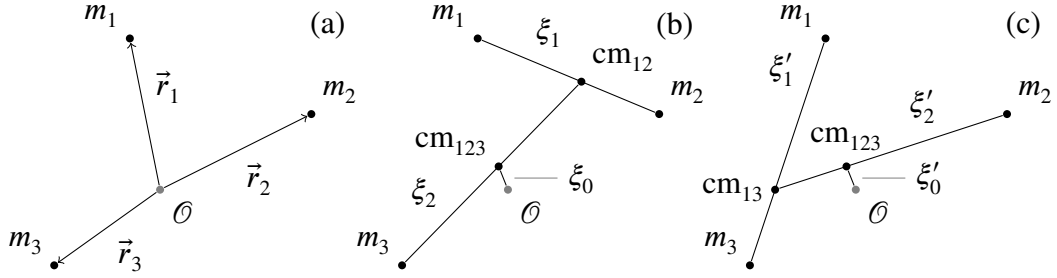
Figure 5.1.: Jacobi coordinates for the three-body system: (a) definition of the single-particle coordinates, (b) and (c) depict the two Jacobi coordinate systems relevant for this chapter. The lines connect the particles, labeled by their masses m_i, and centers of mass cm_{ij}, etc., relevant for the definition of the respective coordinate; $\mathcal{O}$ denotes the origin.

with

$$M_n \equiv \sum_{k=1}^{n} m_k. \tag{5.3}$$

The Jacobi coordinates are a generalization of the relative and c.m. coordinates for the two-body system to systems with more particles. The zeroth coordinate $\vec{\rho}_0$ is the c.m. of the A-body system. The first coordinate $\vec{\rho}_1$ is the relative coordinate of the first two particles. The following coordinates $\vec{\rho}_n$ are the relative coordinates between the c.m. of the first n and the $(n+1)^{\text{st}}$ particle.

In order to be able to use the HO brackets defined in appendix A.4 we need to have a transformation between coordinate systems that is orthogonal and symmetric at the same time. We achieve this by scaling all coordinates by a factor $\sqrt{m_i/m_N}$. Here, the nucleon mass m_N is an arbitrary scale used to fix the units of the new coordinates. The new (reduced) coordinates read

$$\vec{x}_i \equiv \sqrt{\frac{m_i}{m_N}}\vec{r}_i \tag{5.4}$$

$$\vec{\xi}_0 \equiv \frac{1}{\sqrt{M_A}}\sum_{k=1}^{A}\sqrt{m_k}\vec{x}_k \tag{5.5}$$

$$\vec{\xi}_n \equiv \frac{\vec{\rho}_n}{\sqrt{\Omega}b(\mu_n,\Omega)} = \sqrt{\frac{M_n m_{n+1}}{M_{n+1}}}\left(\frac{1}{M_n}\sum_{k=1}^{n}\sqrt{m_k}\vec{x}_k - \frac{1}{m_{n+1}}\vec{x}_{n+1}\right)$$

$$= \frac{1}{\sqrt{M_{n+1}}}\left(\sqrt{\frac{m_{n+1}}{M_n}}\sum_{k=1}^{n}\sqrt{m_k}\vec{x}_k - \sqrt{M_n}\vec{x}_{n+1}\right). \tag{5.6}$$

The symbol $\mu_n = (M_n^{-1} + m_{n+1}^{-1})^{-1}$ denotes the reduced mass of the cluster formed by the first n particles and the $(n+1)^{\text{st}}$ particle. For the three-body system, these equations reduce to

$$\vec{\xi}_0 = \frac{1}{\sqrt{M_3}}\left(\sqrt{m_1}\vec{x}_1 + \sqrt{m_2}\vec{x}_2 + \sqrt{m_3}\vec{x}_3\right) = \frac{1}{\sqrt{M_3}}\left(\sqrt{M_2}\vec{X}_{12} + \sqrt{m_3}\vec{x}_3\right) \tag{5.7}$$

$$\vec{\xi}_1 = \frac{1}{\sqrt{M_2}}\left(\sqrt{m_2}\vec{x}_1 - \sqrt{m_1}\vec{x}_2\right) \tag{5.8}$$

$$\vec{\xi}_2 = \frac{1}{\sqrt{M_3}}\left(\sqrt{\frac{m_3}{M_2}}\left(\sqrt{m_1}\vec{x}_1 + \sqrt{m_2}\vec{x}_2\right) - \sqrt{M_2}\vec{x}_3\right)$$

$$= \frac{1}{\sqrt{M_3}}\left(\sqrt{m_3}\vec{X}_{12} - \sqrt{M_2}\vec{x}_3\right) \tag{5.9}$$

$$\vec{X}_{12} = \frac{1}{\sqrt{M_2}}\left(\sqrt{m_1}\vec{x}_1 + \sqrt{m_2}\vec{x}_2\right) \tag{5.10}$$

where we introduced the reduced center-of-mass coordinate $\vec{X}_{12}$ of particles 1 and 2.

From (5.8) and (5.10) or (5.7) and (5.9), respectively, we get the transformation matrices

$$\begin{pmatrix} \vec{X}_{12} \\ \vec{\xi}_1 \end{pmatrix} = \begin{pmatrix} \sqrt{\frac{m_1}{m_1+m_2}} & \sqrt{\frac{m_2}{m_1+m_2}} \\ \sqrt{\frac{m_2}{m_1+m_2}} & -\sqrt{\frac{m_1}{m_1+m_2}} \end{pmatrix} \begin{pmatrix} \vec{x}_1 \\ \vec{x}_2 \end{pmatrix} \tag{5.11}$$

$$\begin{pmatrix} \vec{\xi}_0 \\ \vec{\xi}_2 \end{pmatrix} = \begin{pmatrix} \sqrt{\frac{m_1+m_2}{m_1+m_2+m_3}} & \sqrt{\frac{m_3}{m_1+m_2+m_3}} \\ \sqrt{\frac{m_3}{m_1+m_2+m_3}} & -\sqrt{\frac{m_1+m_2}{m_1+m_2+m_3}} \end{pmatrix} \begin{pmatrix} \vec{X}_{12} \\ \vec{x}_3 \end{pmatrix}. \tag{5.12}$$

These matrices are of the form shown in (A.22), namely

$$\begin{pmatrix} \vec{V} \\ \vec{v} \end{pmatrix} = \begin{pmatrix} \sqrt{\frac{d}{1+d}} & \sqrt{\frac{1}{1+d}} \\ \sqrt{\frac{1}{1+d}} & -\sqrt{\frac{d}{1+d}} \end{pmatrix} \begin{pmatrix} \vec{v}_1 \\ \vec{v}_2 \end{pmatrix}, \tag{5.13}$$

implying transformation parameters $d = m_1/m_2$ and $d = (m_1 + m_2)/m_3$, respectively.

The relation between single-particle and Jacobi coordinates is illustrated in fig. 5.1. Panel (a) shows the single-particle coordinates of three particles with masses m_1, m_2, and m_3. The Jacobi coordinates ξ_i are depicted in panel (b): The first coordinate gives the relative position of particles 1 and 2, the second marks the position of particle 3 relative to the c.m. of the first two, and the zeroth coordinate locates the three-particle c.m. in space.

The Jacobi basis is not unique, but depends on the labeling of particles. There are thus $A!$ different definitions of Jacobi bases for an A-particle system. However, pairs of these definitions are related by a simple reversal of the first coordinate $\xi_1 \mapsto -\xi_1$ and, in general, all are related via orthogonal transformations. Figure 5.1(c) shows a definition where the first coordinate ξ'_1 is defined by particles 1 and 3 instead of 1 and 2. The center-of-mass coordinates ξ_0 and ξ'_0 are identical, so it suffices to derive the relation between the ξ_1, ξ_2 and the ξ'_1, ξ'_2 to get the orthogonal transformation between both coordinate systems.

We do this by expressing the primed coordinates

$$\vec{\xi}'_1 = \frac{1}{\sqrt{m_1 + m_3}}\left(\sqrt{m_3}\vec{x}_1 - \sqrt{m_1}\vec{x}_3\right) \tag{5.14}$$

$$\vec{\xi}'_2 = \frac{1}{\sqrt{M_3}}\left(\sqrt{\frac{m_2}{m_1 + m_3}}\left(\sqrt{m_1}\vec{x}_1 + \sqrt{m_2}\vec{x}_3\right) - \sqrt{m_1 + m_3}\vec{x}_2\right) \tag{5.15}$$

in terms of the unprimed ones. After a straight-forward derivation (see appendix C.1 for details) we arrive at the relation

$$
\begin{pmatrix} \vec{\xi}_1' \\ \vec{\xi}_2' \end{pmatrix} = \begin{pmatrix} \sqrt{\frac{m_2 m_3}{(m_1+m_2)(m_1+m_3)}} & \sqrt{\frac{m_1(m_1+m_2+m_3)}{(m_1+m_2)(m_1+m_3)}} \\ \sqrt{\frac{m_1(m_1+m_2+m_3)}{(m_1+m_2)(m_1+m_3)}} & -\sqrt{\frac{m_2 m_3}{(m_1+m_2)(m_1+m_3)}} \end{pmatrix} \begin{pmatrix} \vec{\xi}_1 \\ \vec{\xi}_2 \end{pmatrix} .
\tag{5.16}
$$

This transformation corresponds to a parameter $d = m_2 m_3/(m_1(m_1 + m_2 + m_3))$. Note that in this case d is invariant under an exchange of m_2 and m_3.

The relations derived in this section are needed for the antisymmetrization of the three-body Jacobi basis and for the transformation between the single-particle and the Jacobi HO basis. However, they enter only via their respective transformation parameter d.

5.2. Basis Sets

To proceed with our derivation we define multiple basis sets: the product-state basis and its JT-coupled analog for a description in terms of single-particle coordinates, the so-called α basis defined with respect to Jacobi coordinates, and their respective counterparts that are antisymmetric under exchange of the first two or any two particles. To better distinguish quantities referring to Jacobi and single-particle coordinates, we slightly change the notation: single-particle quantities are indexed by letters, while those referring to a specific Jacobi coordinate use Arabic numerals. However, operators that refer to single-particle *slots*, e.g., the permutation operators P_{12} still use numbers.

The product-state basis is spanned by states

$$
|abc\rangle_n \quad \text{with single-particle states} \quad a \equiv \{n_a(l_a s_a)j_a m_a, \mathscr{S}_a t_a \tau_a\}, \dots .
\tag{5.17}
$$

Coupling these states to good total angular momentum and isospin leads to the JT-coupled basis

$$
|[(\tilde{a}\tilde{b})J_{ab}T_{ab}, \tilde{c}]JMTM_T\rangle_n =
$$
$$
\sum_{\substack{m_a m_b \\ \tau_a \tau_b}} \sum_{\substack{M_{ab} m_c \\ \tau_{ab} \tau_c}} \begin{pmatrix} j_a & j_b & J_{ab} \\ m_a & m_b & M_{ab} \end{pmatrix} \begin{pmatrix} J_{ab} & j_c & J \\ M_{ab} & m_c & M \end{pmatrix} \begin{pmatrix} t_a & t_b & T_{ab} \\ \tau_a & \tau_b & \tau_{ab} \end{pmatrix} \begin{pmatrix} T_{ab} & t_c & T \\ \tau_{ab} & \tau_c & M_T \end{pmatrix}
$$
$$
\times |\tilde{a}m_a\tau_a, \tilde{b}m_b\tau_b, \tilde{c}m_c\tau_c\rangle_n
\tag{5.18}
$$

where $\tilde{a} = a \setminus \{m_a \tau_a\}, \dots$ denote the (spin-isospin-reduced) sets of single-particle quantum numbers without angular-momentum and isospin projection. A similar basis that is defined in terms of Jacobi coordinates instead is given by

$$
|(n_{\text{cm}} l_{\text{cm}}, \bar{\alpha})JM\rangle_n =
$$
$$
|(n_{\text{cm}} l_{\text{cm}}, \{[n_1 l_1, (s_a s_b)S_{ab}]j_1, [n_2 l_2, s_c]j_2\}\mathscr{J})JM, [(\mathscr{S}_a t_a \mathscr{S}_b t_b)T_{ab}, \mathscr{S}_c t_c]TM_T\rangle_n
\tag{5.19}
$$

with $\alpha = \{n_1 l_1 j_1 n_2 l_2 j_2 s_a s_b s_c S_{ab} \mathscr{J} \mathscr{M} \mathscr{S}_a \mathscr{S}_b \mathscr{S}_c t_a t_b t_c T_{ab} T M_T\}$ collecting the intrinsic quantum numbers and $\bar{\alpha} = \alpha \setminus \{\mathscr{M}\}$. The intrinsic quantum numbers are the radial and angular-momentum quantum numbers $[n_1 l_1, (s_a s_b)S_{ab}]j_1$ of the first Jacobi coordinate, which describe

the relative motion of the first two particles, the quantum numbers of the second coordinate $(n_2 l_2, s_c) j_2$ for the motion of the third particle with respect to the c.m. of the first two, and the pertinent isospin quantum numbers characterizing the particles. The total angular momenta j_1 and j_2 are coupled to the total intrinsic angular momentum $\mathcal{J}$ with projection $\mathcal{M}$. Additionally, the isospins are coupled to T and M_T.

As we are dealing with fermions, these basis sets need to be antisymmetrized in order to perform actual calculations with them. This, however, is nontrivial in all cases except for the product-state basis whose antisymmetric counterpart is spanned by Slater determinants $|abc\rangle$. For the other sets we have to perform the antisymmetrization via explicit projection onto the antisymmetric subspace (see section 5.3).

For this, it is useful to have a basis that is antisymmetric under exchange of the first two particles. We use the antisymmetrizer

$$\mathscr{A}_{12} = \frac{1}{2}(\mathbf{1} - \boldsymbol{P}_{12}) \tag{5.20}$$

and evaluate the action of the transposition operator $\boldsymbol{P}_{12}$ on a basis state. Using (5.18) and exploiting the symmetry properties of the Clebsch-Gordan coefficients (see appendix A.1) we get

$$\boldsymbol{P}_{12} \,|[(\tilde{a}\tilde{b})J_{ab}T_{ab}, \tilde{c}]JMTM_T\rangle_n = (-1)^{j_a+j_b-J_{ab}+t_a+t_b-T_{ab}} \,|[(\tilde{b}\tilde{a})J_{ab}T_{ab}, \tilde{c}]JMTM_T\rangle_n \tag{5.21}$$

for the JT-coupled basis and, in an analogous way,

$$\boldsymbol{P}_{12} \,|(n_{\mathrm{cm}}l_{\mathrm{cm}}, \bar{\alpha})JM\rangle_n = (-1)^{l_1+s_a+s_b-S_{ab}+t_a+t_b-T_{ab}} \,|(n_{\mathrm{cm}}l_{\mathrm{cm}}, \bar{\alpha}[a \leftrightarrow b])JM\rangle_n \tag{5.22}$$

for the Jacobi HO basis, where $\bar{\alpha}[a \leftrightarrow b]$ is $\bar{\alpha}$ with all subscripts a and b exchanged.[1] Putting everything together, we get

$$|[(\tilde{a}\tilde{b})J_{ab}T_{ab}, \tilde{c}]JMTM_T\rangle_{12} = \left(2 + 2\delta_{\tilde{a}}^{\tilde{b}}\right)^{-1/2}\left(|[(\tilde{a}\tilde{b})J_{ab}T_{ab}, \tilde{c}]JMTM_T\rangle_n \right.$$
$$\left. - (-1)^{j_a+j_b-J_{ab}+t_a+t_b-T_{ab}} \,|[(\tilde{b}\tilde{a})J_{ab}T_{ab}, \tilde{c}]JMTM_T\rangle_n\right) \tag{5.23}$$

$$|(n_{\mathrm{cm}}l_{\mathrm{cm}}, \bar{\alpha})JM\rangle_{12} = \left(2 + 2\delta_{s_b t_b \mathcal{S}_b}^{s_a t_a \mathcal{S}_a}\right)^{-1/2}\left(|(n_{\mathrm{cm}}l_{\mathrm{cm}}, \bar{\alpha})JM\rangle_n \right.$$
$$\left. - (-1)^{l_1+s_a+s_b-S_{ab}+t_a+t_b-T_{ab}} \,|(n_{\mathrm{cm}}l_{\mathrm{cm}}, \bar{\alpha}[a \leftrightarrow b])JM\rangle_n\right) \tag{5.24}$$

and we label states having this kind of exchange symmetry with the subscript 12. The factors in parentheses ensure the normalization of the antisymmetrized states.

5.3. Antisymmetrization of the Jacobi HO Basis

As already alluded to in the previous section, the antisymmetrization of states in three-body space is nontrivial except for product states. This is in contrast to two-body space where the

---

[1] The exchange in coordinate space is equivalent to a reversal of the first Jacobi coordinate that gives a phase factor $(-1)^{l_1}$ from the spherical harmonic.

process is simple.[2] We achieve antisymmetrization of the Jacobi HO basis via explicit projection onto the antisymmetric subspace.

Consider the antisymmetrizer

$$\mathscr{A} = \frac{1}{3!}(1 - P_{12} - P_{13} - P_{23} + P_{23}P_{12} + P_{13}P_{12}). \tag{5.25}$$

The operator $\mathscr{A}$ is Hermitian and idempotent and thus a projection operator. From these properties we conclude that its only possible eigenvalues are $\lambda = 0$ and $\lambda = 1$ and by the spectral theorem we have

$$\mathscr{A} = \sum_i |\phi_i\rangle\langle\phi_i| \tag{5.26}$$

with the $|\phi_i\rangle$ forming an orthonormal set that spans the subspace of eigenvectors to the eigenvalue $\lambda = 1$. This subspace is the antisymmetric subspace of the three-body Hilbert space, so we are left with determining the eigenvectors $|\phi_i\rangle$.

In order to solve the eigenvalue problem we have to calculate matrix elements of $\mathscr{A}$. To simplify the derivation we use the 12-antisymmetric Jacobi HO basis for which

$$P_{12}\,|(n_{\mathrm{cm}}l_{\mathrm{cm}}, \bar{\alpha})JM\rangle_{12} = -\,|(n_{\mathrm{cm}}l_{\mathrm{cm}}, \bar{\alpha})JM\rangle_{12} \tag{5.27}$$

holds. We also use that any transposition operator P_{ij} can be written as a conjugation of two different transpositions $P_{kl}P_{mn}P_{kl}$, in particular we have the relation $P_{13} = P_{12}P_{23}P_{12}$. Exploiting these relations a general matrix element of the antisymmetrizer reads

$$
{}_{12}\langle(n_{\mathrm{cm}}l_{\mathrm{cm}}, \bar{\alpha})JM|\mathscr{A}|(n'_{\mathrm{cm}}l'_{\mathrm{cm}}, \bar{\alpha}')J'M'\rangle_{12} = \frac{1}{6}\,{}_{12}\langle(n_{\mathrm{cm}}l_{\mathrm{cm}}, \bar{\alpha})JM|
$$
$$
\times\,(1 - (-1) - (-1)P_{23}(-1) - P_{23} + P_{23}(-1) + (-1)P_{23})\,|(n'_{\mathrm{cm}}l'_{\mathrm{cm}}, \bar{\alpha}')J'M'\rangle_{12}
$$
$$
= \frac{1}{3}\,{}_{12}\langle(n_{\mathrm{cm}}l_{\mathrm{cm}}, \bar{\alpha})JM|(1 - 2P_{23})|(n'_{\mathrm{cm}}l'_{\mathrm{cm}}, \bar{\alpha}')J'M'\rangle_{12} \tag{5.28}
$$

and the eigenvalue problem of $\mathscr{A}$ reduces to the one of P_{23}.

Next, we disentangle the spin, isospin and spatial degrees of freedom so we can evaluate the action of P_{23} on each of them separately. This is achieved by decoupling the center of mass and switching from a jj to an LS coupling scheme,

$$
{}_{12}\langle(n_{\mathrm{cm}}l_{\mathrm{cm}}, \bar{\alpha})JM|P_{23}|(n'_{\mathrm{cm}}l'_{\mathrm{cm}}, \bar{\alpha}')J'M'\rangle_{12}
$$

$$
= \sum_{\substack{m_{\mathrm{cm}}\mathscr{M} \\ m'_{\mathrm{cm}}\mathscr{M}'}} \sum_{\substack{LS \\ L'S'}} \sum_{\substack{M_L M_S \\ M'_L M'_S}} \hat{j}_1\hat{j}'_1\hat{j}_2\hat{j}'_2\hat{L}\hat{L}'\hat{S}\hat{S}'
\begin{Bmatrix} l_1 & S_{ab} & j_1 \\ l_2 & s_c & j_2 \\ L & S & \mathscr{J} \end{Bmatrix}
\begin{Bmatrix} l'_1 & S'_{ab} & j'_1 \\ l'_2 & s'_c & j'_2 \\ L' & S' & \mathscr{J}' \end{Bmatrix}
$$

$$
\times \begin{pmatrix} l_{\mathrm{cm}} & \mathscr{J} & J \\ m_{\mathrm{cm}} & \mathscr{M} & M \end{pmatrix}
\begin{pmatrix} l'_{\mathrm{cm}} & \mathscr{J}' & J' \\ m'_{\mathrm{cm}} & \mathscr{M}' & M' \end{pmatrix}
\begin{pmatrix} L & S & \mathscr{J} \\ M_L & M_S & \mathscr{M} \end{pmatrix}
\begin{pmatrix} L' & S' & \mathscr{J}' \\ M'_L & M'_S & \mathscr{M}' \end{pmatrix}
$$

$$
\times\,{}_{12}\langle n_{\mathrm{cm}}l_{\mathrm{cm}}m_{\mathrm{cm}}, (n_1 l_1 n_2 l_2)LM_L, [(s_a s_b)S_{ab}, s_c]SM_S, [(\mathscr{S}_a t_a \mathscr{S}_b t_b)T_{ab}, \mathscr{S}_c t_c]TM_T|
$$
$$
\times\,P_{23}
$$
$$
\times\,|n'_{\mathrm{cm}}l'_{\mathrm{cm}}m'_{\mathrm{cm}}, (n'_1 l'_1 n'_2 l'_2)L'M'_L, [(s'_a s'_b)S'_{ab}, s'_c]S'M'_S, [(\mathscr{S}'_a t'_a \mathscr{S}'_b t'_b)T'_{ab}, \mathscr{S}'_c t'_c]T'M'_T\rangle_{12}. \tag{5.29}
$$

---

[2]The two-body Hilbert space is fully decomposable into a symmetric and an antisymmetric part, $\mathscr{H}_2 = \mathscr{H}_1 \otimes \mathscr{H}_1 = \mathscr{H}_2^S \oplus \mathscr{H}_2^A$, which is not possible for spaces with three or more particles.

To evaluate the action of $\boldsymbol{P}_{23}$ we now consider non-antisymmetric states and later use (5.24) to recover the full result.

5.3.1. (Iso-)Spin Part

The coupling scheme of the spin and isospin parts is the same, so the result can be applied to both. Consider a state $|[(s_a s_b)_{12} S_{ab}, s_c] S M_S\rangle_n$ where the subscript of the parenthesized quantum numbers identifies them as belonging to the first two particles. Then, we have

$$
\begin{aligned}
\boldsymbol{P}_{23} |[(s_a s_b)_{12} S_{ab}, s_c] S M_S\rangle_n &= \sum_{\substack{m_a m_b \\ M_{ab} m_c}} \begin{pmatrix} s_a & s_b & S_{ab} \\ m_a & m_b & M_{ab} \end{pmatrix} \begin{pmatrix} S_{ab} & s_c & S \\ M_{ab} & m_c & M_S \end{pmatrix} \boldsymbol{P}_{23} |s_a m_a, s_b m_b, s_c m_c\rangle_n \\
&= \sum_{\substack{m_a m_b \\ M_{ab} m_c}} \begin{pmatrix} s_a & s_b & S_{ab} \\ m_a & m_b & M_{ab} \end{pmatrix} \begin{pmatrix} S_{ab} & s_c & S \\ M_{ab} & m_c & M_S \end{pmatrix} |s_a m_a, s_c m_c, s_b m_b\rangle_n \\
&= |[(s_a s_b)_{13} S_{ab}, s_c] S M_S\rangle_n
\end{aligned}
\tag{5.30}
$$

where the parenthesized quantum numbers now refer to the first and third particle. The full matrix element can be expressed in terms of a $6j$ symbol:

$$
\begin{aligned}
{}_n\langle [(s_a' s_b')_{12} S_{ab}', s_c'] S' M_S' | \boldsymbol{P}_{23} |[(s_a s_b)_{12} S_{ab}, s_c] S M_S\rangle_n \\
= {}_n\langle [(s_a' s_b')_{12} S_{ab}', s_c'] S' M_S' |[(s_a s_b)_{13} S_{ab}, s_c] S M_S\rangle_n \\
= \delta^{s_a' s_c' s_b' S' M_S'}_{s_a s_b s_c S M_S} (-1)^{s_b+s_c+S_{ab}+S_{ab}'} \hat{S}_{ab} \hat{S}_{ab}' \begin{Bmatrix} s_b & s_a & S_{ab} \\ s_c & S & S_{ab}' \end{Bmatrix}.
\end{aligned}
\tag{5.31}
$$

The isospin part has an additional constraint $\delta^{\mathcal{S}_a' \mathcal{S}_c' \mathcal{S}_b'}_{\mathcal{S}_a \mathcal{S}_b \mathcal{S}_c}$ on the strangeness quantum numbers.

5.3.2. Spatial Part

The spatial part depends on the masses of the particles involved and hence on the isospin part. Thus, the constraints from the isospin part have to be kept in mind when deriving the action of $\boldsymbol{P}_{23}$ on this part. This action is most easily evaluated by transforming to single-particle coordinates and decoupling to product states. After a lengthy computation (see appendix C.2) we get

$$
\boldsymbol{P}_{23} |n_{\text{cm}} l_{\text{cm}} m_{\text{cm}}, (n_1 l_1 n_2 l_2) L M_L\rangle = |n_{\text{cm}} l_{\text{cm}} m_{\text{cm}}, (\{n_1 l_1\}_{13} n_2 l_2) L M_L\rangle
\tag{5.32}
$$

where the first Jacobi coordinate now connects the first and the third particle. The isospin part is also permuted by $\boldsymbol{P}_{23}$, effectively exchanging the mass of the second and third particles. The coordinates describing the situation after the permutation are thus the ξ_i' with masses m_a, m_c, m_b and the matrix element can be expressed in terms of a HO bracket:

$$
\begin{aligned}
\langle n_{\text{cm}}' l_{\text{cm}}' m_{\text{cm}}', (n_1' l_1' n_2' l_2') L' M_L' | \boldsymbol{P}_{23} |n_{\text{cm}} l_{\text{cm}} m_{\text{cm}}, (n_1 l_1 n_2 l_2) L M_L\rangle \\
= \delta^{n_{\text{cm}}' l_{\text{cm}}' m_{\text{cm}}' L' M_L'}_{n_{\text{cm}} l_{\text{cm}} m_{\text{cm}} L M_L} \langle\!\langle n_1' l_1', n_2' l_2' \mid n_1 l_1, n_2 l_2 : L \rangle\!\rangle_D
\end{aligned}
\tag{5.33}
$$

where $D = m_b m_c/(m_a(m_a + m_b + m_c))$. The HO bracket also implies conservation of the energy quantum number $E = 2(n_1 + n_2) + (l_1 + l_2)$. This is a major advantage of working in a HO basis because the antisymmetrizer is block diagonal and the eigenvalue problem can be solved exactly for each value of E.

5.3.3. Matrix Elements of the Antisymmetrizer

We now combine the results from the previous sections to get an expression for the full matrix element of $\boldsymbol{P}_{23}$. To shorten the following formulae, we introduce the notation

$$\Delta^{a'b'c'}_{abc} \equiv \delta^{s'_a s'_b s'_c}_{s_a s_b s_c} \delta^{t'_a t'_b t'_c}_{t_a t_b t_c} \delta^{\mathcal{S}'_a \mathcal{S}'_b \mathcal{S}'_c}_{\mathcal{S}_a \mathcal{S}_b \mathcal{S}_c}. \tag{5.34}$$

Starting from (5.29), we get

$$\begin{aligned}
&_n\langle (n_{\mathrm{cm}} l_{\mathrm{cm}}, \bar{\alpha}) J M | \boldsymbol{P}_{23} | (n'_{\mathrm{cm}} l'_{\mathrm{cm}}, \bar{\alpha}') J' M' \rangle_n \\
&= \delta^{n'_{\mathrm{cm}} l'_{\mathrm{cm}}}_{n_{\mathrm{cm}} l_{\mathrm{cm}}} \delta^{T' M'_T}_{T M_T} \Delta^{a'c'b'}_{abc} \sum_{LS} \hat{j}_1 \hat{j}'_1 \hat{j}_2 \hat{j}'_2 \hat{L}^2 \hat{S}^2 \hat{S}_{ab} \hat{S}'_{ab} \hat{T}_{ab} \hat{T}'_{ab} \langle\!\langle n_1 l_1, n_2 l_2 \mid n'_1 l'_1, n'_2 l'_2 : L \rangle\!\rangle_D \\
&\quad \times (-1)^{s_b + s_c + S_{ab} + S'_{ab} + t_b + t_c + T_{ab} + T'_{ab}} \begin{Bmatrix} l_1 & S_{ab} & j_1 \\ l_2 & s_c & j_2 \\ L & S & \mathscr{J} \end{Bmatrix} \begin{Bmatrix} l'_1 & S'_{ab} & j'_1 \\ l'_2 & s'_c & j'_2 \\ L & S & \mathscr{J}' \end{Bmatrix} \begin{Bmatrix} s_b & s_a & S_{ab} \\ s_c & S & S'_{ab} \end{Bmatrix} \begin{Bmatrix} t_b & t_a & T_{ab} \\ t_c & T & T'_{ab} \end{Bmatrix} \\
&\quad \times \sum_{m_{\mathrm{cm}}} \sum_{M_L M_S} \sum_{\mathscr{M} \mathscr{M}'} \begin{pmatrix} l_{\mathrm{cm}} & \mathscr{J} & J \\ m_{\mathrm{cm}} & \mathscr{M} & M \end{pmatrix} \begin{pmatrix} l_{\mathrm{cm}} & \mathscr{J}' & J' \\ m_{\mathrm{cm}} & \mathscr{M}' & M' \end{pmatrix} \begin{pmatrix} L & S & \mathscr{J} \\ M_L & M_S & \mathscr{M} \end{pmatrix} \begin{pmatrix} L & S & \mathscr{J}' \\ M_L & M_S & \mathscr{M}' \end{pmatrix} \\
&= \delta^{n'_{\mathrm{cm}} l'_{\mathrm{cm}} \mathscr{J}' J' M'}_{n_{\mathrm{cm}} l_{\mathrm{cm}} \mathscr{J} J M} \delta^{T' M'_T}_{T M_T} \Delta^{a'c'b'}_{abc} \sum_{LS} \hat{j}_1 \hat{j}'_1 \hat{j}_2 \hat{j}'_2 \hat{L}^2 \hat{S}^2 \hat{S}_{ab} \hat{S}'_{ab} \hat{T}_{ab} \hat{T}'_{ab} \langle\!\langle n_1 l_1, n_2 l_2 \mid n'_1 l'_1, n'_2 l'_2 : L \rangle\!\rangle_D \\
&\quad \times (-1)^{s_b + s_c + S_{ab} + S'_{ab} + t_b + t_c + T_{ab} + T'_{ab}} \begin{Bmatrix} l_1 & S_{ab} & j_1 \\ l_2 & s_c & j_2 \\ L & S & \mathscr{J} \end{Bmatrix} \begin{Bmatrix} l'_1 & S'_{ab} & j'_1 \\ l'_2 & s'_c & j'_2 \\ L & S & \mathscr{J} \end{Bmatrix} \begin{Bmatrix} s_b & s_a & S_{ab} \\ s_c & S & S'_{ab} \end{Bmatrix} \begin{Bmatrix} t_b & t_a & T_{ab} \\ t_c & T & T'_{ab} \end{Bmatrix}
\end{aligned} \tag{5.35}$$

where we exploited the orthogonality relation of the Clebsch-Gordan coefficients to remove sums over the projection quantum numbers. The matrix element is completely independent of the center-of-mass degree of freedom, so we can ignore it in our further considerations. With (5.24), we then get

$$\begin{aligned}
&_{12}\langle \alpha | \boldsymbol{P}_{23} | \alpha' \rangle_{12} \\
&= \mathcal{N} \mathcal{N}' \Big({}_n\langle \alpha | \boldsymbol{P}_{23} | \alpha' \rangle_n \\
&\quad - (-1)^{l_1 + s_a + s_b - S_{ab} + t_a + t_b - T_{ab}} \, {}_n\langle \alpha[a \leftrightarrow b] | \boldsymbol{P}_{23} | \alpha' \rangle_n \\
&\quad - (-1)^{l'_1 + s'_a + s'_b - S'_{ab} + t'_a + t'_b - T'_{ab}} \, {}_n\langle \alpha | \boldsymbol{P}_{23} | \alpha'[a \leftrightarrow b] \rangle_n \\
&\quad + (-1)^{l_1 + l'_1 + s_a + s'_a + s_b + s'_b - S_{ab} - S'_{ab} + t_a + t'_a + t_b + t'_b - T_{ab} - T'_{ab}} \, {}_n\langle \alpha[a \leftrightarrow b] | \boldsymbol{P}_{23} | \alpha'[a \leftrightarrow b] \rangle_n \Big)
\end{aligned}$$

$$= \mathscr{N}\mathscr{N}' \delta^{\mathscr{J}'\mathscr{M}'}_{\mathscr{J}\mathscr{M}} \delta^{T'M'_T}_{T M_T} \hat{j}_1 \hat{j}'_1 \hat{j}_2 \hat{j}'_2 \hat{S}_{ab} \hat{S}'_{ab} \hat{T}_{ab} \hat{T}'_{ab} \sum_{LS} \hat{L}^2 \hat{S}^2 \begin{Bmatrix} l_1 & S_{ab} & j_1 \\ l_2 & s_c & j_2 \\ L & S & \mathscr{J} \end{Bmatrix}$$

$$\times \left(\begin{Bmatrix} l'_1 & S'_{ab} & j'_1 \\ l'_2 & s_b & j'_2 \\ L & S & \mathscr{J} \end{Bmatrix} \begin{Bmatrix} s_b & s_a & S_{ab} \\ s_c & S & S'_{ab} \end{Bmatrix} \begin{Bmatrix} t_b & t_a & T_{ab} \\ t_c & T & T'_{ab} \end{Bmatrix} \langle\!\langle n_1 l_1, n_2 l_2 \mid n'_1 l'_1, n'_2 l'_2 : L \rangle\!\rangle_D \right.$$

$$\times \left((-1)^{s_b+s_c+S_{ab}+S'_{ab}+t_b+t_c+T_{ab}+T'_{ab}} \Delta^{a'c'b'}_{abc} - (-1)^{l'_1+s_a+s_b+2s_c+S_{ab}+t_a+t_b+2t_c+T_{ab}} \Delta^{b'c'a'}_{abc} \right)$$

$$+ \begin{Bmatrix} l'_1 & S'_{ab} & j'_1 \\ l'_2 & s_a & j'_2 \\ L & S & \mathscr{J} \end{Bmatrix} \begin{Bmatrix} s_a & s_b & S_{ab} \\ s_c & S & S'_{ab} \end{Bmatrix} \begin{Bmatrix} t_a & t_b & T_{ab} \\ t_c & T & T'_{ab} \end{Bmatrix} \langle\!\langle n_1 l_1, n_2 l_2 \mid n'_1 l'_1, n'_2 l'_2 : L \rangle\!\rangle_{D'}$$

$$\left. \times \left((-1)^{l_1+l'_1+2(s_a+s_b+s_c)+2(t_a+t_b+t_c)} \Delta^{c'b'a'}_{abc} - (-1)^{l_1+2s_a+s_b+s_c+S'_{ab}+2t_a+t_b+t_c+T'_{ab}} \Delta^{c'a'b'}_{abc} \right) \right),$$

and assuming all particles are spin-*s* fermions yields

$$= -\mathscr{N}\mathscr{N}' \delta^{\mathscr{J}'\mathscr{M}'}_{\mathscr{J}\mathscr{M}} \delta^{T'M'_T}_{T M_T} \hat{j}_1 \hat{j}'_1 \hat{j}_2 \hat{j}'_2 \hat{S}_{ab} \hat{S}'_{ab} \hat{T}_{ab} \hat{T}'_{ab} \sum_{LS} \hat{L}^2 \hat{S}^2 \begin{Bmatrix} l_1 & S_{ab} & j_1 \\ l_2 & s & j_2 \\ L & S & \mathscr{J} \end{Bmatrix} \begin{Bmatrix} l'_1 & S'_{ab} & j'_1 \\ l'_2 & s & j'_2 \\ L & S & \mathscr{J} \end{Bmatrix} \begin{Bmatrix} s & s & S_{ab} \\ s & S & S'_{ab} \end{Bmatrix}$$

$$\times \left(\begin{Bmatrix} t_b & t_a & T_{ab} \\ t_c & T & T'_{ab} \end{Bmatrix} \langle\!\langle n_1 l_1, n_2 l_2 \mid n'_1 l'_1, n'_2 l'_2 : L \rangle\!\rangle_D \right.$$

$$\times \left((-1)^{S_{ab}+S'_{ab}+t_b+t_c+T_{ab}+T'_{ab}} \Delta^{a'c'b'}_{abc} + (-1)^{l'_1+S_{ab}+t_a+t_b+2t_c+T_{ab}} \Delta^{b'c'a'}_{abc} \right)$$

$$+ \begin{Bmatrix} t_a & t_b & T_{ab} \\ t_c & T & T'_{ab} \end{Bmatrix} \langle\!\langle n_1 l_1, n_2 l_2 \mid n'_1 l'_1, n'_2 l'_2 : L \rangle\!\rangle_{D'}$$

$$\left. \times \left((-1)^{l_1+l'_1+2(t_a+t_b+t_c)} \Delta^{c'b'a'}_{abc} + (-1)^{l_1+S'_{ab}+2t_a+t_b+t_c+T'_{ab}} \Delta^{c'a'b'}_{abc} \right) \right) \tag{5.36}$$

with $\mathscr{N}, \mathscr{N}'$ denoting the normalization factors of (5.24) and the transformation parameter $D' = m_a m_c/(m_b(m_a + m_b + m_c)) = D[a \leftrightarrow b]$.

From this formula we can see that the antisymmetrizer is blockdiagonal with respect to the quantum numbers T, M_T, $\mathscr{J}$, $\mathscr{M}$, E, and the orderless set of quantum numbers $\mathscr{X} = \{(s_a t_a \mathscr{S}_a), (s_b t_b \mathscr{S}_b), (s_c t_c \mathscr{S}_c)\}$ defining the species of the participant particles. It is also independent of the projection quantum numbers $\mathscr{M}$ and M_T. We get the dimension of each antisymmetric subspace $\mathscr{V}_a$ by recalling that the trace of a matrix is the sum of its eigenvalues and, because $\mathscr{V}_a$ is an eigenspace of $\mathscr{A}$ with eigenvalue $\lambda = 1$ and the only other eigenvalue is $\lambda = 0$,

$$\operatorname{tr}_{\mathscr{V}} \mathscr{A} = \dim \mathscr{V}_a = \frac{1}{3}(\operatorname{tr}_{\mathscr{V}} \mathbf{1} - 2\operatorname{tr}_{\mathscr{V}} \boldsymbol{P}_{23}) = \frac{1}{3}(\dim \mathscr{V} - 2\operatorname{tr}_{\mathscr{V}} \boldsymbol{P}_{23}), \tag{5.37}$$

where $\operatorname{tr}_{\mathscr{V}}$ denotes the trace over the space $\mathscr{V}$ spanned by the $|\alpha\rangle_{12}$ with given quantum numbers.

The eigenvalue problem of $\mathscr{A}$ can be solved via standard numerical methods, and the solution yields an orthonormal basis of the antisymmetric subspace

$$|\phi_i\rangle \equiv |Ei\mathscr{J}\mathscr{M}\mathscr{X}TM_T\rangle = \sum_\alpha c^{(EJ\mathscr{X}T)}_{i,\alpha} |\alpha\rangle_{12} \tag{5.38}$$

given in terms of the $|\alpha\rangle_{12}$ with coefficients $c_{i,\alpha}^{(EJ\mathscr{X}T)}$. These coefficients are called Coefficients of Fractional Parentage (CFPs). Keep in mind that the eigenvalue problem they were obtained from is highly degenerate, and the numerical solver returns an arbitrary basis choice. We therefore compute the CFPs only once to define the basis and use this basis in all subsequent calculations.

5.4. Transformation to Single-Particle Coordinates

With a properly antisymmetrized Jacobi HO basis in place we are able to perform the SRG evolution in three-body space. However, the many-body calculations in which we want to use the evolved interactions employ a Slater-determinant basis. We thus need to transform to single-particle coordinates and subsequently decouple to the *m* scheme. The first step is described in the following.

The main goal of this derivation is finding an expression for the overlap

$$
T\begin{bmatrix} \tilde{a} & J_{ab} & n_{\mathrm{cm}} & l_{\mathrm{cm}} & S_{ab} & T_{ab} \\ \tilde{b} & \mathscr{J} & n_1 & l_1 & j_1 \\ \tilde{c} & J & n_2 & l_2 & j_2 \end{bmatrix} \equiv {}_{12}\langle (n_{\mathrm{cm}}l_{\mathrm{cm}}, \bar{\alpha})JM \,|\, [(\tilde{a}\tilde{b})J_{ab}T_{ab}, \tilde{c}]JMTM_T\rangle_n, \tag{5.39}
$$

which, as we will see, is independent of total isospin *T* as well as the projection quantum numbers *M* and M_T. As in the previous section we perform the derivation using non-antisymmetric states and employ (5.24) to get the final answer. We also ignore the isospin part of the state to simplify the derivation.[3] We compute the overlap by expressing a state of the *JT*-coupled basis in terms of the Jacobi HO basis. The transformation occurs in eight steps, depicted in the following (the acronyms below the arrows denote the object that effects the desired transformation):

$$
[(\tilde{a}\tilde{b})J_{ab}, \tilde{c}]J \xrightarrow[\mathrm{9j}]{①} \{[(n_a l_a, n_b l_b)L_{ab}, (s_a s_b)S_{ab}]J_{ab}, \tilde{c}\}J
$$

$$
\xrightarrow[\mathrm{HOB}]{②} \{[(N_1 L_1, n_1 l_1)L_{ab}, (s_a s_b)S_{ab}]J_{ab}, \tilde{c}\}J
$$

$$
\xrightarrow[\mathrm{9j}]{③} \{[(N_1 L_1, n_1 l_1)L_{ab}, n_c l_c]L, [(s_a s_b)S_{ab}, s_c]S\}J
$$

$$
\xrightarrow[\mathrm{6j}]{④} \{[(N_1 L_1, n_c l_c)\Lambda, n_1 l_1]L, [(s_a s_b)S_{ab}, s_c]S\}J
$$

$$
\xrightarrow[\mathrm{HOB}]{⑤} \{[(n_{\mathrm{cm}}l_{\mathrm{cm}}, n_2 l_2)\Lambda, n_1 l_1]L, [(s_a s_b)S_{ab}, s_c]S\}J
$$

$$
\xrightarrow[\mathrm{6j}]{⑥} \{[n_{\mathrm{cm}}l_{\mathrm{cm}}, (n_1 l_1, n_2 l_2)\mathscr{L}]L, [(s_a s_b)S_{ab}, s_c]S\}J
$$

$$
\xrightarrow[\mathrm{6j}]{⑦} (n_{\mathrm{cm}}l_{\mathrm{cm}}, \{(n_1 l_1, n_2 l_2)\mathscr{L}, [(s_a s_b)S_{ab}, s_c]S\}\mathscr{J})J
$$

$$
\xrightarrow[\mathrm{9j}]{⑧} (n_{\mathrm{cm}}l_{\mathrm{cm}}, \{[n_1 l_1, (s_a s_b)S_{ab}]j_1, (n_2 l_2, s_c)j_2\}\mathscr{J})J.
$$

---

[3] We assume that the particle masses m_a, m_b, m_c do not depend on the isospin projection. For nucleons and hyperons this approximation is accurate to the sub-percent level.

The acronyms HOB, 6j, and 9j denote HO brackets, Wigner 6j, and Wigner 9j symbols, respectively, the properties of which are summarized in appendix A. We prepare for the first HO bracket by moving the first two particles from a jj to an LS coupling scheme:

$$|[(\tilde{a}\tilde{b})J_{ab}, \tilde{c}]J\rangle_n$$

$$\stackrel{①}{=} \sum_{L_{ab}S_{ab}} \hat{j}_a\hat{j}_b\hat{L}_{ab}\hat{S}_{ab} \begin{Bmatrix} l_a & l_b & L_{ab} \\ s_a & s_b & S_{ab} \\ j_a & j_b & J_{ab} \end{Bmatrix} |\{[(n_al_a, n_bl_b)L_{ab}, (s_as_b)S_{ab}]J_{ab}, \tilde{c}\}JM\rangle_n .$$

We get the first Jacobi coordinate ξ_1 and the center-of-mass coordinate of the first two particles from inserting the HO bracket:

$$\stackrel{②}{=} \sum_{L_{ab}S_{ab}} \sum_{N_1L_1} \sum_{n_1l_1} \hat{j}_a\hat{j}_b\hat{L}_{ab}\hat{S}_{ab} \begin{Bmatrix} l_a & l_b & L_{ab} \\ s_a & s_b & S_{ab} \\ j_a & j_b & J_{ab} \end{Bmatrix} \langle\langle n_al_a, n_bl_b \mid N_1L_1, n_1l_1 : L_{ab}\rangle\rangle_{\frac{m_a}{m_b}}$$

$$\times |\{[(N_1L_1, n_1l_1)L_{ab}, (s_as_b)S_{ab}]J_{ab}, \tilde{c}\}JM\rangle_n ,$$

and to completely move into the Jacobi HO basis we have to couple N_1L_1 and n_cl_c together. First, we couple the orbital angular momenta, yielding

$$\stackrel{③}{=} \sum_{L_{ab}S_{ab}} \sum_{N_1L_1} \sum_{n_1l_1} \sum_{LS} \hat{j}_a\hat{j}_b\hat{j}_c\hat{L}_{ab}\hat{S}_{ab}\hat{J}_{ab}\hat{L}\hat{S} \begin{Bmatrix} l_a & l_b & L_{ab} \\ s_a & s_b & S_{ab} \\ j_a & j_b & J_{ab} \end{Bmatrix} \begin{Bmatrix} L_{ab} & l_c & L \\ S_{ab} & s_c & S \\ J_{ab} & j_c & J \end{Bmatrix}$$

$$\times \langle\langle n_al_a, n_bl_b \mid N_1L_1, n_1l_1 : L_{ab}\rangle\rangle_{\frac{m_a}{m_b}} |\{[(N_1L_1, n_1l_1)L_{ab}, n_cl_c]L, [(s_as_b)S_{ab}, s_c]S\}JM\rangle_n ,$$

and then change the coupling order:

$$\stackrel{④}{=} \sum_{L_{ab}S_{ab}} \sum_{N_1L_1} \sum_{n_1l_1} \sum_{LS} \sum_{\Lambda} (-1)^{\Lambda+L_{ab}+l_1+l_c} \hat{j}_a\hat{j}_b\hat{j}_c\hat{L}_{ab}^2\hat{S}_{ab}\hat{J}_{ab}\hat{L}\hat{S}\hat{\Lambda}$$

$$\times \begin{Bmatrix} l_a & l_b & L_{ab} \\ s_a & s_b & S_{ab} \\ j_a & j_b & J_{ab} \end{Bmatrix} \begin{Bmatrix} L_{ab} & l_c & L \\ S_{ab} & s_c & S \\ J_{ab} & j_c & J \end{Bmatrix} \begin{Bmatrix} l_1 & L_1 & L_{ab} \\ l_c & L & \Lambda \end{Bmatrix}$$

$$\times \langle\langle n_al_a, n_bl_b \mid N_1L_1, n_1l_1 : L_{ab}\rangle\rangle_{\frac{m_a}{m_b}} |\{[(N_1L_1, n_cl_c)\Lambda, n_1l_1]L, [(s_as_b)S_{ab}, s_c]S\}JM\rangle_n .$$

Inserting a second HO bracket,

$$\stackrel{⑤}{=} \sum_{L_{ab}S_{ab}} \sum_{N_1L_1} \sum_{n_1l_1} \sum_{LS} \sum_{\Lambda} \sum_{n_{cm}l_{cm}} \sum_{n_2l_2} (-1)^{\Lambda+L_{ab}+l_1+l_c} \hat{j}_a\hat{j}_b\hat{j}_c\hat{L}_{ab}^2\hat{S}_{ab}\hat{J}_{ab}\hat{L}\hat{S}\hat{\Lambda}$$

$$\times \begin{Bmatrix} l_a & l_b & L_{ab} \\ s_a & s_b & S_{ab} \\ j_a & j_b & J_{ab} \end{Bmatrix} \begin{Bmatrix} L_{ab} & l_c & L \\ S_{ab} & s_c & S \\ J_{ab} & j_c & J \end{Bmatrix} \begin{Bmatrix} l_1 & L_1 & L_{ab} \\ l_c & L & \Lambda \end{Bmatrix}$$

$$\times \langle\langle n_al_a, n_bl_b \mid N_1L_1, n_1l_1 : L_{ab}\rangle\rangle_{\frac{m_a}{m_b}} \langle\langle N_1L_1, n_cl_c \mid n_{cm}l_{cm}, n_2l_2 : \Lambda\rangle\rangle_{\frac{m_a+m_b}{m_c}}$$

$$\times |\{[(n_{cm}l_{cm}, n_2l_2)\Lambda, n_1l_1]L, [(s_as_b)S_{ab}, s_c]S\}JM\rangle_n ,$$

we complete the transformation to the Jacobi HO basis and are left with the task of decoupling the center of mass from the intrinsic degrees of freedom. For that, we change coupling order twice,

$$
\overset{\text{⑥}}{=} \sum_{L_{ab}S_{ab}} \sum_{N_1L_1} \sum_{n_1l_1} \sum_{LS} \sum_{\Lambda} \sum_{n_{\text{cm}}l_{\text{cm}}} \sum_{n_2l_2} \sum_{\mathscr{L}} (-1)^{\Lambda+L_{ab}+l_1+l_c+l_{\text{cm}}+l_1+l_2+L+(l_1+l_2-\mathscr{L})}
$$
$$
\times \hat{j}_a\hat{j}_b\hat{j}_c\hat{L}_{ab}^2\hat{S}_{ab}\hat{J}_{ab}\hat{L}\hat{S}\hat{\Lambda}^2\hat{\mathscr{L}}
$$
$$
\times \begin{Bmatrix} l_a & l_b & L_{ab} \\ s_a & s_b & S_{ab} \\ j_a & j_b & J_{ab} \end{Bmatrix} \begin{Bmatrix} L_{ab} & l_c & L \\ S_{ab} & s_c & S \\ J_{ab} & j_c & J \end{Bmatrix} \begin{Bmatrix} l_1 & L_1 & L_{ab} \\ l_c & L & \Lambda \end{Bmatrix} \begin{Bmatrix} l_{\text{cm}} & l_2 & \Lambda \\ l_1 & L & \mathscr{L} \end{Bmatrix}
$$
$$
\times \langle\!\langle n_al_a,n_bl_b \mid N_1L_1,n_1l_1 : L_{ab}\rangle\!\rangle_{\frac{m_a}{m_b}} \langle\!\langle N_1L_1,n_cl_c \mid n_{\text{cm}}l_{\text{cm}},n_2l_2 : \Lambda\rangle\!\rangle_{\frac{m_a+m_b}{m_c}}
$$
$$
\times |\{[n_{\text{cm}}l_{\text{cm}},(n_1l_1n_2l_2)\mathscr{L}]L,[(s_as_b)S_{ab},s_c]S\}JM\rangle_n
$$

$$
\overset{\text{⑦}}{=} \sum_{L_{ab}S_{ab}} \sum_{N_1L_1} \sum_{n_1l_1} \sum_{LS} \sum_{\Lambda} \sum_{n_{\text{cm}}l_{\text{cm}}} \sum_{n_2l_2} \sum_{\mathscr{L}} \sum_{\mathscr{J}} (-1)^{\Lambda+L+L_{ab}+l_1+l_c+l_{\text{cm}}-\mathscr{L}+l_{\text{cm}}+\mathscr{L}+S+J}
$$
$$
\times \hat{j}_a\hat{j}_b\hat{j}_c\hat{L}_{ab}^2\hat{S}_{ab}\hat{J}_{ab}\hat{L}^2\hat{S}\hat{\Lambda}^2\hat{\mathscr{L}}\hat{\mathscr{J}}
$$
$$
\times \begin{Bmatrix} l_a & l_b & L_{ab} \\ s_a & s_b & S_{ab} \\ j_a & j_b & J_{ab} \end{Bmatrix} \begin{Bmatrix} L_{ab} & l_c & L \\ S_{ab} & s_c & S \\ J_{ab} & j_c & J \end{Bmatrix} \begin{Bmatrix} l_1 & L_1 & L_{ab} \\ l_c & L & \Lambda \end{Bmatrix} \begin{Bmatrix} l_{\text{cm}} & l_2 & \Lambda \\ l_1 & L & \mathscr{L} \end{Bmatrix} \begin{Bmatrix} l_{\text{cm}} & \mathscr{L} & L \\ S & J & \mathscr{J} \end{Bmatrix}
$$
$$
\times \langle\!\langle n_al_a,n_bl_b \mid N_1L_1,n_1l_1 : L_{ab}\rangle\!\rangle_{\frac{m_a}{m_b}} \langle\!\langle N_1L_1,n_cl_c \mid n_{\text{cm}}l_{\text{cm}},n_2l_2 : \Lambda\rangle\!\rangle_{\frac{m_a+m_b}{m_c}}
$$
$$
\times |(n_{\text{cm}}l_{\text{cm}},\{(n_1l_1,n_2l_2)\mathscr{L},[(s_as_b)S_{ab},s_c]S\}\mathscr{J})JM\rangle_n \,,
$$

where the additional (parenthesized) phase factor in step six comes from reversing the coupling order of l_1 and l_2, and we simplified the phase factor in step seven, using that orbital angular momenta are integers. In the last step, we transform from LS to jj coupling in order to recover the α basis:

$$
\overset{\text{⑧}}{=} \sum_{L_{ab}S_{ab}} \sum_{N_1L_1} \sum_{n_1l_1} \sum_{LS} \sum_{\Lambda} \sum_{n_{\text{cm}}l_{\text{cm}}} \sum_{n_2l_2} \sum_{\mathscr{L}} \sum_{\mathscr{J}} \sum_{j_1j_2} (-1)^{\Lambda+L_{ab}+L+S+J+l_1+l_c}
$$
$$
\times \hat{j}_a\hat{j}_b\hat{j}_c\hat{j}_1\hat{j}_2\hat{L}_{ab}^2\hat{S}_{ab}\hat{J}_{ab}\hat{L}^2\hat{S}^2\hat{\Lambda}^2\hat{\mathscr{L}}^2\hat{\mathscr{J}}
$$
$$
\times \begin{Bmatrix} l_a & l_b & L_{ab} \\ s_a & s_b & S_{ab} \\ j_a & j_b & J_{ab} \end{Bmatrix} \begin{Bmatrix} L_{ab} & l_c & L \\ S_{ab} & s_c & S \\ J_{ab} & j_c & J \end{Bmatrix} \begin{Bmatrix} l_1 & l_2 & \mathscr{L} \\ S_{ab} & s_c & S \\ j_1 & j_2 & \mathscr{J} \end{Bmatrix} \begin{Bmatrix} l_1 & L_1 & L_{ab} \\ l_c & L & \Lambda \end{Bmatrix} \begin{Bmatrix} l_{\text{cm}} & l_2 & \Lambda \\ l_1 & L & \mathscr{L} \end{Bmatrix} \begin{Bmatrix} l_{\text{cm}} & \mathscr{L} & L \\ S & J & \mathscr{J} \end{Bmatrix} \times
$$
$$
\times \langle\!\langle n_al_a,n_bl_b \mid N_1L_1,n_1l_1 : L_{ab}\rangle\!\rangle_{\frac{m_a}{m_b}} \langle\!\langle N_1L_1,n_cl_c \mid n_{\text{cm}}l_{\text{cm}},n_2l_2 : \Lambda\rangle\!\rangle_{\frac{m_a+m_b}{m_c}}
$$
$$
\times |(n_{\text{cm}}l_{\text{cm}},\{[n_1l_1,(s_as_b)S_{ab}]j_1,(n_2l_2,s_c)j_2\}\mathscr{J})JM\rangle_n \,. \tag{5.40}
$$

Hence, the expression for the non-antisymmetric T coefficient is

$$
T_n\begin{bmatrix} \tilde{a} & J_{ab} & n_{\text{cm}} & l_{\text{cm}} & S_{ab} \\ \tilde{b} & \mathscr{J} & n_1 & l_1 & j_1 \\ \tilde{c} & J & n_2 & l_2 & j_2 \end{bmatrix} \equiv {}_n\langle(n_{\text{cm}}l_{\text{cm}},\bar{\alpha})JM \mid [(\tilde{a}\tilde{b})J_{ab}T_{ab},\tilde{c}]JMTM_T\rangle_n
$$
$$
= \sum_{L_{ab}} \sum_{N_1L_1} \sum_{LS} \sum_{\Lambda\mathscr{L}} (-1)^{\Lambda+L_{ab}+L+S+J+l_1+l_c} \hat{j}_a\hat{j}_b\hat{j}_c\hat{j}_1\hat{j}_2\hat{L}_{ab}^2\hat{S}_{ab}\hat{J}_{ab}\hat{L}^2\hat{S}^2\hat{\Lambda}^2\hat{\mathscr{L}}^2\hat{\mathscr{J}}
$$

$$\times \begin{Bmatrix} l_a & l_b & L_{ab} \\ s_a & s_b & S_{ab} \\ j_a & j_b & J_{ab} \end{Bmatrix} \begin{Bmatrix} L_{ab} & l_c & L \\ S_{ab} & s_c & S \\ J_{ab} & j_c & J \end{Bmatrix} \begin{Bmatrix} l_1 & l_2 & \mathscr{L} \\ S_{ab} & s_c & S \\ j_1 & j_2 & \mathscr{J} \end{Bmatrix} \begin{Bmatrix} l_1 & L_1 & L_{ab} \\ l_c & L & \Lambda \end{Bmatrix} \begin{Bmatrix} l_{cm} & l_2 & \Lambda \\ l_1 & L & \mathscr{L} \end{Bmatrix} \begin{Bmatrix} l_{cm} & \mathscr{L} & L \\ S & J & \mathscr{J} \end{Bmatrix}$$

$$\times \langle\!\langle n_a l_a, n_b l_b \mid N_1 L_1, n_1 l_1 : L_{ab} \rangle\!\rangle_{\frac{m_a}{m_b}} \langle\!\langle N_1 L_1, n_c l_c \mid n_{cm} l_{cm}, n_2 l_2 : \Lambda \rangle\!\rangle_{\frac{m_a+m_b}{m_c}}, \tag{5.41}$$

which is independent of the isospin quantum numbers T_{ab}, T, and M_T. Additionally, we get constraints from the HO brackets that require $e_a + e_b + e_c = 2n_{cm} + l_{cm} + E$ for nonvanishing T coefficients and effectively eliminate the sum over N_1. In terms of the non-antisymmetric ones the 12-antisymmetric T coefficient reads

$$T\begin{bmatrix} \tilde{a} & J_{ab} & n_{cm} & l_{cm} & S_{ab} & T_{ab} \\ \tilde{b} & \mathscr{J} & n_1 & l_1 & j_1 \\ \tilde{c} & J & n_2 & l_2 & j_2 \end{bmatrix}$$

$$= {}_{12}\langle (n_{cm} l_{cm}, \bar{\alpha}) J M \mid [(\tilde{a}\tilde{b}) J_{ab} T_{ab}, \tilde{c}] J M T M_T \rangle_n$$

$$= \mathscr{N}_n \langle (n_{cm} l_{cm}, \bar{\alpha}) J M \mid \mathscr{A}_{12} \mid [(\tilde{a}\tilde{b}) J_{ab} T_{ab}, \tilde{c}] J M T M_T \rangle_n$$

$$= \mathscr{N} T_n \begin{bmatrix} \tilde{a} & J_{ab} & n_{cm} & l_{cm} & S_{ab} \\ \tilde{b} & \mathscr{J} & n_1 & l_1 & j_1 \\ \tilde{c} & J & n_2 & l_2 & j_2 \end{bmatrix} \left(\Delta^{(abc)_\alpha}_{abc} - (-1)^{l_1+s_a+s_b-S_{ab}+t_a+t_b-T_{ab}} \Delta^{(bac)_\alpha}_{abc} \right), \tag{5.42}$$

with $\mathscr{N} = \left(2 + 2\delta^{s_a t_a \mathscr{S}_a}_{s_b t_b \mathscr{S}_b} \right)^{-1/2}$ and $(abc)_\alpha = \{ s_a(\alpha) t_a(\alpha) \mathscr{S}_a(\alpha), \ldots \}$ referring to the isospin quantum numbers from the α set.

5.5. Transformation to the m Scheme

The last step of the procedure is the transformation back to a Slater-determinant basis. We write

$$|abc\rangle = \sqrt{3!}\,\mathscr{A}\,|abc\rangle_n$$

$$= \sqrt{3!} \sum_{J_{ab}T_{ab}} \sum_{JT} \begin{pmatrix} j_a & j_b \\ m_a & m_b \end{pmatrix} \begin{matrix} J_{ab} \\ M_{ab} \end{matrix} \begin{pmatrix} J_{ab} & j_c \\ M_{ab} & m_c \end{pmatrix} \begin{matrix} J \\ M \end{matrix} \begin{pmatrix} t_a & t_b \\ \tau_a & \tau_b \end{pmatrix} \begin{matrix} T_{ab} \\ \tau_{ab} \end{matrix} \begin{pmatrix} T_{ab} & t_c \\ \tau_{ab} & \tau_c \end{pmatrix} \begin{matrix} T \\ M_T \end{matrix}$$

$$\times \mathscr{A}\,|[(\tilde{a}\tilde{b}) J_{ab} T_{ab}, \tilde{c}] J M T M_T \rangle_n \tag{5.43}$$

and insert a complete set of states $|(n_{cm} l_{cm}, \bar{\alpha}) J M\rangle_{12}$. The overlap between one of these states and the JT-coupled state is a T coefficient (5.42) derived in the previous section. We get

$$|abc\rangle = \sqrt{3!}\,\mathscr{A}\,|abc\rangle_n$$

$$= \sqrt{3!} \sum_{J_{ab}T_{ab}} \sum_{JT} \sum_{\bar{\alpha}} \sum_{n_{cm}l_{cm}} \begin{pmatrix} j_a & j_b \\ m_a & m_b \end{pmatrix} \begin{matrix} J_{ab} \\ M_{ab} \end{matrix} \begin{pmatrix} J_{ab} & j_c \\ M_{ab} & m_c \end{pmatrix} \begin{matrix} J \\ M \end{matrix} \begin{pmatrix} t_a & t_b \\ \tau_a & \tau_b \end{pmatrix} \begin{matrix} T_{ab} \\ \tau_{ab} \end{matrix} \begin{pmatrix} T_{ab} & t_c \\ \tau_{ab} & \tau_c \end{pmatrix} \begin{matrix} T \\ M_T \end{matrix}$$

$$\times T\begin{bmatrix} \tilde{a} & J_{ab} & n_{cm} & l_{cm} & S_{ab} & T_{ab} \\ \tilde{b} & \mathscr{J} & n_1 & l_1 & j_1 \\ \tilde{c} & J & n_2 & l_2 & j_2 \end{bmatrix} \mathscr{A}\,|(n_{cm} l_{cm}, \bar{\alpha}) J M \rangle_{12} \tag{5.44}$$

and after decoupling the center of mass we exploit the spectral decomposition (5.26) of $\mathscr{A}$ together with (5.38), yielding

$$
\begin{aligned}
= \sqrt{3!} & \sum_{J_{ab}T_{ab}} \sum_{JT} \sum_{\alpha} \sum_{n_{\rm cm}l_{\rm cm}} \sum_{m_{\rm cm}} \sum_{i} \\
& \times \begin{pmatrix} j_a & j_b & J_{ab} \\ m_a & m_b & M_{ab} \end{pmatrix} \begin{pmatrix} J_{ab} & j_c & J \\ M_{ab} & m_c & M \end{pmatrix} \begin{pmatrix} t_a & t_b & T_{ab} \\ \tau_a & \tau_b & \tau_{ab} \end{pmatrix} \begin{pmatrix} T_{ab} & t_c & T \\ \tau_{ab} & \tau_c & M_T \end{pmatrix} \begin{pmatrix} l_{\rm cm} & \mathscr{J} & J \\ m_{\rm cm} & \mathscr{M} & M \end{pmatrix} \\
& \times T \begin{bmatrix} \tilde{a} & J_{ab} & n_{\rm cm} & l_{\rm cm} & S_{ab} & T_{ab} \\ \tilde{b} & \mathscr{J} & n_1 & l_1 & j_1 \\ \tilde{c} & J & n_2 & l_2 & j_2 \end{bmatrix}_a \langle n_{\rm cm}l_{\rm cm}m_{\rm cm}, Ei\mathscr{J}\mathscr{M}\mathscr{X}TM_T|n_{\rm cm}l_{\rm cm}m_{\rm cm},\alpha\rangle_{12} \\
& \times |n_{\rm cm}l_{\rm cm}m_{\rm cm}, Ei\mathscr{J}\mathscr{M}\mathscr{X}TM_T\rangle \\
= \sqrt{3!} & \sum_{J_{ab}T_{ab}} \sum_{JT} \sum_{\alpha} \sum_{n_{\rm cm}l_{\rm cm}} \sum_{m_{\rm cm}} \sum_{i} \\
& \times \begin{pmatrix} j_a & j_b & J_{ab} \\ m_a & m_b & M_{ab} \end{pmatrix} \begin{pmatrix} J_{ab} & j_c & J \\ M_{ab} & m_c & M \end{pmatrix} \begin{pmatrix} t_a & t_b & T_{ab} \\ \tau_a & \tau_b & \tau_{ab} \end{pmatrix} \begin{pmatrix} T_{ab} & t_c & T \\ \tau_{ab} & \tau_c & M_T \end{pmatrix} \begin{pmatrix} l_{\rm cm} & \mathscr{J} & J \\ m_{\rm cm} & \mathscr{M} & M \end{pmatrix} \\
& \times T \begin{bmatrix} \tilde{a} & J_{ab} & n_{\rm cm} & l_{\rm cm} & S_{ab} & T_{ab} \\ \tilde{b} & \mathscr{J} & n_1 & l_1 & j_1 \\ \tilde{c} & J & n_2 & l_2 & j_2 \end{bmatrix} c_{i,\tilde{\alpha}}^{(E\mathscr{J}\mathscr{X}T)} |n_{\rm cm}l_{\rm cm}m_{\rm cm}, Ei\mathscr{J}\mathscr{M}\mathscr{X}TM_T\rangle . \quad (5.45)
\end{aligned}
$$

When considering matrix elements of an (induced) irreducible three-body interaction, we exploit translational and rotational invariance, i.e., its independence of the c.m. degrees of freedom and of the projection $\mathscr{M}$. That way, we can sum over the Clebsch-Gordan coefficients involving $l_{\rm cm}$ and $\mathscr{J}$ to get conservation of the total angular momentum J and its projection M. The final expression is

$$
\begin{aligned}
\langle abc & |V|a'b'c'\rangle \\
& = \sum_{J_{ab}J'_{ab}T_{ab}T'_{ab}} \sum_{JT} \sum \begin{pmatrix} j_a & j_b & J_{ab} \\ m_a & m_b & M_{ab} \end{pmatrix} \begin{pmatrix} J_{ab} & j_c & J \\ M_{ab} & m_c & M \end{pmatrix} \begin{pmatrix} t_a & t_b & T_{ab} \\ \tau_a & \tau_b & \tau_{ab} \end{pmatrix} \begin{pmatrix} T_{ab} & t_c & T \\ \tau_{ab} & \tau_c & M_T \end{pmatrix} \\
& \times \begin{pmatrix} j'_a & j'_b & J'_{ab} \\ m'_a & m'_b & M'_{ab} \end{pmatrix} \begin{pmatrix} J'_{ab} & j'_c & J \\ M'_{ab} & m'_c & M \end{pmatrix} \begin{pmatrix} t'_a & t'_b & T'_{ab} \\ \tau'_a & \tau'_b & \tau'_{ab} \end{pmatrix} \begin{pmatrix} T'_{ab} & t'_c & T' \\ \tau'_{ab} & \tau'_c & M'_T \end{pmatrix} \\
& \times \left(3! \sum_{\alpha\alpha'} \sum_{n_{\rm cm}l_{\rm cm}} \sum_{ii'} T \begin{bmatrix} \tilde{a} & J_{ab} & n_{\rm cm} & l_{\rm cm} & S_{ab} & T_{ab} \\ \tilde{b} & \mathscr{J} & n_1 & l_1 & j_1 \\ \tilde{c} & J & n_2 & l_2 & j_2 \end{bmatrix} T \begin{bmatrix} \tilde{a}' & J'_{ab} & n_{\rm cm} & l_{\rm cm} & S'_{ab} & T'_{ab} \\ \tilde{b}' & \mathscr{J} & n'_1 & l'_1 & j'_1 \\ \tilde{c}' & J & n'_2 & l'_2 & j'_2 \end{bmatrix} \times \right. \\
& \left. \times c_{i,\tilde{\alpha}}^{(E\mathscr{J}\mathscr{X}T)} c_{i',\tilde{\alpha}'}^{(E'\mathscr{J}\mathscr{X}'T')} \langle Ei\mathscr{J}\mathscr{X}TM_T|V|E'i'\mathscr{J}\mathscr{X}'T'M'_T\rangle \right) . \quad (5.46)
\end{aligned}
$$

As a tradeoff between computational and storage efficiency, we precompute the part in parentheses, and perform the decoupling to the *m*-scheme on the fly during the many-body calculation. We achieve a further reduction of the number of matrix elements to store by assuming isospin symmetry. This is an approximation in case the two-body interaction contains charge-symmetry-breaking terms, e.g., a Coulomb interaction.

5.6. SRG Evolution in Three-Body Space

We carry out the SRG evolution in the antisymmetric Jacobi HO basis truncated to a maximum total energy $E \leq E_{3\max}^{(\text{SRG})}$. The symmetries of the Hamiltonian allow for evolving each $T\mathcal{J}P$ block separately, which makes the evolution numerically feasible for large model spaces. For that, we need to first compute a matrix representation of the initial Hamiltonian. After the evolution the matrix elements of the Hamiltonian contain a mixture of two- and three-body terms. Since these terms scale differently in a many-body calculation they need to be separated.

5.6.1. Initial Matrix Elements

As a starting point of the evolution as well as for the subsequent subtraction procedure we need matrix elements of two-body operators (the kinetic energy and two-body interactions) in the antisymmetrized three-body Jacobi HO basis. A straight-forward way of calculating these would be a transformation to the m scheme, where Slater rules can be used for the evaluation,[4] followed by a transformation back to the antisymmetric Jacobi HO basis. There is, however, a much more direct way that we take in the following.

Consider a two-body operator $\boldsymbol{v}$ embedded into an $A > 2$ many-body Hilbert space. The embedding

$$V = \sum_{i<j}^{A} \boldsymbol{v}_{ij}, \tag{5.47}$$

where the subscripts denote the particles the operator acts on, can be rewritten using transposition operators such that $\boldsymbol{v}$ always acts on the first two particles:

$$V = \sum_{i<j}^{A} \boldsymbol{P}_{i1}\boldsymbol{P}_{j2}\boldsymbol{v}_{12}\boldsymbol{P}_{j2}\boldsymbol{P}_{i1}. \tag{5.48}$$

Evaluated in an antisymmetric basis $|\phi_i\rangle_a$ we can use the invariance (up to a phase factor) of the basis states under particle transposition and get

$$\langle\phi_k|\boldsymbol{V}|\phi_l\rangle = \sum_{i<j}^{A}(-1)^4\langle\phi_k|\boldsymbol{v}_{12}|\phi_l\rangle = \frac{A(A-1)}{2}\langle\phi_k|\boldsymbol{v}_{12}|\phi_l\rangle. \tag{5.49}$$

To apply this to the three-body Jacobi HO basis, we need to evaluate the matrix element on the right-hand side with states $|Ei\mathcal{J}\mathcal{X}TM_T\rangle$. These are only known in terms of the $|\alpha\rangle_{12}$, so we insert identity operators to the left and right of the operator $\boldsymbol{v}_{12}$. The overlaps $\langle Ei\mathcal{J}\mathcal{X}TM_T|\alpha\rangle_{12}$ are CFPs and we get

$$\langle Ei\mathcal{J}\mathcal{X}TM_T|\boldsymbol{V}|E'i'\mathcal{J}\mathcal{X}'TM_T\rangle = \frac{A(A-1)}{2}\sum_{\alpha,\alpha'}c_{i,\tilde{\alpha}}^{(E\mathcal{J}\mathcal{X}T)}c_{i',\tilde{\alpha}'}^{(E'\mathcal{J}\mathcal{X}'T')}{}_{12}\langle\alpha|\boldsymbol{v}_{12}|\alpha'\rangle_{12}. \tag{5.50}$$

---

[4]see [Bin10] for an elegant derivation of these rules for arbitrary operator particle rank.

The first two particles of the state $|\alpha\rangle_{12}$ are properly antisymmetrized and the coupling scheme is the same as for the two-body interaction in two-body space. Thus, the matrix element

$$
\begin{aligned}
{}_{12}\langle\alpha|\boldsymbol{v}_{12}|\alpha'\rangle_{12} &= {}_{12}\langle\{[n_1 l_1,(s_a s_b)S_{ab}]j_1,(n_2 l_2,s_c)j_2\}\mathcal{J}\mathcal{M},[(\mathcal{S}_a t_a \mathcal{S}_b t_b)T_{ab},\mathcal{S}_c t_c]TM_T| \\
&\quad \times \boldsymbol{v}_{12}\,|\{[n_1' l_1',(s_a' s_b')S_{ab}']j_1',(n_2' l_2',s_c')j_2'\}\mathcal{J}\mathcal{M},[(\mathcal{S}_a' t_a'\mathcal{S}_b' t_b')T_{ab}',\mathcal{S}_c' t_c']TM_T\rangle_{12} \\
&= {}_{12}\langle[n_1 l_1,(s_a s_b)S_{ab}]j_1,(\mathcal{S}_a t_a\mathcal{S}_b t_b)T_{ab}|\boldsymbol{v}_{12}|[n_1' l_1',(s_a' s_b')S_{ab}']j_1',(\mathcal{S}_a' t_a'\mathcal{S}_b' t_b')T_{ab}'\rangle_{12} \\
&\quad \times \delta_{n_2 l_2 s_c j_2 \mathcal{S}_c t_c}^{n_2' l_2' s_c' j_2' \mathcal{S}_c' t_c'}
\end{aligned}
\tag{5.51}
$$

resolves to a two-body matrix element and constraints on the second Jacobi coordinate. Note that this expression is valid only for a scalar-isoscalar operator. For nonscalar operators it is necessary to decouple the second coordinate completely.

5.6.2. Model Space and Frequency Conversion

For practical calculations the model space is always truncated to some $E \leq E_{3\max}^{(\text{SRG})}$. This truncation induces an ultraviolet scale that has to be large enough to capture all relevant parts of the interaction and failure to do so leads to artifacts in the many-body calculation [RCL$^+$14]. The scale can be increased by enlarging the HO energy truncation $E_{3\max}^{(\text{SRG})}$. However, due to the steep increase of basis dimensions with this parameter the maximum value that can be handled computationally is quite limited (see section 5.7). The other parameter that influences the ultraviolet scale is the basis frequency Ω, which can be changed without affecting the computational demands of the SRG evolution but has a strong influence on the convergence of observables with respect to the size of the many-body basis. The optimal basis parameters often differ significantly between observables, especially between those that are sensitive to the long-range behavior of the wavefunction, like radii or electromagnetic transitions, and energies, which are more sensitive to the short-range behavior.

The solution to this is a decoupling of the basis parameters used for the SRG evolution and the many-body calculation [Cal14]. We effect this by converting the basis frequency after the subtraction step described in section 5.6.3. Let Ω and ω denote the frequencies for the SRG evolution and many-body calculation, respectively. Then, for a matrix element with basis frequency ω we have

$$
\begin{aligned}
{}^{\omega}\langle &Ei\mathcal{J}\mathcal{X}TM_T|V|E'i'\mathcal{J}\mathcal{X}'TM_T\rangle^{\omega} \\
&= \sum_{\substack{\tilde{E}\tilde{\imath} \\ \tilde{E}'\tilde{\imath}'}} {}^{\omega}\langle Ei\mathcal{J}\mathcal{X}TM_T|\tilde{E}\tilde{\imath}\mathcal{J}\mathcal{X}TM_T\rangle^{\Omega}\,{}^{\Omega}\langle\tilde{E}\tilde{\imath}\mathcal{J}\mathcal{X}TM_T|V|\tilde{E}'\tilde{\imath}'\mathcal{J}\mathcal{X}'TM_T\rangle^{\Omega} \\
&\quad \times {}^{\Omega}\langle\tilde{E}'\tilde{\imath}'\mathcal{J}\mathcal{X}'TM_T|E'i'\mathcal{J}\mathcal{X}'TM_T\rangle^{\omega},
\end{aligned}
\tag{5.52}
$$

where the superscripts denote the oscillator frequencies of the basis states. The overlaps can be evaluated in the 12-antisymmetric Jacobi HO basis (the CFPs do not depend on the basis frequency):

$$
{}^{\Omega}\langle Ei\mathcal{J}\mathcal{X}TM_T|E'i'\mathcal{J}'\mathcal{X}'T'M_T'\rangle^{\omega} = \sum_{\alpha\alpha'} c_{i,\tilde{\alpha}}^{(E\mathcal{J}\mathcal{X}T)} c_{i',\tilde{\alpha}'}^{(E'\mathcal{J}'\mathcal{X}'T')}\,{}^{\Omega}_{12}\langle\alpha|\alpha'\rangle_{12}^{\omega}
\tag{5.53}
$$

with

$$
{}^{\Omega}_{12}\langle\alpha|\alpha'\rangle^{\omega}_{12} =
$$

$$
\delta^{\mathscr{J}\mathscr{M}S_{ab}T_{ab}TM_T}_{\mathscr{J}'\mathscr{M}'S'_{ab}T'_{ab}T'M'_T}\delta^{l_1 j_1 l_2 j_2}_{l'_1 j'_1 l'_2 j'_2}\left(1 + \delta^{s_a t_a \mathscr{S}_a}_{s_b t_b \mathscr{S}_b}\right)^{-1/2}\left(1 + \delta^{s'_a t'_a \mathscr{S}'_a}_{s'_b t'_b \mathscr{S}'_b}\right)^{-1/2}\left(\Delta^{a'b'c'}_{abc} + (-1)^{l_1 + S_{ab} + t_a + t_b - T_{ab}}\Delta^{b'a'c'}_{abc}\right)
$$

$$
\times \int \mathrm{d}r_1\, r_1^2\, R_{n_1 l_1}(r_1, b(\mu_1, \Omega))\, R_{n'_1 l_1}(r_1, b(\mu_1, \omega))
$$

$$
\times \int \mathrm{d}r_2\, r_2^2\, R_{n_2 l_2}(r_2, b(\mu_2, \Omega))\, R_{n'_2 l_2}(r_2, b(\mu_2, \omega)). \tag{5.54}
$$

Since the radial HO wavefunction

$$
R_{nl}(r, b) = \sqrt{\frac{2n!}{\Gamma(n + l + 3/2)b^3}}\, e^{-\frac{1}{2}\left(\frac{r}{b}\right)^2}\left(\frac{r}{b}\right)^l L_n^{(l+1/2)}\left(\frac{r^2}{b^2}\right) \equiv \frac{1}{b^{3/2}}\tilde{R}_{nl}\left(\frac{r}{b}\right), \tag{5.55}
$$

with the associated Laguerre polynomial $L_n^{(\alpha)}(x)$, depends on b in a simple manner we can perform a variable transformation $\rho = r/b$, introducing $b = b(\mu, \Omega)$ and $b' = b(\mu, \omega)$, so that

$$
\int \mathrm{d}r\, r^2 R_{nl}(r, b) R_{n'l}(r, b') = b^3 \int \mathrm{d}\rho\, \rho^2 R_{nl}(b\rho, b) R_{n'l}(b\rho, b')
$$

$$
= \left(\frac{b}{b'}\right)^{3/2} \int \mathrm{d}\rho\, \rho^2 \tilde{R}_{nl}(\rho) \tilde{R}_{n'l}(\rho b/b')
$$

$$
= \beta^{3/2} \int \mathrm{d}\rho\, \rho^2 \tilde{R}_{nl}(\rho) \tilde{R}_{n'l}(\rho\beta), \tag{5.56}
$$

where $\beta \equiv b/b' = \sqrt{\omega/\Omega}$ is the square root of the ratio of both frequencies. The overlap thus only depends on this ratio. Analytic expressions are given in appendix D.

5.6.3. Subtraction

The irreducible three-body part of the evolved Hamiltonian has to be separated from those parts that can be represented by a two-body operator embedded into three-body space in order to be usable in a many-body calculation. We achieve this by forming the matrix representation of a Hamiltonian containing the two-body interaction evolved in *two-body* space and subtracting it from the Hamiltonian evolved in three-body space. The difference is the irreducible three-body part that is transformed to the *JT*-coupled scheme described in section 5.5.

Choosing the truncation $E^{(\mathrm{SRG})}_{2\mathrm{max}}$ of the model space for the two-body evolution of the matrix elements to be subtracted is a subtle problem. The effective model-space truncation of two particles interacting in three-body space depends on the state of the spectator particle.

Consider the subspace of $|\alpha\rangle_{12}$ states with energy $e_2 = 2n_2 + l_2$ for the second Jacobi coordinate in an $E^{(\mathrm{SRG})}_{3\mathrm{max}}$-truncated space. Due to the truncation, the energy available for the first coordinate is $e_1 \leq E^{(\mathrm{SRG})}_{3\mathrm{max}} - e_2$, and the evolution of the reducible two-body interaction effectively happens in a space with $E^{(\mathrm{SRG})}_{2\mathrm{max}} = E^{(\mathrm{SRG})}_{3\mathrm{max}} - e_2$. To exactly subtract this reducible part, we need to evolve the interaction in two-body space with the same truncation.
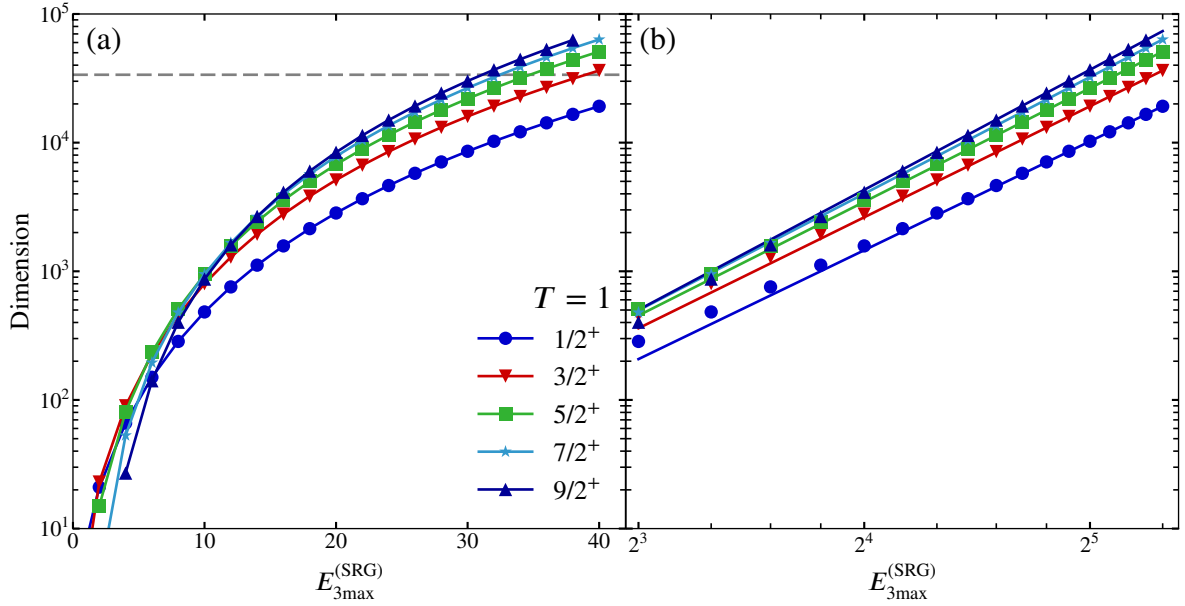
Figure 5.2.: (a) Dimension of the antisymmetric basis for different channels. The dashed line marks the maximum dimension that our code can evolve on a single compute node with 128 GiB of RAM. (b) A subset of the same data in a doubly-logarithmic plot. The lines are power laws fitted to the four rightmost points.

Hence, we would have to perform two-body evolutions for all $E_{2\text{max}}^{(\text{SRG})} \leq E_{3\text{max}}^{(\text{SRG})}$, but, in the end, we only keep the low-energy part ($E \leq E_{3\text{max}}$) of the interaction for the many-body calculation. The high-energy part, along with any errors introduced there during the subtraction, is discarded. For low-energy matrix elements the effective model-space truncation for the two-body evolution is at least $E_{3\text{max}}^{(\text{SRG})} - E_{3\text{max}}$. If this truncation is large enough to converge the two-body evolution, subtracting an interaction evolved with a larger truncation is still accurate. For this reason we subtract a two-body interaction evolved in a space with $E_{2\text{max}}^{(\text{SRG})} = E_{3\text{max}}^{(\text{SRG})}$.

5.7. Computational Considerations

The three-body evolution is a challenging computational task requiring large amounts of storage and computing time. Due to Λ-Σ conversion the dimensions of the $T\mathcal{J}P$ blocks are larger than in nucleonic calculations, especially in $T = 1$ channels where the particle isospins can be coupled in different ways.

Figure 5.2 shows the dimension of the antisymmetric Jacobi basis as a function of the energy truncation $E_{3\text{max}}^{(\text{SRG})}$. The channels shown are the low-$\mathcal{J}$ channels of largest dimension. The model-space dimensions exhibit approximate power-law scaling with exponents that increase with total angular momentum.

The maximum total angular momentum that needs to be computed depends on the energy truncation used in the many-body calculation: since each additional quantum of orbital angular momentum increases the HO energy, a Jacobi-basis state with angular momenta l_1, l_2 has total
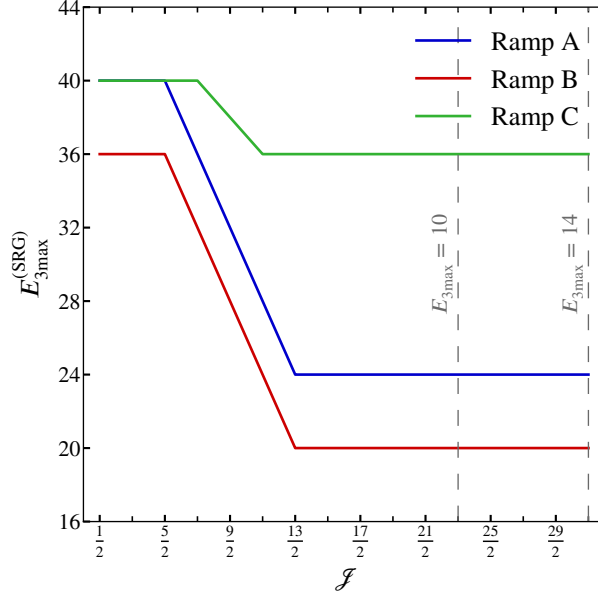
Figure 5.3.: Comparison of SRG truncation ramps. Ramp A is used throughout this work, we use ramp B to check convergence of the SRG evolution; ramp C, commonly employed for heavier nuclei, is shown for comparison. See text for the definition of the ramps.

energy $E \geq l_1 + l_2$. Simultaneously, we can couple three spin-1/2 fermions to a total angular momentum $\mathcal{J} \leq l_1 + l_2 + 3/2 \leq E + 3/2$, so the total angular momenta appearing in a truncated model space are limited by $\mathcal{J} \leq J_{\max} = E_{3\max} + 3/2$.

Due to the scaling of the model-space dimension with $\mathcal{J}$ the maximum feasible energy truncation in the large-$\mathcal{J}$ channels is relatively low in the YNN sector. In contrast, we need to perform the SRG evolution in a model space that is as large as possible in order to minimize artifacts. To balance this against the model-space size, we use a truncation scheme with a $\mathcal{J}$-dependent energy truncation $E_{3\max}^{(\text{SRG})}(\mathcal{J})$.

Fortunately, observables of light nuclei depend only weakly on the three-body channels with higher angular momenta. Assuming that this observation also holds for hypernuclei, we adopt the approach of Roth et al. [RCL$^+$14] and successively lower the truncation for high-angular-momentum channels down to a reasonable minimum. The truncation of the SRG model spaces is thus defined by a ramp function

$$E_{\text{Ramp}}(\mathcal{J}; E_l, \mathcal{J}_l, E_h, m) = \begin{cases} E_l & : \mathcal{J} \leq \mathcal{J}_l \\ E_l - m(\mathcal{J} - \mathcal{J}_l) & : \mathcal{J}_l < \mathcal{J} \leq \mathcal{J}_l + \frac{E_l - E_h}{m} \\ E_h & : \text{else,} \end{cases} \quad (5.57)$$

parametrized by the low-$\mathcal{J}$ energy E_l, the ramp start $\mathcal{J}_l$ and slope m, and the high-$\mathcal{J}$ energy E_h.

In the following, we will perform computations with ramp A defined by

$$E_A(\mathcal{J}) = E_{\text{Ramp}}(\mathcal{J}; E_l = 40, \mathcal{J}_l = 5/2, E_h = 24, m = 4). \quad (5.58)$$
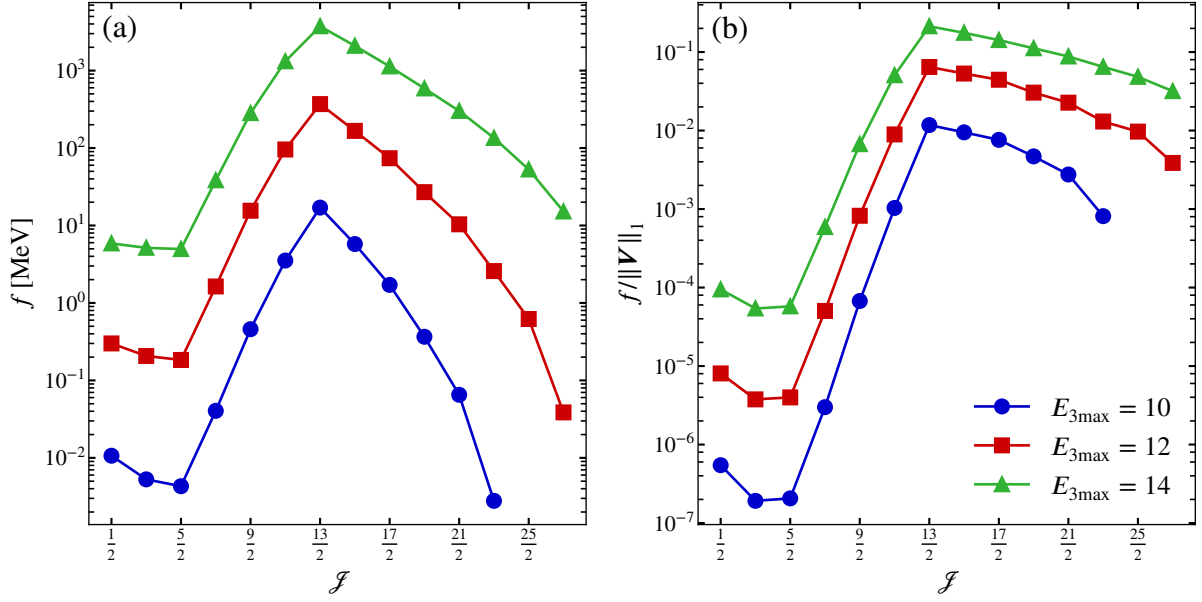
Figure 5.4.: Error introduced by the frequency conversion for ramp A, converting the induced YNN terms at $\alpha = 0.08\,\mathrm{fm}^4$ from $\Omega = 36\,\mathrm{MeV}$ to $\omega = 20\,\mathrm{MeV}$. Shown in the left panel is the figure of merit $f_{T\mathcal{J}P}(E_{3\mathrm{max}})$ from (5.59) on a logarithmic scale over $\mathcal{J}$ for the positive-parity $T = 0$ blocks and three values of $E_{3\mathrm{max}}$. The right panel contains the same data divided by the 1-norm of the matrix.

Convergence of the SRG model space can be checked by using a lower truncation ramp B with $E_B(\mathcal{J}) = E_{\mathrm{Ramp}}(\mathcal{J}; E_l = 36, \mathcal{J}_l = 5/2, E_h = 20, m = 4)$. The ramps are shown in fig. 5.3, along with ramp C, $E_C(\mathcal{J}) = E_{\mathrm{Ramp}}(\mathcal{J}; E_l = 40, \mathcal{J}_l = 7/2, E_h = 36, m = 2)$, used commonly in calculations for heavier nuclei.

The frequency-conversion step also requires large model spaces, depending on the difference in oscillator lengths. We numerically check the error introduced due to the finite model space by converting the SRG-evolved matrix elements to the lower frequency and back, and comparing the resulting low-energy matrix elements to those before the conversion. We define the figure of merit to be

$$f_{T\mathcal{J}P}(E_{3\mathrm{max}}) =$$
$$\sum_{\substack{EE' \\ ii' \\ \mathcal{X}\mathcal{X}'}}^{E_{3\mathrm{max}}} \left| \langle Ei\mathcal{J}\mathcal{X}TM_T | V | E'i'\mathcal{J}\mathcal{X}'TM_T \rangle - \langle Ei\mathcal{J}\mathcal{X}TM_T | \tilde{V} | E'i'\mathcal{J}\mathcal{X}'TM_T \rangle \right|, \quad (5.59)$$

where $\tilde{V}$ is the frequency-converted interaction. The results are shown in fig. 5.4 for ramp A, converting the induced YNN terms at $\alpha = 0.08\,\mathrm{fm}^4$ from $\Omega = 36\,\mathrm{MeV}$ to $\omega = 20\,\mathrm{MeV}$. Since the comparison uses two conversions, which lose information, and the transformation matrix is very symmetric, the deviation of the potential at $\omega = 20\,\mathrm{MeV}$ after a single conversion is about half of the shown value.

For the low-$\mathcal{J}$ blocks, the conversion is very precise both in absolute and relative terms. The model-space size ramps down beyond $\mathcal{J} = 5/2$, leading to a steep rise of the absolute and

relative error. Since the induced YNN interaction is much weaker in the higher-$\mathcal{J}$ blocks, the absolute error drops, giving the figure-of-merit plot an almost triangular shape. The relative error, however, shows much less variation. Comparing the different curves, we notice that each step in $E_{3\text{max}}$ incurs an order-of-magnitude increase in relative error. For the small angular momenta the error is still negligible at $E_{3\text{max}} = 14$, but rises to almost 20 % for higher ones. For heavier systems, which are sensitive to these high-angular-momentum blocks, the main source of uncertainty is the SRG model space itself and increasing it will simultaneously lower the conversion error.

The SRG flow equation is solved numerically via a standard explicit Runge-Kutta-Fehlberg solver using a fifth-order rule embedded in a fourth-order rule that is used to estimate the solution error and adjust the step size. The solver itself requires six matrices of workspace to store intermediate evaluations of the right-hand side of the flow equation, four additional matrices are required for step-size control, and three matrices are needed to store the matrix representation of the kinetic-energy operator, the SRG generator and the resulting Hamiltonian.

In total, we need 13 matrices, which, for the largest blocks, is more than a single compute node can currently handle. Memory requirements can be reduced by lowering the order of the integrator or using a fixed step size. These measures, however, massively increase the computational demands because smaller steps are needed to achieve the same accuracy and the step size is not increased dynamically.

Hence, we parallelize the solution of the flow equation to multiple compute nodes where each node holds only a slice of each of the matrices. Only the evaluation of the right-hand side then requires exchanging matrix slices between nodes, the rest of the evolution is computed node-locally. Two additional matrices are required for communication,[5] so the total amount of memory required is 15 matrices.

5.8. Results

With the induced YNN terms included, we first need to confirm that the conclusions from chapter 4 were not skewed by a lack of convergence, and validate our calculation by comparing absolute and hyperon separation energies for the $A = 4$ system to results obtained in other approaches. Then, we study the structure of light neutron-rich hypernuclei and try to answer the question whether the hypernuclear neutron drip line changes due to the attraction provided by the hyperon, compared to the nucleonic one. Finally, we consider a doubly-strange system, $^{6}_{\Lambda\Lambda}\text{He}$, exploring the possibility of targeting these systems, and disentangling contributions to the hyperon separation energy due to the YY interaction and due to polarization of the nucleonic core. All investigations employ a $E_{3\text{max}} = 10$ truncation for the induced YNN terms, which is at the limit of what we can conveniently handle in a calculation. The other parameters are unchanged compared to those used in section 4.6. Some of these results are published in [WR16; WR18].

---

[5]Communication and computation are overlapped so that the total time taken is determined by the speed of the matrix multiplication, provided that the slices are large enough.
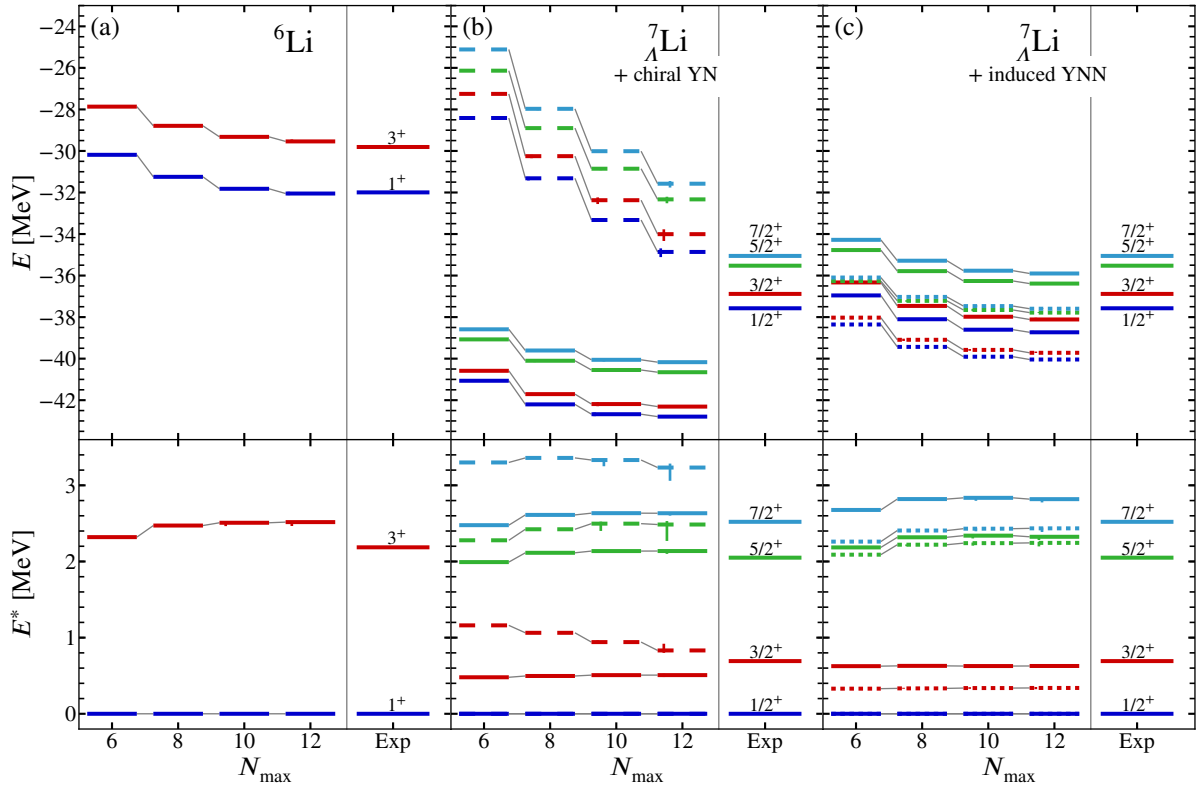
Figure 5.5.: Absolute and excitation energies of (a) ^{6}Li and (b) its daughter hypernucleus $^7_\Lambda$Li using a bare (dashed lines) or SRG-evolved (solid lines) YN interaction with cutoff $\Lambda_Y = 700\,\mathrm{MeV/c}$. Panel (c) shows the calculation including induced YNN terms, for YN interaction cutoffs $\Lambda_Y = 700\,\mathrm{MeV/c}$ (solid lines) and $\Lambda_Y = 600\,\mathrm{MeV/c}$ (dotted lines). The basis frequency is $\Omega = 20\,\mathrm{MeV}$ and the SRG flow parameter is $\alpha = 0.08\,\mathrm{fm}^4$. Vertical bars denote threshold-extrapolation uncertainties. Experimental values taken from [Dav05; HT06; WAW$^+$12; TCG$^+$02].

	$\langle T_{\mathrm{int}} \rangle$	$\langle V_{\mathrm{NN}} \rangle$	$\langle V_{\mathrm{3N}} \rangle$	$\langle V_{\mathrm{YN}} \rangle$	$\langle V_{\mathrm{YNN}} \rangle$	$\langle H \rangle$
evolved YN	108.71	−123.34	0.24	−28.83	0	−43.22
+ induced YNN	101.49	−119.55	−0.12	−24.47	2.95	−39.69
Difference	−7.22	3.79	−0.36	4.37	2.95	3.52

Table 5.1.: Expectation values in MeV of terms of the Hamiltonian in the ground state of $^7_\Lambda$Li at $N_{\mathrm{max}} = 12$. The values are not extrapolated to vanishing importance threshold, but taken at $\kappa_{\mathrm{min}} = 10^{-5}$.

5.8.1. Hypernuclei from the p Shell

We again consider the three symmetric hypernuclei from section 4.6: $^7_\Lambda$Li, $^9_\Lambda$Be, and $^{13}_\Lambda$C. Figure 5.5 shows the absolute and excitation energies of the nucleonic parent ^{6}Li in panel (a), which is identical to panel (a) from fig. 4.3. In panel (b), we show the results for $^7_\Lambda$Li without induced YNN terms, for the bare YN interaction and the YN interaction evolved to a flow parameter of $\alpha_Y = 0.08\,\mathrm{fm}^4$. Evolving the interaction causes the absolute energies to drop. Simultaneously, convergence is greatly improved, but the calculation overbinds the hypernucleus by more than 5 MeV. The spectra are also affected: The doublet states follow the convergence pattern of the respective state in the parent. The centroid of the $5/2^+$, $7/2^+$ doublet shifts down, and the splittings among both doublets are reduced.

With the inclusion of the induced YNN terms, a large part of the overbinding is removed while the improved convergence is preserved. The induced YNN terms increase the doublet splittings, bringing the excitation energy of the $3/2^+$ into very good agreement with the experimental value. The upper doublet is shifted upwards so both states are approximately 300 keV too high, but this discrepancy is carried over from the nucleonic parent. The conclusions regarding the cutoff dependence do not change: the 600 MeV/c cutoff provides approximately 3 MeV more binding, and the doublet splittings are halved compared to the 700 MeV/c cutoff.

We can further analyze the effect of the induced YNN terms by studying their effect on the expectation values of parts of the Hamiltonian presented in table 5.1. Adding the YNN terms changes the wavefunction itself, not only the energy. The contributions of the intrinsic kinetic energy and the three-nucleon interaction (which has only a small expectation value here) are lowered, which is compensated by an increase in the expectation values of the two-nucleon and YN interactions. The induced YNN terms contribute 3 MeV of the resulting energy difference of 3.5 MeV; the remainder comes from the other terms. This shows that the induced YNN terms really change the structure of the eigenstate and do not merely change the energy.

In $^9_\Lambda$Be (cf. fig. 5.6), the conclusions are similar to $^7_\Lambda$Li. The evolved interaction without YNN terms increases the splitting of the excited-state doublet. The induced YNN terms counteract this and gives excitation energies very similar to the bare ones. This is remarkable because the absolute energies are much further from convergence for the bare than for the evolved interaction, and, from the $^7_\Lambda$Li results, we expect some variation between the bare and induced-YNN results. The near-degeneracy of the doublet is stable with respect to cutoff variations, and the $3/2^+$ state is predicted to be the lower state, so the interchange of the doublet states does not seem to be an artifact of the incomplete convergence of the bare calculation.

The absolute energies for $^{13}_\Lambda$C, shown in fig. 5.7, are converged to a similar degree as those for $^9_\Lambda$Be. We also see the same pattern with the splitting in the excited-state doublet being a cancellation of the evolved YN and induced YNN terms. The cutoff dependence of the excitation energies is relatively weak, but they show an upward trend with little sign of convergence.

The improved convergence allows for a reliable extrapolation of absolute energies. We are also able to calculate hyperon separation energies with high precision, which we can compare to results from other methods and to experimental data. For the extrapolation, we fit three-parameter exponentials and a four-parameter extension with an additional N_{max}^2 term,

$$E(N_{\mathrm{max}}) = E_\infty + a \exp(-b N_{\mathrm{max}} - c N_{\mathrm{max}}^2), \tag{5.60}$$
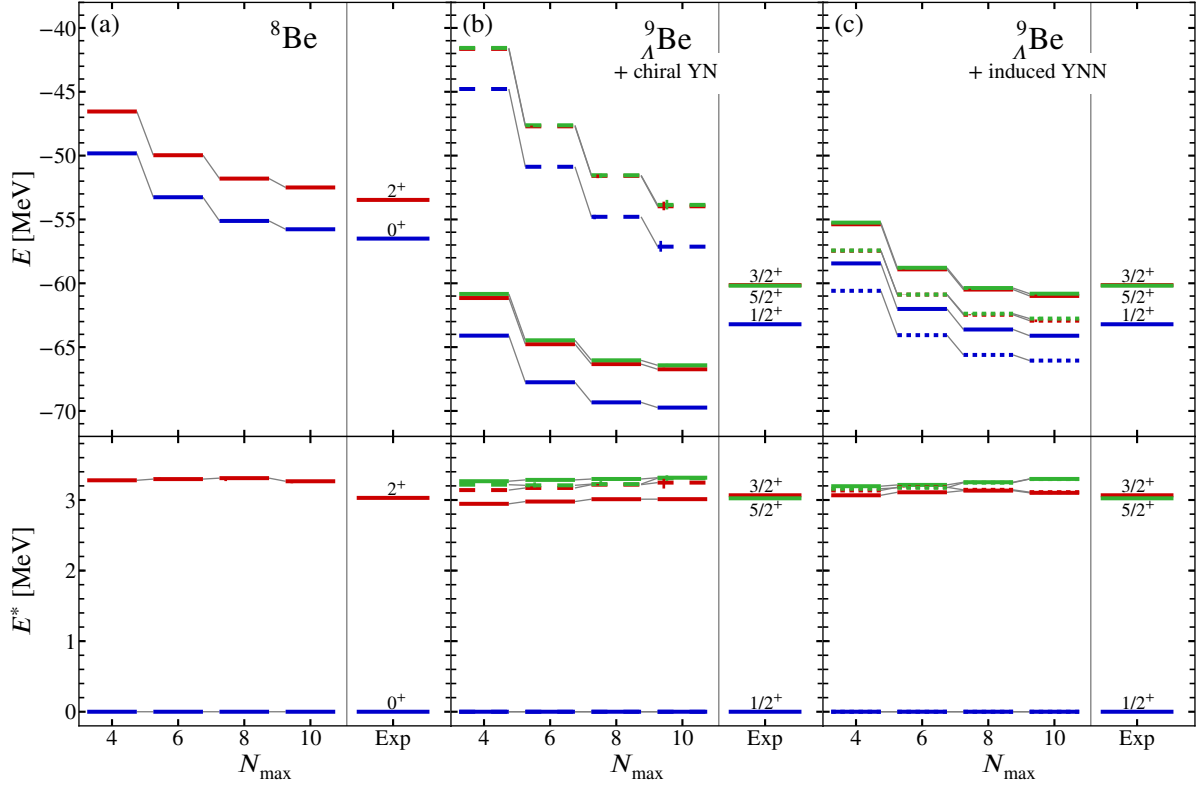
Figure 5.6.: Absolute and excitation energies of (a) ^{8}Be and (b) its daughter hypernucleus $^9_\Lambda$Be using a bare (dashed lines) or SRG-evolved (solid lines) YN interaction with cutoff $\Lambda_Y = 700\,\text{MeV/c}$ without and (c) with induced YNN terms, for cutoffs $\Lambda_Y = 700\,\text{MeV/c}$ (solid lines) and $\Lambda_Y = 600\,\text{MeV/c}$ (dotted lines). Notations and parameters like in fig. 5.5. Experimental values taken from [Dav05; HT06; WAW$^+$12; TKG$^+$04].

		YN	YN + ind. YNN		
	Parent E_0	700	600	700	Expt.
$^4_\Lambda$He	-7.72	$-11.80(3)$	$-10.23(6)$	$-10.15(6)$	$-10.11(3)$
$^7_\Lambda$He	$-29.09(9)$	$-39.32(5)$	$-36.76(5)$	$-35.33(6)$	$-34.95(25)$
$^7_\Lambda$Li	$-32.36(4)$	$-42.94(8)$	$-40.20(7)$	$-39.25(4)$	$-37.57(3)$
$^9_\Lambda$Be	$-56.24(29)$	$-70.3(4)$	$-66.6(4)$	$-64.7(4)$	$-63.21(4)$
$^{13}_\Lambda$C	$-98.7(8)$	$-123.7(8)$	$-116.2(7)$	$-113.1(8)$	$-103.85(12)$

Table 5.2.: Extrapolated absolute ground-state energies of selected hypernuclei and their parent nuclei. The uncertainties shown for the calculations are N_{max}-extrapolation uncertainties. All values in MeV. Experimental data taken from [WAW$^+$12; NMO$^+$13; Dav05].
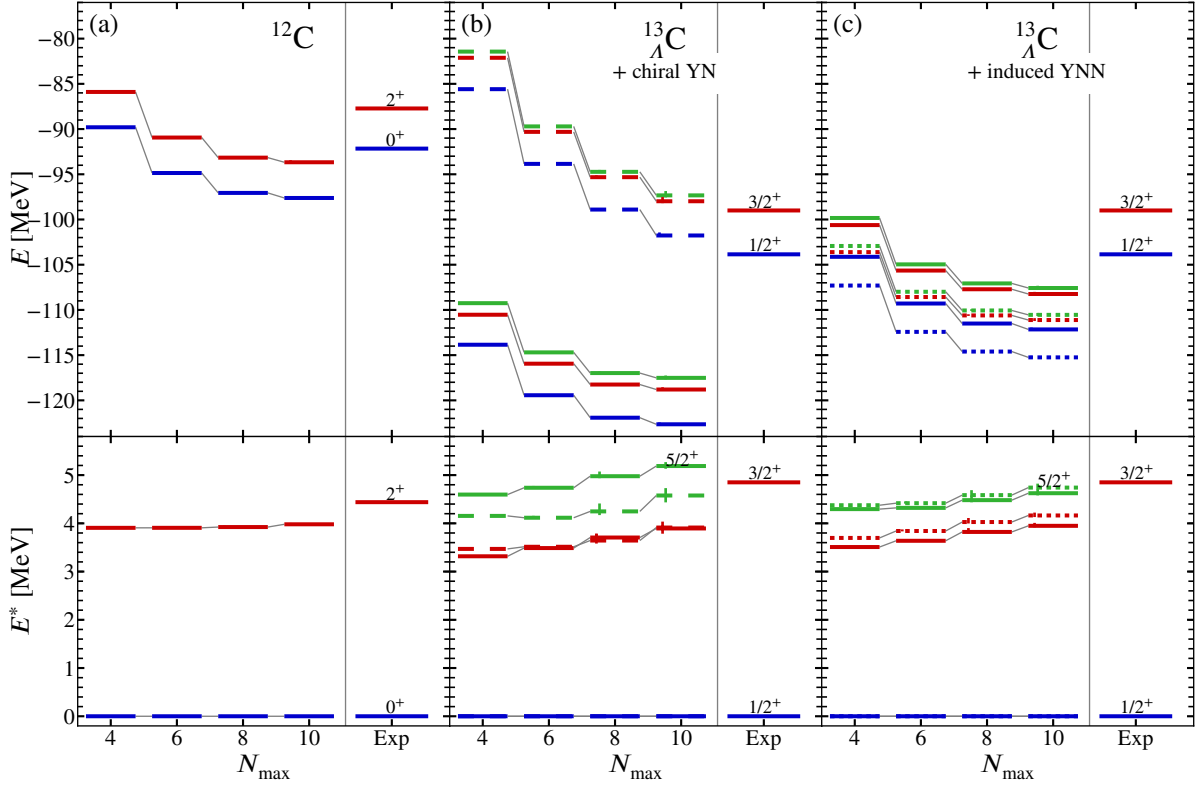
Figure 5.7.: Absolute and excitation energies of (a) ^{12}C and (b) its daughter hypernucleus $^{13}_{\Lambda}$C using a bare (dashed lines) or SRG-evolved (solid lines) YN interaction with cutoff $\Lambda_Y = 700\,\text{MeV/c}$ without and (c) with induced YNN terms, for cutoffs $\Lambda_Y = 700\,\text{MeV/c}$ (solid lines) and $\Lambda_Y = 600\,\text{MeV/c}$ (dotted lines). Notations and parameters like in fig. 5.5. Experimental values taken from [Dav05; HT06; WAW$^+$12; Ajz90].

| | YN | YN + ind. YNN | | | |
	700	600	700	AFDMC	Expt.
$^4_{\Lambda}$He	4.08(3)	2.51(6)	2.43(6)	1.22(9)	2.39(3)
$^7_{\Lambda}$He	10.23(11)	7.67(11)	6.24(11)	5.95(25)	5.68(25)
$^7_{\Lambda}$Li	10.58(9)	7.84(8)	6.89(6)		5.58(3)
$^9_{\Lambda}$Be	14.1(5)	10.4(5)	8.5(5)		6.71(4)
$^{13}_{\Lambda}$C	25.0(11)	17.5(11)	14.5(11)	11.20(40)	11.69(12)

Table 5.3.: Extrapolated hyperon separation energies B_{Λ} of selected hypernuclei, compared to Auxiliary-Field Diffusion Monte Carlo (AFDMC) results from [LPG14] and experimental data from [NMO$^+$13; Dav05]. The uncertainties shown for the NCSM calculations are N_{max}-extrapolation uncertainties.
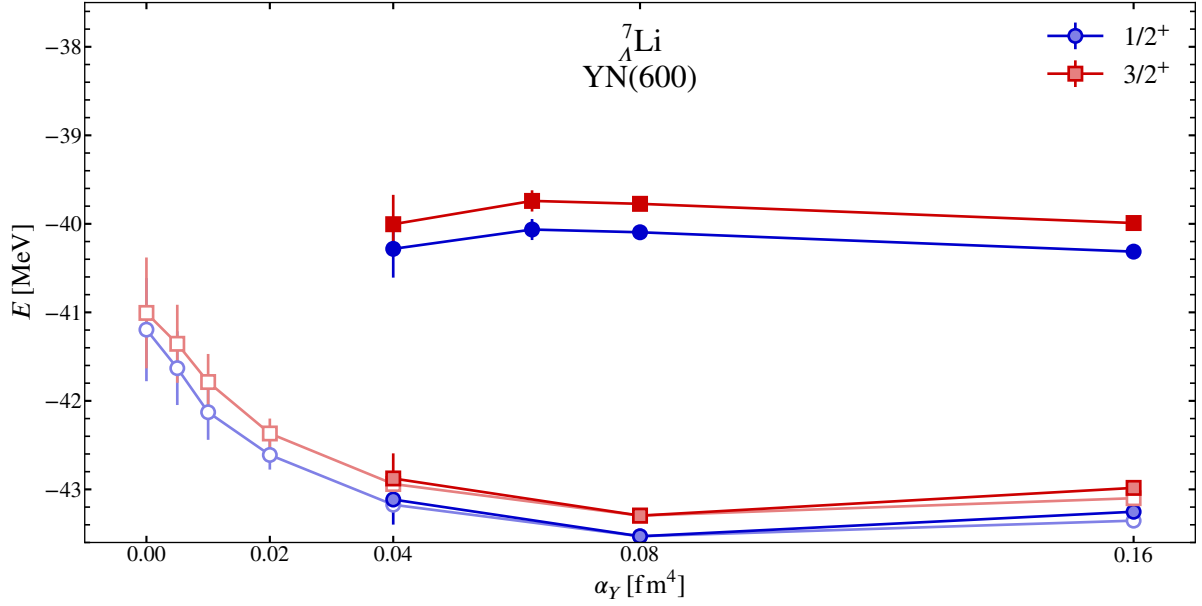
Figure 5.8.: Flow-parameter variation for $^7_\Lambda$Li including induced YNN terms. Empty symbols are extrapolated absolute energies of the ground-state doublet without induced YNN terms for a nucleonic flow parameter of $\alpha_N = 0.08\,\mathrm{fm}^4$ (same as in fig. 4.10). The (half-) filled symbols are results computed with (without) induced YNN terms for $\alpha_N = \alpha_Y$.

to five different subsets of the N_{max} sequence consisting of four to six points. The mean and standard deviation of these ten fit results comprise the extrapolated value and its uncertainty.

The absolute energies of the hypernuclei considered before are tabulated together with those for $^4_\Lambda$He and $^7_\Lambda$He in table 5.2. For the lightest hypernucleus considered, $^4_\Lambda$He, we get very good agreement with experimental data if we include the induced YNN terms. Already for this light system, the calculation without these terms overbinds by 1.7 MeV. The calculations for both interaction cutoffs also agree within extrapolation uncertainties with the Jacobi NCSM calculations presented in [WGN+18] that were performed using a bare Hamiltonian. This shows that there are no induced YNNN terms at this level. The other hypernuclei are more and more overbound with increasing A. We also note that the $\Lambda_Y = 600\,\mathrm{MeV/c}$ interaction gives consistently lower ground-state energies, and that the YNN terms shift the energy closer to the experimental value in all cases.

Some of the overbinding stems from the nucleonic Hamiltonian. The experimental ground-state energy of ^{12}C, for example, is $-92.16\,\mathrm{MeV}$ [WAW+12], which is 6.5(8) MeV above the result of our calculation. To account for that, we consider the hyperon separation energies B_Λ, tabulated in table 5.3. The separation energy in $^{13}_\Lambda$C is only 4(1) MeV too high for the $\Lambda_Y = 700\,\mathrm{MeV/c}$ interaction, compared to the 10 MeV difference in the absolute energies. For $^4_\Lambda$He, we get 2.43(6) MeV and 2.51(6) MeV separation energy for the $\Lambda_Y = 700\,\mathrm{MeV/c}$ and $\Lambda_Y = 600\,\mathrm{MeV/c}$ cutoff, respectively. This hypernucleus was targeted in a Faddeev-Yakubovsky calculation with the same interaction [HMN+07], yielding 2.41 MeV and 2.48 MeV for these
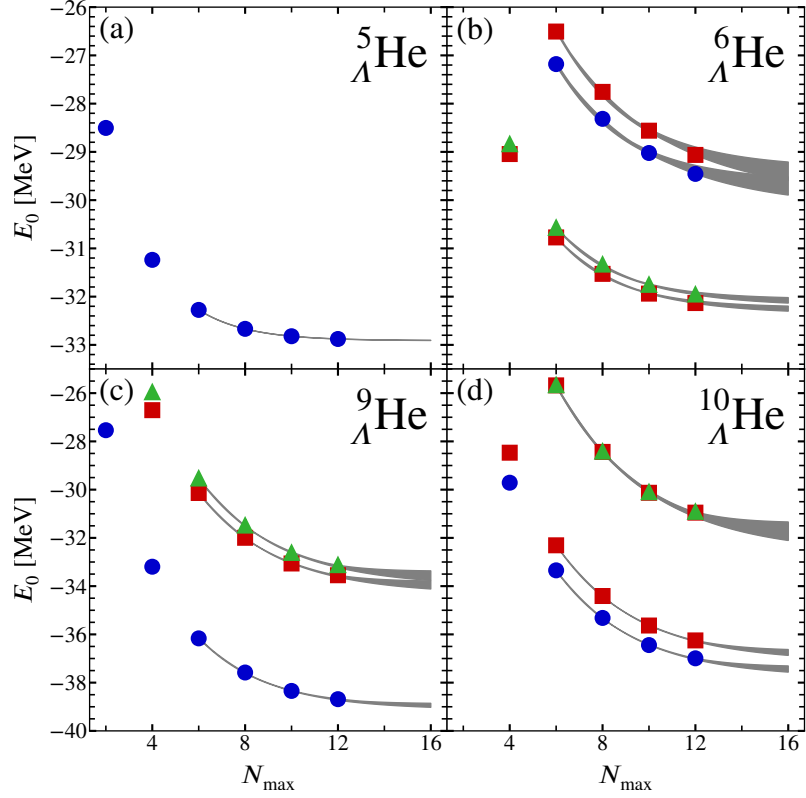
Figure 5.9.: Absolute energies of the low-lying spectrum of four helium hypernuclei for the YN interaction with $\Lambda_Y = 700$ MeV/c cutoff. The colors denote angular momenta: blue for $J = 0$ (1/2), red for $J = 1$ (3/2), green for $J = 2$ (5/2) for even (odd) systems. The gray bands mark the envelope of the fit functions used to extrapolate the energies to infinite model-space size. Note that the hypernuclei shown in (a) and (c) are particle stable while those in (b) and (d) are not, according to the calculation.

cutoff values,[6] which is in excellent agreement with our results.

We also compare the separation energies to those calculated in an Auxiliary-Field Diffusion Monte Carlo (AFDMC) approach [LPG14]. The AFDMC calculation works in a scheme with only Λ hyperons and uses a phenomenological ΛNN interaction fitted to reproduce the experimental hyperon separation energies of $^5_\Lambda$He and $^{17}_\Lambda$O. Consequently, the separation energies for $^7_\Lambda$He and $^{13}_\Lambda$C in this approach are very close to the experimental values. However, our results for these hypernuclei are remarkably close given that the LO interaction is only fitted to $A \leq 3$ data.

In order to confirm the flow-parameter independence of the absolute energies, we perform a flow-parameter variation like we have done in section 4.7, this time including the induced YNN terms. The results are given in fig. 5.8. The faded empty symbols show the previous calculations without induced terms that were already shown in fig. 4.10. Since we need to have

---

[6]The labeling of Table 5 in [HMN$^+$07] is erroneous: the first two result columns correspond to cutoffs 550 and 600. The values for $^4_\Lambda$He have been obtained by adding the CSB-0$^+$ value to the $^4_\Lambda$H separation energy.
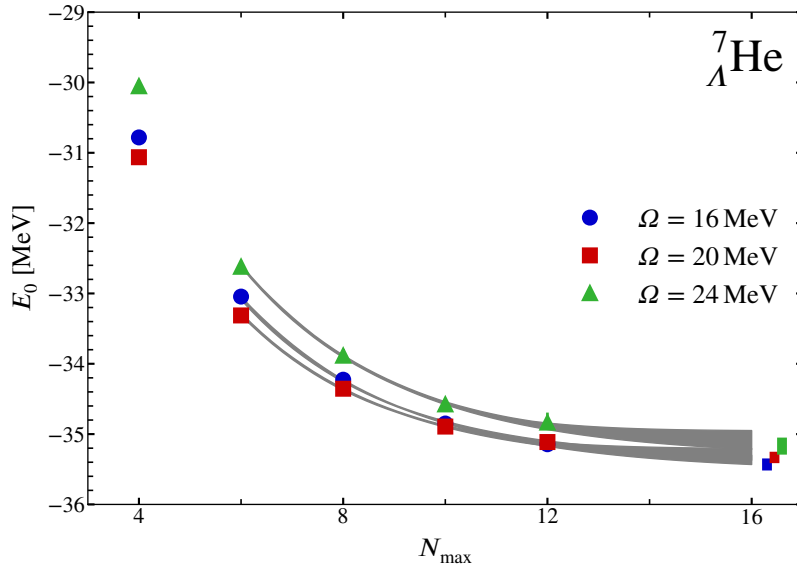
Figure 5.10.: Ground-state energy of $^{7}_{\Lambda}$He as a function of N_{max} and Ω for the YN interaction with $\Lambda_Y = 700\,\text{MeV/c}$ cutoff. The gray bands mark the envelope of the fit functions used to extrapolate the energies to infinite model-space size. The colored boxes denote the uncertainty band of the extrapolated energy for each basis frequency.

the same flow parameter in the nucleonic and the hyperonic sector when performing the SRG evolution in three-body space, we perform a flow-parameter variation over a smaller range with $\alpha_Y = \alpha_N$, which is shown with half-filled symbols. The change of the nucleonic flow parameter has only a small effect on the energy.

Including the induced YNN terms shifts the energies upward and removes the flow-parameter dependence, indicating that we have indeed captured the bulk of the induced many-body contributions. The extrapolations seem to be slightly underbound compared to the point at $\alpha_Y = 0\,\text{fm}^4$, but, for this point, the extrapolation distance is very large, which makes the extrapolation unreliable. Also, we expect a small effect from induced YNN terms due to the evolution in the nucleonic sector, which amount to 0.3 MeV in $^{4}_{\Lambda}$He [WGN$^+$18].

In conclusion, we have established that including the induced YNN terms reduces overbinding in the hypernuclei considered, and brings the spectra in agreement with those calculated with the bare YN interaction. The improved convergence of the SRG-evolved Hamiltonian allows us to extrapolate the absolute energies and compute hyperon separation energies with better than 10 % precision. The flow-parameter variation confirms that energies are independent of the SRG flow parameter. The emergence of a strong repulsive three-body interaction with the flow points to a solution of the hyperon puzzle in neutron-star physics, which is discussed in chapter 7.

5.8.2. Light Neutron-Rich Hypernuclei

Having found good agreement with other calculations and experimental data, we are in a position to tackle other physics questions. Here, we study the helium and lithium hypernuclear chains

up to the netron drip line, and investigate whether the additional attraction due to the hyperon can shift the hypernuclear neutron drip line compared to the nucleonic one. This study is the subject of [WR18].

To address this question, we use the hypernuclear IT-NCSM and calculate the low-lying states of single-Λ hypernuclei throughout the helium and lithium isotopic chains. For all but the lightest isotopes considered, this is the first time these hypernuclei have been addressed in an *ab initio* framework with chiral interactions. We compute the four lowest states up to $N_{\mathrm{max}} = 12$ with a basis frequency of $\Omega = 20\,\mathrm{MeV}$, and we always show the low-lying states with natural parity, which, in all the cases considered, is the parity of the calculated ground state. Our calculations do not include continuum degrees of freedom, which are important for states close to or above a particle-emission threshold, and may lower the absolute energies of these states.

Figure 5.9 shows N_{max} sequences for a set of helium hypernuclei. The ground state of $^{5}_{\Lambda}\mathrm{He}$ (panel a) is practically converged at $N_{\mathrm{max}} = 12$. The heavier system $^{9}_{\Lambda}\mathrm{He}$ (panel c) converges more slowly so that we resort to extrapolation for the infinite-model-space result. We perform the extrapolation by fitting three-parameter exponentials and a four-parameter extension with an additional N_{max}^{2} term to five different subsets of the N_{max} sequence consisting of four to six points. The mean and standard deviation of these ten fit results comprise the extrapolated value and its uncertainty. The envelope of the extrapolation functions for the ground state shows only little spread and allows for a reliable extraction of the converged energy for $^{9}_{\Lambda}\mathrm{He}$. The excited states, as well as the ground states of $^{6}_{\Lambda}\mathrm{He}$ and $^{10}_{\Lambda}\mathrm{He}$, show a slower convergence. These states are particle unbound, which manifests itself in the different convergence behavior.

Using $^{7}_{\Lambda}\mathrm{He}$ as a representative hypernucleus, we also check the basis-frequency dependence of the ground-state energies, shown in fig. 5.10. The figure shows the N_{max} sequences for the ground-state energy for three different basis frequencies. We see that $\Omega = 20\,\mathrm{MeV}$, which we use in the following, is close to the variational minimum for all values of N_{max}. As model spaces grow larger, the calculation seems to slightly prefer smaller frequencies. Overall, the extrapolated ground-state energy is robust with respect to variations of the basis frequency.

The full set of N_{max} sequences for the low-lying natural-parity states of helium hypernuclei and their nucleonic parents is presented in fig. 5.11. In all cases, convergence is sufficient to allow for an extrapolation to the infinite model space. In fig. 5.12, we show the resulting extrapolated absolute energies. The nucleonic calculation slightly underbinds the helium isotopes beyond $^{4}\mathrm{He}$, but correctly reproduces the particle-instability of $^{5}\mathrm{He}$ and $^{7}\mathrm{He}$. Experimental data on hyperon separation energies is only available for the isotopes up to $^{7}_{\Lambda}\mathrm{He}$. The $700\,\mathrm{MeV}/c$ cutoff moderately overbinds $^{5}_{\Lambda}\mathrm{He}$; as mentioned before, this is a long-standing issue with YN interactions that reproduce the binding energies of the $A = 4$ system [GH95; GHM16]. The overbinding in $^{6}_{\Lambda}\mathrm{He}$ and $^{7}_{\Lambda}\mathrm{He}$ is only a few hundred keV, but this is in part due to the nucleonic calculation underbinding the helium isotopes. The YN interaction with $600\,\mathrm{MeV}/c$ cutoff overbinds all these isotopes by about $2\,\mathrm{MeV}$.

The nonstrange helium isotopes show a marked odd-even staggering that renders the odd isotopes unstable against neutron emission. The additional binding provided by the hyperon does not suffice to stabilize $^{6}_{\Lambda}\mathrm{He}$, which is again an artifact of the overbinding in $^{5}_{\Lambda}\mathrm{He}$. The ground-state doublet of $^{8}_{\Lambda}\mathrm{He}$ is predicted to be at the neutron-emission threshold within extrapolation uncertainties for the $700\,\mathrm{MeV}/c$ cutoff. The $600\,\mathrm{MeV}/c$ cutoff puts the ground state $0.26(6)\,\mathrm{MeV}$
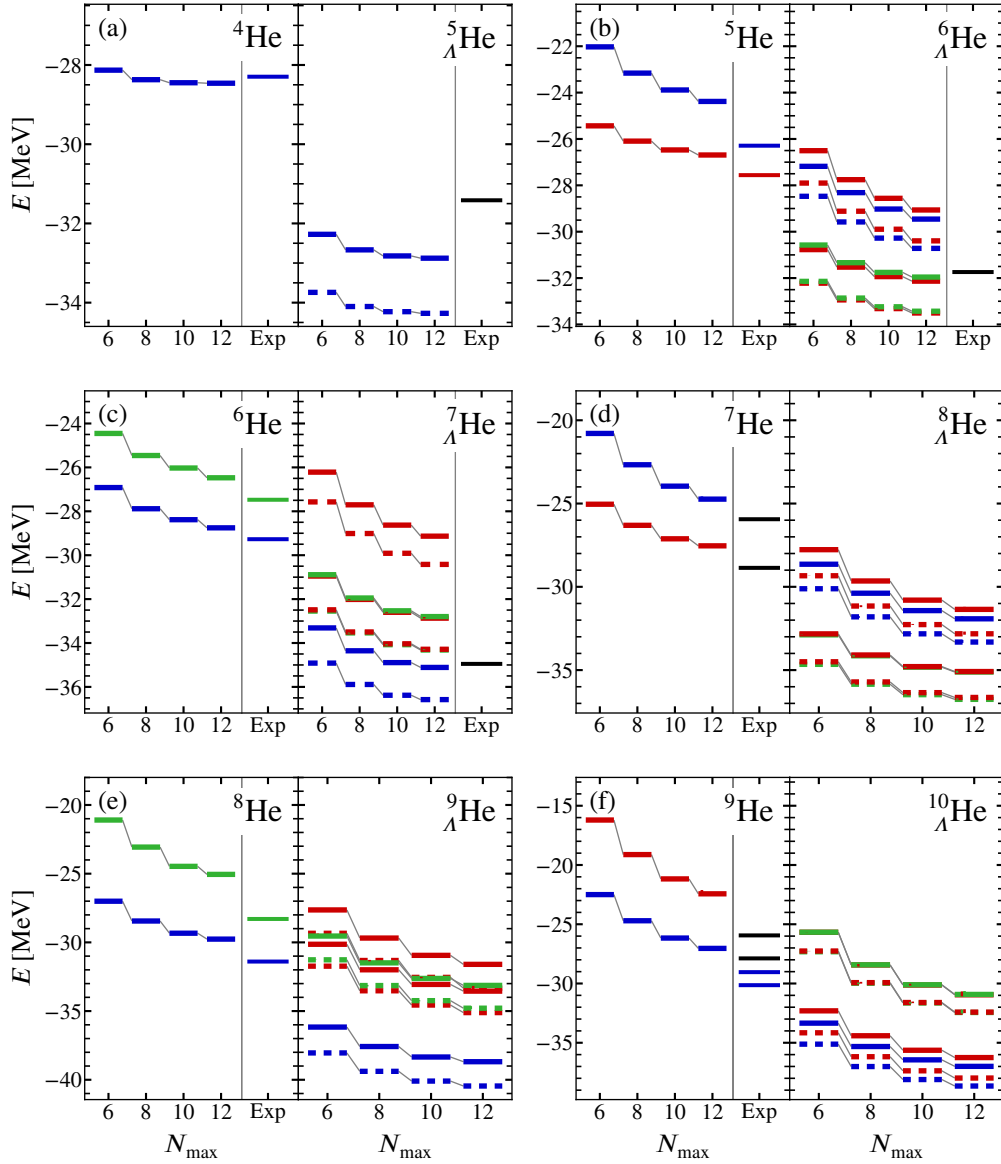
Figure 5.11.: Absolute energies of low-lying natural-parity states of helium hypernuclei as a function of N_{max}. Shown are the nucleonic parents and the single-Λ hypernuclei for two values of the YN interaction regulator $\Lambda_Y = 600\,\text{MeV/c}$ (dashed lines) and $\Lambda_Y = 700\,\text{MeV/c}$ (solid lines). Experimental values from [WAW+12; Dav05; HT06; TCG+02; TKG+04; NMO+13], vertical lines denote threshold-extrapolation uncertainties. The colors denote angular momenta: blue for $J = 0$ (1/2), red for $J = 1$ (3/2), green for $J = 2$ (5/2) and light blue for $J = 3$ (7/2) for even (odd) systems; black is used for unknown J.
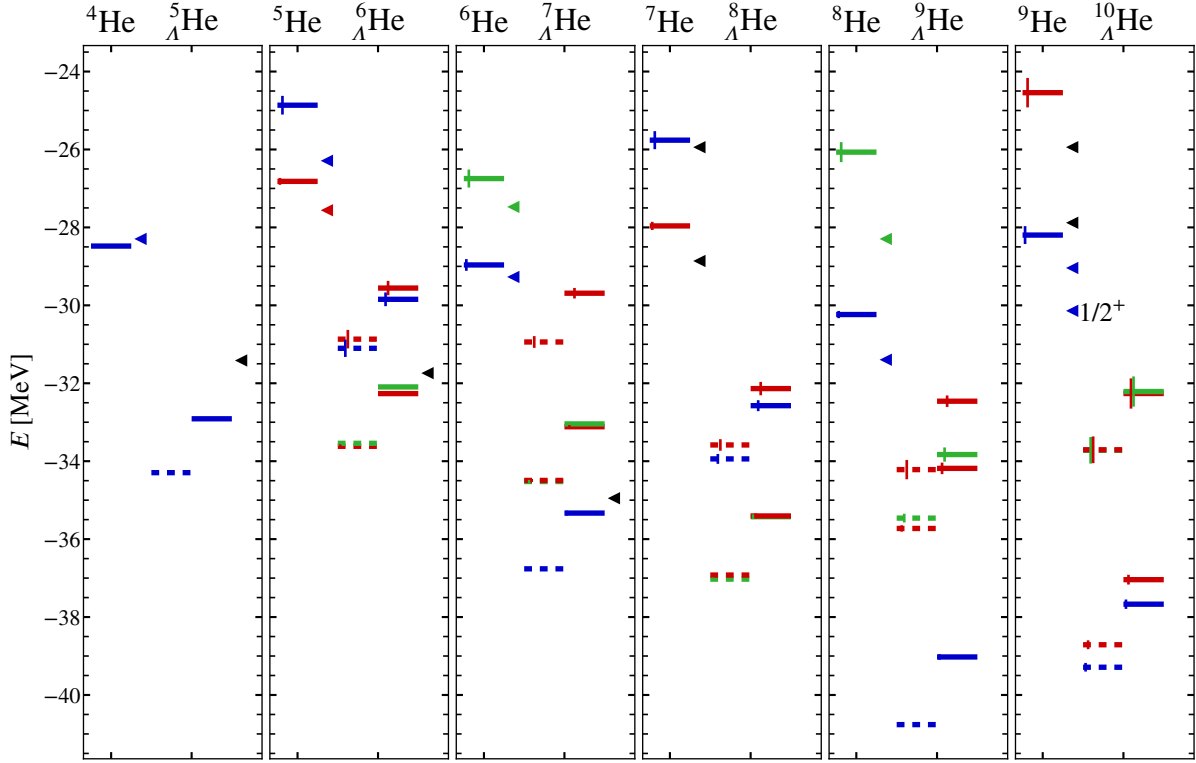
Figure 5.12.: Extrapolated energies of low-lying natural-parity states of helium hypernuclei. Notations as in fig. 5.11. Experimental values from [WAW$^+$12; Dav05; HT06; TCG$^+$02; TKG$^+$04; NMO$^+$13] are marked by triangles, vertical lines denote model-space extrapolation uncertainties.

below the $^7_\Lambda$He $+\,n$ threshold, stabilizing it.

The staggering is also reflected in the neutron separation energies shown in fig. 5.13. Our results agree with experiment at the level of a few hundred keV, only the separation energy in ^{5}He is too low because the $3/2^-$ resonance is predicted too high. Conversely, the separation energy in the daughter hypernucleus $^6_\Lambda$He is too low because the Hamiltonian overbinds $^5_\Lambda$He. Unlike the absolute ground-state energies, the neutron separation energies of the hypernuclei are remarkably robust against variation of the regulator cutoff of the YN interaction.

The separation energies of the hypernuclei follow the trend of their nucleonic parents with a shift, as expected by the 1 MeV-per-additional-nucleon increase of the hyperon separation energy. This behavior holds up to $^9_\Lambda$He, which has a neutron separation energy of approximately 3.6 MeV, compared to 2.3 MeV in ^{8}He. Surprisingly, the neutron separation energy of the next hypernucleus along the chain, $^{10}_\Lambda$He, is essentially the same as the experimental value for ^{9}He and well in the unbound region. At the $N = 8$ shell closure, $^{11}_\Lambda$He shows a similar behavior. The hyperon provides very little additional binding, if any, for these very neutron-rich systems and the neutron drip line is the same as for the nonstrange isotopes. From an mean-field perspective, this may be interpreted as the hyperon lowering the $\nu 0 p_{3/2}$ orbit by 1 MeV while leaving the energy of the $\nu 0 p_{1/2}$ unaffected.

The low-lying states of hypernuclei and their nucleonic parents along the lithium isotopic
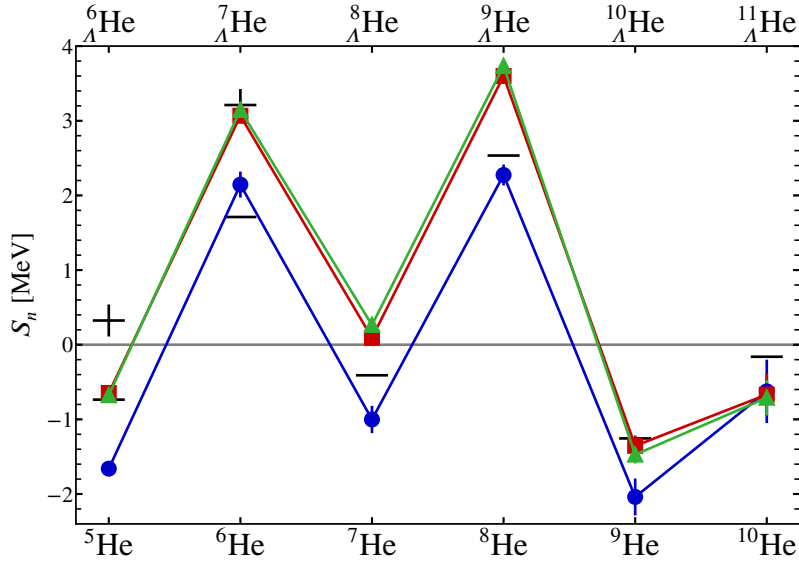
Figure 5.13.: Neutron separation energies of helium (hyper-)isotopes. Shown are the separation energies calculated for the nucleonic parents (blue circles) and for their daughter hypernuclei using the $\Lambda_Y = 700$ MeV/c (red squares) and $\Lambda_Y = 600$ MeV/c (green triangles) cutoffs. Experimental values are shown as black bars (crosses) for the (hyper-)nuclei. Vertical lines indicate extrapolation uncertainties.

chain are shown in fig. 5.14, the extrapolated energies are presented in fig. 5.15. Overall, the calculations for the nucleonic parents are well converged for the lighter isotopes, and we get agreement between the extrapolated and experimental binding energies to better than 1 MeV. The notable exception is ^{10}Li, where we fail to reproduce the parity inversion and the lowest negative-parity state is predicted at an excitation energy of 1.2(5) MeV. For the heaviest isotope considered, ^{11}Li, convergence is not complete at $N_{max} = 12$, and the ground state is slightly overbound. The excited state is probably a resonance, which converges slowly in the IT-NCSM and, therefore, has larger extrapolation uncertainties. Given the halo nature of systems like ^{9}Li and ^{11}Li, the level of agreement with experimental data is surprising.

The description of the hypernuclear states is similar in quality to the more symmetric hypernuclei that we considered previously [WR16]. The 700 MeV/c cutoff reproduces the spectrum of $^7_\Lambda$Li and the known ground-state energies with a systematic overbinding of 1 to 2 MeV. The 600 MeV/c cutoff overbinds more strongly by 2 to 3 MeV and produces smaller splittings among the hypernuclear doublet states.

The ground-state energies show a common trend with both cutoffs: the addition of a neutron to $^7_\Lambda$Li lowers the ground state by approximately 8 MeV with 7 MeV originating from the additional binding of the nucleonic core. The remainder stems from the increase of the Λ binding energy, which is in line with the commonly observed value of 1 MeV per additional nucleon [Dav05]. After the initial drop the ground-state energies continue to decrease more slowly with a slight odd-even staggering, following the trend of the nucleonic parents.

At $^{10}_\Lambda$Li, the energies start to saturate, indicating proximity to the neutron drip line. The core of $^{11}_\Lambda$Li, which is predicted to be particle unstable with respect to neutron emission, is stabilized

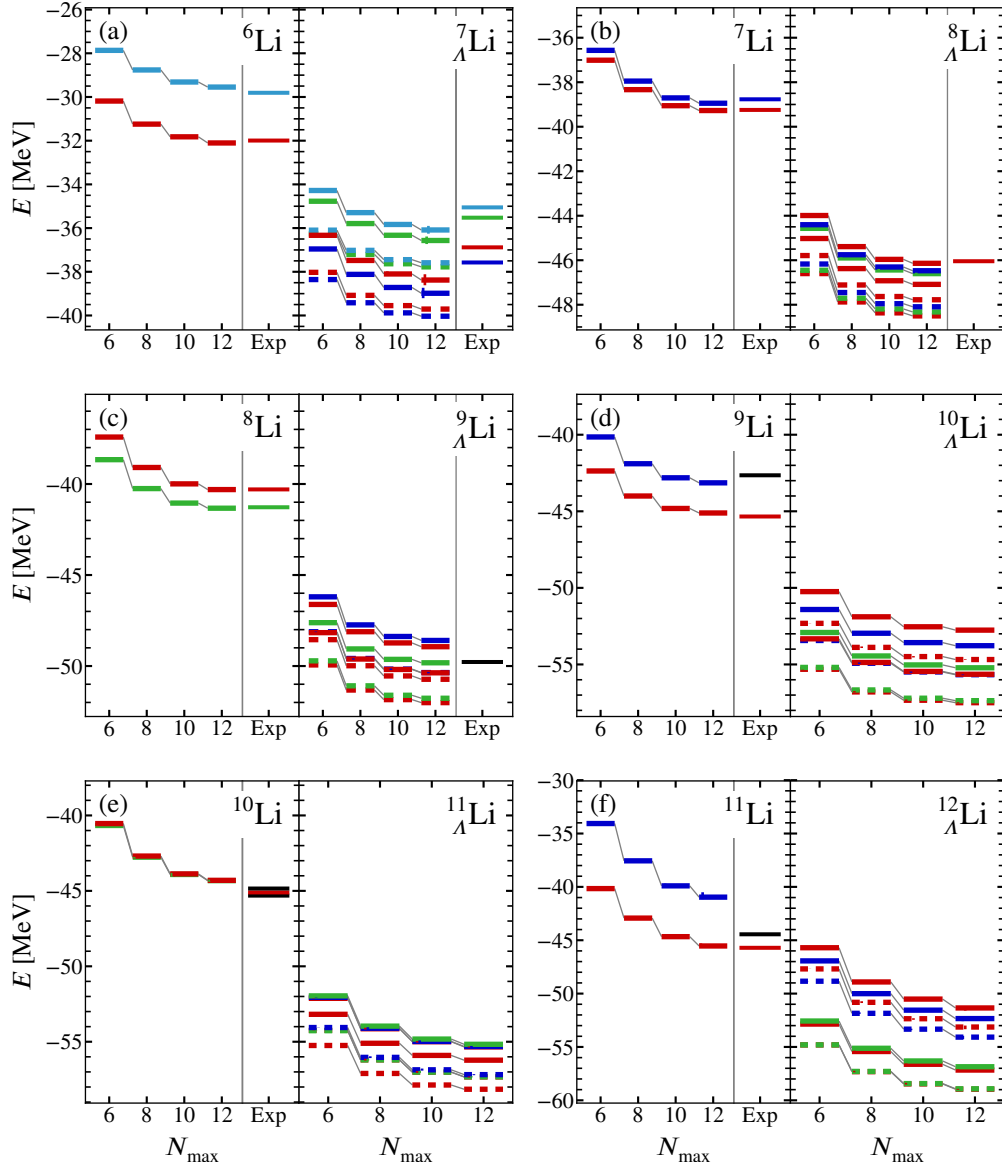Figure 5.14.: Like fig. 5.11, but for the lithium chain. Experimental values are taken from [WAW+12; Dav05; HT06; TCG+02; TKG+04; KKP+12].
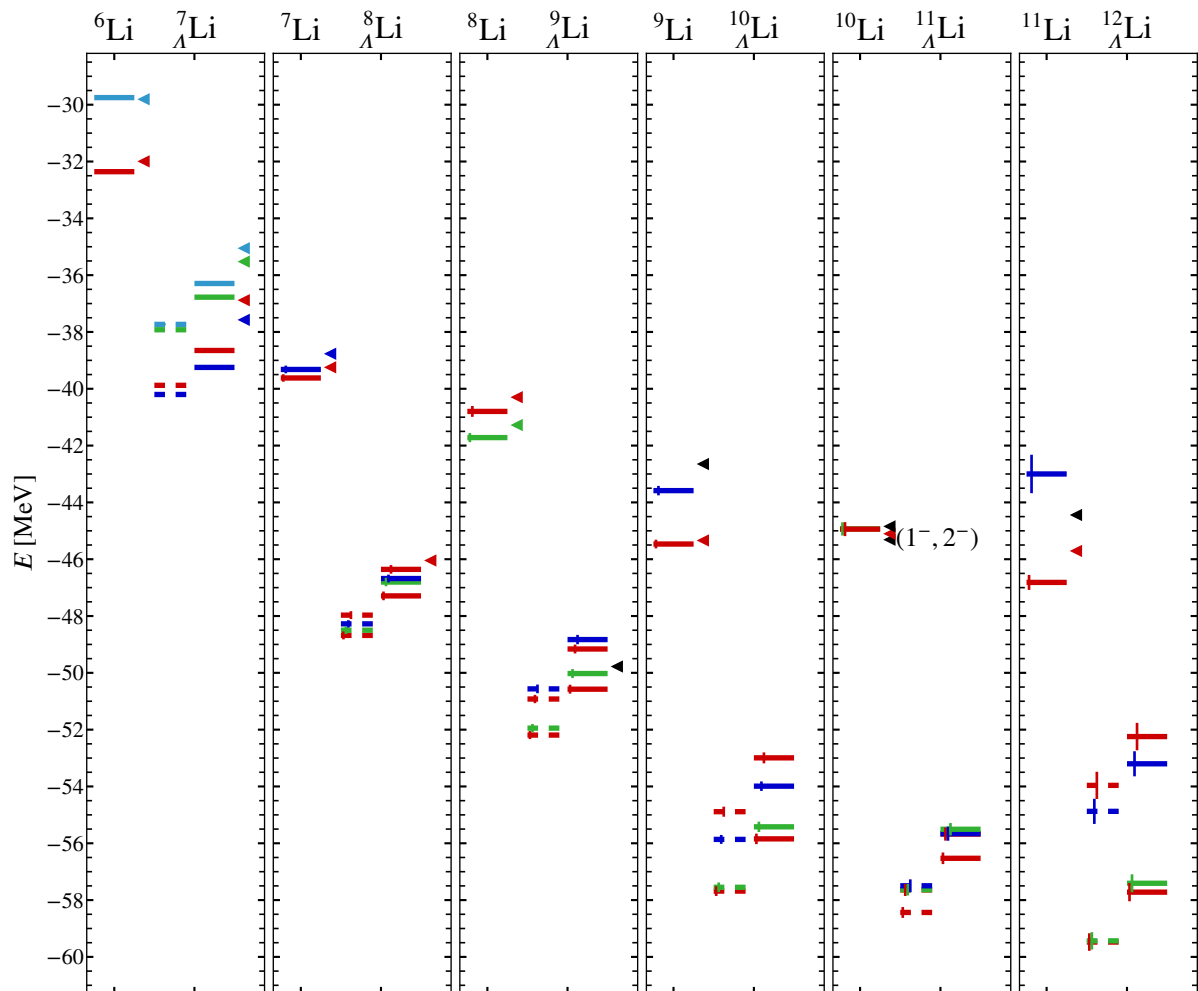
Figure 5.15.: Like fig. 5.12, but for the lithium chain. Experimental values are taken from [WAW⁺12; Dav05; HT06; TCG⁺02; TKG⁺04; KKP⁺12].
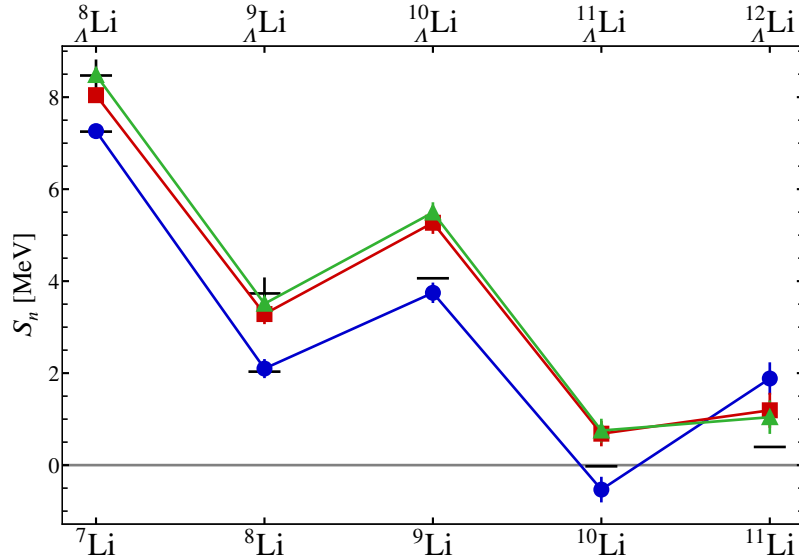
Figure 5.16.: Same as fig. 5.13, but for lithium (hyper-)isotopes.

by the presence of the hyperon (cf. fig. 5.16). Note that the doublets originating from the 1^+ ground state and the very low-lying 2^+ excitation in ^{10}Li completely overlap, forming an isolated $3/2^+$ ground state and a nearly-degenerate triplet very close to the $^{10}_{\Lambda}$Li + n threshold.

The nucleon separation energies, shown in fig. 5.16, are less sensitive to the YN cutoff than the absolute binding energies. The nucleonic Hamiltonian reproduces the experimental values to a few hundred keV, except for ^{11}Li, for which the separation energy is 1.5(4) MeV too high. As for the helium chain, the neutron separation energies of the hypernuclei are shifted to higher values compared to their nucleonic parents. The YN interaction with 600 MeV/c cutoff reproduces the experimentally known neutron separation energies of $^{8}_{\Lambda}$Li and $^{9}_{\Lambda}$Li almost within extrapolation uncertainties. The larger cutoff provides systematically smaller separation energies.

While the ground-state doublet of $^{12}_{\Lambda}$Li is particle stable, the behavior of the neutron separation energies is different from the lighter isotopes: the nucleonic core has a neutron separation energy of 1.9(4) MeV, but the additional hyperon lowers this value to 1.2(4) MeV (1.0(4) MeV) for the 700 MeV/c (600 MeV/c) cutoff. The experimental value for the ^{11}Li neutron separation energy is only 0.40 MeV and the calculation overestimates this value because the nucleonic Hamiltonian overbinds the ^{11}Li ground state. Thus, when using a Hamiltonian that correctly reproduces the ^{11}Li ground state, the neutron separation energy of $^{12}_{\Lambda}$Li will be lower and very close to the $^{11}_{\Lambda}$Li + n threshold. The lack of additional binding due to the hyperon indicates that no neutrons beyond the $N = 8$ shell closure will be bound. The hypernuclear drip line is thus not different from the nucleonic one.

To summarize, our calculations for the ground and first-excited states of the nucleonic parents show good agreement with experimental data, except for ^{8}He and ^{11}Li, which show larger discrepancies, as well as ^{9}He and ^{10}Li, where the calculation fails to reproduce the parity inversion of the ground state. Some of these deficiencies can be attributed to missing continuum degrees of freedom from the calculation [BNQ13; LNQ$^+$15; CNR$^+$16].
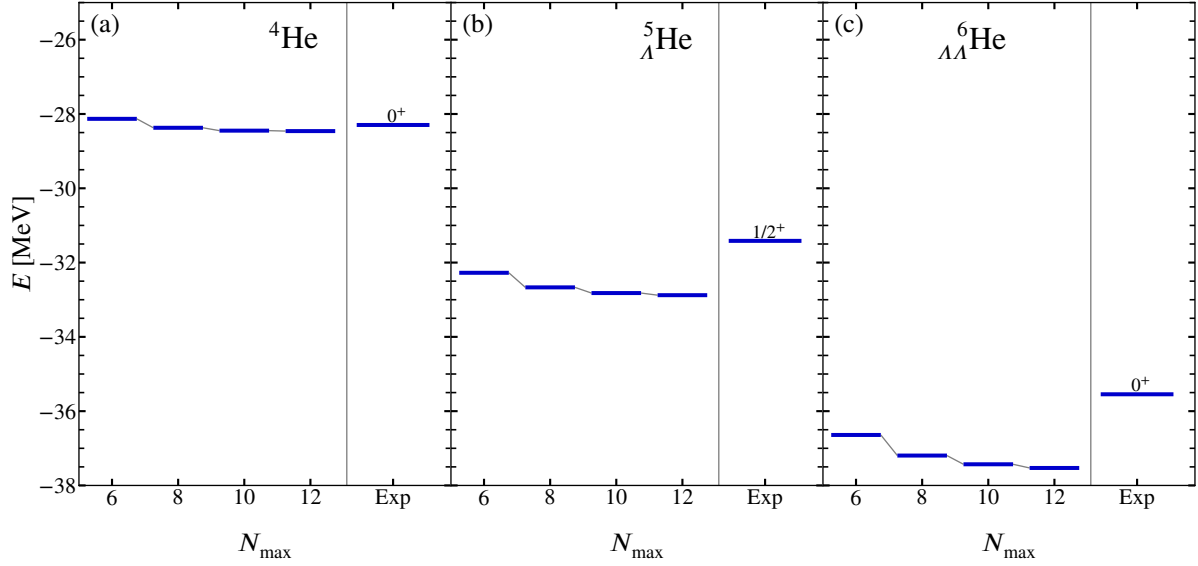
Figure 5.17.: Absolute ground-state energies of ^{4}He, $^5_\Lambda$He, and $^6_{\Lambda\Lambda}$He for the $\Lambda_Y = 700\,\text{MeV/c}$ interaction without YY interactions.

Consistent with the previous findings, the absolute energies show a large cutoff dependence. The YN interaction with $600\,\text{MeV/c}$ cutoff overbinds systematically and the $700\,\text{MeV/c}$ cutoff is consistently closer to experiment. If one takes a slightly more phenomenological approach with the aim of providing a good description of the available data, these results can be used to select a specific cutoff and, in this way, tune the interaction parameters to achieve this.

The overbinding is relatively constant across the isotopic chains so that differential quantities like neutron separation energies are less sensitive to the cutoff of the YN interaction regulator. We achieve a reproduction of experimental neutron separation energies to better than $100\,\text{keV}$ for the hypernuclei we considered, except for $^6_\Lambda$He, for which the separation energy is skewed by overbinding of the $^5_\Lambda$He ground state. For the nonstrange nuclei, experimental values are reproduced to better than $1\,\text{MeV}$. We find indications that $^{12}_\Lambda$Li, which has an $N = 8$ neutron shell closure, is at the drip line. Contrary to the naive expectation, in the helium chain the hyperon does not provide additional binding to neutrons beyond $N = 6$ so that the heaviest particle-stable isotope is $^9_\Lambda$He.

5.8.3. The Double-Λ Hypernucleus $^6_{\Lambda\Lambda}$He

The hypernucleus $^6_{\Lambda\Lambda}$He is the strange counterpart to the α particle, with filled s shells for protons, neutrons and Λ hyperons. It is one of the few doubly-strange systems that have been observed [Nak10; GM11]. Given that the YY interaction is even less constrained than the YN interaction, the available data play a crucial role in determining the parameters of the YY interaction. The two-hyperon separation energy $B_{\Lambda\Lambda}$ can be separated into two parts: the effect due to the binding of the individual hyperons to the nucleus, and a correction that accounts not only for the YY interaction itself but also for polarization effects of the nucleonic core. These polarization effects arise because the presence of the second hyperon modifies the nucleonic

core compared to the single-Λ hypernucleus. The binding of the isolated hyperons to the nucleonic core is $2B_\Lambda$, twice the hyperon separation energy in $^5_\Lambda$He; hence, $B_{\Lambda\Lambda} = 2B_\Lambda + \Delta B_{\Lambda\Lambda}$, where $\Delta B_{\Lambda\Lambda}$ captures the residual effects.

We currently cannot use YY interactions in our implementation, but a calculation without YY interaction is still useful because it helps disentangle the polarization from the interaction contribution to $\Delta B_{\Lambda\Lambda}$. Figure 5.17 shows the absolute ground-state energies of ^{4}He, $^5_\Lambda$He, and $^6_{\Lambda\Lambda}$He as a function of N_{max}, compared to the experimental values. All energies are sufficiently converged, so we can extrapolate them reliably. We get $E_0(^4\text{He}) = -28.474(9)$ MeV, $E_0(^5_\Lambda\text{He}) = -32.914(4)$ MeV, and $E_0(^6_{\Lambda\Lambda}\text{He}) = -37.602(1)$ MeV, which translates to the separation energies $B_\Lambda = 4.440(10)$ MeV and $B_{\Lambda\Lambda} = 9.128(9)$ MeV. Thus, the difference, which is entirely caused by polarization effects, amounts to $\Delta B_{\Lambda\Lambda,\text{pol.}} = 0.248(21)$ MeV. Compared to the experimental value $\Delta B_{\Lambda\Lambda} = 0.67(17)$ MeV [Nak10], the polarization contribution amounts to roughly 40 %. From this, we conclude that the YY interaction is weak, having a net effect of the order of only 0.4 MeV.

A limitation of this calculation is the omission of induced YYN terms, which can play a role here. If these are repulsive, they can lower the polarization contribution to $\Delta B_{\Lambda\Lambda}$. The origin of these terms is the SRG evolution in the YN sector, but since a three-body diagram due to Λ-Σ conversion, as discussed in section 4.7, cannot link the two hyperon lines and the nucleon line, we expect them to be smaller than the induced YNN terms. Also, the YNN terms can couple the two hyperons to six nucleon pairs, while the YYN terms connect both hyperons to the four nucleons, leading to a relative suppression of $4/(2 \times 6) = 1/3$.

6. Towards Medium-Mass Hypernuclei

While the IT-NCSM is a powerful quasi-exact *ab initio* method, its range of applicability is severely limited by the combinatorial growth of the many-body basis with particle number. Other approaches work in a many-body basis that is never constructed explicitly but accessed through a correlation operator $\boldsymbol{\Omega}$ acting on a reference state $|\boldsymbol{\Phi}\rangle$ [HLK17]. Depending on the form of $\boldsymbol{\Omega}$ and the way its parameters are determined, one obtains the Coupled-Cluster approach [Coe58; SB09], the In-Medium SRG [HBM$^+$16] or many-body perturbation theory [RPP$^+$06; TLB$^+$16].

Since $\boldsymbol{\Omega}$ is in general a genuine A-body operator one has to expand it in terms of a hierarchy of correlations and truncate that expansion to make calculations feasible. This truncation introduces a dependence on the reference state and the single-particle basis that are employed for the calculation, and both influence the rate of convergence of the expansion. For closed-shell systems, the Hartree-Fock determinant and single-particle basis provide an ideal foundation on which these expansions can be built.

6.1. The Hartree-Fock Method

The Hartree-Fock method [SO96] provides a Slater determinant that minimizes the energy expectation value of the Hamiltonian, i.e., the solution to

$$\min_{\{\alpha_i\}} E[\{\alpha_i\}] \quad \text{with} \quad E[\{\alpha_i\}] = \langle \alpha_1, \alpha_2, \dots, \alpha_A | \boldsymbol{H} | \alpha_1, \alpha_2, \dots, \alpha_A \rangle, \tag{6.1}$$

subject to the constraint that all single-particle states should be normalized. To start, we set $|\boldsymbol{\Phi}\rangle = |\alpha_1, \alpha_2, \dots, \alpha_A\rangle$ and express the creation and annihilation operators of the solution basis $c_\alpha^\dagger, c_\alpha$ in terms of a calculation basis $a_i^\dagger, a_i$ as

$$c_\alpha^\dagger = \sum_i u_{i,\alpha} a_i^\dagger, \qquad\qquad c_\alpha = \sum_i u_{i,\alpha}^* a_i, \tag{6.2}$$

$$a_i^\dagger = \sum_\alpha u_{i,\alpha}^* c_\alpha^\dagger, \qquad\qquad a_i = \sum_\alpha u_{i,\alpha} c_\alpha. \tag{6.3}$$

The matrix u is unitary and relates both bases, both c_α and a_i fulfill the canonical anticommutation relations.

Writing the energy functional in second quantization, we get

$$E[\{c_i\}] = H^{[0]} + \sum_{ij} \langle i | H^{[1]} | j \rangle \langle \boldsymbol{\Phi} | a_i^\dagger a_j | \boldsymbol{\Phi} \rangle + \frac{1}{4} \sum_{\substack{ij \\ kl}} \langle ij | H^{[2]} | kl \rangle \langle \boldsymbol{\Phi} | a_i^\dagger a_j^\dagger a_l a_k | \boldsymbol{\Phi} \rangle$$

$$+ \frac{1}{36} \sum_{\substack{ijk \\ lmn}} \langle ijk|H^{[3]}|lmn\rangle \langle\Phi|a_i^\dagger a_j^\dagger a_k^\dagger a_n a_m a_l|\Phi\rangle. \tag{6.4}$$

The expectation values on the right-hand side are density matrix elements that can be easily evaluated because $|\Phi\rangle$ is a Slater determinant:

$$\rho_{i,j} = \langle\Phi|a_i^\dagger a_j|\Phi\rangle = \sum_\alpha u_{i,\alpha}^* u_{j,\alpha} \tag{6.5}$$

$$\rho_{ij,kl}^{[2]} = \langle\Phi|a_i^\dagger a_j^\dagger a_l a_k|\Phi\rangle = \sum_{\alpha\beta}\sum_{\gamma\delta} u_{i,\alpha}^* u_{j,\beta}^* u_{l,\delta} u_{k,\gamma}(\delta_{\gamma\delta}^{\alpha\beta} - \delta_{\delta\gamma}^{\alpha\beta})$$

$$= \sum_{\alpha\beta}(u_{i,\alpha}^* u_{k,\alpha} u_{j,\beta}^* u_{l,\beta} - u_{i,\alpha}^* u_{l,\alpha} u_{j,\beta}^* u_{k,\beta}) \tag{6.6}$$

$$\rho_{ijk,lmn}^{[3]} = \langle\Phi|a_i^\dagger a_j^\dagger a_k^\dagger a_n a_m a_l|\Phi\rangle = \sum_{\alpha\beta\gamma}(u_{i,\alpha}^* u_{l,\alpha} u_{j,\beta}^* u_{m,\beta} u_{k,\gamma}^* u_{n,\gamma} \pm \text{perms.}), \tag{6.7}$$

where the sums are over occupied states only. Using antisymmetry of the matrix elements, we can insert this into the energy functional to get

$$E[\{u_{i,\alpha}\}] = H^{[0]} + \sum_{ij\alpha} \langle i|H^{[1]}|j\rangle u_{i,\alpha}^* u_{j,\alpha} + \frac{1}{2} \sum_{ijkl} \sum_{\substack{\alpha\beta \\ \text{occ.}}} \langle ij|H^{[2]}|kl\rangle u_{i,\alpha}^* u_{k,\alpha} u_{j,\beta}^* u_{l,\beta}$$

$$+ \frac{1}{6} \sum_{\substack{ijk \\ lmn}} \sum_{\substack{\alpha\beta\gamma \\ \text{occ.}}} \langle ijk|H^{[3]}|lmn\rangle u_{i,\alpha}^* u_{l,\alpha} u_{j,\beta}^* u_{m,\beta} u_{k,\gamma}^* u_{n,\gamma}. \tag{6.8}$$

Next, we implement the normalization constraint by introducing a Lagrange multiplier for each state and vary the coefficients $u_{i,\alpha}^*$ and $u_{i,\alpha}$, introducing one-body density matrix elements where applicable:

$$\tilde{E}[\{u_{i,\alpha}\}] = E[\{u_{i,\alpha}\}] - \sum_\alpha \epsilon_\alpha \sum_i u_{i,\alpha}^* u_{i,\alpha} \tag{6.9}$$

$$\delta\tilde{E}[\{u_{i,\alpha}\}] = \sum_p \sum_{\substack{\sigma \\ \text{occ.}}} \delta u_{p,\sigma}^* \Bigg(\sum_i \langle p|H^{[1]}|i\rangle u_{i,\sigma} + \sum_{ijk} \langle pj|H^{[2]}|ik\rangle \rho_{j,k} u_{i,\sigma}$$

$$+ \frac{1}{2} \sum_{\substack{ijk \\ lm}} \langle pjk|H^{[3]}|ilm\rangle \rho_{j,l}\rho_{k,m} u_{i,\sigma} - \epsilon_\sigma u_{p,\sigma} \Bigg) + \text{h.c.} \tag{6.10}$$

The parenthesized expression has to vanish for a stationary point of the energy functional, so that[1]

$$\sum_i \Bigg(\langle p|H^{[1]}|i\rangle + \sum_{jk} \langle pj|H^{[2]}|ik\rangle \rho_{j,k} + \frac{1}{2} \sum_{\substack{jk \\ lm}} \langle pjk|H^{[3]}|ilm\rangle \rho_{j,l}\rho_{k,m} \Bigg) u_{i,\sigma} = \epsilon_\sigma u_{p,\sigma}. \tag{6.11}$$

---

[1] Note that the stationarity condition makes no statement about the unoccupied states, but we choose them such that they also fulfill the condition.

This is the eigenvalue equation of the so-called mean-field Hamiltonian or Fock operator $\boldsymbol{h}[\rho]$, which depends on the one-body density matrix ρ. Since the eigenvectors $\vec{u}_\sigma$ of the occupied states enter the one-body density matrix, this eigenvalue problem is nonlinear and is commonly solved by iterating until the one-body density matrix does not change between iterations anymore.[2]

Up to this point, we did not put any constraints on the symmetry of ρ, so that each of the single-particle states σ can have different occupation numbers, even within a single orbit. For closed-shell systems, the orbits are either completely filled or empty, so that $\rho_{k,l} = \rho_{\bar{k},\bar{l}} \delta^{j_k m_k}_{j_l m_l}$. Together with the rotational invariance of the Hamiltonian, this enables us to derive angular-momentum coupled forms of the terms appearing in the eigenvalue equation that greatly reduce the computational effort needed to solve the Hartree-Fock equations (cf. appendix E). Additionally, the eigenvalue problem decomposes into blocks with good particle species, orbital and total angular momentum, and the total angular-momentum projection m can be ignored.

6.2. Equal-Filling Approximation

This computational efficiency can be carried over to open-shell systems via an equal-filling approximation that assumes *m*-independent *fractional* occupation numbers for the open shells. The equal-filling approximation is trivial to implement given a code that solves the angular-momentum-coupled Hartree-Fock equations and is, therefore, often used *ad hoc*. For singly-strange hypernuclei, which are intrinsically open-shell systems, it is crucial to understand the physical situation that is described by this approximation.

The most general ansatz one can make for the system is a density operator $\rho[\{u_{i,\alpha}\}]$ of states depending on the basis transformation coefficients. The energy functional on which the Hartree-Fock method is based then becomes

$$E[\{u_{i,\alpha}\}] = \text{tr}(\boldsymbol{\rho}\boldsymbol{H}) = H^{[0]} + \sum_{ij} \langle i|H^{[1]}|j\rangle \, \text{tr}(\boldsymbol{\rho}\boldsymbol{a}_i^\dagger \boldsymbol{a}_j) + \frac{1}{4} \sum_{ijkl} \langle ij|H^{[2]}|kl\rangle \, \text{tr}(\boldsymbol{\rho}\boldsymbol{a}_i^\dagger \boldsymbol{a}_j^\dagger \boldsymbol{a}_l \boldsymbol{a}_k)$$

$$+ \frac{1}{36} \sum_{\substack{ijk \\ lmn}} \langle ijk|H^{[3]}|lmn\rangle \, \text{tr}(\boldsymbol{\rho}\boldsymbol{a}_i^\dagger \boldsymbol{a}_j^\dagger \boldsymbol{a}_k^\dagger \boldsymbol{a}_n \boldsymbol{a}_m \boldsymbol{a}_l). \tag{6.12}$$

The nontrivial condition that casts (6.12) into the form of the original Hartree-Fock energy functional (6.8), with $\rho_{i,j} = \text{tr}(\boldsymbol{\rho}\boldsymbol{a}_i^\dagger \boldsymbol{a}_j)$, is that the higher density matrices factorize into products of one-body densities. This puts some constraints on the density operator: Some of the occupation numbers need to be fractional, so the it cannot correspond to a single Slater determinant. It also cannot correspond to an ensemble containing multi-determinantal states because these, in general, induce nontrivial many-body correlations that prevent a factorization of the many-body density matrices.

Thus, the solution to the Hartree-Fock problem employing the equal-filling approximation minimizes the average energy of an unknown ensemble of Slater determinants, which we try to determine using the factorization conditions. The most general density operator for such an

---

[2]One can also use root-finding algorithms that provide faster convergence than a simple fixed-point iteration, but the gain in speed does not warrant the additional complexity of the implementation.

ensemble providing occupation numbers $n_i = 1$ ($n_q = 0$) for the fully-occupied (unoccupied) states and fractional n_{v_k} for the valence orbital with valence indices v_k is

$$\rho = p_C |C\rangle\langle C| + \sum_{n=1}^{2j_v+1} \sum_{v_1 < \cdots < v_n} p_{v_1 \cdots v_n} c_{v_1}^\dagger \cdots c_{v_n}^\dagger |C\rangle\langle C| c_{v_n} \cdots c_{v_1} \equiv \sum_\mu p_\mu |\phi_\mu\rangle\langle\phi_\mu|, \quad (6.13)$$

where $|C\rangle$ denotes the core of fully-occupied states, and the $p_{v_1 \cdots v_n}$ are nonnegative, symmetric under exchange of any two indices, and vanish if two indices coincide.

In the basis with respect to which the Slater determinants are given (which will become the Hartree-Fock basis at the stationary point of the energy functional), we have

$$\gamma_{i,j} = \sum_\mu p_\mu \langle\phi_\mu|c_i^\dagger c_j|\phi_\mu\rangle = \sum_\mu p_\mu n_i^{(\mu)} \delta_j^i = \sum_\mu p_\mu \langle\phi_\mu|n_i|\phi_\mu\rangle \delta_j^i = \text{tr}(\rho n_i)\delta_j^i \quad (6.14)$$

$$\gamma_{ij,kl} = \sum_\mu p_\mu \langle\phi_\mu|c_i^\dagger c_j^\dagger c_l c_k|\phi_\mu\rangle = \text{tr}(\rho n_i n_j)(\delta_k^i \delta_l^j - \delta_l^i \delta_k^j) \quad (6.15)$$

$$\gamma_{ijk,lmn} = \sum_\mu p_\mu \langle\phi_\mu|c_i^\dagger c_j^\dagger c_k^\dagger c_n c_m c_l|\phi_\mu\rangle = \text{tr}(\rho n_i n_j n_k)(\delta_l^i \delta_m^j \delta_n^k \pm \text{perms.}) \quad (6.16)$$

with occupation number operators $n_i = c_i^\dagger c_i$ and their eigenvalues $n_i |\phi_\mu\rangle = n_i^{(\mu)} |\phi_\mu\rangle$. Matrix elements involving occupied or unoccupied indices factorize automatically because the respective occupation number can be pulled out of the expectation value. The nontrivial matrix elements are thus those where every index is from the partially-occupied (valence) orbital. Furthermore, the density matrix elements vanish unless their upper indices are a permutation of the lower ones, in which case they differ only by a phase from the diagonal matrix element with identical upper and lower indices. Thus, for the diagonal elements of the density matrices with indices in the valence orbital, we have to ensure that

$$\text{tr}(\rho) = p_C + \sum_{n=1}^{2j_v+1} \sum_{v_1 < \cdots < v_n} p_{v_1 \cdots v_n} \stackrel{!}{=} 1 \quad (6.17a)$$

$$\gamma_{j,j} = p_j + \sum_{n=2}^{2j_v+1} \sum_{v_2 < \cdots < v_n} p_{jv_2 \cdots v_n} \stackrel{!}{=} \frac{N_v}{2j_v + 1} \quad (6.17b)$$

$$\gamma_{jk,jk} = p_{jk} + \sum_{n=3}^{2j_v+1} \sum_{v_3 < \cdots < v_n} p_{jkv_3 \cdots v_n} \stackrel{!}{=} \left(\frac{N_v}{2j_v + 1}\right)^2 (1 - \delta_k^j) \quad (6.17c)$$

$$\gamma_{jkl,jkl} = p_{jkl} + \sum_{n=4}^{2j_v+1} \sum_{v_4 < \cdots < v_n} p_{jklv_4 \cdots v_n} \stackrel{!}{=} \left(\frac{N_v}{2j_v + 1}\right)^3 (1 - \delta_k^j - \delta_l^j - \delta_l^k + 2\delta_k^j \delta_l^k), \quad (6.17d)$$

where $0 < N_v < 2j_v + 1$ is the number of particles in the valence orbital, subject to the nonnegativity constraint on the p's.

Equations (6.17) are a system of

$$\sum_{n=0}^{3} \binom{2j_v + 1}{n} \text{ linear equations in } \sum_{n=0}^{2j_v+1} \binom{2j_v + 1}{n} = 2^{2j_v+1} \text{ unknowns,}$$

which admits infinitely many solutions if we neglect the nonnegativity constraints. If we require that *all* higher densities factorize, we get a unique solution with a simple structure:[3]

$$p_C = \frac{1}{\mathscr{Z}} \tag{6.18}$$

$$p_{v_1 \cdots v_n} = \frac{x^n}{\mathscr{Z}} [v_1 \cdots v_n] \tag{6.19}$$

$$\mathscr{Z} = (1 + x)^{2j_v + 1} \tag{6.20}$$

$$\gamma_{j_1 \cdots j_k, j_1 \cdots j_k} = \frac{x^k}{\mathscr{Z}} + \sum_{n=k+1}^{2j_v+1} \frac{x^n}{\mathscr{Z}} \sum_{v_{k+1} < \cdots < v_n} [j_1 \cdots j_k v_{k+1} \cdots v_n] = \frac{x^k}{\mathscr{Z}} + \frac{1}{\mathscr{Z}} \sum_{n=k+1}^{2j_v+1} \binom{2j_v + 1 - k}{n - k} x^n$$

$$= \frac{x^k}{\mathscr{Z}} + \frac{x^k}{\mathscr{Z}} \sum_{n=1}^{2j_v+1-k} \binom{2j_v + 1 - k}{n} x^n = \frac{x^k}{\mathscr{Z}} \sum_{n=0}^{2j_v+1-k} \binom{2j_v + 1 - k}{n} x^n$$

$$= \frac{x^k}{(1 + x)^k}, \tag{6.21}$$

which for γ_{j_1, j_1} fixes $x = N_v/(2j_v + 1 - N_v)$. The quantity $[v_1 \cdots v_n]$ is equal to one when the v's are pairwise distinct and zero otherwise. The sum over the remaining indices in the first equality of (6.21) evaluates to a binomial coefficient because

$$\sum_{v_{k+1} < \cdots < v_n} [j_1 \cdots j_k v_{k+1} \cdots v_n]$$

$$= \frac{1}{(n - k)!} \sum_{v_{k+1} \cdots v_n} [j_1 \cdots j_k v_{k+1} \cdots v_n]$$

$$= \frac{1}{(n - k)!} \sum_{\substack{v_{k+1} \\ v_{k+1} \neq j_1, \ldots, j_k}} \sum_{\substack{v_{k+2} \\ v_{k+2} \neq j_1, \ldots, j_k \\ v_{k+2} \neq v_{k+1}}} \cdots \sum_{\substack{v_n \\ v_n \neq j_1, \ldots, j_k \\ v_n \neq v_{k+1}, \ldots v_{n-1}}} 1$$

$$= \frac{1}{(n - k)!} (2j_v + 1 - k)(2j_v + 1 - k - 1) \cdots (2j_v + 1 - n + 1)$$

$$= \frac{(2j_v + 1 - k)!}{(n - k)!(2j_v + 1 - n)!} = \frac{(2j_v + 1 - k)!}{(n - k)!(2j_v + 1 - k - (n - k))!}$$

$$= \binom{2j_v + 1 - k}{n - k}, \tag{6.22}$$

which counts the number of ways one can construct a valid set of subscripts for $p_{j_1 \cdots j_k v_{k+1} \cdots v_n}$ by selecting $n - k$ index values out of the $2j_v + 1 - k$ not already used by the j_i's, without regard to order. This solution also has the correct behavior for $N_v \to 0$ ($N_v \to 2j_v + 1$) which yield density operators consisting of a single Slater determinant with the valence orbital empty (filled).

So, in general, the ensemble of Slater determinants spans all nuclei in the valence orbital. The weights are shown in fig. 6.1 and their distribution can be very wide, especially when the

---

[3]This solution can also be obtained via a density operator $\rho = \exp(-\sum_i \epsilon_i n_i)$, which can be interpreted as belonging to a grand-canonical ensemble [Gau60; PR08].
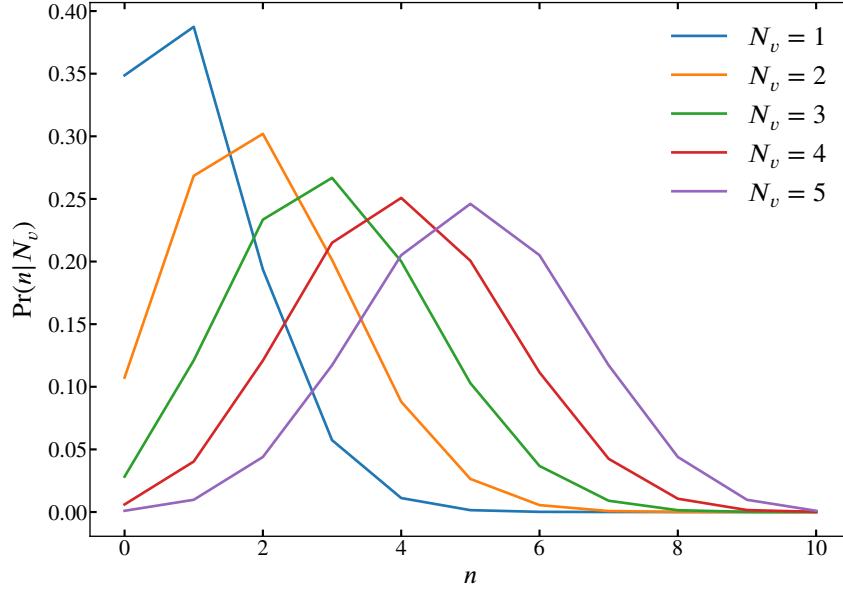
Figure 6.1.: Distribution of the number of particles in the valence orbital for an equal-filling ensemble in a $j_v = 9/2$ shell with N_v occupancies. The distributions for higher occupancies $N_v' = 2j_v + 1 - N_v$ can be obtained by noting that $x' = x^{-1}$, such that $\Pr(n|N_v') = \Pr(2j_v + 1 - n|N_v)$.

number of particles N_v is close to half-filling the orbital. Furthermore, since the probabilities are independent of the total angular-momentum projection m, there is an additional average over states with different total angular momentum J. For example, for two particles in the j_v orbital, we have

$$\sum_{m_1 < m_2} x^2 \, |C, j_v m_1, j_v m_2\rangle \langle C, j_v m_1, j_v m_2| = \frac{x^2}{2} \sum_{JM} |C, (j_v j_v) J M\rangle \langle C, (j_v j_v) J M| . \qquad (6.23)$$

For singly-strange hypernuclei with a closed-subshell nucleonic core, the equal-filling ensemble is

$$\rho = \frac{1}{4} \left|^{A-1}Z\right\rangle \left\langle^{A-1}Z\right| + \frac{1}{4} \sum_{M=-1/2}^{+1/2} \left|^{A}_{\Lambda}Z, M\right\rangle \left\langle^{A}_{\Lambda}Z, M\right| + \frac{1}{4} \left|^{A+1}_{\Lambda\Lambda}Z\right\rangle \left\langle^{A+1}_{\Lambda\Lambda}Z\right| \qquad (6.24)$$

and, because we rewrite the ground-state energies of the two hypernuclei as sum of the ground-state energy of the parent and the hyperon separation energies, the energy expectation value becomes

$$\operatorname{tr}(\rho H) = \tfrac{1}{4} E\left(^{A-1}Z\right) + \tfrac{1}{2}\left(E\left(^{A-1}Z\right) - B_\Lambda\right) + \tfrac{1}{4}\left(E\left(^{A-1}Z\right) - B_{\Lambda\Lambda}\right)$$
$$= E\left(^{A-1}Z\right) - B_\Lambda - \tfrac{1}{4}\Delta B_{\Lambda\Lambda} \qquad (6.25)$$

The quantity $\Delta B_{\Lambda\Lambda} = B_{\Lambda\Lambda} - 2B_\Lambda$ gives the additional separation energy of the doubly-strange hypernucleus due to the YY interaction and polarization effects of the nucleonic core. In absence of a YY interaction it is negligible so that the energy expectation value of the ensemble actually coincides with that of the hypernucleus.

6.3. Normal Ordering

Since the implicit-basis methods are based on a reference state, it is beneficial to have a basis of creation and annihilation operators that is adapted to this reference state. Many computations are carried out simpler than in the original operator basis and the adapted basis also provides approximations for the Hamiltonian. The adaptation is the so-called normal ordering [Wic50]: we define a new set of many-body operators $\{c_{i_1}^\dagger \cdots c_{i_n}^\dagger c_{j_n} \cdots c_{j_1}\}$ for a single-determinantal reference state $|\Phi\rangle$ (which can be the Fock-space vacuum), which is obtained by placing all creators of unoccupied states and annihilators of occupied ones to the left of the remaining operators. For these normal-ordered operators, we have by construction

$$\langle \Phi | \{c_{i_1}^\dagger \cdots c_{i_n}^\dagger c_{j_n} \cdots c_{j_1}\} | \Phi \rangle = 0. \tag{6.26}$$

This property greatly simplifies calculations because in implicit-basis methods one often deals with expectation values of operators with respect to the reference state, for which all terms except for the normal-ordered zero-body term vanish.

The original and normal-ordered basis can be related by starting from a string of creation and annihilation operators and, using the canonical anticommutation relations, commuting them until one gets the required ordering. However, Wick's theorem [Wic50] provides a more elegant way of bringing a string of creation and annihilation operators into normal order. We first define a general string of operators in normal order $\{A_1 \cdots A_n\}$, where the A's are creation or annihilation operators, to have the following properties:

$$\{A_1 \cdots A_i \cdots A_j \cdots A_n\} = -\{A_1 \cdots A_j \cdots A_i \cdots A_n\} \quad \text{(antisymmetry)}, \tag{6.27a}$$

$$\{\lambda A_1 \cdots A_n\} = \lambda \{A_1 \cdots A_n\} \quad \text{(linearity)}, \tag{6.27b}$$

$$\{\} = \{\mathbf{1}\} = \mathbf{1} \quad \text{(identity preservation)}. \tag{6.27c}$$

Next, we define a *contraction* as the number

$$\dot{A}_1 \dot{A}_2 = \langle \Phi | A_1 A_2 | \Phi \rangle. \tag{6.28}$$

The only nonvanishing contractions are of $c^\dagger c$- or $cc^\dagger$-type:

$$\dot{c}_i^\dagger \dot{c}_j = \rho_{i,j} \tag{6.29}$$

$$\dot{c}_i \dot{c}_j^\dagger = (\delta_j^i - \rho_{i,j}). \tag{6.30}$$

Now, Wick's theorem states

$$A_1 \cdots A_n = \{A_1 \cdots A_n\}$$
$$+ \sum_{\substack{i_1 i_2 \\ \text{contr.}}} (\pm 1) \dot{A}_{i_1} \dot{A}_{i_2} \{A_1 \cdots A_{i_1-1} A_{i_1+1} \cdots A_{i_2-1} A_{i_2+1} \cdots A_n\}$$
$$+ \sum_{\substack{i_1 i_2 i_3 i_4 \\ \text{double contr.}}} (\pm 1) \dot{A}_{i_1} \dot{A}_{i_2} \ddot{A}_{i_3} \ddot{A}_{i_4} \{A_1 \cdots A_{i_1-1} A_{i_1+1} \cdots A_{i_2-1} A_{i_2+1} \cdots A_{i_3-1}$$
$$\times A_{i_3+1} \cdots A_{i_4-1} A_{i_4+1} \cdots A_n\}$$
$$\vdots$$

$$+ \sum_{\substack{i_1 \cdots i_n \\ \text{full contr.}}} (\pm 1) \dot{\boldsymbol{A}}_{i_1} \ddot{\boldsymbol{A}}_{i_2} \cdots \ddot{\boldsymbol{A}}_{i_{n-1}} \ddot{\boldsymbol{A}}_{i_n}, \tag{6.31}$$

where the sums are over all possible contractions and the phase factors arise because the operators to be contracted have to be brought adjacent to each other before the contraction itself can be performed. The operators to be contracted themselves have to remain in order because exchanging them changes the type of the contraction. The different numbers of dots over the contracted operators are used to distinguish contractions.

Wick's theorem can be generalized[4] to products of normal-ordered operators as

$$
\begin{aligned}
\{ &\boldsymbol{A}_1 \cdots \boldsymbol{A}_m \} \{ \boldsymbol{B}_1 \cdots \boldsymbol{B}_n \} \\
&= \{ \boldsymbol{A}_1 \cdots \boldsymbol{A}_m \boldsymbol{B}_1 \cdots \boldsymbol{B}_n \} \\
&\quad + \sum_{\substack{i_1 j_1 \\ \text{ext. contr.}}} (\pm 1) \dot{\boldsymbol{A}}_{i_1} \dot{\boldsymbol{B}}_{j_1} \{ \boldsymbol{A}_1 \cdots \boldsymbol{A}_{i_1-1} \boldsymbol{A}_{i_1+1} \cdots \boldsymbol{A}_m \boldsymbol{B}_1 \cdots \boldsymbol{B}_{j_1-1} \boldsymbol{B}_{j_1+1} \cdots \boldsymbol{B}_n \} \\
&\quad \vdots \\
&\quad + \sum_{\substack{i_1 \cdots i_m \\ j_1 \cdots j_m \\ \text{ext. contr.}}} (\pm 1) \dot{\boldsymbol{A}}_{i_1} \dot{\boldsymbol{B}}_{j_1} \cdots \ddot{\boldsymbol{A}}_{i_m} \ddot{\boldsymbol{B}}_{j_m} \{ \boldsymbol{B}_{j_{m+1}} \cdots \boldsymbol{B}_{j_n} \}
\end{aligned} \tag{6.32}
$$

for $m \leq n$, without loss of generality. The sums are over external contractions only with $j_{m+1}, \ldots, j_n$ collecting the remaining uncontracted indices. The phases again arise from permuting the operators such that the $\boldsymbol{A}$'s and $\boldsymbol{B}$'s to be contracted are adjacent in the combined normal-ordered product.

The most commonly needed expressions are for those operators that appear in the Hamiltonian:

$$c_p^\dagger c_q = \{ c_p^\dagger c_q \} + \rho_{p,q} \tag{6.33}$$

$$
\begin{aligned}
c_p^\dagger c_q^\dagger c_s c_r &= \{ c_p^\dagger c_q^\dagger c_s c_r \} \\
&\quad + \rho_{p,r} \{ c_q^\dagger c_s \} - \rho_{p,s} \{ c_q^\dagger c_r \} + \rho_{q,s} \{ c_p^\dagger c_r \} - \rho_{q,r} \{ c_p^\dagger c_s \} \\
&\quad + \rho_{p,r} \rho_{q,s} - \rho_{p,s} \rho_{q,r}
\end{aligned} \tag{6.34}
$$

$$
\begin{aligned}
c_p^\dagger c_q^\dagger c_r^\dagger c_u c_t c_s &= \{ c_p^\dagger c_q^\dagger c_r^\dagger c_u c_t c_s \} \\
&\quad + \rho_{p,s} \{ c_q^\dagger c_r^\dagger c_u c_t \} \pm \cdots \\
&\quad + (\rho_{p,s} \rho_{q,t} - \rho_{p,t} \rho_{q,s}) \{ c_r^\dagger c_u \} \pm \cdots \\
&\quad + \rho_{p,s} \rho_{q,t} \rho_{r,u} \pm \cdots .
\end{aligned} \tag{6.35}
$$

These can be inserted into the Hamiltonian to get it into normal-ordered form

$$\boldsymbol{H} = E_0 + \sum_{pq} f_{p,q} \{ c_p^\dagger c_q \} + \frac{1}{4} \sum_{pqrs} \Gamma_{pq,rs} \{ c_p^\dagger c_q^\dagger c_s c_r \} + \frac{1}{36} \sum_{pqrstu} W_{pqr,stu} \{ c_p^\dagger c_q^\dagger c_r^\dagger c_u c_t c_s \}. \tag{6.36}$$

---

[4]There is a further extension to multi-determinantal reference states and ensembles [KM97].

The matrix elements

$$E_0 = H^{[0]} + \sum_{pq} H^{[1]}_{p,q}\rho_{p,q} + \frac{1}{2}\sum_{pqrs} H^{[2]}_{pq,rs}\rho_{p,r}\rho_{q,s} + \frac{1}{6}\sum_{\substack{pqr\\stu}} H^{[3]}_{pqr,stu}\rho_{p,s}\rho_{q,t}\rho_{r,u}, \tag{6.37}$$

$$f_{p,q} = H^{[1]}_{p,q} + \sum_{rs} H^{[2]}_{pr,qs}\rho_{r,s} + \frac{1}{2}\sum_{rstu} H^{[3]}_{prs,qtu}\rho_{r,t}\rho_{s,u} \tag{6.38}$$

$$\Gamma_{pq,rs} = H^{[2]}_{pq,rs} + \sum_{tu} H^{[3]}_{pqt,rsu}\rho_{t,u}, \tag{6.39}$$

$$W_{pqr,stu} = H^{[3]}_{pqr,stu} \tag{6.40}$$

are linear combinations of the matrix elements in the original basis. The zero-body part is the energy expectation value in the reference state and the matrix elements of the one-body part coincide with those of the Fock operator $h[\rho]$.

For most implicit-basis methods the inclusion of the full three-body interaction leads to an increase in the number of terms that contribute to the calculation. Furthermore, these additional terms tend to scale unfavorably compared to the terms present when only two-body interactions are used. The normal-ordered Hamiltonian provides a basis for lower-particle-rank approximations, the so-called normal-ordered n-body (NOnB) approximations: the matrix elements of the normal-ordered Hamiltonian contain contributions from higher particle ranks. When returning from the normal-ordered to the original form of the Hamiltonian, these contributions cancel and one recovers the original matrix elements. When one neglects, e.g., the three-body term before transforming back, some of the terms needed for the cancellation are not present so that corrections to the two-, one- and zero-body matrix elements remain, which contain information about the three-body interaction. The Hamiltonian itself, however, is a two-body operator. The back-transformation for the one- and two-body part reads

$$\{c^\dagger_p c_q\} = c^\dagger_p c_q - \rho_{p,q} \tag{6.41}$$

$$\begin{aligned}\{c^\dagger_p c^\dagger_q c_s c_r\} = {}& c^\dagger_p c^\dagger_q c_s c_r \\ & - \rho_{p,r}c^\dagger_q c_s + \rho_{p,s}c^\dagger_q c_r - \rho_{q,s}c^\dagger_p c_r + \rho_{q,r}c^\dagger_p c_s \\ & + \rho_{p,r}\rho_{q,s} - \rho_{p,s}\rho_{q,r}, \end{aligned} \tag{6.42}$$

so that the NOnB Hamiltonians are

$$\begin{aligned}\boldsymbol{H}^{[\mathrm{NO2B}]} &= E_0 + \sum_{pq} f_{p,q}(c^\dagger_p c_q - \rho_{p,q}) + \frac{1}{4}\sum_{pqrs}\Gamma_{pq,rs}(c^\dagger_p c^\dagger_q c_s c_r - 4\rho_{q,s}c^\dagger_p c_r + 2\rho_{p,r}\rho_{q,s}) \\ &= \left(E_0 - \sum_{pq} f_{p,q}\rho_{p,q} + \frac{1}{2}\sum_{pqrs}\Gamma_{pq,rs}\rho_{p,r}\rho_{q,s}\right) + \sum_{pq}\left(f_{p,q} - \sum_{rs}\Gamma_{pr,qs}\rho_{r,s}\right)c^\dagger_p c_q \\ &\quad + \frac{1}{4}\sum_{pqrs}\Gamma_{pq,rs}c^\dagger_p c^\dagger_q c_s c_r \\ &= \left(H^{[0]} + \frac{1}{6}\sum_{\substack{pqr\\stu}} H^{[3]}_{pqr,stu}\rho_{p,s}\rho_{q,t}\rho_{r,u}\right) + \sum_{pq}\left(H^{[1]}_{p,q} - \frac{1}{2}\sum_{rstu} H^{[3]}_{prs,qtu}\rho_{r,t}\rho_{s,u}\right)c^\dagger_p c_q\end{aligned}$$

$$+ \frac{1}{4} \sum_{pqrs} \left(H^{[2]}_{pq,rs} + \sum_{tu} H^{[3]}_{pqt,rsu} \rho_{t,u} \right) c^\dagger_p c^\dagger_q c_s c_r \qquad (6.43)$$

$$H^{[\text{NO1B}]} = E_0 + \sum_{pq} f_{p,q}(c^\dagger_p c_q - \rho_{p,q}) = \left(E_0 - \sum_{pq} f_{p,q} \rho_{p,q} \right) + \sum_{pq} f_{p,q} c^\dagger_p c_q$$

$$= \left(H^{[0]} - \frac{1}{2} \sum_{pqrs} H^{[2]}_{pq,rs} \rho_{p,r} \rho_{q,s} - \frac{1}{3} \sum_{\substack{pqr \\ stu}} H^{[3]}_{pqr,stu} \rho_{p,s} \rho_{q,t} \rho_{r,u} \right)$$

$$+ \sum_{pq} \left(H^{[1]}_{p,q} + \sum_{rs} H^{[2]}_{pr,qs} \rho_{r,s} + \frac{1}{2} \sum_{rstu} H^{[3]}_{prs,qtu} \rho_{r,t} \rho_{s,u} \right) c^\dagger_p c_q. \qquad (6.44)$$

Both Hamiltonians have the same Hartree-Fock solution as the original approximation. This is easy to see for the NO1B Hamiltonian since the matrix elements of the one-body part coincide with those of the Fock operator. For the NO2B Hamiltonian, the Fock operator has matrix elements

$$h_{p,q} = H^{[\text{NO2B},1]}_{p,q} + \sum_{rs} H^{[\text{NO2B},2]}_{pr,qs} \rho_{r,s} = H^{[1]}_{p,q} + \sum_{rs} H^{[2]}_{pr,qs} \rho_{r,s} + \frac{1}{2} \sum_{rstu} H^{[3]}_{prs,qtu} \rho_{r,t} \rho_{s,u}, \qquad (6.45)$$

which are identical to those of the original Fock operator.

This shows that the NO2B Hamiltonian cannot be distinguished from the original one at the mean-field level, which gives rise to the assumption that it provides a good approximation to the full Hamiltonian for calculations that include correlations. This assumption has been tested for closed-shell nuclei in an IT-NCSM framework [RBV+12] and in Coupled-Cluster theory [BPC+13], and deviations from ground-state energies calculated using the Hamiltonian with full 3N terms were found to be below 1 %; except for ^{4}He, which showed 2 % difference.

6.4. Many-Body Perturbation Theory

Many-body perturbation theory (MBPT) is probably the simplest many-body method beyond the mean-field approximation. Starting from the Schrödinger equation for the many-body system

$$H \left| \Psi \right\rangle = E \left| \Psi \right\rangle, \qquad (6.46)$$

we partition the Hamiltonian

$$H = H_0 + \lambda W \qquad (6.47)$$

into an unperturbed part H_0 and a perturbation W and expand both the eigenstate and energy in a formal power series in powers of the parameter λ:

$$E(\lambda) = \sum_{k=0}^{\infty} \lambda^k E^{(k)}, \qquad (6.48)$$

$$\left| \Psi(\lambda) \right\rangle = \sum_{k=0}^{\infty} \lambda^k \left| \Psi^{(k)} \right\rangle. \qquad (6.49)$$

Substituting this back into the Schrödinger equation and sorting powers of λ, we recover at order λ^0 the eigenvalue problem of the unperturbed Hamiltonian and at order λ^k

$$(\boldsymbol{H}_0 - E^{(0)}) |\Psi^{(k)}\rangle = E^{(k)} |\Psi^{(0)}\rangle + \sum_{l=1}^{k-1} E^{(l)} |\Psi^{(k-l)}\rangle - \boldsymbol{W}|\Psi^{(k-1)}\rangle . \tag{6.50}$$

The zero-order correction $|\Psi^{(0)}\rangle$ is an eigenstate of the unperturbed Hamiltonian, whose eigenbasis we denote by $\{|\phi_i\rangle\}$ with eigenvalues $\{\epsilon_i\}$. We set $|\Psi^{(0)}\rangle = |\phi_0\rangle = |\Phi\rangle$ and employ intermediate normalization of the perturbed state, i.e., $\langle\Phi|\Psi(\lambda)\rangle = 1$, which implies $\langle\Phi|\Psi^{(k)}\rangle = 0$ for $k > 0$.

Assuming a nondegenerate reference state $|\Phi\rangle$, we can project (6.50) onto the reference state to get the kth energy correction

$$E^{(k)} = \langle\Phi|\boldsymbol{W}|\Psi^{(k-1)}\rangle , \tag{6.51}$$

and onto the remainder of the unperturbed eigenbasis to get the state correction

$$\langle\phi_i|\Psi^{(k)}\rangle = \frac{1}{\epsilon_i - \epsilon_0}\Big(\sum_{l=1}^{k-1} E^{(l)} \langle\phi_i|\Psi^{(k-l)}\rangle - \langle\phi_i|\boldsymbol{W}|\Psi^{(k-1)}\rangle\Big). \tag{6.52}$$

The first two state corrections are

$$\langle\phi_i|\Psi^{(1)}\rangle = -\frac{\langle\phi_i|\boldsymbol{W}|\Phi\rangle}{\epsilon_i - \epsilon_0} \tag{6.53}$$

$$\langle\phi_i|\Psi^{(2)}\rangle = \sum_{j\neq 0} \frac{\langle\phi_i|\boldsymbol{W}|\phi_j\rangle \langle\phi_j|\boldsymbol{W}|\Phi\rangle}{(\epsilon_i - \epsilon_0)(\epsilon_j - \epsilon_0)} - E^{(1)}\frac{\langle\phi_i|\boldsymbol{W}|\Phi\rangle}{(\epsilon_i - \epsilon_0)^2}, \tag{6.54}$$

from which we get the energy corrections up to third order

$$E^{(1)} = \langle\Phi|\boldsymbol{W}|\Phi\rangle \tag{6.55}$$

$$E^{(2)} = -\sum_{i\neq 0} \frac{|\langle\phi_i|\boldsymbol{W}|\Phi\rangle|^2}{\epsilon_i - \epsilon_0} \tag{6.56}$$

$$E^{(3)} = \sum_{i,j\neq 0} \frac{\langle\Phi|\boldsymbol{W}|\phi_i\rangle \langle\phi_i|\boldsymbol{W}|\phi_j\rangle \langle\phi_j|\boldsymbol{W}|\Phi\rangle}{(\epsilon_i - \epsilon_0)(\epsilon_j - \epsilon_0)} - E^{(1)}\sum_{i\neq 0} \frac{|\langle\phi_i|\boldsymbol{W}|\Phi\rangle|^2}{(\epsilon_i - \epsilon_0)^2}. \tag{6.57}$$

6.4.1. Hartree-Fock Perturbation Theory

These considerations are completely general, except for the nondegeneracy assumption and the use of the eigenbasis of $\boldsymbol{H}_0$, and in order to perform an actual calculation, we need to select a partitioning. The partitioning itself has a strong influence on the convergence of the perturbation series and even decides whether the series converges at all [TLB+16]. In the following, we consider *Møller-Plesset* partitioning for a two-body Hamiltonian in a Hartree-Fock basis where the unperturbed part of the Hamiltonian is the (shifted) Fock operator $\boldsymbol{h}$.

6. Towards Medium-Mass Hypernuclei

We define

$$H_0 = h + E_0 - \sum_i \epsilon_i = \sum_{pq} h_{p,q}\{c_p^\dagger c_q\} + E_0, \tag{6.58}$$

$$\Gamma = \frac{1}{4}\sum_{pqrs} H^{[2]}_{pq,rs}\{c_p^\dagger c_q^\dagger c_s c_r\} \tag{6.59}$$

with $E_0 = \langle \Phi | H | \Phi \rangle$ the Hartree-Fock expectation value, such that

$$W = H - H_0 = \Gamma + \sum_{pq}(f_{p,q} - h_{p,q})\{c_p^\dagger c_q\}. \tag{6.60}$$

Since $f_{p,q} = h_{p,q}$ the perturbation is purely a two-body operator and we have

$$E^{(0)} = E_0, \tag{6.61}$$

$$E^{(1)} = 0, \tag{6.62}$$

$$E^{(2)} = -\frac{1}{4}\sum_{ijab} \frac{|\langle \Phi | \Gamma | \Phi^{ab}_{ij}\rangle|^2}{\epsilon_a + \epsilon_b - \epsilon_i - \epsilon_j}, \tag{6.63}$$

$$E^{(3)} = \frac{1}{16}\sum_{\substack{ijkl \\ abcd}} \frac{\langle \Phi | \Gamma | \Phi^{ab}_{ij}\rangle \langle \Phi^{ab}_{ij} | \Gamma | \Phi^{cd}_{kl}\rangle \langle \Phi^{cd}_{kl} | \Gamma | \Phi\rangle}{(\epsilon_a + \epsilon_b - \epsilon_i - \epsilon_j)(\epsilon_c + \epsilon_d - \epsilon_k - \epsilon_l)}, \tag{6.64}$$

where $|\Phi^{ab}_{ij}\rangle = \{c_a^\dagger c_b^\dagger c_j c_i\}|\Phi\rangle$ and $a, b, \dots$ $(i, j, \dots)$ denote particle (hole) indices. There are no singly-excited intermediate states because by the generalized Wick theorem Γ cannot be fully contracted with a one-body operator.

Evaluating the contractions, we get

$$E^{(2)} = -\frac{1}{4}\sum_{ijab} \frac{|H^{[2]}_{ij,ab}|^2}{\epsilon_a + \epsilon_b - \epsilon_i - \epsilon_j} \tag{6.65}$$

for the second-order correction. The third-order correction can be separated into three parts:

$$E^{(3)}_{\text{pp}} = \frac{1}{8}\sum_{\substack{ij \\ abcd}} \frac{H^{[2]}_{ij,ab} H^{[2]}_{ab,cd} H^{[2]}_{cd,ij}}{(\epsilon_a + \epsilon_b - \epsilon_i - \epsilon_j)(\epsilon_c + \epsilon_d - \epsilon_i - \epsilon_j)}, \tag{6.66}$$

$$E^{(3)}_{\text{hh}} = \frac{1}{8}\sum_{\substack{ijkl \\ ab}} \frac{H^{[2]}_{ab,ij} H^{[2]}_{ij,kl} H^{[2]}_{kl,ab}}{(\epsilon_a + \epsilon_b - \epsilon_i - \epsilon_j)(\epsilon_a + \epsilon_b - \epsilon_k - \epsilon_l)}, \tag{6.67}$$

$$E^{(3)}_{\text{ph}} = -\sum_{\substack{ijk \\ abc}} \frac{H^{[2]}_{ji,ab} H^{[2]}_{kb,jc} H^{[2]}_{ac,ki}}{(\epsilon_a + \epsilon_b - \epsilon_i - \epsilon_j)(\epsilon_a + \epsilon_c - \epsilon_i - \epsilon_k)}. \tag{6.68}$$
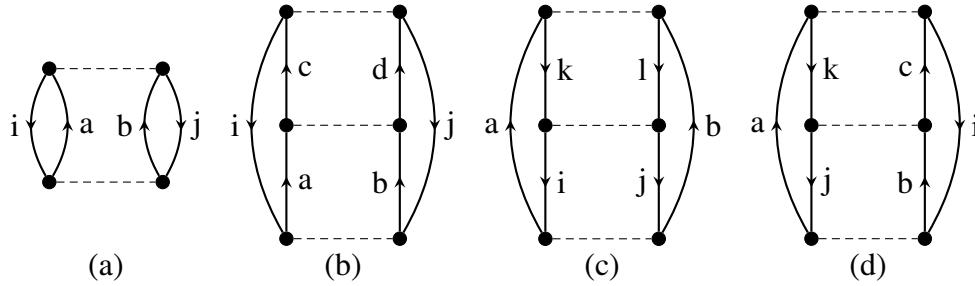
Figure 6.2.: ASG diagrams of the (a) second and (b-d) third-order *hh*, *pp* and *ph* energy corrections.

6.4.2. Diagrammatic Construction

Construction of the perturbative corrections from (6.51) and (6.52) with subsequent evaluation of the possible contractions becomes more and more tedious with increasing order. To simplify this task and to visualize the resulting expressions, one can use antisymmetrized Goldstone (ASG) diagrams [SO96; SB09]. Each interaction matrix element is identified with a part of the diagram:

$$H^{[2]}_{pq,rs} = \quad\quad\quad\quad\quad\quad f_{p,q} - h_{p,q} = \quad\quad\quad\quad\quad .$$

Upgoing lines are particles, downgoing ones are holes, and there is always one incoming and one outgoing line at every vertex. The order of indices is important: exchanging two indices swaps their places in the matrix element and leads to a phase factor.

An order-*n* energy diagram is built from *n* interactions (one- or two-body) drawn above one another and connected by particle and hole lines such that no external lines remain. The diagrams have to be linked, i.e., they may not consist of separate components not connected by any line. Each such diagram corresponds to a term in the perturbation expansion of the energy: one starts by writing a product of the interaction matrix elements. The denominators are determined by considering a line drawn between each pair of successive interactions. The denominator is the sum of single-particle energies of all hole lines minus all particle lines crossing this line. Finally, there is a phase factor (-1) for every hole line and every closed loop and a factor of 1/2 for each pair of equivalent lines, i.e., lines connecting the same two interactions. This expression is then summed over all occurring indices. The second- and third-order diagrams are shown in fig. 6.2.

6.4.3. Perturbation Theory for Hypernuclei

Since we solve the Hartree-Fock problem for singly-strange hypernuclei in an equal-filling approximation, there are slight differences to the canonical Hartree-Fock case. The matrix elements $h_{p,q}$ of the Fock operator that determines the basis and unperturbed energies does not coincide with the normal-ordered one-body part of the Hamiltonian with respect to one of the

two possible reference states. Hence, additional diagrams containing one-body interactions contribute to the perturbation series. Also, because we want to work within a spherical scheme we invoke rotational invariance of the Hamiltonian and compute *m*-averaged energy corrections.

We take the reference states $c_{\bar{v},\mu}^{\dagger}|C\rangle$, where $\bar{v}$ denotes the singly-occupied valence orbital and C is a closed nucleonic core. We get different normal-ordered one-body parts $f_{p,q}^{(\mu)}$ of the Hamiltonian and a perturbation expansion of the energy E_{μ} for each of these reference states. The average energy is

$$\bar{E}(\lambda) = \frac{1}{2j_v + 1} \sum_{k=0}^{\infty} \lambda^k \sum_{\mu=-j_v}^{+j_v} E_{\mu}^{(k)} = \sum_{k=0}^{\infty} \lambda^k \bar{E}^{(k)}, \tag{6.69}$$

so, at second order, we have to compute

$$\bar{E}^{(2)} = \frac{1}{2j_v + 1} \sum_{\mu} \left(i \bigotimes a \quad b \bigotimes j \quad + \quad i \bigotimes a \right)_{\mu}, \tag{6.70}$$

where the subscript denotes that particle and hole indices are defined with respect to the μth determinant.

In the one-body diagram the perturbation is (*c* denotes a core index, the unprimed v has $m_v = \mu$)

$$f_{i,a}^{(\mu)} - h_{i,a} = H_{i,a}^{[1]} - H_{i,a}^{[1]} + \sum_c H_{ic,ac}^{[2]} + H_{iv,av}^{[2]} - \sum_c H_{ic,ac}^{[2]} - \sum_{m_v'} H_{iv',av'}^{[2]} \frac{1}{2j_v + 1}$$

$$= \sum_{m_v'} H_{iv',av'}^{[2]} \left(\delta_{\mu}^{m_v'} - \frac{1}{2j_v + 1} \right), \tag{6.71}$$

and with

$$H_{iv',av'}^{[2]} = \sum_{JM} \begin{pmatrix} j_i & j_v & J \\ m_i & m_v' & M \end{pmatrix} \begin{pmatrix} j_a & j_v & J \\ m_a & m_v' & M \end{pmatrix} {}^{J}H_{\overline{iv},\overline{av}}^{[2]}, \tag{6.72}$$

where ${}^{J}H_{\bar{a}\bar{b},\bar{i}\bar{j}}^{[2]} = \langle(\bar{a}\bar{b})J|H^{[2]}|(\bar{i}\bar{j})J\rangle$ is a *J*-coupled matrix element, we can carry out the sum over m_v' and get

$$f_{i,a}^{(\mu)} - h_{i,a} = H_{iv,av}^{[2]} - \frac{1}{2j_v + 1} \sum_{m_v'} \sum_{JM} \begin{pmatrix} j_i & j_v & J \\ m_i & m_v' & M \end{pmatrix} \begin{pmatrix} j_a & j_v & J \\ m_a & m_v' & M \end{pmatrix} {}^{J}H_{\overline{iv},\overline{av}}^{[2]}$$

$$= H_{iv,av}^{[2]} - \delta_{j_a m_a}^{j_i m_i} \sum_J \frac{\hat{J}^2}{\hat{j}_v^2 \hat{j}_i^2} {}^{J}H_{\overline{iv},\overline{av}}^{[2]} = H_{iv,av}^{[2]} - \delta_{j_a m_a}^{j_i m_i} \bar{H}_{\overline{iv},\overline{av}}^{[2]}, \tag{6.73}$$

where we introduced the averaged matrix element $\bar{H}_{\overline{iv},\overline{av}}^{[2]}$, and used the identity $(2j_v + 1) = \hat{j}_v^2$ in order to shorten the following formulae. Clearly, the particle-hole matrix element $a = v' \neq i = v$ inside the valence space vanishes because the first term in that case is forbidden by antisymmetry and the second term is only nonzero for $m_i = m_a$, which would imply that $v = v'$.

Introducing shorthands

$$\epsilon^{\bar{a}_1\cdots\bar{a}_n}_{\bar{i}_1\cdots\bar{i}_n} = \epsilon_{\bar{a}_1} + \cdots + \epsilon_{\bar{a}_n} - \epsilon_{\bar{i}_1} - \cdots - \epsilon_{\bar{i}_n} \tag{6.74}$$

for the energy denominators, the formula for the one-body diagram from (6.70) is

$$
\begin{aligned}
\bar{E}^{(2,1)} &= -\frac{1}{2j_v + 1} \sum_{\mu} \sum_{ia} \frac{(f^{(\mu)}_{i,a} - h_{i,a})^2}{\epsilon^{\bar{a}}_{\bar{i}}} \\
&= -\frac{1}{2j_v + 1} \sum_{\mu} \sum_{ia} \frac{1}{\epsilon^{\bar{a}}_{\bar{i}}} \left((H^{[2]}_{iv,av})^2 - 2H^{[2]}_{iv,av} \delta^{j_i m_i}_{j_a m_a} \bar{H}^{[2]}_{\bar{i}\bar{v},\bar{a}\bar{v}} + \delta^{j_i m_i}_{j_a m_a} (\bar{H}^{[2]}_{\bar{i}\bar{v},\bar{a}\bar{v}})^2 \right) \\
&= -\frac{1}{2j_v + 1} \sum_{\mu} \sum_{ia} \frac{(H^{[2]}_{iv,av})^2}{\epsilon^{\bar{a}}_{\bar{i}}} + \sum_{\substack{\bar{i}\bar{a} \\ j_i = j_a}} \hat{j}_i^2 \frac{(\bar{H}^{[2]}_{\bar{i}\bar{v},\bar{a}\bar{v}})^2}{\epsilon^{\bar{a}}_{\bar{i}}}.
\end{aligned}
\tag{6.75}
$$

We split the two-body term into sums over core, valence and particle indices. Since there is only one valence particle, at most one of the hole indices can belong to the valence orbital such that the denominator cannot vanish and we get (the unprimed v has $m_v = \mu$ while the primed ones have $m'_v \neq \mu$)

$$
\begin{aligned}
\bar{E}^{(2,2)} = -\frac{1}{2j_v + 1} \sum_{\mu} \Bigg(&\frac{1}{4} \sum_{cc'pp'} \frac{|H^{[2]}_{cc',pp'}|^2}{\epsilon^{\bar{p}\bar{p}'}_{\bar{c}\bar{c}'}} + \frac{1}{2} \sum_{cc'v'p} \frac{|H^{[2]}_{cc',v'p}|^2}{\epsilon^{\bar{v}\bar{p}}_{\bar{c}\bar{c}'}} + \frac{1}{4} \sum_{cc'v'v''} \frac{|H^{[2]}_{cc',v'v''}|^2}{\epsilon^{\bar{v}\bar{v}}_{\bar{c}\bar{c}'}} \\
&+ \frac{1}{2} \sum_{cpp'} \frac{|H^{[2]}_{vc,pp'}|^2}{\epsilon^{\bar{p}\bar{p}'}_{\bar{v}\bar{c}}} + \sum_{cv'p} \frac{|H^{[2]}_{vc,v'p}|^2}{\epsilon^{\bar{p}}_{\bar{c}}} + \frac{1}{2} \sum_{cv'v''} \frac{|H^{[2]}_{vc,v'v''}|^2}{\epsilon^{\bar{v}}_{\bar{c}}} \Bigg). \quad (6.76)
\end{aligned}
$$

The square of the matrix element can be written as

$$|H^{[2]}_{ab,ij}|^2 = \sum_{JJ'MM'} \begin{pmatrix} j_a & j_b \\ m_a & m_b \end{pmatrix} \begin{matrix} J \\ M \end{matrix} \begin{pmatrix} j_a & j_b \\ m_a & m_b \end{pmatrix} \begin{matrix} J' \\ M' \end{matrix} \begin{pmatrix} j_i & j_j \\ m_i & m_j \end{pmatrix} \begin{matrix} J \\ M \end{matrix} \begin{pmatrix} j_i & j_j \\ m_i & m_j \end{pmatrix} \begin{matrix} J' \\ M' \end{matrix} {}^J H^{[2]}_{\bar{a}\bar{b},\bar{i}\bar{j}} {}^{J'} H^{[2]}_{\bar{a}\bar{b},\bar{i}\bar{j}}. \tag{6.77}$$

Exploiting rotational invariance of the single-particle energies, we carry out the sums over m quantum numbers where possible, which yields

$$
\begin{aligned}
\bar{E}^{(2,2)} = &-\frac{1}{4} \sum_{\bar{c}\bar{c}'\bar{p}\bar{p}'} \sum_J \hat{j}^2 \frac{|{}^J H^{[2]}_{\bar{c}\bar{c}',\bar{p}\bar{p}'}|^2}{\epsilon^{\bar{p}\bar{p}'}_{\bar{c}\bar{c}'}} \\
&-\frac{1}{2} \sum_{\bar{c}\bar{c}'\bar{p}} \sum_J \hat{j}^2 \left(1 - \frac{1}{2j_v + 1}\right) \frac{|{}^J H^{[2]}_{\bar{c}\bar{c}',\bar{v}\bar{p}}|^2}{\epsilon^{\bar{v}\bar{p}}_{\bar{c}\bar{c}'}} \\
&-\frac{1}{4} \sum_{\bar{c}\bar{c}'} \sum_J \hat{j}^2 \left(1 - \frac{1}{2j_v + 1}\right)^2 \frac{|{}^J H^{[2]}_{\bar{c}\bar{c}',\bar{v}\bar{v}}|^2}{\epsilon^{\bar{v}\bar{v}}_{\bar{c}\bar{c}'}} \\
&-\frac{1}{2} \sum_{\bar{c}\bar{p}\bar{p}'} \sum_J \hat{j}^2 \frac{1}{2j_v + 1} \frac{|{}^J H^{[2]}_{\bar{v}\bar{c},\bar{p}\bar{p}'}|^2}{\epsilon^{\bar{p}\bar{p}'}_{\bar{v}\bar{c}}}
\end{aligned}
$$

$$-\sum_{\bar{c}\bar{p}}\sum_{J}\hat{J}^2\frac{1}{2j_v+1}\frac{|{}^{J}H^{[2]}_{\bar{v}\bar{c},\bar{v}\bar{p}}|^2}{\epsilon^{\bar{p}}_{\bar{c}}}+\frac{1}{2j_v+1}\sum_{cp\mu}\frac{|H_{vc,vp}|^2}{\epsilon^{\bar{p}}_{\bar{c}}}$$

$$-\frac{1}{2}\sum_{\bar{c}}\sum_{J}\hat{J}^2\frac{1}{2j_v+1}\frac{|{}^{J}H^{[2]}_{\bar{v}\bar{c},\bar{v}\bar{v}}|^2}{\epsilon^{\bar{v}}_{\bar{c}}}+\frac{1}{2j_v+1}\sum_{cv'\mu}\frac{|H^{[2]}_{vc,vv'}|^2}{\epsilon^{\bar{v}}_{\bar{c}}}. \tag{6.78}$$

Combined, the second terms on the last two lines cancel the first term in (6.75). Letting

$$n_{\bar{q}}=\begin{cases}1 & :\bar{q}\in C\\ \frac{1}{2j_v+1} & :\bar{q}=\bar{v}\\ 0 & :\text{else}\end{cases} \tag{6.79a}$$

$$\tilde{n}_{\bar{q}}=1-n_{\bar{q}} \tag{6.79b}$$

the (anti) occupation numbers, we can combine the first three terms to a single one with a sum over valence and unoccupied orbitals, denoted by summation indices $\bar{a}$. In order to also include the remaining terms, except the ones that cancel parts of the one-body diagram, we add two zeros:

$$\bar{E}^{(2,2)}=-\frac{1}{4}\sum_{\bar{c}\bar{c}'\bar{a}\bar{a}'}\sum_{J}\hat{J}^2\tilde{n}_{\bar{a}}\tilde{n}'_{\bar{a}}\frac{|{}^{J}H^{[2]}_{\bar{c}\bar{c}',\bar{a}\bar{a}'}|^2}{\epsilon^{\bar{a}\bar{a}'}_{\bar{c}\bar{c}'}}-\frac{1}{2}\sum_{\bar{c}\bar{p}\bar{p}'}\sum_{J}\hat{J}^2 n_{\bar{v}}\frac{|{}^{J}H^{[2]}_{\bar{v}\bar{c},\bar{p}\bar{p}'}|^2}{\epsilon^{\bar{p}\bar{p}'}_{\bar{v}\bar{c}}}$$

$$-\sum_{\bar{c}\bar{p}}\sum_{J}\hat{J}^2 n_{\bar{v}}\tilde{n}_{\bar{v}}\frac{|{}^{J}H^{[2]}_{\bar{v}\bar{c},\bar{v}\bar{p}}|^2}{\epsilon^{\bar{p}}_{\bar{c}}}-\sum_{\bar{c}\bar{p}}\sum_{J}\hat{J}^2 n^2_{\bar{v}}\frac{|{}^{J}H^{[2]}_{\bar{v}\bar{c},\bar{v}\bar{p}}|^2}{\epsilon^{\bar{p}}_{\bar{c}}}$$

$$-\frac{1}{2}\sum_{\bar{c}}\sum_{J}\hat{J}^2 n_{\bar{v}}\tilde{n}^2_{\bar{v}}\frac{|{}^{J}H^{[2]}_{\bar{v}\bar{c},\bar{v}\bar{v}}|^2}{\epsilon^{\bar{v}}_{\bar{c}}}-\frac{1}{2}\sum_{\bar{c}}\sum_{J}\hat{J}^2 n^2_{\bar{v}}(2-n_{\bar{v}})\frac{|{}^{J}H^{[2]}_{\bar{v}\bar{c},\bar{v}\bar{v}}|^2}{\epsilon^{\bar{v}}_{\bar{c}}}$$

$$+\frac{1}{2j_v+1}\sum_{cp\mu}\frac{|H_{vc,vp}|^2}{\epsilon^{\bar{p}}_{\bar{c}}}+\frac{1}{2j_v+1}\sum_{cv'\mu}\frac{|H^{[2]}_{vc,vv'}|^2}{\epsilon^{\bar{v}}_{\bar{c}}}. \tag{6.80}$$
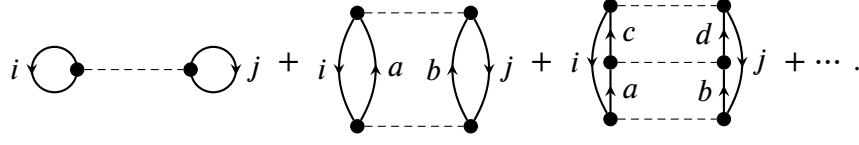
Thus, the second-order correction reads

$$\bar{E}^{(2)}=-\frac{1}{4}\sum_{\bar{u}\bar{u}'\bar{a}\bar{a}'}\sum_{J}\hat{J}^2(1-\delta^{\bar{u}\bar{u}'}_{\bar{v}\bar{v}})n_{\bar{u}}n'_{\bar{u}}\tilde{n}_{\bar{a}}\tilde{n}'_{\bar{a}}\frac{|{}^{J}H^{[2]}_{\bar{u}\bar{u}',\bar{a}\bar{a}'}|^2}{\epsilon^{\bar{a}\bar{a}'}_{\bar{u}\bar{u}'}}$$

$$-\sum_{\bar{c}\bar{a}}\sum_{J}\hat{J}^2 n^2_{\bar{v}}\left(1-\frac{n_{\bar{a}}}{2}\right)\frac{|{}^{J}H^{[2]}_{\bar{v}\bar{c},\bar{v}\bar{a}}|^2}{\epsilon^{\bar{a}}_{\bar{c}}}+\sum_{\substack{\bar{\imath}\bar{a}\\ j_i=j_a}}\hat{J}^2_i\frac{(\bar{H}^{[2]}_{\bar{\imath}\bar{v},\bar{a}\bar{v}})^2}{\epsilon^{\bar{a}}_{\bar{\imath}}}. \tag{6.81}$$

6.5. Brueckner-Bethe-Goldstone Theory

Medium-mass many-body methods like Coupled-Cluster theory and the In-Medium SRG can be interpreted as resummation of certain classes of Goldstone diagrams to infinite order. One

class of diagrams resummed by these methods is the class of particle-ladder diagrams

The expressions for these diagrams read

$$E_{\text{lad}} = \frac{1}{2} \sum_{ij} H^{[2]}_{ij,ij} + \frac{1}{4} \sum_{ijab} \frac{H^{[2]}_{ij,ab} H^{[2]}_{ab,ij}}{\epsilon_i + \epsilon_j - \epsilon_a - \epsilon_b}$$

$$+ \frac{1}{8} \sum_{ij} \sum_{abcd} \frac{H^{[2]}_{ij,ab} H^{[2]}_{ab,cd} H^{[2]}_{cd,ij}}{(\epsilon_i + \epsilon_j - \epsilon_a - \epsilon_b)(\epsilon_i + \epsilon_j - \epsilon_c - \epsilon_d)} + \cdots \qquad (6.82)$$

and, in general, the order-n particle-ladder diagram has two hole lines, n pairs of equivalent lines, and all energy denominators refer to the same two hole states i and j.

6.5.1. The G Matrix

Defining

$$\Gamma^{Q}_{pq,rs}(\omega) = \frac{Q_{pq,rs}}{\omega - \epsilon_p - \epsilon_q} \qquad (6.83)$$

with

$$Q_{pq,rs} = \begin{cases} \frac{1}{2}(\delta^{pq}_{rs} - \delta^{pq}_{sr}) : p,q \in \text{particles} \\ 0 : \text{else,} \end{cases} \qquad (6.84)$$

we rewrite E_{lad} in terms of a trace over matrix products:

$$E_{\text{lad}} = \frac{1}{2} \text{tr}_h \left(H^{[2]} + H^{[2]} \Gamma^{Q}(\epsilon_i + \epsilon_j) H^{[2]} + H^{[2]} \Gamma^{Q}(\epsilon_i + \epsilon_j) H^{[2]} \Gamma^{Q}(\epsilon_i + \epsilon_j) H^{[2]} + \cdots \right)$$

$$\equiv \frac{1}{2} \text{tr}_h G(\epsilon_i + \epsilon_j), \qquad (6.85)$$

where $\text{tr}_h A = \sum_{ij} A_{ij,ij}$ is a trace over hh states. The upright symbols denote matrices such that $(AB)_{12,34} = \sum_{pq} A_{12,pq} B_{pq,34}$.

The argument of the trace is a matrix generalization of a geometric series

$$G(\omega) = H^{[2]} \sum_{n=0}^{\infty} \left(\Gamma^{Q}(\omega) H^{[2]} \right)^n = \sum_{n=0}^{\infty} \left(H^{[2]} \Gamma^{Q}(\omega) \right)^n H^{[2]} = \left(1 - H^{[2]} \Gamma^{Q}(\omega) \right)^{-1} H^{[2]} \qquad (6.86)$$

and can be rewritten as the Bethe-Goldstone equation

$$G(\omega) = H^{[2]} + H^{[2]} \Gamma^{Q}(\omega) G(\omega) = H^{[2]} + G(\omega) \Gamma^{Q}(\omega) H^{[2]}. \qquad (6.87)$$
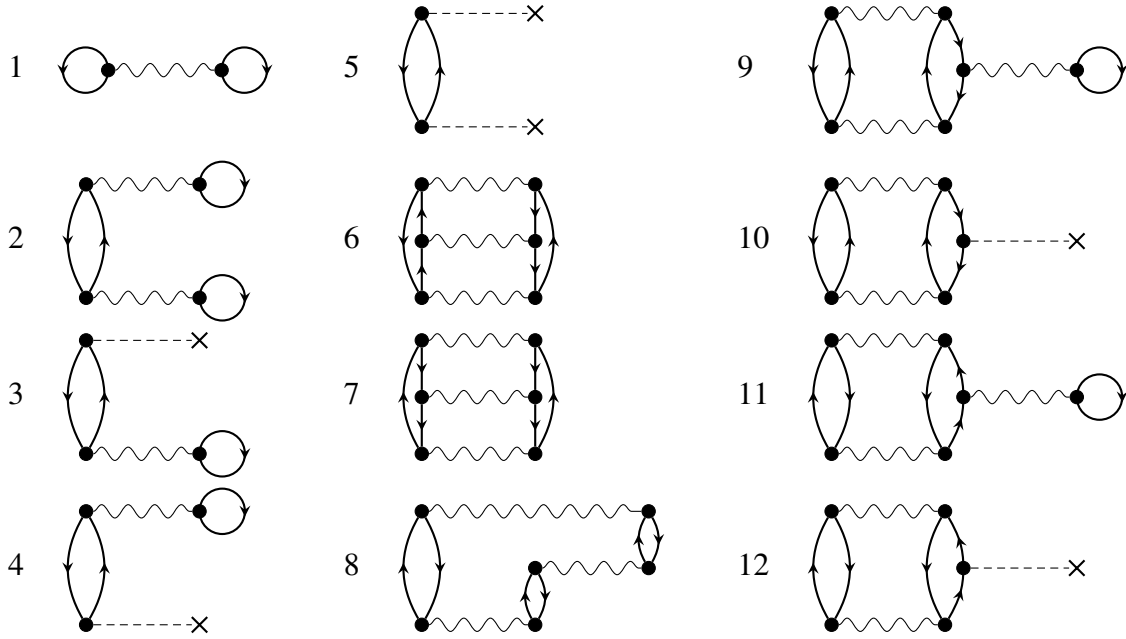
Figure 6.3.: Diagrams of the Brueckner-Bethe-Goldstone expansion up to third order in the G-matrix interaction. The third-order diagrams that vanish after the self-consistency procedure have been suppressed.

The matrix defined this way is Brueckner's G matrix. For infinite matter, where the unperturbed states are plane waves, (6.87) becomes an integral equation that describes two-particle scattering in the presence of the medium. The only difference to the Lippmann-Schwinger equation for the T matrix is the presence of a projection operator on particle states in the unperturbed propagator Γ^Q that implements the Pauli principle.

Since the G matrix resums particle ladders, it provides the basis of a more economical expansion of the correlation energy: by replacing insertions of the perturbation with G matrices, each Goldstone diagram in ordinary perturbation theory generates a whole class of perturbation diagrams. This so-called Brueckner-Bethe-Goldstone (BBG) expansion contains less diagrams at each order because no diagram can contain a particle ladder of G matrix interactions. These would resum the same class of perturbation-theory diagrams twice. Thus, the diagrams up to third order in the G matrix interaction (or one-body potential) are shown in fig. 6.3, with insertions of the G matrix denoted by wavy lines. One-body diagrams are included because the perturbation contains a one-body operator with matrix elements $H_{pq}^{[1]} - h_{pq}$ from the one-body part of the Hamiltonian and from the subtraction of the unperturbed Hamiltonian $\boldsymbol{H}_0$.

Analogous to the Hartree-Fock case, we can choose the unperturbed Hamiltonian such that it cancels the one-body part and work in its eigenbasis, using a Slater determinant of eigenstates as reference state. This removes diagram 3 to 5 from fig. 6.3 because these diagrams reference *ph* matrix elements of the diagonal one-body operator. Furthermore, we can use the unperturbed Hamiltonian to cancel the bubble diagrams 3 and 5 with the insertions of the one-body part in

diagrams 4 and 6. This requires that

$$h_{pq} = H_{pq}^{[1]} + \sum_i G_{pi,qi}(\omega),$$ (6.88)

which is the equation for the Hartree-Fock mean-field Hamiltonian with the two-body part of the interaction replaced by $G(\omega)$. These two requirements call for a self-consistent solution so that h_{pq} remains diagonal when calculated via (6.88) in its eigenbasis. The G matrix itself depends on both the eigenstates and eigenenergies through the Pauli-blocking propagator Γ^Q. The self-consistency procedure is the same as the Hartree-Fock procedure, but with an update of the G matrix after each iteration step.

6.5.2. Energy Dependence

There is another difference to the Hartree-Fock procedure: the G matrix depends on a starting energy ω that has to be chosen to cancel the bubble diagrams. For the hh matrix elements, we consider the energy denominator of the fourth-order Goldstone diagram of diagram 3,
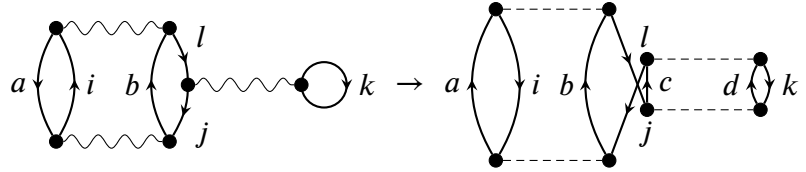

(6.89)

This diagram has an energy denominator of

$$\Delta_1 = (\epsilon_i + \epsilon_j - \epsilon_a - \epsilon_b)(\epsilon_i + \epsilon_j + \epsilon_k + \epsilon_l - \epsilon_a - \epsilon_b - \epsilon_c - \epsilon_d)(\epsilon_i + \epsilon_l - \epsilon_a - \epsilon_b),$$ (6.90)

which implies that the starting energy depends on all particle and hole indices and is impossible to cancel using (6.88) where ω can only depend on the two external indices and the hole that is summed over.

However, Brueckner and Goldman [BG60] noted that if one includes a fourth-order diagram with a different arrangement of interactions,
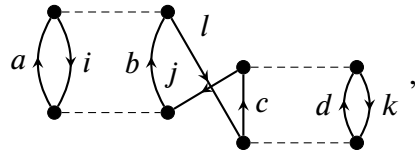
(6.91)

with the same interaction matrix elements and an energy denominator

$$\Delta_2 = (\epsilon_k + \epsilon_l - \epsilon_c - \epsilon_d)(\epsilon_i + \epsilon_j + \epsilon_k + \epsilon_l - \epsilon_a - \epsilon_b - \epsilon_c - \epsilon_d)(\epsilon_i + \epsilon_l - \epsilon_a - \epsilon_b),$$ (6.92)

we can sum both diagrams and the combination has a denominator

$$(\Delta_1^{-1} + \Delta_2^{-1})^{-1} = (\epsilon_i + \epsilon_j + \epsilon_k + \epsilon_l - \epsilon_a - \epsilon_b - \epsilon_c - \epsilon_d)(\epsilon_i + \epsilon_l - \epsilon_a - \epsilon_b)$$
$$\times [(\epsilon_k + \epsilon_l - \epsilon_c - \epsilon_d)^{-1} + (\epsilon_i + \epsilon_j - \epsilon_a - \epsilon_b)^{-1}]^{-1}$$

$$= (\epsilon_i + \epsilon_j - \epsilon_a - \epsilon_b)(\epsilon_k + \epsilon_l - \epsilon_c - \epsilon_d)(\epsilon_i + \epsilon_l - \epsilon_a - \epsilon_b), \tag{6.93}$$

where the middle term contains only energies of the particles participating in the ladder. This result has been generalized to all orders in perturbation theory [BBP63] so we can use it for G matrices. Moreover, by replacing interactions with G matrices, diagrams of the type shown in (6.91) generate a class of BBG diagrams that is exactly canceled by choosing the starting energy "on shell", i.e., $\omega = \epsilon_k + \epsilon_l$ [Day67]. These findings generalize to all bubble diagrams involving hole states, so that this cancellation carries over from Hartree-Fock perturbation theory.

For particle states, the situation is different. Consider, e.g., the second-order expansion of the middle G matrix in diagram 5,

$$\tag{6.94}$$

The energy denominator between the second and third interaction is $\epsilon_i + \epsilon_j + \epsilon_k - \epsilon_a - \epsilon_c - \epsilon_d$. Particles c and d belong to the ladder, thus the starting energy is $\omega = \epsilon_i + \epsilon_j + \epsilon_k - \epsilon_a$. The rearrangement of interactions used to arrive at (6.91) does not work here because it would turn the particle line b into a hole line.

Thus, we have to settle for an approximate cancellation. The particle energies are on average much larger than the hole energies so that replacing ϵ_a by ϵ_b makes little difference for the resulting energy denominators and the hole energies can be approximated by an average over all the occupied states. Hence, we might approximate the starting energy by $\omega = 2\epsilon_{\text{avg}} + \epsilon_k - \epsilon_b$ in order to achieve at least a partial cancellation of the bubble diagrams involving particle states.

Diagrams like diagram 2 occur during the self-consistency procedure but vanish for the self-consistent potential because the bubble contribution becomes diagonal and cannot connect particle and hole states. To get the appropriate starting energy, we consider the following third-order diagram generated by diagram 2:

$$\tag{6.95}$$

From this diagram, we can read off the starting energy as $\omega = \epsilon_i + \epsilon_j$. This choice cancels all diagrams where the first or last interaction is of bubble type.

In practice, we use a Hermitized on-shell modification of G,

$$\tilde{G}_{ij,kl} = \frac{1}{2}(G_{ij,kl}(\epsilon_i + \epsilon_j) + G_{ij,kl}(\epsilon_k + \epsilon_l)) \tag{6.96a}$$

$$\tilde{G}_{ai,jk} = G_{ai,jk}(\epsilon_j + \epsilon_k) \tag{6.96b}$$

$$\tilde{G}_{jk,ai} = G_{jk,ai}(\epsilon_j + \epsilon_k) \tag{6.96c}$$

$$\tilde{G}_{ai,bj} = \frac{1}{2}(G_{ai,bj}(2\epsilon_{\text{avg}} + \epsilon_i - \epsilon_a) + G_{ai,bj}(2\epsilon_{\text{avg}} + \epsilon_j - \epsilon_b)), \tag{6.96d}$$

which can be used in an ordinary Hartree-Fock calculation. The energy expectation value resulting from the Hartree-Fock calculation is identical to the value of diagram 1, which is why a truncation of the BBG expansion that includes only this diagram is called the Brueckner-Hartree-Fock (BHF) approximation. Our choice of unperturbed Hamiltonian causes all second-order diagrams as well as diagrams 9 and 10 to cancel exactly, diagrams 11 and 12 cancel in an approximate sense.

In nuclear matter, it can be shown that an expansion in terms of the number of G matrix interactions does not lead to an order-by-order decrease of contributions to the correlation energy. Instead, adding G matrices between particle states does not reduce the size of the contribution compared to the original diagram. Based on the assumption of a hard core in the potential, however, one can show that each new hole line suppresses the importance significantly [Bet65; Day67; RB67].

With this observation, the BBG expansion becomes an expansion in the number of hole lines. This comes with the drawback that, once there are three simultaneous particle lines in a diagram, we can generate a class of additional diagrams with the same number of hole lines by inserting G matrices between alternating lines, such that no two successive G matrices act on the same pair of particle lines. All diagrams from this class have the same importance and, thus, need to be considered simultaneously, which gives rise to a matrix equation (or, for nuclear matter, an integral equation) in three-body space [RB67]. For this reason, most works, including this one, use the BHF approximation in order to avoid the need to solve the three-body equation, which is computationally expensive.

The BHF calculation starts with a converged HF calculation. Since we cannot include explicit three-body forces at the BHF level, we include the 3N and YNN interaction via an NO2B approximation with respect to the HF determinant. In each iteration of the BHF procedure, we first calculate $\tilde{G}$ by (6.86) using the eigenstates and eigenenergies of the mean-field Hamiltonian that resulted from the previous iteration for the Pauli-blocking operator and single-particle energies. Then, we perform a regular HF iteration with the resulting $\tilde{G}$, which generates a new mean-field Hamiltonian with a new set of eigenstates and eigenenergies. We repeat the process until the one-body density, which characterizes the reference determinant, converges. Equation (6.86) is solved by full LU decomposition because functions that perform the decomposition and solve the linear system by forward and backward substitution are readily available. However, the starting energy depends on the matrix element that is calculated and each LU decomposition is used to solve exactly one linear system. Additionally, we do not need a high precision solution during the iteration, so an iterative solver may prove more efficient than the current approach.

6.5.3. Brueckner-Hartree-Fock in (Hyper-) Nuclear Matter

Due to its simplicity, the BHF approximation is very popular in calculations of the nuclear-matter equation of state [HH00; VP08; PHK+16; LHS+16; Has17]. Since infinite nuclear matter is translation invariant, the eigenstates of the unperturbed Hamiltonian have to be plane waves and only the single-particle energies can change during the self-consistency procedure. Due to momentum conservation, all diagrams involving one-body ph excitations, like diagram 2 in fig. 6.3, vanish.

To further simplify the calculation, one commonly uses additional approximations. In nuclear

matter, all single-particle states with momentum k larger than the Fermi momentum k_F are particle states. For an excitation not blocked by the Pauli-blocking operator $\mathbf{Q}$ inside the propagator we thus need to have $k_1 > k_F$ and $k_2 > k_F$. This separate dependence on both single-particle momenta implies that $\mathbf{Q}$ depends both on the relative and c.m. momentum of the excitation, which due to momentum conservation is the same as that of the two hole states that were excited, as well as the angle between them. The angular dependence prevents a partial-wave decomposition of the problem that dramatically reduces the dimension of the matrices involved in the calculation. Hence, the first approximation consists of replacing the Pauli-blocking operator $\mathbf{Q}$ by its value averaged over the angle between the relative and c.m. momentum. Also, the single-particle momenta k_1 and k_2 are replaced by their angle averages to remove the dependence on the direction of the relative momentum. The partial-wave decomposed G matrix $G^{(J)}_{\nu,\nu'}(k, k'; K, \omega)$ then depends only on the relative momenta, the c.m. momentum, and the starting energy.

Since the single-particle states are fixed, the single-particle potential $U(k_1)$ is the central object of the BHF calculation. The potential enters the G-matrix equation through the energy denominator, so it also has to be spherical in order to enable a partial-wave decomposition. It is determined by an integral over the momentum $\vec{k}_2$ of the second particle in the Fermi sea. The integral is rewritten in terms of the relative momentum $\vec{k}$, which together with $\vec{k}_1$ determines the c.m. momentum $\vec{K}$. The modulus of $\vec{K}$ itself depends on the angle between $\vec{k}_1$ and $\vec{k}$ so that different G matrices have to be constructed and evaluated for each integration point. In a final averaging step, K is replaced with its angle average, reducing the number of G matrices to be constructed to one per momentum shell.

All these approximations are uncontrolled and introduce uncertainties in addition to the truncation of the BBG expansion at the BHF level. Convergence of the hole-line expansion for nuclear matter has been demonstrated only recently by explicit calculation of the three-hole line diagrams, which turn out to be a few percent of the BHF contribution [LLC$^+$17].

The situation for hypernuclear matter is less clear because no such explicit calculation has been done. Since the SRG-induced YNN terms are strong and three-particle diagrams that can contain a genuine three-body interaction first appear at the three-hole-line level, we naively expect a much stronger effect than in ordinary nuclear matter. The SRG makes the three-body terms explicit so we can include them via the NO2B approximation. We, therefore, expect our calculations for finite systems to receive a smaller correction at the three-hole-line level than calculations with bare YN interactions.

6.6. A Survey of Medium-Mass Hypernuclei

Aside from the work presented in [HXW$^+$17], the BHF results shown in the following section are the first of their kind employing a modern approach with RG-evolved interactions. In contrast to that work, we additionally use three-body forces in the NO2B approximation with respect to the HF ground state (cf. section 6.3). To ensure that the BHF approximation gives reasonable estimates of nuclear ground-state energies, we benchmark it against perturbative and nonperturbative approaches. We compare the BHF results to energy estimates from second- and third-order many-body perturbation theory (MBPT), denoted by MBPT(2) and MBPT(3)
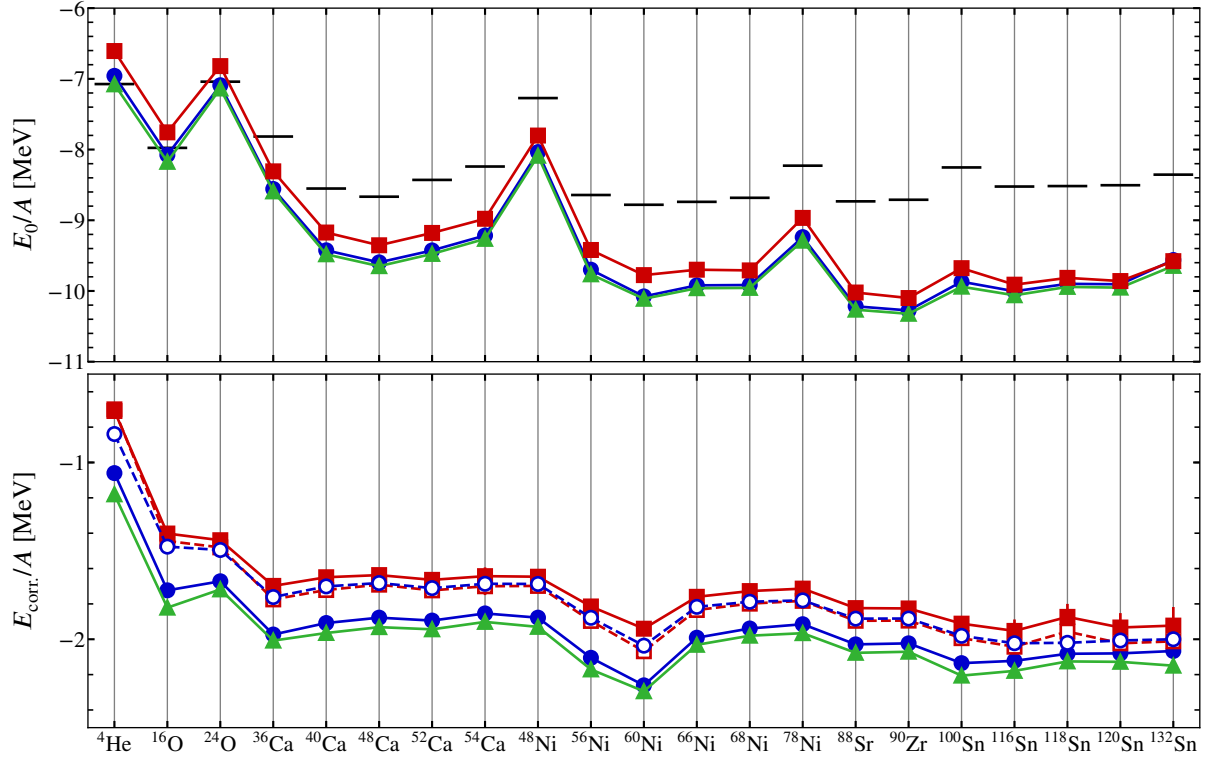
Figure 6.4.: Comparison of ground-state and correlation energies of closed-subshell nuclei up to the tin region, obtained with different many-body methods. Blue circles mark results from 2nd- (open) and 3rd-order (filled) perturbation theory. Red squares denote results stemming from a resummation of particle-particle ladder diagrams (open), or the full BHF calculation (filled). The green triangles mark CR-CC(2,3) coupled-cluster results [BLC^{+}14]. The 3rd-order perturbation theory results taken from [TLB^{+}16], experimental data (black bars) is taken from [WAW^{+}12].

in the following, and to a Coupled-Cluster calculation with a sophisticated triples correction, the so-called CR-CC(2,3) truncation [PW05; RGP09; BLC$^+$14]. The calculations employ a three-nucleon interaction with a reduced regulator cutoff $\Lambda_{3N} = 400\,\text{MeV/c}$. This interaction is fitted to reproduce the triton β-decay half life and the ^{4}He binding energy [RCL$^+$14], and induces less 4N terms during the SRG evolution than the 3N interaction used in the previous calculations. The first step in all methods is a HF calculation, in which we include all single-particle HO states up to $e_{\max} = 12$, i.e., 13 major shells. Three-nucleon forces are included with an $E_{3\max}$ truncation. The BHF and MBPT(2) calculations are performed at $\Omega = 20\,\text{MeV}$ and $E_{3\max} = 14$, the MBPT(3) and CR-CC(2,3) results were taken from [TLB$^+$16] and [BLC$^+$14], respectively, and were performed at $\Omega = 24\,\text{MeV}$ and $E_{3\max} = 18$.

The upper panel of fig. 6.4 shows the binding energy per nucleon for a range of closed-subshell nuclei up to the tin region, computed within CR-CC, MBPT(3), and the BHF approximation. The CR-CC and third-order results are practically indistinguishable on this scale and reproduce the experimental values up to oxygen to a good degree while the BHF results are slightly underbound. This indicates that the effect of correlations beyond those included in CR-CC(2,3) are small whereas those at third order MBPT not included in the BHF approximation are not negligible.

Going to heavier nuclei, all results show increasing overbinding compared to the experimental values. Since this is observed with multiple methods, we can attribute this behavior to the Hamiltonian. Apart from that, the general trend along the isotopic chains is reproduced. The BHF results show an almost constant shift with respect to the other methods, except for the tin isotopes, where the BHF result is much closer to the other methods. This is an artifact of the lower $E_{3\max}$ truncation of the three-nucleon interaction matrix elements: already at the HF level, the energies for $E_{3\max} = 14$ and $E_{3\max} = 18$ differ by $38\,\text{MeV}$ in ^{132}Sn, with the $E_{3\max} = 14$ interaction providing more attraction.

To compare the finer details, we consider the correlation energy $E_{\text{corr.}} \equiv E_0 - E_{\text{HF}}$ in the lower panel of fig. 6.4. Here, we also show results of MBPT(2) and a summation of particle-particle ladders up to infinite order, which is effected by calculating the $\tilde{G}$ matrix in HF basis and taking its expectation value with respect to the HF ground state. For this SRG-evolved interaction, the correlation energy is a relatively small effect of the order of $2\,\text{MeV}$ per nucleon, compared to the 8 to $10\,\text{MeV}$ total binding energy per nucleon. The difference in correlation energy between the CR-CC and MBPT(3) results is visible but small, which implies that most correlations are already captured at the third order of the perturbation expansion. The MBPT(2) results have a few hundred keV less correlation energy per nucleon, the ladder summation has only a very small effect, which is repulsive in helium and oxygen and becomes slightly attractive in heavier nuclei. The full self-consistency procedure of the BHF method yields a repulsive correction compared to MBPT(2).

This difference can be explained from perturbation theory: In [TLB$^+$16], the authors showed that, for SRG-evolved interactions, the MBPT expansion converges order by order. Additionally, they decomposed the third-order energy correction into contributions from each of the three diagrams (cf. fig. 6.2). Their result was that the particle-particle diagram has a very small repulsive contribution that is counteracted by the hole-hole and particle-hole diagrams, which has the largest contribution of the three diagrams. The ladder summation neglects both the hole-hole and particle-particle contribution, missing the cancellation and the additional attraction

provided by them. The BHF self-consistency additionally changes the single-particle basis away from the HF minimum, and, since the HF contribution dominates the binding energy, even a change of a few percent has a large effect on the correlation energy.

The smallness of the particle-particle ladder diagrams is actually desirable. The resummation was historically used to renormalize the hard core of the baryon-baryon interaction because matrix elements of the bare interaction between states with finite amplitudes inside the core radius are ill defined. The ladders resum the short-range correlations induced by the hard core and yield finite matrix elements. In our approach, the SRG evolution tames these short-range correlations, so the smallness of the ladder contribution is natural. In conclusion, it might be more appropriate for SRG-evolved interactions to resum also the hole-hole and particle-particle ladder diagrams in order to capture the cancellations and additional attractive contributions. This has the additional advantage that the resummation contains all third-order diagrams, and should yield correlation energies similar to MBPT(3).

The BHF approximation yields reasonable ground-state energies in closed-shell nuclei. In the next step, we compute the ground-state energies of the associated hypernuclei. For this, we employ the equal-filling approximation for the computation of the HF and BHF one-body densities. The YNN terms are included in NO2B approximation with truncation $E_{3\text{max}} = 10$. We also perform MBPT(2) calculations including the noncanonical corrections derived in section 6.4.3. The results are shown in fig. 6.5. Since these are the first calculations for medium-mass hypernuclei with a chiral Hamiltonian, where the only approximation is the use of the equal-filling approximation when calculating expectation values,[5] we cannot compare to other, more sophisticated methods, like in the nucleonic case. Instead, we compare the BHF to the MBPT(2) and HF results, checking their internal consistency.

The ground-state energies per nucleon show a similar behavior to the nuclei discussed before: the HF energy provides the bulk of the binding energy; the MBPT(2) and BHF corrections are almost indistinguishable and contribute of the order of 2 MeV per nucleon. The only remarkable case is $^{13}_{\Lambda}$C, where the correction is larger than expected from the surrounding hypernuclei, and there is a visible difference between the BHF and MBPT(2) results. This can be attributed to the weak subshell closure in ^{12}C that enhances corrections due to low-lying particle states. In $^{133}_{\Lambda}$Sn, convergence with respect to the single-particle truncation has not yet been achieved. We also omitted the hypernucleus $^{119}_{\Lambda}$Sn because the HF calculation predicts the nucleonic parent to be an open-shell nucleus, so we can neither use the MBPT(2) formulae from section 6.4.3 nor the equal-filling approximation to compute the BHF energy. We compare the calculation results to an extended Bethe-Weizsäcker mass formula (BWMH) [SCB06] that includes strange baryons and reproduces the known hyperon separation energies with a root-mean-square error of 1.4 MeV. The overbinding seen in heavier hypernuclei is, again, a feature of the nucleonic Hamiltonian.

Contrasting the difference between the HF and the MBPT(2) and BHF results in the ground-state energies, the calculated hyperon separation energies are practically independent of the calculation method if induced YNN terms are included. This means that the binding of the hyperon is essentially achieved by the mean field, and the correlations included in MBPT(2)

---

[5]Previous works like [Hal93] or [Ban81] use HO states as single-particle states and neglect the presence of the hyperon in the Pauli-blocking operator.
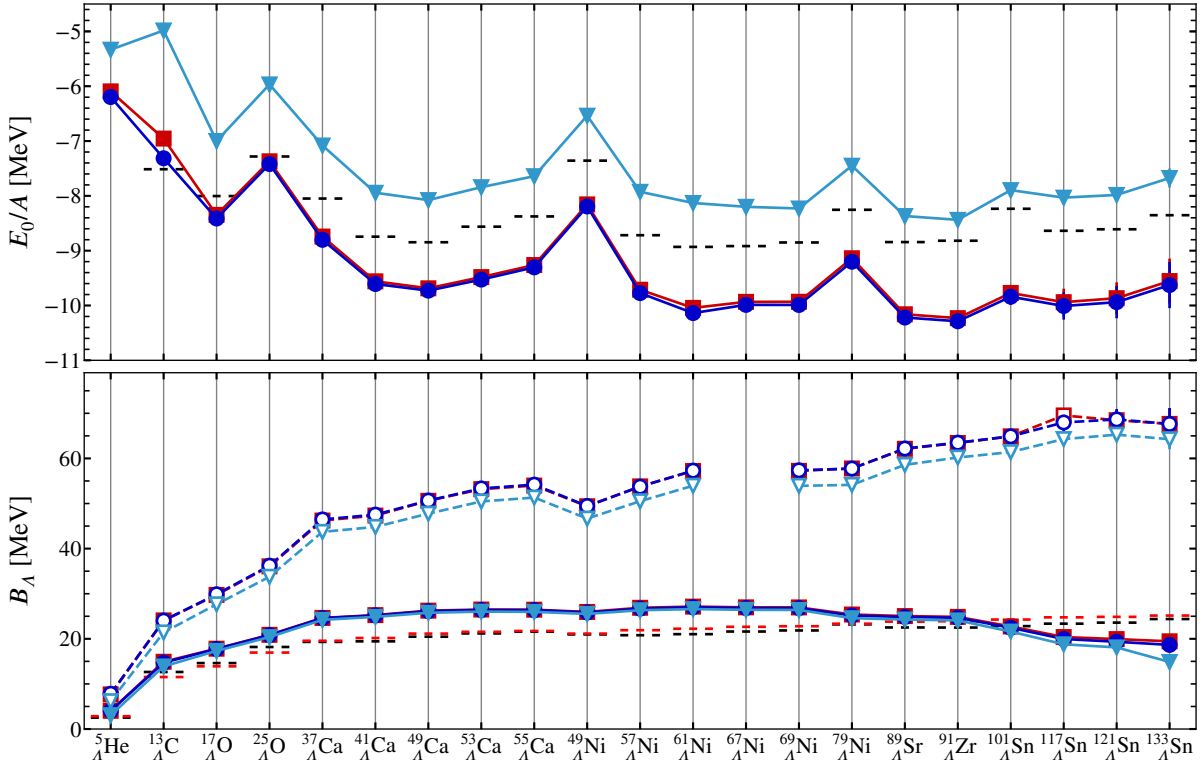
Figure 6.5.: Ground-state energy per nucleon (upper panel) and hyperon separation energies (lower panel) of closed-subshell hypernuclei up to the tin region, obtained from HF (light blue triangles), 2nd-order perturbation theory (blue circles), and BHF calculations (red squares). The filled (hollow) symbols are computed with (without) induced YNN terms. Calculations are for the $\Lambda = 700$ MeV/c cutoff, $\Omega = 20$ MeV, and include 11 major shells. The black dashed bars mark predictions by the semiempirical BWMH mass formula [SCB06], the red ones in the lower panel result from a simple fit of experimental hyperon separation energies to a quadratic polynomial in $A^{-2/3}$ (cf. fig. 6.6).

and BHF are unaffected by the presence of the hyperon. Thus, the correlation energy in the parent nucleus cancels the one in the hypernucleus when calculating the separation energy. This picture might change in more sophisticated calculations, but assuming that the third-order correction is suppressed to a similar degree in hypernuclei and ordinary nuclei, the change can only be relatively small.

Omitting the induced YNN terms has a large effect on the separation energies, as expected from our NCSM calculations. In $^{67}_{\Lambda}$Ni, the evolved YN interaction changes the order of the neutron orbits so that the nucleonic core becomes open-shell, which is why we omitted the results from the plot. The hyperon separation energies show a lot more variation along the isotopic chains than those with induced YNN terms, which increase only very slowly beyond oxygen. Also, correlation effects play a small role and shift the separation energies to slightly higher values compared to the HF calculation. Still, there is essentially no difference between the MBPT(2) and the BHF result.

For comparison, we show the separation energies predicted by the BWMH and by a quadratic polynomial in $A^{-2/3}$ fitted to the known hyperon separation energies. Both predictions roughly agree on the shown scale, but our results with induced YNN terms are overbound by 20 %, as expected from previous calculations. The calculations without induced terms predict separation energies that are too high by a factoer of two to three.

The behavior of the separation energies including YNN terms is peculiar in the isotopes beyond nickel. The separation energy becomes lower with increasing mass, contrary to the experimental values that show an increasing trend roughly linear in $A^{-2/3}$ with a separation energy of approximately 28 MeV in infinite nuclear matter [Dav05; SCB06]. The discrepancy might be an artifact of the truncation of the YNN or 3N matrix elements, although we would expect more repulsion when increasing this truncation, not less. Another possibility is that the LO YN interaction starts to break down at this point and higher-order terms in the chiral EFT expansion become important. This has to be investigated in the future.

We can compare the results obtained from the BHF calculations to experiment and to Quantum Monte-Carlo results. The left panel of fig. 6.6 shows our calculations with and without induced YNN terms as a function of $A^{-2/3}$ (up to the nickel isotopic chain), compared to experimental separation energies across the hypernuclear chart. The experimental trends are reproduced with a slight offset by the BHF calculation with induced YNN terms while the one without shows a very different scaling with respect to particle number. Both the experimental values and the BHF results are well described by a quadratic polynomial fit that can be used to (approximately) extract the depth of the hyperonic potential well in infinite nuclear matter at saturation density that is generated by the YN interaction. The extrapolation of the experimental values yields 29.8(4) MeV while our results predict a well depth of 35.1(4) MeV. Thus, the overbinding of 20 % that is observed in our IT-NCSM calculations for light hypernuclei carries over to the medium-mass regime.

The right panel of fig. 6.6 shows Quantum Monte-Carlo results from [LPG14] using a scheme with only Λ hyperons. The calculations with only ΛN interactions behave even more extreme than our calculations without YNN terms. The hyperon separation energies scale almost linear with A and show little signs of saturation in larger systems. Addition of a ΛNN interaction fitted such that a variational calculation reproduces the separation energies in $^{5}_{\Lambda}$He and $^{17}_{\Lambda}$O (ΛNN(I)) changes the behavior drastically and brings the calculation much closer to experiment. When
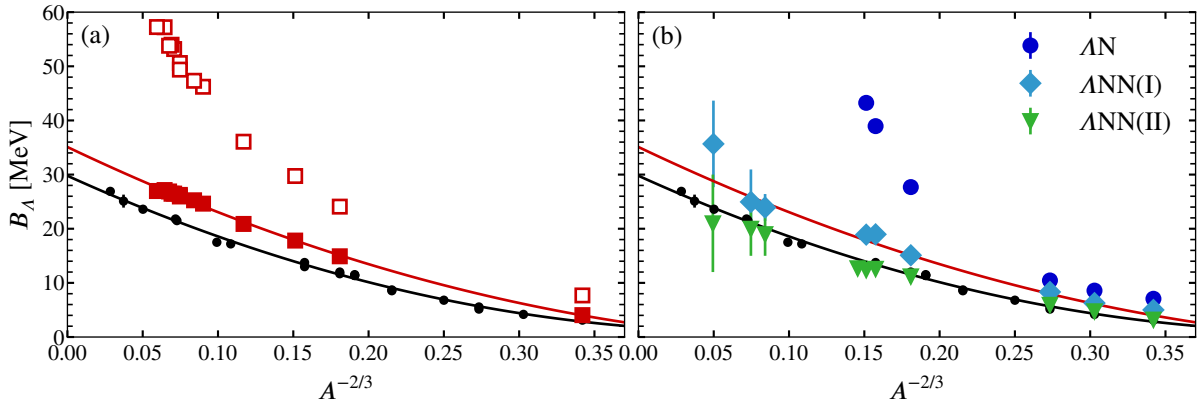
Figure 6.6.: (a) The same calculations as in fig. 6.5, as a function of particle number $A^{-2/3}$. Experimental separation energies (black dots) taken from [GHM16]. The lines are quadratic polynomials fitted to the experimental data (black) and to the calculation results (red). (b) Quantum Monte-Carlo results from [LPG14], for a pure ΛN interaction (blue) and the same interaction plus two parameter sets of a ΛNN interaction (light blue and green). The fit polynomials from (a) are repeated for comparison.

the ΛNN interaction is further adjusted to reproduce the same separation energies in the full Auxiliary-Field Diffusion Monte-Carlo calculation (ΛNN(II)), the calculations are on top of the experimental values within error bars. Our results with YNN terms lie between the two ΛNN curves, which is surprisingly close given that our YN interaction was fitted to $A \leq 3$ data only.

Approaches rooted in perturbation theory seem to be a good starting point for studying medium-mass hypernuclei. The first results presented here look promising, but there are still some uncertainties regarding truncations of the three-body interaction matrix elements and the correlations that are taken into account by the many-body method. This success may prompt developments of higher-order MBPT or more sophisticated methods like the Coupled-Cluster approach or the In-Medium SRG [HLK17]. A remaining challenge is the open-shell nature of singly-strange hypernuclei. In part, this challenge can be overcome by employing the equal-filling approximation, but this approximation introduces additional (small) uncertainties and may generate terms that are not present in the original theory, e.g., the noncanonical corrections in MBPT.

7. Neutron-Star Structure and the Hyperon Puzzle

Neutron stars belong to the most extreme objects in the universe [Lat12]. As remnants formed in core-collapse supernovae of massive stars, they concentrate more than a solar mass ($M_\odot$) in a compact object with a radius of only a dozen kilometers. They can also possess very high magnetic fields or have surface rotation speeds of a significant fraction of the speed of light. However, their compactness poses a challenge to observation and most neutron stars are observed as pulsars, which emit electromagnetic radiation towards earth at regular intervals. To date, only a few properties of pulsars can be measured, but the recent observation of a binary neutron-star merger in both gravitational waves and across the electromagnetic spectrum [AAA+17] has opened up new opportunities to pin down neutron-star structure.

Since they are composed of strongly interacting matter, studying neutron stars can also shed light on properties of nuclei and vice versa. One of the central objects of interest here is the equation of state $\varepsilon(p)$ of neutron-star matter that determines the energy density as a function of pressure. Using the general-relativistic equations for hydrostatic equilibrium, the Tolman-Oppenheimer-Volkoff (TOV) equations [OV39],

$$\frac{\mathrm{d}p}{\mathrm{d}r} = -\frac{G}{c^2}\frac{(p + \varepsilon(p))(m + 4\pi r^3 p/c^2)}{r(r - 2Gm/c^2)}, \tag{7.1a}$$

$$\frac{\mathrm{d}m}{\mathrm{d}r} = 4\pi r^2 \frac{\varepsilon(p)}{c^2}, \tag{7.1b}$$

with pressure p, enclosed mass m and radius r, we can determine the total mass M and radius R of the neutron star, given a central pressure p_c. By varying p_c and integrating the coupled system of ODEs from $m = r = 0$ to the point where the pressure $p(r)$ vanishes, we can map out the relation between the mass and the radius of neutron stars as it is predicted by the equation of state (EoS). Figure 7.1 illustrates the mass-radius relation for three related EoS models [LLG+15] that assume neutrons and Λ hyperons as degrees of freedom and are fitted to Quantum Monte-Carlo (QMC) results.[1] The mass-radius relation is multi-valued for a range of masses below a critical mass M_{max} (cf. the blue curve). Only one of the solutions corresponds to a minimum of the free energy of the system and is, therefore, stable while the other one is unstable. Above M_{max}, there are no solutions, which means that there is a maximum neutron-star mass that the EoS can support.

The masses of many pulsars are known, some with high precision [Lat12]. This puts constraints on the EoS, because the largest observed neutron-star mass rules out all EoS that predict

---

[1] The results there differ from those presented here. Although it is not stated in the paper, that work probably uses a more sophisticated treatment of the low- and high-density EoS as described in [GCR12; GCR+14], which increases the radius, but has nearly no effect on the maximum mass.
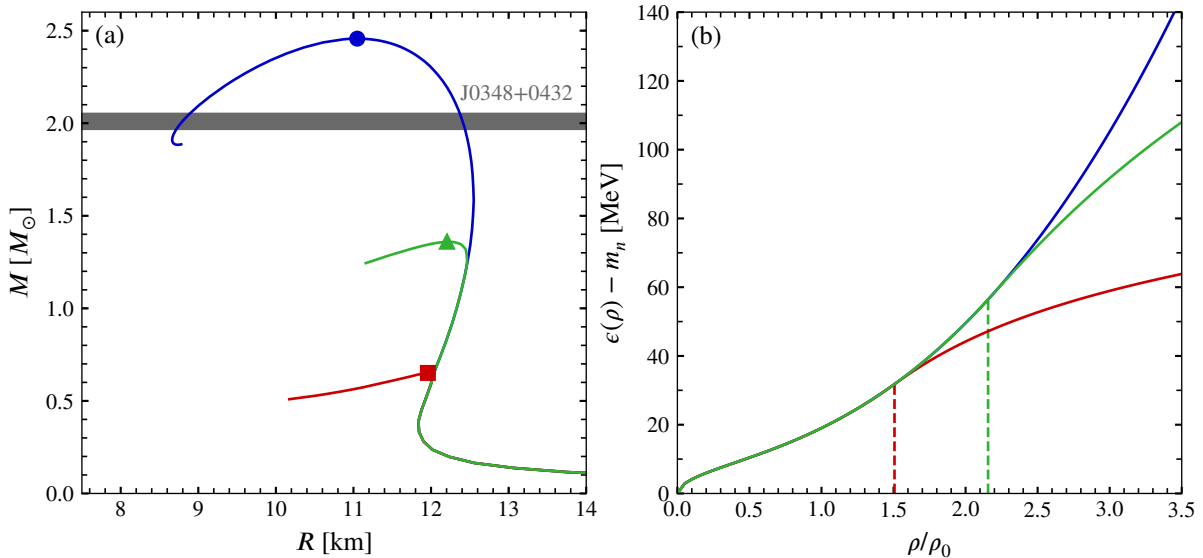
Figure 7.1.: (a) Mass-radius relation and (b) energy per particle as a function of density for three equations of state derived from QMC calculations [LLG$^+$15]. The first EoS (blue line) represents a stiff equation with only neutrons. The second one (red line) extends the first by adding Λ hyperons. The third EoS (green line) includes additional repulsive three-body terms. The symbols in panel (a) mark the maximum-mass points, the mass of a $2M_\odot$ pulsar is indicated by the shaded band [AFW$^+$13]. Vertical dashed lines in panel (b) mark the threshold density above which hyperons are present, $\rho_0 = 0.16\,\text{fm}^{-3}$ is the nuclear saturation density.

a lower maximum mass. Recent observations of neutron stars with precisely-known masses of approximately $2M_\odot$ [DPR$^+$10; AFW$^+$13] exclude some EoS [OHK$^+$17].

Equations of state can be modeled in many ways, using different degrees of freedom and methods to treat the many-body problem (see [OHK$^+$17] for some examples). In the following, we consider baryons as degrees of freedom. In a microscopic approach, we use a given baryon-baryon interaction and compute the energy per particle $\epsilon(\{\rho_i\})$ for given densities $\{\rho_i\}$ of each particle species using, e.g., a BHF calculation or QMC methods. The composition, i.e., the fractions of neutrons, protons, and hyperons, is fixed by imposing weak-interaction equilibrium and charge conservation. Thus, the proton fraction is fixed by requiring that $\mu_p + \mu_e - \mu_n = 0$, where the $\mu_i = \partial(\rho\epsilon)/(\partial\rho_i)$ are the chemical potentials for each particle species i, and ρ is the total density.

If we add Λ hyperons as degrees of freedom, their chemical potential is tied to that of the neutrons, $\mu_n = \mu_\Lambda$ [BG97; LLG$^+$15]. Due to the rest-mass difference, this condition cannot be fulfilled for low neutron chemical potentials and no hyperons are present. Hyperons only start to appear at higher densities once the increase in energy caused by adding a neutron to the system outweighs the increase caused by the addition of a hyperon.

With many EoS that include hyperons, the pressure as a function of density rises much slower once hyperons appear compared to the behavior without hyperons—the EoS becomes softer. This softening leads to a decrease in the maximum neutron-star mass. Calculations with different

kinds of interactions, which describe the available YN data, find that the maximum mass is lowered from above $2M_{\odot}$ to below the typical neutron-star mass of 1.4 to $1.5M_{\odot}$ [GHM16].

This is the so-called hyperon puzzle in neutron-star physics. There is no principle that forbids the appearance of hyperons at higher densities, but any calculation finds maximum masses far below the observed ones. The red and green curves in fig. 7.1 illustrate this: the EoS corresponding to them are modifications of the EoS of the blue curve that add Λ hyperons with no (red curve) and moderate (green curve) three-body repulsion.

In the microscopic description we consider here, the hyperon puzzle is addressed by adding a repulsive three-body force between hyperons and nucleons [VLP$^+$11; LLG$^+$15]. For the BHF calculations presented in [VLP$^+$11], the three-body terms raise the maximum mass by $0.2M_{\odot}$, but the resulting range of 1.3 to $1.6M_{\odot}$ is still far away from the observational constraint. The QMC calculations (using the same ΛNN interaction as those mentioned in the previous chapter) from [LLG$^+$15] have a very strong three-body repulsion that shifts the appearance of hyperons to beyond the densities required for a $2M_{\odot}$ neutron star. The ΛNN terms are added *ad hoc*, without an underlying theory that justifies their presence or provides a means of calculating them.

At least for the latter type of calculation in a scheme with only Λ hyperons, we can provide that justification. From our investigations in chapters 4 and 5, we know that a unitary decoupling of the Λ and Σ hyperons, which transforms to a scheme with only Λ hyperons, induces strong repulsive YNN terms. We can, thus, use the SRG to continuously shift between the initial scheme with Σ hyperons and no three-body force and the final scheme without Σs and a strong repulsive three-body force while keeping all observables invariant.

Our calculations for medium-mass hypernuclei with induced YNN terms, which, neglecting convergence issues, gives the same result as a calculation using the bare Hamiltonian without any YNN terms, follows the QMC results that include the ΛNN terms. Neglecting the YNN terms has a similar effect as neglecting the ΛNN terms in the QMC calculation. Hence, we can conclude that the ΛNN terms are the equivalent of the induced YNN terms in our calculation. The strong repulsive three-body force required to bring the QMC results into agreement with experimental data is, therefore, a natural consequence of integrating out the Σ hyperons from the scheme. In a scheme with Σ hyperons, a large part of the required repulsion is generated through Λ-Σ conversion in the two-body interaction.

The situation for BHF calculations like those shown in [VLP$^+$11] is less clear, because these include the Σs. However, the calculation starts from a bare Hamiltonian, and the G matrix prescription renormalizes the interaction by resumming the particle-particle ladders. Some of the missing three-hole-line terms generate genuine three-body interactions, which may be seen as analog to the induced terms in our scheme. Our BHF calculations for medium-mass hypernuclei use evolved interactions and the ladder summation is hardly distinguishable from the MBPT(2) result because the renormalization is done during the SRG evolution, and the induced three-body terms are explicitly included. The G matrix, thus, needs to renormalize the interaction to a much smaller degree, and higher-order terms are likely small.

8. Conclusions

Nuclear structure theory has entered an era where precision *ab initio* calculations of nuclear properties are possible. The goal of this work is to transfer these advances to hypernuclei in order to calculate their properties and to better constrain the YN interaction.

The first step on this path was establishing a Hamiltonian for a hypernuclear system. Here, a marked difference to nucleonic calculations is that the particles comprising the hypernucleus have significantly different masses, necessitating the introduction of a mass term in the Hamiltonian. The YN interaction itself is weaker than the NN interaction so that there is no bound two-body state. Also, the mass difference between the lightest hyperon multiplets, Λ and Σ, is so small that we have to consider interaction terms that convert between ΛN and ΣN states. This leads to a coupled particle-channel problem, where eigenstates of the Hamiltonian do not have definite numbers of protons, neutrons, and individual hyperons; only their total number, charge, and strangeness is conserved.

A Hamiltonian based on NN, 3N, and YN interactions derived from chiral effective field theory was the starting point of the following investigations. The nucleonic part is well tested in *ab initio* calculations, for the YN part we use a leading-order interaction because the available YN scattering data alone is insufficient to constrain the parameters of subleading interaction terms.

The next step was a unitary SRG transformation of the Hamiltonian that accelerates model-space convergence of the subsequent IT-NCSM calculation. Without such a transformation, the model-space sizes that are required for sufficiently converged calculations are only feasible for very light systems. We considered the transformation of a general baryon-baryon interaction in two-body space, using a generator that prediagonalizes the Hamiltonian in momentum space. We demonstrated that the SRG evolution of the YN interaction achieves the desired prediagonalization, but also suppresses the Λ-Σ conversion terms.

The first focus of this work was the IT-NCSM for hypernuclei. We developed all extensions necessary for including hyperons, like handling model spaces with different particle content or generalizing the importance-truncation scheme. While these extensions were mostly straight-forward, they required rederiving a large part of the calculation infrastructure, like the formulae for transforming the interaction from relative to single-particle coordinates, due to the unequal rest masses.

Calculations with unevolved YN interactions showed the ability of the method to get reliable predictions for excitation energies, which can be confronted with experimental data. The overall agreement was remarkable for a leading-order YN interaction. However, other observables like hyperon-separation energies or absolute energies were inaccessible due to lack of model-space convergence. The SRG evolution of the YN interaction should overcome this obstacle and provide converged energies, but the evolution in two-body space creates strong induced YNN terms leading to a strong overbinding in calculations that do not include them. These YNN

terms are generated by the suppression of Λ-Σ conversion terms, which we noticed before.

Thus, the second focus was the calculation and inclusion of these induced terms. To this end, we created a framework for representing the Hamiltonian in HO states with respect to relative Jacobi coordinates for the three-body system. Instead of diagonalizing, we used this framework to solve the SRG flow equation in three-body space in order to extract the genuine induced YNN terms. After transforming them from Jacobi to single-particle coordinates, these terms can be used in an IT-NCSM calculation. All these steps require considerable implementation effort and computational resources. The SRG framework presented here is flexible enough for not only computing induced YNN, but also induced YYN and YYY interactions.

We subsequently confirmed that including the induced YNN terms removes the flow-parameter dependence of the absolute energies and we revisited the hypernuclei considered before with the bare YN interaction. There, we showed that, in addition to the improved rate of convergence of absolute energies, the excitation spectra are unchanged compared to the bare interaction, while they were slightly distorted in calculations with only the evolved YN interaction.

The improved rate of convergence allowed us to compute absolute binding energies and hyperon-separation energies in the p shell. This is the first time that these observables can be tackled in an *ab initio* framework with a chiral Hamiltonian. We used these advances to study two physics cases: the neutron drip line in light hypernuclei and core-polarization effects in $^{6}_{\Lambda\Lambda}$He.

Naively, one would expect that, since the hyperon provides additional binding energy to the hypernucleus for each added nucleon, the neutron drip line of a given isotope is pushed towards higher neutron numbers. We found that, contrary to this expectation, the hypernuclear neutron drip line is unchanged compared to the nucleonic one in helium and lithium isotopes. The hyperon does not provide additional binding energy to the neutrons beyond the $N = 8$ shell closure.

Next, we explored the structure of double-Λ hypernuclei. In a double-Λ hypernucleus, there are two effects that affect the separation energy of hyperons compared to a single-Λ one: the YY interaction and additional core-polarization effects, which arise because the two hyperons modify the nucleonic core compared to the core of the single-Λ hypernucleus. We studied the latter and we find that the residual effect of the YY interaction has to be very small, comparing the calculation without YY interaction to the experimental $\Delta B_{\Lambda\Lambda}$ value.

The final two chapters focused on heavier systems. Based on a spherical Hartree-Fock scheme for hypernuclei and the equal-filling approximation, we implemented second-order many-body perturbation theory and the Brueckner-Hartree-Fock approximation to Brueckner-Bethe-Goldstone theory for closed-shell nuclei and hypernuclei with a closed-shell nucleonic parent. We showed that the BHF approximation does not improve upon MBPT(2) for SRG-evolved interactions, and that there is some missing correlation energy in closed-shell nuclei that is captured only in higher-order calculations like MBPT(3) or CR-CC(2,3). In hypernuclei, we found that correlations have only a small effect on the hyperon-separation energy, and we saw that, in calculations without induced YNN terms, the hyperon-separation energies are much too high and continue to increase with particle number instead of saturating. When we included the induced terms, we got the same slight overbinding as in IT-NCSM calculations for light hypernuclei.

The findings from the previous chapters—the emergence of strong repulsive YNN terms in

the SRG due to suppression of the Λ-Σ conversion, and the continuing increase of hyperon-separation energies with particle number when these terms are not accounted for—lead to an explanation of the hyperon puzzle in neutron-star physics. Microscopic calculations in a scheme with only Λ hyperons need strongly repulsive ΛNN terms in order to generate an equation of state stiff enough to support a $2\,M_\odot$ neutron star. The ΛNN terms are of phenomenological origin. The SRG evolution of the YN interaction integrates out the Σ hyperons, creating a Λ-only scheme. During this evolution, repulsive ΛNN terms are generated naturally from suppressing the Λ-Σ conversion, reducing or eliminating the need for an initial three-body interaction. The closeness of the calculated hyperon-separation energies in medium-mass hypernuclei to experimental data shows that the main discrepancy is a slight overbinding, which is rooted partly in the YN interaction and, hence, can probably be reduced by tuning its parameters. A contribution to the overbinding might also stem from the nucleonic Hamiltonian, which systematically overbinds medium-mass nuclei and yields overly compact nuclear wave functions.

The achievements of this work open up a wide range of possibilities for further progress in *ab initio* hypernuclear physics. The first frontier is the study and improvement of YN interactions: in this work, we used the LO interaction because its parameters can be determined from hypernuclear data alone. However, there is an NLO interaction, fitted in part to NN data, and we can compare its predictions to those made with the LO interaction and confront both with experimental data. Also, we can relax the *ab initio* constraints and tune the cutoff and LECs of the LO interaction to achieve a better overall description of the available data on *p*-shell hypernuclei. This "*ab exitu*" approach can be used to achieve the accuracy necessary to guide experimental efforts in that region.

The second frontier is the move towards *ab initio* calculations for heavier hypernuclei. On this path, we have already made some progress by implementing the HF method on which more sophisticated many-body methods can be built. Also, we have shown that the correlation energy in MBPT(2) and BHF is small compared to the HF energy, so the many-body problem is likely perturbative. A possible next step is the implementation of MBPT(3) to test that assumption. If a low-order treatment is sufficient, we have a computationally cheap yet precise method for accessing ground-state energies of hypernuclei with closed-shell nucleonic parents. In the long run, a many-body method able to access open-shell hypernuclei, like an extension of the Multi-Reference In-Medium SRG, will provide access to the full hypernuclear chart.

For the solution of the hyperon puzzle, we need an *ab initio* many-body method to compute the equation of state of hypernuclear matter; not with only Λs and neutrons, but also with protons and Σs. While a direct diagonalization may prove too difficult, we could extend perturbative approaches or the In-Medium SRG to extract the ground state of matter in a box with periodic boundary conditions. With such a framework, we can explicitly demonstrate that the induced YNN terms increase the maximum neutron-star mass beyond the current bound set by observation.

A. Basic Ingredients

This work makes heavy use of objects that mediate between different angular-momentum coupling schemes, such as the Wigner 6j and 9j symbols, and coordinate systems. This appendix provides short summaries of their properties, symmetries and use cases.

A.1. Clebsch-Gordan Coefficients

The Clebsch-Gordan coefficients are the basic building blocks dealing with angular-momentum coupling. They provide the overlap

$$\langle j_1 m_1, j_2 m_2 | (j_1 j_2) J M \rangle = \begin{pmatrix} j_1 & j_2 \\ m_1 & m_2 \end{pmatrix} \begin{matrix} J \\ M \end{matrix} \tag{A.1}$$

between states in uncoupled and coupled schemes. All other angular-momentum-coupling objects can be expressed in terms of sums over products of Clebsch-Gordan coefficients, although there are often more efficient ways of calculating these objects. The coefficients are chosen real-valued and are only nonvanishing if $m_1 + m_2 = M$ and the triangular condition $|j_1 - j_2| \leq J \leq j_1 + j_2$ hold.

The Clebsch-Gordan coefficients possess the symmetries [VMK88, sec. 8.4.3]

$$\begin{pmatrix} j_1 & j_2 \\ m_1 & m_2 \end{pmatrix} \begin{matrix} J \\ M \end{matrix} = (-1)^{J - j_1 - j_2} \begin{pmatrix} j_2 & j_1 \\ m_2 & m_1 \end{pmatrix} \begin{matrix} J \\ M \end{matrix} \tag{A.2}$$

$$= (-1)^{J - j_1 - j_2} \begin{pmatrix} j_1 & j_2 \\ -m_1 & -m_2 \end{pmatrix} \begin{matrix} J \\ -M \end{matrix} \tag{A.3}$$

$$= (-1)^{j_1 - m_1} \frac{\hat{J}}{\hat{j}_2} \begin{pmatrix} j_1 & J \\ m_1 & -M \end{pmatrix} \begin{matrix} j_2 \\ -m_2 \end{matrix} \tag{A.4}$$

$$= (-1)^{j_1 - m_1} \frac{\hat{J}}{\hat{j}_2} \begin{pmatrix} J & j_1 \\ M & -m_1 \end{pmatrix} \begin{matrix} j_2 \\ m_2 \end{matrix} \tag{A.5}$$

$$= (-1)^{j_2 + m_2} \frac{\hat{J}}{\hat{j}_1} \begin{pmatrix} J & j_2 \\ -M & m_2 \end{pmatrix} \begin{matrix} j_1 \\ -m_1 \end{matrix} \tag{A.6}$$

$$= (-1)^{j_2 + m_2} \frac{\hat{J}}{\hat{j}_1} \begin{pmatrix} j_2 & J \\ -m_2 & M \end{pmatrix} \begin{matrix} j_1 \\ m_1 \end{matrix} \tag{A.7}$$

and are related to the Wigner 3jm symbols via [VMK88, eq. 8.1(12)]

$$\begin{pmatrix} j_1 & j_2 \\ m_1 & m_2 \end{pmatrix} \begin{matrix} J \\ M \end{matrix} = (-1)^{j_1 - j_2 + M} \hat{J} \begin{pmatrix} j_1 & j_2 & J \\ m_1 & m_2 & -M \end{pmatrix}, \tag{A.8}$$

which possess a higher degree of symmetry and are therefore preferred in some calculations. Here, we introduced the short notation $\hat{j}_i \equiv \sqrt{2j_i + 1}$ for the multiplicity factors.

The coefficients also have two orthogonality relations:

$$\sum_{JM} \begin{pmatrix} j_1 & j_2 & J \\ m_1 & m_2 & M \end{pmatrix} \begin{pmatrix} j_1 & j_2 & J \\ m'_1 & m'_2 & M \end{pmatrix} = \delta^{m_1 m_2}_{m'_1 m'_2} \tag{A.9}$$

$$\sum_{m_1 m_2} \begin{pmatrix} j_1 & j_2 & J \\ m_1 & m_2 & M \end{pmatrix} \begin{pmatrix} j_1 & j_2 & J' \\ m_1 & m_2 & M' \end{pmatrix} = \delta^{JM}_{J'M'}, \tag{A.10}$$

with shorthands $\delta^{ab}_{a'b'} \equiv \delta^a_{a'} \delta^b_{b'}$.

A.2. Wigner 6j Symbols

The 6j symbols mediate the change of coupling order of three angular momenta. They provide the overlaps [VMK88, sec. 9.1.1]

$$\langle [(j_1 j_2) j_{12}, j_3] J M | [j_1, (j_2 j_3) j_{23}] J' M' \rangle = \delta^{JM}_{J'M'} (-1)^{j_1 + j_2 + j_3 + J} \hat{j}_{12} \hat{j}_{23} \begin{Bmatrix} j_1 & j_2 & j_{12} \\ j_3 & J & j_{23} \end{Bmatrix} \tag{A.11}$$

$$\langle [(j_1 j_2) j_{12}, j_3] J M | [(j_1 j_3)_{13} j_{13}, j_2] J' M' \rangle = \delta^{JM}_{J'M'} (-1)^{j_2 + j_3 + j_{12} + j_{13}} \hat{j}_{12} \hat{j}_{13} \begin{Bmatrix} j_2 & j_1 & j_{12} \\ j_3 & J & j_{13} \end{Bmatrix} \tag{A.12}$$

$$\langle [j_1, (j_2 j_3) j_{23}] J M | [(j_1 j_3)_{13} j_{13}, j_2] J' M' \rangle = \delta^{JM}_{J'M'} (-1)^{j_1 + J + j_{23}} \hat{j}_{13} \hat{j}_{23} \begin{Bmatrix} j_1 & j_3 & j_{13} \\ j_2 & J & j_{23} \end{Bmatrix}, \tag{A.13}$$

where, in the second and third equation, we explicitly specified the coupling particles to remove the ambiguity of coupling particles 1 and 2 from coupling 1 and 3. The subscript is omitted where the coupling order is obvious.

The 6j symbol is invariant under transposition of any two columns and under simultaneous interchange of the upper and lower argument in two columns.[1] It is nonvanishing only if the upper row fulfills a triangular condition, which, combined with the symmetries, gives four independent conditions.

There are two orthogonality relations:

$$\sum_{j_{12}} \hat{j}_{12} \hat{j}_{23} \begin{Bmatrix} j_1 & j_2 & j_{12} \\ j_3 & J & j_{23} \end{Bmatrix} \begin{Bmatrix} j_1 & j_2 & j_{12} \\ j_3 & J & j'_{23} \end{Bmatrix} = \delta^{j_{23}}_{j'_{23}} \tag{A.14}$$

$$\sum_{j_{23}} \hat{j}_{12} \hat{j}_{23} \begin{Bmatrix} j_1 & j_2 & j_{12} \\ j_3 & J & j_{23} \end{Bmatrix} \begin{Bmatrix} j_1 & j_2 & j'_{12} \\ j_3 & J & j_{23} \end{Bmatrix} = \delta^{j_{12}}_{j'_{12}}. \tag{A.15}$$

---

[1]There are additional Regge symmetries, so that groups of 144 symbols are related [VMK88, sec. 9.4.2].

A.3. Wigner 9j Symbols

The 9j symbols mediate the change of coupling order of four angular momenta. They provide the overlaps [VMK88, sec. 9.1.1]

$$\langle[(j_1j_2)j_{12},(j_3j_4)j_{34}]JM\,|\,[(j_1j_3)_{13}j_{13},(j_2j_4)_{24}j_{24}]J'M'\rangle$$

$$= \delta^{JM}_{J'M'}\hat{j}_{12}\hat{j}_{34}\hat{j}_{13}\hat{j}_{24}\begin{Bmatrix} j_1 & j_2 & j_{12} \\ j_3 & j_4 & j_{34} \\ j_{13} & j_{24} & J \end{Bmatrix} \tag{A.16}$$

$$\langle[(j_1j_2)j_{12},(j_3j_4)j_{34}]JM\,|\,[(j_1j_4)_{14}j_{14},(j_2j_3)_{23}j_{23}]J'M'\rangle$$

$$= \delta^{JM}_{J'M'}(-1)^{j_3+j_4-j_{34}}\hat{j}_{12}\hat{j}_{34}\hat{j}_{14}\hat{j}_{23}\begin{Bmatrix} j_1 & j_2 & j_{12} \\ j_4 & j_3 & j_{34} \\ j_{14} & j_{23} & J \end{Bmatrix} \tag{A.17}$$

$$\langle[(j_1j_3)_{13}j_{13},(j_2j_4)_{24}j_{24}]JM\,|\,[(j_1j_4)_{14}j_{14},(j_2j_3)_{23}j_{23}]J'M'\rangle$$

$$= \delta^{JM}_{J'M'}(-1)^{j_3-j_4-j_{23}+j_{24}}\hat{j}_{13}\hat{j}_{24}\hat{j}_{14}\hat{j}_{23}\begin{Bmatrix} j_1 & j_3 & j_{13} \\ j_4 & j_2 & j_{24} \\ j_{14} & j_{23} & J \end{Bmatrix}. \tag{A.18}$$

The 9j symbol is invariant under exchange of rows and columns (matrix transpose), an odd permutation of rows or columns incurs a phase of $(-1)^\sigma$, where σ is the sum of all entries. It is nonvanishing only if each row and column fulfills a triangular condition.

There are two orthogonality relations:

$$\sum_{j_{13}j_{24}} \hat{j}_{13}\hat{j}_{24}\begin{Bmatrix} j_1 & j_2 & j_{12} \\ j_3 & j_4 & j_{34} \\ j_{13} & j_{24} & J \end{Bmatrix}\begin{Bmatrix} j_1 & j_2 & j'_{12} \\ j_3 & j_4 & j'_{34} \\ j_{13} & j_{24} & J \end{Bmatrix} = \delta^{j_{12}j_{34}}_{j'_{12}j'_{34}} \tag{A.19}$$

$$\sum_{j_{12}j_{34}} \hat{j}_{13}\hat{j}_{24}\begin{Bmatrix} j_1 & j_2 & j_{12} \\ j_3 & j_4 & j_{34} \\ j_{13} & j_{24} & J \end{Bmatrix}\begin{Bmatrix} j_1 & j_2 & j_{12} \\ j_3 & j_4 & j_{34} \\ j'_{13} & j'_{24} & J \end{Bmatrix} = \delta^{j_{13}j_{24}}_{j'_{13}j'_{24}}. \tag{A.20}$$

A.4. Harmonic-Oscillator Brackets

The Harmonic-Oscillator or Talmi-Moshinsky Brackets (HOBs) are the overlaps of HO product states with respect to two different coordinate systems

$$\langle\!\langle NL,nl\,|\,n_1l_1,n_2l_2:\Lambda\rangle\!\rangle_d \equiv \langle(NL(\vec{R}),nl(\vec{r}))\Lambda\lambda|(n_1l_1(\vec{r}_1),n_2l_2(\vec{r}_2))\Lambda\lambda\rangle, \tag{A.21}$$

where the coordinate systems $\vec{R},\vec{r}$ and $\vec{r}_1,\vec{r}_2$ are related by a symmetric orthogonal transformation[2]

$$\begin{pmatrix} \vec{R} \\ \vec{r} \end{pmatrix} = \begin{pmatrix} \sqrt{\frac{d}{1+d}} & \sqrt{\frac{1}{1+d}} \\ \sqrt{\frac{1}{1+d}} & -\sqrt{\frac{d}{1+d}} \end{pmatrix}\begin{pmatrix} \vec{r}_1 \\ \vec{r}_2 \end{pmatrix}. \tag{A.22}$$

---

[2]This is the definition by Kamuntavičius et al. [KKB⁺01], which provides a high degree of symmetry. There are other conventions, also regarding the ordering of the coordinates.

A. Basic Ingredients

The HOBs are independent of the angular momentum projection and have the following symmetries [KKB$^+$01]:

$$\langle\!\langle NL, nl \mid n_1l_1, n_2l_2 : \Lambda \rangle\!\rangle_d = \langle\!\langle n_1l_1, n_2l_2 \mid NL, nl : \Lambda \rangle\!\rangle_d \tag{A.23}$$

$$= (-1)^{L+l_2} \langle\!\langle n_2l_2, n_1l_1 \mid nl, NL : \Lambda \rangle\!\rangle_d \tag{A.24}$$

$$= (-1)^{\Lambda-L} \langle\!\langle n_2l_2, n_1l_1 \mid NL, nl : \Lambda \rangle\!\rangle_{1/d} \tag{A.25}$$

$$= (-1)^{\Lambda-l_1} \langle\!\langle n_1l_1, n_2l_2 \mid nl, NL : \Lambda \rangle\!\rangle_{1/d}. \tag{A.26}$$

Furthermore, the HOBs conserve the sum of HO quanta $E + e = e_1 + e_2$ or $2N + L + 2n + l = 2n_1 + l_1 + 2n_2 + l_2$. The orthogonal transformation between the coordinates is parametrized by a single nonnegative parameter d. The case $d = 0$ is an exchange of coordinates $(\vec{R}, \vec{r} = \vec{r}_2, \vec{r}_1)$, $d \to \infty$ is a reversal of the second coordinate $(\vec{R}, \vec{r} = \vec{r}_1, -\vec{r}_2)$. In both cases the HOBs are trivial:

$$\langle\!\langle NL, nl \mid n_1l_1, n_2l_2 : \Lambda \rangle\!\rangle_{d=0} = (-1)^{L+l-\Lambda} \delta^{NL}_{n_2l_2} \delta^{nl}_{n_1l_1} \tag{A.27}$$

$$\langle\!\langle NL, nl \mid n_1l_1, n_2l_2 : \Lambda \rangle\!\rangle_{d\to\infty} = (-1)^{l} \delta^{NL}_{n_1l_1} \delta^{nl}_{n_2l_2}. \tag{A.28}$$

B. Additional Intrinsic Operators for the NCSM

B.1. Intrinsic Kinetic Energy

The intrinsic kinetic energy T_{int} can be calculated in the following way: neglecting the operator nature of the quantities considered, we express the total mass and the center-of-mass coordinate and momentum

$$M = \sum_{i=1}^{A} m_i, \quad \vec{R} = \frac{1}{M} \sum_{i=1}^{A} m_i \vec{r}_i \quad \text{and} \quad \vec{P} = \sum_{i=1}^{A} \vec{p}_i \tag{B.1}$$

in terms of the absolute single-particle coordinates $\vec{r}_i$, momenta $\vec{p}_i$ and masses m_i. The coordinates $\vec{\rho}_i$ and momenta $\vec{\pi}_i$ of the particles relative to the center of mass then become

$$\vec{\rho}_i = \vec{r}_i - \vec{R} = \vec{r}_i - \frac{1}{M} \sum_{j=1}^{A} m_j \vec{r}_j \tag{B.2}$$

$$\vec{\pi}_i = m_i \dot{\vec{\rho}}_i = \vec{p}_i - \frac{m_i}{M} \sum_{j=1}^{A} \vec{p}_j = \vec{p}_i - \frac{m_i}{M} \vec{P}. \tag{B.3}$$

Additionally, we have, for each pair of particles i and j, the relative coordinates and momenta in their center-of-mass system:

$$\vec{r}_{ij} = \vec{r}_j - \vec{r}_i \tag{B.4}$$

$$\vec{q}_{ij} = \mu_{ij} \dot{\vec{r}}_{ij} = \mu_{ij}(\dot{\vec{r}}_j - \dot{\vec{r}}_i) = \mu_{ij}\left(\frac{\vec{p}_j}{m_j} - \frac{\vec{p}_i}{m_i} \right), \tag{B.5}$$

where $\mu_{ij} = m_i m_j / (m_i + m_j)$ is the reduced mass of particles i and j. Using these coordinates, we write the intrinsic kinetic energy as

$$T_{\text{int}} = \sum_{i=1}^{A} \frac{\pi_i^2}{2m_i} = \sum_i \frac{1}{2m_i} \left(\vec{p}_i - \frac{m_i}{M} \sum_j \vec{p}_j \right)^2$$

$$= \sum_i \frac{p_i^2}{2m_i} - \frac{1}{M} \sum_{ij} \vec{p}_i \cdot \vec{p}_j + \sum_{ijk} \frac{m_i}{2M^2} \vec{p}_j \cdot \vec{p}_k$$

$$= \sum_i \frac{p_i^2}{2m_i} - \frac{1}{2M} \sum_{ij} \vec{p}_i \cdot \vec{p}_j$$

$$= \sum_i \frac{p_i^2}{2m_i} - \frac{1}{2M} \sum_{ij} m_i m_j \frac{\vec{p}_i \cdot \vec{p}_j}{m_i m_j}, \tag{B.6}$$

where we used the definition of the total mass M to eliminate sums over particle masses. The scalar product can be expressed in terms of squared momenta:

$$\frac{\vec{p}_i \cdot \vec{p}_j}{m_i m_j} = \frac{p_i^2}{2m_i^2} + \frac{p_j^2}{2m_j^2} - \frac{1}{2}\left(\frac{\vec{p}_j}{m_j} - \frac{\vec{p}_i}{m_i}\right)^2 = \frac{p_i^2}{2m_i^2} + \frac{p_j^2}{2m_j^2} - \frac{q_{ij}^2}{2\mu_{ij}^2}. \tag{B.7}$$

Inserting this into (B.6) and simplifying, we get

$$T_{\text{int}} = \sum_i \frac{p_i^2}{2m_i} - \frac{1}{2} \sum_i \left(\frac{p_i^2}{2m_i} + \frac{p_i^2}{2m_i}\right) + \frac{1}{2M} \sum_{ij} \frac{m_i m_j}{2\mu_{ij}^2} q_{ij}^2$$

$$= \frac{1}{2} \sum_{ij} \frac{m_i + m_j}{M} \frac{q_{ij}^2}{2\mu_{ij}} = \sum_{i<j} \frac{m_i + m_j}{M} T_{ij,\text{rel}}, \tag{B.8}$$

where $T_{ij,\text{rel}} = q_{ij}^2/(2\mu_{ij})$ is the relative kinetic energy in the two-body system of particles i and j.

B.2. Radii

One of the most readily accessible groups of observables that are also of experimental interest are nuclear radii. The mean-square radius is defined as

$$R_{\text{MS}}^2 = \frac{1}{A} \sum_{i=1}^A (\vec{r}_i - \vec{R})^2, \tag{B.9}$$

where the $\vec{r}_i$ are the absolute coordinates of the particles and

$$\vec{R} = \frac{1}{M} \sum_{j=1}^A m_j \vec{r}_j \tag{B.10}$$

is their center of mass. Inserting (B.10) into (B.9), suppressing the summation limits for brevity, yields

$$R_{\text{MS}}^2 = \frac{1}{A} \sum_i \left(\vec{r}_i - \frac{1}{M} \sum_j m_j \vec{r}_j\right)^2$$

$$= \frac{1}{A} \sum_i r_i^2 - \frac{2}{AM} \sum_{ij} m_j \vec{r}_i \cdot \vec{r}_j + \frac{1}{AM^2} \sum_{ijk} m_j m_k \vec{r}_j \cdot \vec{r}_k$$

$$= \frac{1}{A} \sum_i r_i^2 - \frac{2}{AM} \sum_{ij} m_j \vec{r}_i \cdot \vec{r}_j + \frac{1}{M^2} \sum_{jk} m_j m_k \vec{r}_j \cdot \vec{r}_k. \tag{B.11}$$

The scalar products $\vec{r}_i \cdot \vec{r}_j$ can be expressed in terms of squared distances:

$$\vec{r}_i \cdot \vec{r}_j = \frac{1}{2}r_i^2 + \frac{1}{2}r_j^2 - \frac{1}{2}r_{ij}^2, \tag{B.12}$$

where $\vec{r}_{ij} = \vec{r}_j - \vec{r}_i$. Inserting this into (B.11) we get

$$
\begin{aligned}
R_{\mathrm{MS}}^2 &= \frac{1}{A}\sum_i r_i^2 - \frac{1}{AM}\sum_{ij} m_j(r_i^2 + r_j^2 - r_{ij}^2) + \frac{1}{2M^2}\sum_{jk} m_j m_k(r_j^2 + r_k^2 - r_{jk}^2) \\
&= \frac{1}{AM}\sum_{ij} m_j r_{ij}^2 - \frac{1}{2M^2}\sum_{ij} m_i m_j r_{ij}^2 = \frac{1}{2M}\sum_{ij}\left(\frac{2m_j}{A} - \frac{m_i m_j}{M}\right) r_{ij}^2 \\
&= \frac{1}{M}\sum_{i<j}\left(\frac{m_i + m_j}{A} - \frac{m_i m_j}{M}\right) r_{ij}^2,
\end{aligned} \tag{B.13}
$$

which can be rewritten as the application of Slater rules to a two-body operator

$$\boldsymbol{R}_{\mathrm{MS}}^2 = \left(\frac{\boldsymbol{m}_1 + \boldsymbol{m}_2}{AM} - \frac{\boldsymbol{m}_1 \boldsymbol{m}_2}{M^2}\right) \boldsymbol{r}_{12}^2. \tag{B.14}$$

Note that the total mass $\boldsymbol{M}$ is also an operator, but as it is diagonal in the basis we use, an eigenvalue relation can be used prior to evaluating the Slater rules for $\boldsymbol{R}_{\mathrm{MS}}^2$. The actual two-body operator that is evaluated when computing matrix elements between basis states is therefore different for each particle content of these states.

This derivation can be extended to calculate separate mean-square radii for each particle species. However, care has to be taken because the particle numbers N_χ are not conserved. We introduce a projection operator

$$\boldsymbol{P}_i^\chi = \begin{cases} \boldsymbol{1} & \text{if particle } i \text{ is of species } \chi \\ 0 & \text{else} \end{cases} \tag{B.15}$$

$$\boldsymbol{n}_\chi = \sum_{i=1}^{A} \boldsymbol{P}_i^\chi \tag{B.16}$$

and write the particle mean-square radius as

$$R_{\chi,\mathrm{MS}}^2 = \frac{1}{\langle \boldsymbol{n}_\chi \rangle}\sum_i P_i^\chi(\vec{r}_i - \vec{R})^2. \tag{B.17}$$

The derivation follows the same steps as for the species-agnostic mean-square radius and yields

$$R_{\chi,\mathrm{MS}}^2 = \frac{1}{M\langle \boldsymbol{n}_\chi \rangle}\sum_{i<j}\left(m_i P_j^\chi + m_j P_i^\chi - n_\chi \frac{m_i m_j}{M}\right) r_{ij}^2 \tag{B.18}$$

and, noting that $\boldsymbol{n}_\chi$ can also be directly evaluated using an eigenvalue relation, we rewrite this as an application of Slater rules to the two-body operator

$$\boldsymbol{R}_{\chi,\mathrm{MS}}^2 = \left(\frac{\boldsymbol{m}_1 \boldsymbol{P}_2^\chi + \boldsymbol{m}_2 \boldsymbol{P}_1^\chi}{\langle \boldsymbol{n}_\chi \rangle M} - \frac{n_\chi}{\langle \boldsymbol{n}_\chi \rangle}\frac{\boldsymbol{m}_1 \boldsymbol{m}_2}{M^2}\right) \boldsymbol{r}_{12}^2. \tag{B.19}$$

The expectation values of these mean-square radii can also be used to calculate a nuclear charge radius by convolving the particle densities with the charge distributions of each particle species. Since we are only interested in the mean-square charge radius, it is sufficient to assume isotropic distributions with variance $\langle R^2_{\chi,\mathrm{ch}} \rangle$ for the charge densities. These variances are determined from experiment or from theoretical calculations.

The total charge distribution

$$\rho(\vec{r}) = \sum_\chi \rho_\chi(\vec{r}) \tag{B.20}$$

is a superposition of charge distributions $\rho_\chi(\vec{r})$ for each particle species, which are in turn convolutions of the respective particle densities $\rho^{\mathrm{sp}}_\chi(\vec{r})$ with their charge densities $\rho^{\mathrm{ch}}_\chi(\vec{r})$. Let the charge distributions be chosen such that the charge of the respective particle is

$$Q_\chi = \int \mathrm{d}\vec{r}\, \rho^{\mathrm{ch}}_\chi(\vec{r}) \tag{B.21}$$

and let the particle densities be normalized to the respective particle number expectation value. Then, the total mean-square charge radius reads

$$\begin{aligned}
\langle R^2_{\mathrm{ch,MS}} \rangle &= \frac{1}{Q} \int \mathrm{d}\vec{r}\, r^2 \sum_\chi \rho_\chi(\vec{r}) = \frac{1}{Q} \sum_\chi \int \mathrm{d}\vec{r} \int \mathrm{d}\vec{r}'\, r^2 \rho^{\mathrm{sp}}_\chi(\vec{r}') \rho^{\mathrm{ch}}_\chi(\vec{r} - \vec{r}') \\
&= \frac{1}{Q} \sum_\chi \int \mathrm{d}\vec{r} \int \mathrm{d}\vec{r}'\, (\vec{r} + \vec{r}')^2 \rho^{\mathrm{sp}}_\chi(\vec{r}') \rho^{\mathrm{ch}}_\chi(\vec{r}) \\
&= \frac{1}{Q} \sum_\chi \int \mathrm{d}\vec{r} \int \mathrm{d}\vec{r}'\, (r^2 + 2\vec{r} \cdot \vec{r}' + r'^2) \rho^{\mathrm{sp}}_\chi(\vec{r}') \rho^{\mathrm{ch}}_\chi(\vec{r}) \\
&= \frac{1}{Q} \sum_\chi \langle n_\chi \rangle \left(\langle R^2_{\chi,\mathrm{ch}} \rangle + Q_\chi \langle R^2_{\chi,\mathrm{MS}} \rangle \right),
\end{aligned} \tag{B.22}$$

where we used the substitution $\vec{r} \mapsto \vec{r} + \vec{r}'$. The scalar product term vanishes because the charge distributions are isotropic and, consequently, the integrand is odd in $\vec{r}$.

B.3. Center-of-Mass Hamiltonian

As discussed in section 4.3 we lift the degeneracy of eigenstates of the intrinsic Hamiltonian with respect to the center-of-mass state by adding a HO Hamiltonian

$$H_{\mathrm{c.m.}} = \frac{1}{2M} P^2 + \frac{1}{2} M \Omega^2 R^2 - \frac{3}{2}\Omega \tag{B.23}$$

acting on the center-of-mass coordinate and momentum

$$\vec{R} = \frac{1}{M} \sum_{i=1}^{A} m_i \vec{r}_i, \tag{B.24}$$

$$\vec{P} = \sum_{i=1}^{A} \vec{p}_i, \tag{B.25}$$

with single-particle coordinates $\vec{r}_i$ and momenta $\vec{p}_i$. The offset is introduced so that the ground state has zero energy. Using relation (B.7),

$$\frac{\vec{p}_i \cdot \vec{p}_j}{m_i m_j} = \frac{p_i^2}{2m_i^2} + \frac{p_j^2}{2m_j^2} - \frac{q_{ij}^2}{2\mu_{ij}^2},$$

(B.26)

for the single-particle momenta $\vec{p}_i, \vec{p}_j$, this Hamiltonian can be separated into zero-, one- and two-body parts:

$$\frac{1}{2M}P^2 + \frac{1}{2}M\Omega^2 R^2 - \frac{3}{2}\Omega$$

$$= \frac{1}{2M}\sum_{i=1}^{A}\sum_{j=1}^{A}\left(\vec{p}_i \cdot \vec{p}_j + \Omega^2 m_i m_j \vec{r}_i \cdot \vec{r}_j\right) - \frac{3}{2}\Omega$$

$$= \frac{1}{2M}\sum_{ij}\left(m_i m_j \frac{\vec{p}_i \cdot \vec{p}_j}{m_i m_j} + \Omega^2 m_i m_j \vec{r}_i \cdot \vec{r}_j\right) - \frac{3}{2}\Omega$$

$$= \frac{1}{2M}\sum_{ij}\left(m_j\frac{p_i^2}{2m_i} + m_i\frac{p_j^2}{2m_j} - m_i m_j\frac{q_{ij}^2}{2\mu_{ij}^2} + \frac{1}{2}\Omega^2 m_i m_j(r_i^2 + r_j^2 - r_{ij}^2)\right)$$

$$- \frac{3}{2}\Omega$$

$$= -\frac{3}{2}\Omega + \sum_i\left(\frac{p_i^2}{2m_i} + \frac{1}{2}m_i\Omega^2 r_i^2\right) - \frac{1}{M}\sum_{i<j}\left(\frac{m_i m_j}{2\mu_{ij}^2}q_{ij}^2 + \frac{1}{2}\Omega^2 m_i m_j r_{ij}^2\right)$$

$$= -\frac{3}{2}\Omega + \sum_i\left(\frac{p_i^2}{2m_i} + \frac{1}{2}m_i\Omega^2 r_i^2\right) - \sum_{i<j}\frac{m_i + m_j}{M}\left(\frac{q_{ij}^2}{2\mu_{ij}} + \frac{1}{2}\mu_{ij}\Omega^2 r_{ij}^2\right). \qquad \text{(B.27)}$$

Hence, the center-of-mass Hamiltonian separates into a constant part, a HO Hamiltonian for each of the particles and a relative two-body hamonic oscillator for each particle pair. The one-body part can be evaluated by using an eigenvalue relation with respect to the single particle states; the two-body part may be calculated using Slater rules after using the eigenvalue relation of **M**.

C. Details of the Treatment of Three-Body Forces

C.1. Transformation between Jacobi Coordinate sets

The coordinates in the 1-3 basis are

$$\vec{\xi}_0' = \vec{\xi}_0 \tag{C.1}$$

$$\vec{\xi}_1' = \frac{1}{\sqrt{m_1 + m_3}} \left(\sqrt{m_3}\vec{x}_1 - \sqrt{m_1}\vec{x}_3 \right) \tag{C.2}$$

$$\vec{\xi}_2' = \frac{1}{\sqrt{M_3}} \left(\sqrt{\frac{m_2}{m_1 + m_3}} \left(\sqrt{m_1}\vec{x}_1 + \sqrt{m_3}\vec{x}_3 \right) - \sqrt{m_1 + m_3}\vec{x}_2 \right), \tag{C.3}$$

where $M_3 = m_1 + m_2 + m_3$, while those in the 1-2 basis read

$$\vec{\xi}_0 = \vec{\xi}_0 \tag{C.4}$$

$$\vec{\xi}_1 = \frac{1}{\sqrt{M_2}} \left(\sqrt{m_1}\vec{x}_2 - \sqrt{m_2}\vec{x}_1 \right) \tag{C.5}$$

$$\vec{\xi}_2 = \frac{1}{\sqrt{M_3}} \left(\sqrt{\frac{m_3}{M_2}} \left(\sqrt{m_1}\vec{x}_1 + \sqrt{m_2}\vec{x}_2 \right) - \sqrt{M_2}\vec{x}_3 \right). \tag{C.6}$$

We express ξ_1' in terms of the unprimed coordinates by constructing a linear combination that eliminates x_2. We find

$$\sqrt{\frac{m_2}{M_2 m_1}}\vec{\xi}_1 + \sqrt{\frac{M_3}{M_2 m_3}}\vec{\xi}_2 = \frac{1}{\sqrt{m_1}}\vec{\xi}_1 - \frac{1}{\sqrt{m_3}}\vec{\xi}_3 \tag{C.7}$$

and multiplying by $\sqrt{m_1 m_3/(m_1 + m_3)}$ we recover the first Jacobi coordinate

$$\vec{\xi}_1' = \sqrt{\frac{m_2 m_3}{M_2(m_1 + m_3)}}\vec{\xi}_1 + \sqrt{\frac{m_1 M_3}{M_2(m_1 + m_3)}}\vec{\xi}_2. \tag{C.8}$$

The only way to get x_3 is from ξ_2, so we fix its coefficient to get the term of ξ_2' proportional to x_3:

$$-\sqrt{\frac{m_2 m_3}{M_2(m_1 + m_3)}}\vec{\xi}_2 = \frac{1}{\sqrt{M_3}} \left(-\sqrt{\frac{m_1 m_2}{m_1 + m_3}}\frac{m_3}{M_2}\vec{x}_1 - \frac{m_2 m_3}{M_2\sqrt{m_1 + m_3}}\vec{x}_2 + \sqrt{\frac{m_2 m_3}{m_1 + m_3}}\vec{x}_3 \right). \tag{C.9}$$

Next, we choose the coefficient of ξ_1 such that the linear combination yields the x_1-proportional term of ξ_2':

$$
\sqrt{\frac{m_1 M_3}{M_2(m_1 + m_3)}}\vec{\xi}_1 = \sqrt{\frac{m_1 M_2}{M_3(m_1 + m_3)}}\left(1 + \frac{m_3}{m_1 + m_2}\right)\vec{\xi}_1
$$

$$
= \frac{1}{\sqrt{M_3}}\left(\sqrt{\frac{m_1 m_2}{m_1 + m_3}}\left(1 + \frac{m_3}{m_1 + m_2}\right)\vec{x}_1 - \frac{m_1 M_3}{M_2\sqrt{m_1 + m_3}}\vec{x}_2\right). \quad \text{(C.10)}
$$

Combining (C.9) and (C.10) we get

$$
\sqrt{\frac{m_1 M_3}{M_2(m_1 + m_3)}}\vec{\xi}_1 - \sqrt{\frac{m_2 m_3}{M_2(m_1 + m_3)}}\vec{\xi}_2 = \frac{1}{\sqrt{M_1}}\left(\sqrt{\frac{m_2}{m_1 + m_3}}\left(\sqrt{m_1}\vec{x}_1 + \sqrt{m_3}\vec{x}_3\right)\right.
$$

$$
\left. - \underbrace{\frac{m_1 M_3 + m_2 m_3}{M_2\sqrt{m_1 + m_3}}}_{\frac{m_1 M_2 + (m_1 + m_2)m_3}{M_2\sqrt{m_1 + m_3}}}\vec{x}_2\right) = \vec{\xi}_2'. \quad \text{(C.11)}
$$

In conclusion, the transformation is

$$
\vec{\xi}_1' = \sqrt{\frac{m_2 m_3}{M_2(m_1 + m_3)}}\vec{\xi}_1 + \sqrt{\frac{m_1 M_3}{M_2(m_1 + m_3)}}\vec{\xi}_2
$$

$$
\vec{\xi}_2' = \sqrt{\frac{m_1 M_3}{M_2(m_1 + m_3)}}\vec{\xi}_1 - \sqrt{\frac{m_2 m_3}{M_2(m_1 + m_3)}}\vec{\xi}_2 \quad \text{(C.12)}
$$

and the transformation parameter is given by

$$
1 + d = \frac{M_2(m_1 + m_3)}{m_1 M_3} = \frac{m_1(m_1 + m_2 + m_3) + m_2 m_3}{m_1 M_3} = 1 + \frac{m_2 m_3}{m_1 M_3}
$$

$$
\Leftrightarrow \quad d = \frac{m_2 m_3}{m_1 M_3}. \quad \text{(C.13)}
$$

C.2. Transposition Operator on Spatial Part

We evaluate the action of P_{23} on an L-coupled state

$$
P_{23}\,|n_{\text{cm}}l_{\text{cm}}m_{\text{cm}}, (n_1 l_1, n_2 l_2)LM_L\rangle
$$

$$
= \sum_{\mathcal{L}\mathcal{M}}\left(\begin{array}{cc|c}l_{\text{cm}} & L & \mathcal{L}\\ m_{\text{cm}} & M_L & \mathcal{M}\end{array}\right) P_{23}\,|[n_{\text{cm}}l_{\text{cm}}, (n_1 l_1, n_2 l_2)L]\mathcal{L}\mathcal{M}\rangle.
$$

Reordering the coupling for the first HO Bracket we get

$$
= \sum_{\mathcal{L}\mathcal{M}}\sum_{\Lambda}(-1)^{l_{\text{cm}}+\mathcal{L}+L}\hat{L}\hat{\Lambda}\left(\begin{array}{cc|c}l_{\text{cm}} & L & \mathcal{L}\\ m_{\text{cm}} & M_L & \mathcal{M}\end{array}\right)\left\{\begin{array}{ccc}l_{\text{cm}} & l_2 & \Lambda\\ l_1 & \mathcal{L} & L\end{array}\right\} P_{23}\,|[(n_{\text{cm}}l_{\text{cm}}, n_2 l_2)\Lambda, n_1 l_1]\mathcal{L}\mathcal{M}\rangle
$$

$$
= \sum_{\mathscr{L}\mathscr{M}} \sum_{\Lambda} \sum_{\substack{N_1 L_1 \\ n_c l_c}} (-1)^{l_{\text{cm}}+\mathscr{L}+L} \hat{L}\hat{\Lambda} \begin{pmatrix} l_{\text{cm}} & L & \mathscr{L} \\ m_{\text{cm}} & M_L & \mathscr{M} \end{pmatrix} \begin{Bmatrix} l_{\text{cm}} & l_2 & \Lambda \\ l_1 & \mathscr{L} & L \end{Bmatrix}
$$

$$
\times \langle\!\langle N_1 L_1, n_c l_c \mid n_{\text{cm}} l_{\text{cm}}, n_2 l_2 : \Lambda \rangle\!\rangle_{\frac{m_a+m_b}{m_c}} \boldsymbol{P}_{23} \mid [(N_1 L_1, n_c l_c)\Lambda, n_1 l_1] \mathscr{L}\mathscr{M}\rangle
$$

and changing the coupling order again for the second HO Bracket yields

$$
= \sum_{\mathscr{L}\mathscr{M}} \sum_{\Lambda\lambda} \sum_{\substack{N_1 L_1 \\ n_c l_c}} (-1)^{l_{\text{cm}}+l_1+l_c+\mathscr{L}+L+\Lambda+\lambda} \hat{L}\hat{\Lambda}^2\hat{\lambda} \begin{pmatrix} l_{\text{cm}} & L & \mathscr{L} \\ m_{\text{cm}} & M_L & \mathscr{M} \end{pmatrix} \begin{Bmatrix} l_{\text{cm}} & l_2 & \Lambda \\ l_1 & \mathscr{L} & L \end{Bmatrix} \begin{Bmatrix} l_c & L_1 & \Lambda \\ l_1 & \mathscr{L} & \lambda \end{Bmatrix}
$$

$$
\times \langle\!\langle N_1 L_1, n_c l_c \mid n_{\text{cm}} l_{\text{cm}}, n_2 l_2 : \Lambda \rangle\!\rangle_{\frac{m_a+m_b}{m_c}} \boldsymbol{P}_{23} \mid [(N_1 L_1, n_1 l_1)\lambda, n_c l_c] \mathscr{L}\mathscr{M}\rangle
$$

$$
= \sum_{\mathscr{L}\mathscr{M}} \sum_{\Lambda\lambda} \sum_{\substack{N_1 L_1 \\ n_c l_c}} \sum_{\substack{n_a l_a \\ n_b l_b}} (-1)^{l_{\text{cm}}+l_1+l_c+\mathscr{L}+L+\Lambda+\lambda} \hat{L}\hat{\Lambda}^2\hat{\lambda} \begin{pmatrix} l_{\text{cm}} & L & \mathscr{L} \\ m_{\text{cm}} & M_L & \mathscr{M} \end{pmatrix} \begin{Bmatrix} l_{\text{cm}} & l_2 & \Lambda \\ l_1 & \mathscr{L} & L \end{Bmatrix} \begin{Bmatrix} l_c & L_1 & \Lambda \\ l_1 & \mathscr{L} & \lambda \end{Bmatrix}
$$

$$
\times \langle\!\langle N_1 L_1, n_c l_c \mid n_{\text{cm}} l_{\text{cm}}, n_2 l_2 : \Lambda \rangle\!\rangle_{\frac{m_a+m_b}{m_c}} \langle\!\langle n_a l_a, n_b l_b \mid N_1 L_1, n_1 l_1 : \lambda \rangle\!\rangle_{\frac{m_a}{m_b}}
$$

$$
\times \boldsymbol{P}_{23} \mid [(n_a l_a, n_b l_b)\lambda, n_c l_c] \mathscr{L}\mathscr{M}\rangle \,.
$$

Next, we decouple to the *m*-scheme and apply the transposition operator:

$$
= \sum_{\mathscr{L}\mathscr{M}} \sum_{\Lambda\lambda} \sum_{\substack{N_1 L_1 \\ n_c l_c}} \sum_{\substack{n_a l_a \\ n_b l_b}} \sum_{\substack{m_a m_b \\ m_c \mu}} (-1)^{l_{\text{cm}}+l_1+l_c+\mathscr{L}+L+\Lambda+\lambda} \hat{L}\hat{\Lambda}^2\hat{\lambda} \begin{pmatrix} l_{\text{cm}} & L & \mathscr{L} \\ m_{\text{cm}} & M_L & \mathscr{M} \end{pmatrix} \begin{pmatrix} l_a & l_b & \lambda \\ m_a & m_b & \mu \end{pmatrix} \begin{pmatrix} \lambda & l_c & \mathscr{L} \\ \mu & m_c & \mathscr{M} \end{pmatrix}
$$

$$
\times \begin{Bmatrix} l_{\text{cm}} & l_2 & \Lambda \\ l_1 & \mathscr{L} & L \end{Bmatrix} \begin{Bmatrix} l_c & L_1 & \Lambda \\ l_1 & \mathscr{L} & \lambda \end{Bmatrix} \langle\!\langle N_1 L_1, n_c l_c \mid n_{\text{cm}} l_{\text{cm}}, n_2 l_2 : \Lambda \rangle\!\rangle_{\frac{m_a+m_b}{m_c}}
$$

$$
\times \langle\!\langle n_a l_a, n_b l_b \mid N_1 L_1, n_1 l_1 : \lambda \rangle\!\rangle_{\frac{m_a}{m_b}} \mid n_a l_a m_a, n_c l_c m_c, n_b l_b m_b\rangle \,. \tag{C.14}
$$

Reversing the decoupling steps we get a state in a Jacobi HO bases where the first coordinate is defined by the first and third instead of the first and second particle:

$$
= \mid n_{\text{cm}} l_{\text{cm}} m_{\text{cm}}, (\{n_1 l_1\}_{13}, n_2 l_2) L M_L\rangle \,. \tag{C.15}
$$

C.3. Structure of the JT-Coupled Basis

Despite its straight-forward definition[1],

$$
\mid [(\tilde{a}\tilde{b})J_{ab}T_{ab}, \tilde{c}]J M T M_T\rangle
$$

$$
= \sum_{\substack{m_a m_b m_c \\ \tau_a \tau_b \tau_c}} \begin{pmatrix} j_a & j_b & J_{ab} \\ m_a & m_b & M_{ab} \end{pmatrix} \begin{pmatrix} t_a & t_b & T_{ab} \\ \tau_a & \tau_b & \tau_{ab} \end{pmatrix} \begin{pmatrix} J_{ab} & j_c & J \\ M_{ab} & m_c & M \end{pmatrix} \begin{pmatrix} T_{ab} & t_c & T \\ \tau_{ab} & \tau_c & M_T \end{pmatrix} \mid abc\rangle
$$

$$
= \sqrt{3!}\,\mathscr{A} \mid [(\tilde{a}\tilde{b})J_{ab}T_{ab}, \tilde{c}]J M T M_T\rangle_n \,, \tag{C.16}
$$

---

[1]The *p* suffix denotes a product state.

C. Details of the Treatment of Three-Body Forces

the antisymmetric JT-coupled three-body basis has some intricacies. Consider the overlap of two states

$$\langle[(\tilde{a}\tilde{b})J_{ab}T_{ab}, \tilde{c}]JMTM_T|[(\tilde{a}'\tilde{b}')J'_{ab}T'_{ab}, \tilde{c}']J'M'T'M'_T\rangle$$

$$= 3!\,_n\langle[(\tilde{a}\tilde{b})J_{ab}T_{ab}, \tilde{c}]JMTM_T|\mathscr{A}|[(\tilde{a}'\tilde{b}')J'_{ab}T'_{ab}, \tilde{c}']J'M'T'M'_T\rangle_n$$

$$= \sum_{\pi}\mathrm{sgn}\,\pi\,_n\langle[(\tilde{a}\tilde{b})J_{ab}T_{ab}, \tilde{c}]JMTM_T|\boldsymbol{P}_{\pi}|[(\tilde{a}'\tilde{b}')J'_{ab}T'_{ab}, \tilde{c}']J'M'T'M'_T\rangle_n. \qquad \text{(C.17)}$$

Using (E.18), we can express this as

$$= \sum_{\pi} C(j'_a j'_b j'_c J'_{ab}, J_{ab}J, \pi)C(t'_a t'_b t'_c T'_{ab}, T_{ab}T, \pi)$$

$$\times\,_n\langle[(\tilde{a}\tilde{b})J_{ab}T_{ab}, \tilde{c}]JMTM_T|[(\pi(\tilde{a}')\pi(\tilde{b}'))J'_{ab}T'_{ab}, \pi(\tilde{c}')]J'M'T'M'_T\rangle_n$$

$$= \sum_{\pi} \hat{J}'_{ab}\hat{T}'_{ab}C(j'_a j'_b j'_c J'_{ab}, J_{ab}J, \pi)C(t'_a t'_b t'_c T'_{ab}, T_{ab}T, \pi)\delta^{JM}_{J'M'}\delta^{TM_T}_{T'M'_T}\delta^{\tilde{a}\tilde{b}\tilde{c}}_{\pi(\tilde{a}')\pi(\tilde{b}')\pi(\tilde{c}')}. \qquad \text{(C.18)}$$

This shows that basis states with different single-particle states are orthogonal, as are basis states with different total (iso-) spin. If the single-particle states of the bra- and ket states are the same, i.e., $\tilde{a} = \tilde{a}'$, $\tilde{b} = \tilde{b}'$, and $\tilde{c} = \tilde{c}'$, we can distinguish five cases:

- $\tilde{a} \neq \tilde{b} \neq \tilde{c} \neq \tilde{a}$: when all states are different only the identity permutation contributes to the sum, so that

$$\langle[(\tilde{a}\tilde{b})J_{ab}T_{ab}, \tilde{c}]JT|[(\tilde{a}\tilde{b})J'_{ab}T'_{ab}, \tilde{c}]JT\rangle = \delta^{J'_{ab}}_{J_{ab}}\delta^{T'_{ab}}_{T_{ab}}. \qquad \text{(C.19)}$$

- $\tilde{a} = \tilde{b} \neq \tilde{c}$: permutations $\{123\}$ and $\{213\}$ contribute, so that

$$\langle[(\tilde{a}\tilde{a})J_{ab}T_{ab}, \tilde{c}]JT|[(\tilde{a}\tilde{a})J'_{ab}T'_{ab}, \tilde{c}]JT\rangle = (1 - (-)^{J_{ab}+T_{ab}-2t_a})\delta^{J'_{ab}}_{J_{ab}}\delta^{T'_{ab}}_{T_{ab}}. \qquad \text{(C.20)}$$

  The states with even $J_{ab} + T_{ab} - 2t_a$ have zero norm because they are forbidden by antisymmetry, the allowed ones have a norm of $\sqrt{2}$.

- $\tilde{a} = \tilde{c} \neq \tilde{b}$: permutations $\{123\}$ and $\{321\}$ contribute, so that

$$\langle[(\tilde{a}\tilde{b})J_{ab}T_{ab}, \tilde{a}]JT|[(\tilde{a}\tilde{b})J'_{ab}T'_{ab}, \tilde{a}]JT\rangle$$

$$= \delta^{J'_{ab}}_{J_{ab}}\delta^{T'_{ab}}_{T_{ab}} - (-)^{2T}\hat{J}'_{ab}\hat{J}_{ab}\hat{T}'_{ab}\hat{T}_{ab}\begin{Bmatrix} j_a & j_b & J_{ab} \\ j_a & J & J'_{ab} \end{Bmatrix}\begin{Bmatrix} t_a & t_b & T_{ab} \\ t_a & T & T'_{ab} \end{Bmatrix}. \qquad \text{(C.21)}$$

- $\tilde{a} \neq \tilde{b} = \tilde{c}$: permutations $\{123\}$ and $\{132\}$ contribute, so that

$$\langle[(\tilde{a}\tilde{b})J_{ab}T_{ab}, \tilde{b}]JT|[(\tilde{a}\tilde{b})J'_{ab}T'_{ab}, \tilde{b}]JT\rangle$$

$$= \delta^{J'_{ab}}_{J_{ab}}\delta^{T'_{ab}}_{T_{ab}} - (-)^{J_{ab}+J'_{ab}+T_{ab}+T'_{ab}+2t_b}\hat{J}'_{ab}\hat{J}_{ab}\hat{T}'_{ab}\hat{T}_{ab}\begin{Bmatrix} j_b & j_a & J_{ab} \\ j_b & J & J'_{ab} \end{Bmatrix}\begin{Bmatrix} t_b & t_a & T_{ab} \\ t_b & T & T'_{ab} \end{Bmatrix}. \qquad \text{(C.22)}$$

- $\tilde{a} = \tilde{b} = \tilde{c}$: all permutations contribute, so that

$$\langle [(\tilde{a}\tilde{a})J_{ab}T_{ab}, \tilde{a}]JT | [(\tilde{a}\tilde{a})J'_{ab}T'_{ab}, \tilde{a}]JT \rangle$$

$$= (1 - (-)^{J'_{ab}+T'_{ab}-2t_a}) \left(\delta^{J'_{ab}}_{J_{ab}} \delta^{T'_{ab}}_{T_{ab}} \right.$$

$$\left. - (-)^{2t_a}(1 - (-)^{J_{ab}+T_{ab}-2t_a}) \hat{J}'_{ab}\hat{J}_{ab}\hat{T}'_{ab}\hat{T}_{ab} \begin{Bmatrix} j_a & j_a & J_{ab} \\ j_a & J & J'_{ab} \end{Bmatrix} \begin{Bmatrix} t_a & t_a & T_{ab} \\ t_a & T & T'_{ab} \end{Bmatrix} \right). \tag{C.23}$$

The phase factors have been simplified by noting that sums of quantum numbers that can be permuted to the top row of the $6j$ symbol, like $T + T_{ab} + t_a$, are integers.

In all cases except for the first two, we have nonzero overlap between states with different J_{ab}, T_{ab}. The basis is hence not orthogonal, but the overlap matrix (the Gramian) is block diagonal whenever the the last single-particle state is equal to one of the first two.

We can further analyze the structure of these nonorthogonal subspaces. Consider again the case $\tilde{a} \neq \tilde{b} = \tilde{c}$: we take the Gramian of such a set of basis states as a matrix over a combined index (J_{ab}, T_{ab}) and diagonalize it. The equation for an eigenvalue λ is

$$0 = \sum_{J_{ab}T_{ab}} \left((1 - \lambda)\delta^{J'_{ab}}_{J_{ab}} \delta^{T'_{ab}}_{T_{ab}} - (-)^{J_{ab}+J'_{ab}+T_{ab}+T'_{ab}+2t_b} \hat{J}'_{ab}\hat{J}_{ab}\hat{T}'_{ab}\hat{T}_{ab} \begin{Bmatrix} j_b & j_a & J_{ab} \\ j_b & J & J'_{ab} \end{Bmatrix} \begin{Bmatrix} t_b & t_a & T_{ab} \\ t_b & T & T'_{ab} \end{Bmatrix} \right)$$

$$\times \upsilon(J_{ab}, T_{ab}, J''_{ab}, T''_{ab}) \quad \text{(C.24)}$$

and we choose

$$\upsilon(J_{ab}, T_{ab}, J''_{ab}, T''_{ab}) = (-)^{J''_{ab}+T''_{ab}-2t_b} \hat{J}''_{ab}\hat{J}_{ab}\hat{T}''_{ab}\hat{T}_{ab} \begin{Bmatrix} j_a & j_b & J_{ab} \\ j_b & J & J''_{ab} \end{Bmatrix} \begin{Bmatrix} t_a & t_b & T_{ab} \\ t_b & T & T''_{ab} \end{Bmatrix}. \tag{C.25}$$

The eigenvalue equation becomes

$$0 = (1 - \lambda)\upsilon(J'_{ab}, T'_{ab}, J''_{ab}, T''_{ab})$$

$$- \hat{J}''_{ab}\hat{J}'_{ab}\hat{T}''_{ab}\hat{T}'_{ab} \left(\sum_{J_{ab}} (-)^{J_{ab}+J'_{ab}+J''_{ab}} \hat{J}^2_{ab} \begin{Bmatrix} j_b & j_a & J_{ab} \\ j_b & J & J'_{ab} \end{Bmatrix} \begin{Bmatrix} j_a & j_b & J_{ab} \\ j_b & J & J''_{ab} \end{Bmatrix} \right)$$

$$\times \left(\sum_{T_{ab}} (-)^{T_{ab}+T'_{ab}+T''_{ab}} \hat{T}^2_{ab} \begin{Bmatrix} t_b & t_a & T_{ab} \\ t_b & T & T'_{ab} \end{Bmatrix} \begin{Bmatrix} t_a & t_b & T_{ab} \\ t_b & T & T''_{ab} \end{Bmatrix} \right). \tag{C.26}$$

This type of sum over $6j$ symbols can be executed analytically [VMK88, eq. 9.8(4)]:

$$\sum_X (-)^{p+q+X} \hat{X}^2 \begin{Bmatrix} a & b & X \\ c & d & p \end{Bmatrix} \begin{Bmatrix} a & b & X \\ d & c & q \end{Bmatrix} = \begin{Bmatrix} a & c & q \\ b & d & p \end{Bmatrix} = \begin{Bmatrix} b & c & p \\ a & d & q \end{Bmatrix}. \tag{C.27}$$

Hence, we get

$$0 = (1 - \lambda)\upsilon(J'_{ab}, T'_{ab}, J''_{ab}, T''_{ab}) - \hat{J}''_{ab}\hat{J}'_{ab}\hat{T}''_{ab}\hat{T}'_{ab} \begin{Bmatrix} j_a & j_b & J'_{ab} \\ j_b & J & J''_{ab} \end{Bmatrix} \begin{Bmatrix} t_a & t_b & T'_{ab} \\ t_b & T & T''_{ab} \end{Bmatrix}$$

$$= ((1 - \lambda) - (-)^{J''_{ab} + T''_{ab} - 2t_b}) v(J'_{ab}, T'_{ab}, J''_{ab}, T''_{ab}), \tag{C.28}$$

where we could flip the signs of J''_{ab} and T''_{ab} in the phase factor because these quantities are integers. Thus, we have found a full set of eigenvectors with eigenvalues $\lambda = 1 - (-)^{J''_{ab} + T''_{ab} - 2t_b} \in \{0, 2\}$. The linear combinations of states identified by the eigenvectors have norm $\sqrt{2}$ or zero depending on whether they are allowed or forbidden by antisymmetry. Incidentally, the eigenvector is (up to a global phase) equal to the coefficient C from (E.18) that transforms this type of state to the $|[(\tilde{b}\tilde{b})J''_{ab}T''_{ab}, \tilde{a}]JT\rangle$ coupling scheme.

Analogously, we can analyze the case where all single-particle states are equal. Since rows and columns with $J_{ab} + T_{ab} - 2t_a$ even are zero, we have eingenvectors

$$u(J_{ab}T_{ab}, J''_{ab}T''_{ab}) = (1 + (-)^{J_{ab} + T_{ab} - 2t_a}) \delta^{J''_{ab}}_{J_{ab}} \delta^{T''_{ab}}_{T_{ab}}, \quad J''_{ab} + T''_{ab} - 2t_a \text{ even} \tag{C.29}$$

with eigenvalue zero. The other eigenvectors (with $J''_{ab} + T''_{ab} - 2t_a$ odd) are

$$v_\pm(J_{ab}T_{ab}, J''_{ab}T''_{ab}) = \frac{1 - (-)^{J_{ab} + T_{ab} - 2t_a}}{2} \frac{1 - (-)^{J''_{ab} + T''_{ab} - 2t_a}}{2}$$
$$\times \left(\delta^{J''_{ab}}_{J_{ab}} \delta^{T''_{ab}}_{T_{ab}} - (-)^{2t_a} x_\pm \hat{J}''_{ab} \hat{J}_{ab} \hat{T}''_{ab} \hat{T}_{ab} \begin{Bmatrix} j_a & j_a & J_{ab} \\ j_a & J & J''_{ab} \end{Bmatrix} \begin{Bmatrix} t_a & t_a & T_{ab} \\ t_a & T & T''_{ab} \end{Bmatrix} \right) \tag{C.30}$$

with $x_+ = 2$, $x_- = -1$ and eigenvalues $\lambda_+ = 6$ and $\lambda_- = 0$. Obviously, we have two eigenvectors for each valid combination of J''_{ab} and T''_{ab}, so only half of them can be linearly independent. Furthermore, $v_\pm(J_{ab}T_{ab}, J'_{ab}T'_{ab}) = v_\pm(J'_{ab}T'_{ab}, J_{ab}T_{ab})$ and the overlap between two eigenvectors is

$$\sum_{J_{ab}T_{ab}} v_\pm(J_{ab}T_{ab}, J'_{ab}T'_{ab}) v_\pm(J_{ab}T_{ab}, J''_{ab}T''_{ab}) = \frac{4 + x_\pm}{2} v_\pm(J'_{ab}T'_{ab}, J''_{ab}T''_{ab}), \tag{C.31}$$

which also shows (by interchanging arguments and interpreting the result as vector over the primed quantum numbers) that any vector can be expressed as a linear combination of all others.

Numerical experiments show that all the v_+ are proportional to each other while the v_- form a basis if one leaves out any single vector, but we could not prove these properties in general. For certain combinations of j_a, t_a and J, T the whole Gramian vanishes, indicating that there are no antisymmetric states for these quantum numbers. The occurrance of this situation seems to depend on the value of individual $6j$ symbols and does not follow a simple rule.

In conclusion, one can build an orthogonal basis by choosing the proper basis states from the overcomplete set of coupled states: For three different single-particle states the state is uniquely specified. When two single-particle states are identical take the $[(\tilde{a}\tilde{a})J_{ab}T_{ab}, \tilde{b}]$-type basis states with a constraint on J_{ab}. When three states are identical take the linear combination identified by one of the v_+ if the Gramian does not vanish.

D. Overlap of HO Wavefunctions with Different Oscillator Lengths

For the frequency conversion step, we need overlaps between HO wave functions $\phi_{nl}(r, b)$ with different oscillator lengths b. These overlaps are most easily computed by numerical integration, but there exists an analytical expression, which we will derive in the following.

We start with the overlap integral

$$\langle \phi_{nlm}(b) | \phi_{n'l'm'}(b') \rangle = \int_0^\infty dr\, r^2 \int d\Omega\, R_{nl}(r, b) R_{n'l'}(r, b') Y_{lm}^*(\Omega) Y_{l'm'}(\Omega)$$

$$= \delta_{ll'} \delta_{mm'} \int_0^\infty dr\, r^2 R_{nl}(r, b) R_{n'l}(r, b'). \tag{D.1}$$

The radial integral can be decomposed further because

$$rR_{nl}(r, b) = \sqrt{\frac{2\Gamma(n+1)}{b\Gamma(n+l+3/2)}} \exp\left(-\tfrac{1}{2}\left(\tfrac{r}{b}\right)^2\right) \left(\tfrac{r}{b}\right)^{l+1} L_n^{(l+1/2)}\left(\left(\tfrac{r}{b}\right)^2\right) = \mathcal{N}_{nl} b^{-1/2} f_{nl}\left(\tfrac{r}{b}\right) \tag{D.2}$$

factorizes into a normalization factor and a function that depends only on the ratio r/b. We thus have

$$I_l(nb, n'b') \equiv \int_0^\infty dr\, r^2 R_{nl}(r, b) R_{n'l}(r, b') = \mathcal{N}_{nl} \mathcal{N}_{n'l} (bb')^{-1/2} \int_0^\infty dr\, f_{nl}\left(\tfrac{r}{b}\right) f_{n'l}\left(\tfrac{r}{b'}\right) \tag{D.3}$$

and by substituting $\rho = r/b$ we can make the integral depend only on the ratio $a = b/b'$ of the oscillator parameters:

$$I_l(nb, n'b') = \mathcal{N}_{nl} \mathcal{N}_{n'l} a^{l+3/2} \int_0^\infty d\rho\, \exp\left(-\tfrac{1}{2}(1+a^2)\rho^2\right) \rho^{2l+2} L_n^{(l+1/2)}(\rho^2) L_{n'}^{(l+1/2)}(a^2\rho^2). \tag{D.4}$$

Another substitution $x = 1/2(1+a^2)\rho^2$ brings the integration weight into the form that is needed to exploit the orthogonality of the associated Laguerre polynomials:

$$I_l(nb, n'b') = \frac{\mathcal{N}_{nl} \mathcal{N}_{n'l}}{2} \left(\frac{2}{a+a^{-1}}\right)^{l+3/2}$$

$$\times \int_0^\infty dx\, x^{l+1/2} \exp(-x) L_n^{(l+1/2)}\left(\frac{2x}{1+a^2}\right) L_{n'}^{(l+1/2)}\left(\frac{2a^2x}{1+a^2}\right). \tag{D.5}$$

The associated Laguerre polynomials still depend on scaled arguments, so we employ the multiplication theorem [DLMF, eq. 18.18.12]

$$L_n^{(\alpha)}(\lambda x) = \sum_{k=0}^n \binom{n}{k} \lambda^k (1-\lambda)^{n-k} \frac{L_n^{(\alpha)}(0)}{L_k^{(\alpha)}(0)} L_k^{(\alpha)}(x) \tag{D.6}$$

to convert them to polynomials depending on the unscaled variable. Making use of the orthogonality relation

$$\int_0^\infty dx\, x^\alpha \exp(-x) L_n^{(\alpha)}(x) L_{n'}^{(\alpha)}(x) = \delta_{nn'} \frac{\Gamma(n+\alpha+1)}{n!} \tag{D.7}$$

we carry out the integration, which leaves us with

$$\begin{aligned}
I_l(nb, n'b') = (-1)^n \frac{\mathcal{N}_{nl}\mathcal{N}_{n'l}}{2} \left(\frac{2}{a+a^{-1}}\right)^{l+3/2} \left(1+a^2\right)^{-(n+n')} \sum_{k=0}^{n_<} \frac{(-1)^k}{k!} \binom{n}{k}\binom{n'}{k} \\
\times \frac{L_n^{(l+1/2)}(0) L_{n'}^{(l+1/2)}(0)}{\left[L_k^{(l+1/2)}(0)\right]^2} \Gamma(k+l+3/2)(2a)^{2k}(1-a^2)^{n+n'-2k},
\end{aligned} \tag{D.8}$$

where $n_< = \min(n, n')$. The explicit expression for the Laguerre polynomials in terms of Gamma functions [DLMF, eq. 18.5.12],

$$L_n^{(\alpha)}(x) = \sum_{k=0}^{n} \frac{(-x)^k}{k!} \frac{\Gamma(n+\alpha+1)}{(n-k)!\Gamma(k+\alpha+1)}, \tag{D.9}$$

can be used to further simplify the occurrences of $L_n^{(\alpha)}(0)$, yielding

$$\begin{aligned}
I_l(nb, n'b') &= (-1)^n \left(\frac{2}{a+a^{-1}}\right)^{l+3/2} \left(1+a^2\right)^{-(n+n')} \sum_{k=0}^{n_<} \frac{(-1)^k}{k!} \frac{\sqrt{n!n'!}}{(n-k)!(n'-k)!} \\
&\quad \times \frac{\sqrt{\Gamma(n+l+3/2)\Gamma(n'+l+3/2)}}{\Gamma(k+l+3/2)}(2a)^{2k}(1-a^2)^{n+n'-2k} \\
&= (-1)^n \left(\frac{2}{a+a^{-1}}\right)^{l+3/2} \left(\frac{1-a^2}{1+a^2}\right)^{n+n'} \sum_{k=0}^{n_<} \frac{(-1)^k}{k!} \frac{\sqrt{n!n'!}}{(n-k)!(n'-k)!} \\
&\quad \times \frac{\sqrt{\Gamma(n+l+3/2)\Gamma(n'+l+3/2)}}{\Gamma(k+l+3/2)}\left(\frac{2a}{1-a^2}\right)^{2k}.
\end{aligned} \tag{D.10, D.11}$$

The second equation (D.11) shows that the overlap possesses a high degree of symmetry:

$$\begin{aligned}
I_l(nb, n'b') &= (-1)^{n+n'} I_l(n'b, nb') \tag{D.12} \\
&= (-1)^{n+n'} I_l(nb', n'b) \tag{D.13} \\
&= I_l(n'b', nb) \tag{D.14}
\end{aligned}$$

The first relation arises because the only asymmetry between n and n' is the phase factor. To get the second, we note that exchanging the oscillator lengths replaces a by its reciprocal, which only appears in symmetric expressions or fractions that can be returned to their original form by expanding with a power of a. The only change is a factor of $(-1)^{n+n'}$ from the third term.

E. Angular-Momentum-Coupled Spherical Hartree-Fock

A computation-intensive task during a Hartree-Fock calculation is computing the Fock operator

$$\langle p|\boldsymbol{f}|p'\rangle = \langle p|\boldsymbol{H}^{[1]}|p'\rangle + \sum_{qq'} \langle pq|\boldsymbol{H}^{[2]}|p'q'\rangle\, \rho_{qq'} + \frac{1}{2}\sum_{\substack{qq'\\rr'}} \langle pqr|\boldsymbol{H}^{[3]}|p'q'r'\rangle\, \rho_{qq'}\rho_{rr'} \quad \text{(E.1)}$$

from a Hamiltonian $\boldsymbol{H} = \boldsymbol{H}^{[1]} + \boldsymbol{H}^{[2]} + \boldsymbol{H}^{[3]}$ and a one-body density matrix ρ. For spherical Hartree-Fock, we can exploit rotational invariance of the Hamiltonian and the density matrix to simplify the formulae, partition the problem and to carry out part of the sums analytically.

Rotational invariance constrains the dependence of matrix elements on the total angular momentum and its projection; specifically, we have

$$\langle p|\boldsymbol{H}^{[1]}|p'\rangle = \langle \bar{p}|\boldsymbol{H}^{[1]}|\bar{p}'\rangle\, \delta^{j'_p m'_p}_{j_p m_p} \quad \text{(E.2)}$$

$$\rho_{pp'} = \rho_{\bar{p}\bar{p}'}\,\delta^{j'_p m'_p}_{j_p m_p}, \quad \text{(E.3)}$$

so the matrix elements are diagonal in the total angular momentum and independent of its projection. We rewrite the density matrix $\tilde{\rho}_{pp'} = \hat{j}_p^2 \rho_{pp'}$ so that its eigenvalues are equal to the number of particles in the respective orbit.

E.1. Two-Body Part

The two-body part of the fock operator reads[1]

$$\sum_{qq'} \langle pq|\boldsymbol{H}^{[2]}|p'q'\rangle\, \rho_{qq'}$$

$$= \sum_{qq'}\sum_{JM} \begin{pmatrix} j_p & j_q \,\Big|\, J \\ m_p & m_q \,\Big|\, M \end{pmatrix} \begin{pmatrix} j'_p & j'_q \,\Big|\, J \\ m'_p & m'_q \,\Big|\, M \end{pmatrix} \langle (\bar{p}\bar{q})J|\boldsymbol{H}^{[2]}|(\bar{p}'\bar{q}')J\rangle\, \hat{j}_q^{-2}\tilde{\rho}_{\bar{q}\bar{q}'}\,\delta^{j'_q m'_q}_{j_q m_q}$$

$$= \sum_{\substack{\bar{q}\bar{q}'\\j_q=j'_q}}\sum_{J} \langle (\bar{p}\bar{q})J|\boldsymbol{H}^{[2]}|(\bar{p}'\bar{q}')J\rangle\,\tilde{\rho}_{\bar{q}\bar{q}'}\,\hat{j}_q^{-2}\sum_{m_q M} \begin{pmatrix} j_p & j_q \,\Big|\, J \\ m_p & m_q \,\Big|\, M \end{pmatrix} \begin{pmatrix} j'_p & j_q \,\Big|\, J \\ m'_p & m_q \,\Big|\, M \end{pmatrix}.$$

---

[1] The coupled states are, per convention, not normalized to unity, but such that there are no additional factors during matrix-element decoupling.

The last sum is an average over the angular-momentum projection of q. Employing (A.6), we get

$$= \sum_{\substack{\bar{q}\bar{q}'J \\ j_q=j_q'}} \langle (\bar{p}\bar{q})J | H^{[2]} | (\bar{p}'\bar{q}')J \rangle \, \tilde{\rho}_{\bar{q}\bar{q}'} \sum_{m_q M} (-1)^{2(j_q+m_q)} \frac{\hat{J}^2}{\hat{j}_p'\hat{j}_p\hat{j}_q^2} \begin{pmatrix} J & j_q \\ -M & m_q \end{pmatrix} \begin{vmatrix} j_p \\ -m_p \end{pmatrix} \begin{pmatrix} J & j_q \\ -M & m_q \end{pmatrix} \begin{vmatrix} j_p' \\ -m_p' \end{pmatrix}.$$

The phase factor vanishes and we can carry out the summation over m_q and M:

$$= \sum_{\substack{\bar{q}\bar{q}' \\ j_q'=j_q}} \sum_J \frac{\hat{J}^2}{\hat{j}_p^2\hat{j}_q^2} \langle (\bar{p}\bar{q})J | H^{[2]} | (\bar{p}'\bar{q}')J \rangle \, \tilde{\rho}_{\bar{q}\bar{q}'} \delta_{j_p m_p}^{j_p' m_p'}. \tag{E.4}$$

The constraint $j_q = j_q'$ ($j_p = j_p'$) together with strangeness and charge conservation causes all quantum numbers of $\bar{q}, \bar{q}'$ ($\bar{p}, \bar{p}'$) to be identical, except for the radial quantum numbers. Thus the fock operator decomposes into blocks, identified by the quantum numbers $\mathcal{S}_p t_p \tau_p, l_p j_p$, that can be calculated separately. The sum can also be separated into parts with given $\mathcal{S}_q t_q \tau_q, l_q j_q$.[2]

Since the result is diagonal in and independent of the projection of j_p, we can sum both sides of the equation over m_p and divide by the multiplicity and get the same result. This manipulation reveals that the two-body part is an average of the m-scheme matrix element over m_p and m_q, multiplied by a density-matrix element:

$$\sum_{qq'} \langle pq | H^{[2]} | p'q' \rangle \, \rho_{qq'} = \sum_{\bar{q}\bar{q}'} \tilde{\rho}_{\bar{q}\bar{q}'} \frac{1}{\hat{J}_p^2\hat{J}_q^2} \sum_{m_p m_q} \langle pq | H^{[2]} | p'q' \rangle \equiv \sum_{\bar{q}\bar{q}'} \tilde{\rho}_{\bar{q}\bar{q}'} \overline{\langle \bar{p}\bar{q} | H^{[2]} | \bar{p}'\bar{q}' \rangle}. \tag{E.5}$$

E.2. Three-Body Part

The three-body part can be calculated in an analogous fashion when coupled matrix elements are avaliable for all permutations of single-particle quantum numbers. To reduce the amount of memory required for the three-body matrix elements, however, we store only one of the $(3!)^2$ permutations in a coupled form $\langle [(\bar{a}\bar{b})J_{ab}, \bar{c}]J \rangle | H^{[3]} | [(\bar{a}'\bar{b}')J_{ab}', \bar{c}']J \rangle$. For simplicity, we consider isospin-decoupled matrix elements. This decoupling step is independent of the following manipulations.

The three-body part is

$$\frac{1}{2} \sum_{\substack{qq' \\ rr'}} \langle pqr | H^{[3]} | p'q'r' \rangle \, \rho_{qq'} \rho_{rr'} = \frac{1}{2} \sum_{\substack{qq' \\ rr'}} \langle pqr | H^{[3]} | p'q'r' \rangle \, \hat{j}_q^{-2} \tilde{\rho}_{\bar{q}\bar{q}'} \delta_{j_q m_q}^{j_q' m_q'} \hat{j}_r^{-2} \tilde{\rho}_{\bar{r}\bar{r}'} \delta_{j_r m_r}^{j_r' m_r'}, \tag{E.6}$$

Again, the central part is the average over m_q and m_r

$$\frac{1}{\hat{j}_q^2 \hat{j}_r^2} \sum_{m_q m_r} \langle pqr | H^{[3]} | p'q'r' \rangle$$

$$= \frac{1}{\hat{j}_q^2 \hat{j}_r^2} \sum_{m_q m_r} \sum_{\substack{J_{ab} M_{ab} \\ J_{ab}' M_{ab}'}} \sum_{JM} \begin{pmatrix} j_{\pi(p)} & j_{\pi(q)} \\ m_{\pi(p)} & m_{\pi(q)} \end{pmatrix} \begin{vmatrix} J_{ab} \\ M_{ab} \end{pmatrix} \begin{pmatrix} j_{\pi(p')} & j_{\pi(q')} \\ m_{\pi(p')} & m_{\pi(q')} \end{pmatrix} \begin{vmatrix} J_{ab}' \\ M_{ab}' \end{pmatrix} \begin{pmatrix} J_{ab} & j_{\pi(r)} \\ M_{ab} & m_{\pi(r)} \end{pmatrix} \begin{vmatrix} J \\ M \end{pmatrix}$$

---

[2] Each term of the sum can be interpreted as the mean field for a particle of given species in a certain $l_p j_p$ orbit group, caused by particles of a (possibly different) type in another $l_q j_q$ orbit group.

$$\times \begin{pmatrix} J'_{ab} & j_{\pi(r')} \\ M'_{ab} & m_{\pi(r')} \end{pmatrix} J \\ M \end{pmatrix} \langle [(\pi(\bar{p})\pi(\bar{q}))J_{ab}, \pi(\bar{r})]J | \boldsymbol{H}^{[3]} | [(\pi(\bar{p}')\pi(\bar{q}'))J'_{ab}, \pi(\bar{r}')]J \rangle, \quad \text{(E.7)}$$

where π denotes the permutation that brings the quantum numbers of the ket into the order stored in the matrix element file and we have used (5.46). The Clebsch-Gordan coefficients can be analyzed via the diagrammatic technique presented in [VMK88, ch. 11]. Since the only external lines in the diagrammatic representation of this expression correspond to j'_p, m'_p and j_p, m_p, we have $j'_p = j_p$ and $m'_p = m_p$ and the expression is equal to its m_p-average [VMK88, 11.4.2(c)]. Thus, we can write equivalently

$$\frac{1}{\hat{j}_p^2 \hat{j}_q^2 \hat{j}_r^2} \sum_{m_p m_q m_r} \langle pqr | \boldsymbol{H}^{[3]} | p'q'r' \rangle$$

$$= \delta_{j_p m_p}^{j'_p m'_p} \frac{1}{\hat{j}_p^2 \hat{j}_q^2 \hat{j}_r^2} \sum_{m_p m_q m_r} \sum_{\substack{J_{ab} M_{ab} \\ J'_{ab} M'_{ab}}} \sum_{JM}$$

$$\times \begin{pmatrix} j_{\pi(p)} & j_{\pi(q)} \\ m_{\pi(p)} & m_{\pi(q)} \end{pmatrix} J_{ab} \\ M_{ab} \end{pmatrix} \begin{pmatrix} j_{\pi(p')} & j_{\pi(q')} \\ m_{\pi(p')} & m_{\pi(q')} \end{pmatrix} J'_{ab} \\ M'_{ab} \end{pmatrix} \begin{pmatrix} J_{ab} & j_{\pi(r)} \\ M_{ab} & m_{\pi(r)} \end{pmatrix} J \\ M \end{pmatrix} \begin{pmatrix} J'_{ab} & j_{\pi(r')} \\ M'_{ab} & m_{\pi(r')} \end{pmatrix} J \\ M \end{pmatrix}$$

$$\times \langle [(\pi(\bar{p})\pi(\bar{q}))J_{ab}, \pi(\bar{r})]J | \boldsymbol{H}^{[3]} | [(\pi(\bar{p}')\pi(\bar{q}'))J'_{ab}, \pi(\bar{r}')]J \rangle$$

$$\equiv \overline{\langle \bar{p}\bar{q}\bar{r} | \boldsymbol{H}^{[3]} | \bar{p}'\bar{q}'\bar{r}' \rangle}. \quad \text{(E.8)}$$

It is now easy to see that one can use completeness relations of the Clebsch-Gordan Coefficients to remove the sums over the projections, leaving the constraint $J_{ab} = J'_{ab}$ and an additional factor of $\hat{J}^2$ due to the remaining sum over M.

Up to this point we have ignored that the permutations σ and π that have to be applied to the bra and ket quantum numbers, respectively, in order to arrive at a stored matrix element are not necessarily the same. Since all antisymmetric states are eigenstates of the permutation operator $\boldsymbol{P}_\xi$ with eigenvalue $\text{sgn}\,\xi$, we can let $\xi = \pi \circ \sigma^{-1}$ and rewrite

$$\overline{\langle \bar{p}\bar{q}\bar{r} | \boldsymbol{H}^{[3]} | \bar{p}'\bar{q}'\bar{r}' \rangle} = \frac{\text{sgn}\,\xi}{\hat{j}_p^2 \hat{j}_q^2 \hat{j}_r^2} \sum_{J'_{ab} J} \hat{J}^2 \langle [(\pi(\bar{p})\pi(\bar{q}))J'_{ab}, \pi(\bar{r})]J | \boldsymbol{P}_{\xi^{-1}}^\dagger \boldsymbol{H}^{[3]} | [(\pi(\bar{p}')\pi(\bar{q}'))J'_{ab}, \pi(\bar{r}')]J \rangle$$

$$= \frac{\text{sgn}\,\xi}{\hat{j}_p^2 \hat{j}_q^2 \hat{j}_r^2} \sum_{J'_{ab} J} \hat{J}^2 \sqrt{3!} \,_n\langle [(\xi(a)\xi(b))J'_{ab}, \xi(c)]J | \boldsymbol{P}_{\xi^{-1}}^\dagger \mathscr{A} \boldsymbol{H}^{[3]} | [(a'b')J'_{ab}, c']J \rangle$$

$$\text{(E.9)}$$

where we introduced shorthands $a, b, c = \sigma(p), \sigma(q), \sigma(r)$ and $a', b', c' = \pi(p'), \pi(q'), \pi(r')$ for the permuted quantum numbers, pulled out the antisymmetrizer and commuted it with the permutation operator. The subscript n denotes that the bra state is now a nonantisymmetric state. The last line of (E.9) depends only on the relative permutation ξ.

Decoupling, acting with the permutation operator on the state, and recoupling the permuted state, we get

$$\text{sgn}\,\xi \boldsymbol{P}_{\xi^{-1}} | [(\xi(a)\xi(b))J'_{ab}, \xi(c)]J \rangle_n$$

$$= \text{sgn}\,\xi \sum_{m_a m_b m_c} \begin{pmatrix} j_{\xi(a)} & j_{\xi(b)} \\ m_{\xi(a)} & m_{\xi(b)} \end{pmatrix} J'_{ab} \\ M'_{ab} \end{pmatrix} \begin{pmatrix} J_{ab} & j_{\xi(c)} \\ M_{ab} & m_{\xi(c)} \end{pmatrix} J \\ M \end{pmatrix} \boldsymbol{P}_{\xi^{-1}} | \xi(a)\xi(b)\xi(c) \rangle_n$$

$$= \begin{cases} |[(ab)J'_{ab}, c]J\rangle_n & : \xi = \{123\} \\ -(-)^{J'_{ab}+j_a+j_b} |[(ab)J'_{ab}, c]J\rangle_n & : \xi = \{213\} \\ (-)^{J-J'_{ab}-j_a} |[a, (bc)J'_{ab}]J\rangle_n & : \xi = \{231\} \\ -(-)^{J-j_a-j_b-j_c} |[a, (bc)J'_{ab}]J\rangle_n & : \xi = \{321\} \\ (-)^{J'_{ab}-j_a-j_c} |[(ac)_{13}J'_{ab}, b]J\rangle_n & : \xi = \{312\} \\ - |[(ac)_{13}J'_{ab}, b]J\rangle_n & : \xi = \{132\} \end{cases}. \tag{E.10}$$

Next, we introduce an identity to switch the coupling order back to $[(ab)J_{ab}, c]J$ (cf. appendix A.2), which yields

$$\mathrm{sgn}\,\xi\, P_{\xi^{-1}} |[(\xi(a)\xi(b))J'_{ab}, \xi(c)]J\rangle_p = \sum_{J_{ab}} |[(ab)J_{ab}, c]J\rangle_n$$

$$\times \begin{cases} \delta^{J_{ab}}_{J'_{ab}} & : \xi = \{123\} \\ -(-)^{J'_{ab}+j_a+j_b}\delta^{J_{ab}}_{J'_{ab}} & : \xi = \{213\} \\ -(-)^{J'_{ab}+j_b+j_c}\hat{J}_{ab}\hat{J}'_{ab} \begin{Bmatrix} j_a & j_b & J_{ab} \\ j_c & J & J'_{ab} \end{Bmatrix} & : \xi = \{231\} \\ +\hat{J}_{ab}\hat{J}'_{ab} \begin{Bmatrix} j_a & j_b & J_{ab} \\ j_c & J & J'_{ab} \end{Bmatrix} & : \xi = \{321\} \\ -(-)^{J_{ab}+j_a+j_b}\hat{J}_{ab}\hat{J}'_{ab} \begin{Bmatrix} j_b & j_a & J_{ab} \\ j_c & J & J'_{ab} \end{Bmatrix} & : \xi = \{312\} \\ -(-)^{J_{ab}+J'_{ab}+j_b+j_c}\hat{J}_{ab}\hat{J}'_{ab} \begin{Bmatrix} j_b & j_a & J_{ab} \\ j_c & J & J'_{ab} \end{Bmatrix} & : \xi = \{132\} \end{cases}. \tag{E.11}$$

Inserting this result back into (E.9), we get the coupled formula for the averaged matrix element

$$\overline{\langle \bar{p}\bar{q}\bar{r}|H^{[3]}|\bar{p}'\bar{q}'\bar{r}'\rangle} = \sum_{J_{ab}J'_{ab}J} \frac{\hat{J}^2}{\hat{j}_p^2 \hat{j}_q^2 \hat{j}_r^2} \langle[(\bar{a}\bar{b})J_{ab}, \bar{c}]J|H^{[3]}|[(\bar{a}'\bar{b}')J'_{ab}, \bar{c}']J\rangle$$

$$\times \begin{cases} \delta^{J_{ab}}_{J'_{ab}} & : \xi = \{123\} \\ -(-)^{J'_{ab}+j_a+j_b}\delta^{J_{ab}}_{J'_{ab}} & : \xi = \{213\} \\ -(-)^{J'_{ab}+j_b+j_c}\hat{J}_{ab}\hat{J}'_{ab} \begin{Bmatrix} j_a & j_b & J_{ab} \\ j_c & J & J'_{ab} \end{Bmatrix} & : \xi = \{231\} \\ +\hat{J}_{ab}\hat{J}'_{ab} \begin{Bmatrix} j_a & j_b & J_{ab} \\ j_c & J & J'_{ab} \end{Bmatrix} & : \xi = \{321\} \\ -(-)^{J_{ab}+j_a+j_b}\hat{J}_{ab}\hat{J}'_{ab} \begin{Bmatrix} j_b & j_a & J_{ab} \\ j_c & J & J'_{ab} \end{Bmatrix} & : \xi = \{312\} \\ -(-)^{J_{ab}+J'_{ab}+j_b+j_c}\hat{J}_{ab}\hat{J}'_{ab} \begin{Bmatrix} j_b & j_a & J_{ab} \\ j_c & J & J'_{ab} \end{Bmatrix} & : \xi = \{132\} \end{cases}. \tag{E.12}$$

Substituting this into the original expression for the three-body part, we get

$$\frac{1}{2} \sum_{\substack{qq' \\ rr'}} \langle pqr | \boldsymbol{H}^{[3]} | p'q'r' \rangle \, \rho_{qq'} \rho_{rr'} = \frac{1}{2} \sum_{\substack{\bar{q}\bar{q}' \\ j_q = j_q'}} \sum_{\substack{\bar{r}\bar{r}' \\ j_r = j_r'}} \overline{\langle \bar{p}\bar{q}\bar{r} | \boldsymbol{H}^{[3]} | \bar{p}'\bar{q}'\bar{r}' \rangle} \tilde{\rho}_{\bar{q}\bar{q}'} \, \tilde{\rho}_{\bar{r}\bar{r}'}. \tag{E.13}$$

The prefactor can be removed by using invariance of the equation under renaming the summation indices $(q, q') \leftrightarrow (r, r')$.

E.3. Two-Body Part of the Normal-Ordered Two-Body Approximation

The previous two sections considered those sums over one-body densities that are necessary for a Hartree-Fock calculation. To compute a normal-ordered two-body approximation of the three-body part of the Hamiltonian with respect to a reference state consisting of a single Slater Determinant, e.g., the Hartree-Fock ground state, we only need the additional ingredient

$$\langle (\bar{p}\bar{q})J | \tilde{\boldsymbol{H}}^{[3]} | (\bar{p}'\bar{q}')J' \rangle = \sum_{\substack{m_p m_q \\ m_p' m_q'}} \begin{pmatrix} j_p & j_q \, \big| \, J \\ m_p & m_q \, \big| \, M \end{pmatrix} \begin{pmatrix} j_p' & j_q' \, \big| \, J' \\ m_p' & m_q' \, \big| \, M' \end{pmatrix} \sum_{rr'} \langle pqr | \boldsymbol{H}^{[3]} | p'q'r' \rangle \, \rho_{rr'}. \tag{E.14}$$

Again using rotational invariance of the density and operator, we rephrase the equation as an average over the projection m_r:

$$\langle (\bar{p}\bar{q})J | \tilde{\boldsymbol{H}}^{[3]} | (\bar{p}'\bar{q}')J' \rangle = \sum_{\substack{\bar{r}\bar{r}' \\ j_r = j_r'}} \hat{j}_r^{-2} \sum_{\substack{m_p m_q m_r \\ m_p' m_q'}} \begin{pmatrix} j_p & j_q \, \big| \, J \\ m_p & m_q \, \big| \, M \end{pmatrix} \begin{pmatrix} j_p' & j_q' \, \big| \, J' \\ m_p' & m_q' \, \big| \, M' \end{pmatrix} \langle pqr | \boldsymbol{H}^{[3]} | p'q'r' \rangle \, \tilde{\rho}_{\bar{r}\bar{r}'}. \tag{E.15}$$

We only consider the *m*-dependent part, along with the pertinent sums. Expanding the three-body matrix element, we have

$$\sum_{\substack{m_p m_q m_r \\ m_p' m_q'}} \begin{pmatrix} j_p & j_q \, \big| \, J \\ m_p & m_q \, \big| \, M \end{pmatrix} \begin{pmatrix} j_p' & j_q' \, \big| \, J' \\ m_p' & m_q' \, \big| \, M' \end{pmatrix} \langle pqr | \boldsymbol{H}^{[3]} | p'q'r' \rangle$$

$$= \sum_{\substack{m_p m_q m_r \\ m_p' m_q'}} \sum_{\substack{J_{ab} M_{ab} \\ J_{ab}' M_{ab}'}} \sum_{\mathcal{J}\mathcal{M}} \begin{pmatrix} j_p & j_q \, \big| \, J \\ m_p & m_q \, \big| \, M \end{pmatrix} \begin{pmatrix} j_p & j_q \, \big| \, J_{ab} \\ m_p & m_q \, \big| \, M_{ab} \end{pmatrix} \begin{pmatrix} j_p' & j_q' \, \big| \, J' \\ m_p' & m_q' \, \big| \, M' \end{pmatrix} \begin{pmatrix} j_p' & j_q' \, \big| \, J_{ab}' \\ m_p' & m_q' \, \big| \, M_{ab}' \end{pmatrix}$$

$$\times \begin{pmatrix} J_{ab} & j_r \, \big| \, \mathcal{J} \\ M_{ab} & m_r \, \big| \, \mathcal{M} \end{pmatrix} \begin{pmatrix} J_{ab}' & j_r \, \big| \, \mathcal{J} \\ M_{ab}' & m_r \, \big| \, \mathcal{M} \end{pmatrix} \langle [(\bar{p}\bar{q})J_{ab}, \bar{r}]\mathcal{J} | \boldsymbol{H}^{[3]} | [(\bar{p}'\bar{q}')J_{ab}', \bar{r}']\mathcal{J} \rangle$$

$$= \sum_{\mathcal{J}\mathcal{M} m_r} (-1)^{2(j_r + m_r)} \frac{\hat{\mathcal{J}}^2}{\hat{J}\hat{J}'} \begin{pmatrix} j_r & \mathcal{J} \, \big| \, J \\ -m_r & \mathcal{M} \, \big| \, M \end{pmatrix} \begin{pmatrix} j_r & \mathcal{J} \, \big| \, J' \\ -m_r & \mathcal{M} \, \big| \, M' \end{pmatrix} \langle [(\bar{p}\bar{q})J, \bar{r}]\mathcal{J} | \boldsymbol{H}^{[3]} | [(\bar{p}'\bar{q}')J', \bar{r}']\mathcal{J} \rangle$$

$$= \delta_{JM}^{J'M'} \sum_{\mathcal{J}} \frac{\hat{\mathcal{J}}^2}{\hat{J}^2} \langle [(\bar{p}\bar{q})J, \bar{r}]\mathcal{J} | \boldsymbol{H}^{[3]} | [(\bar{p}'\bar{q}')J', \bar{r}']\mathcal{J} \rangle. \tag{E.16}$$

E. Angular-Momentum-Coupled Spherical Hartree-Fock

To map the coupled matrix elements to the ones present in the matrix-element file, we insert permutation operators

$$= \delta_{JM}^{J'M'} \sum_{\mathscr{J}} \operatorname{sgn} \sigma \operatorname{sgn} \pi \frac{\hat{\mathscr{J}}^2}{\hat{J}^2} \,_n\langle [(\bar{p}\bar{q})J, \bar{r}]\mathscr{J} | P_\sigma^\dagger \mathscr{A} H^{[3]} \mathscr{A} P_\pi | [(\bar{p}'\bar{q}')J, \bar{r}']\mathscr{J}\rangle_n . \tag{E.17}$$

The action of the permutation operator is

$$\operatorname{sgn} \pi P_\pi |[(\bar{p}'\bar{q}')J, \bar{r}']\mathscr{J}\rangle_n = \operatorname{sgn} \pi \sum_{m'_p m'_q m'_r} \begin{pmatrix} j'_p & j'_q \\ m'_p & m'_q \end{pmatrix} \begin{pmatrix} J \\ M \end{pmatrix} \begin{pmatrix} J & j'_r \\ M & m'_r \end{pmatrix} \begin{pmatrix} \mathscr{J} \\ \mathscr{M} \end{pmatrix} |\pi(p')\pi(q')\pi(r')\rangle_n$$

$$= \begin{cases} |[(\pi(\bar{p}')\pi(\bar{q}'))J, \pi(\bar{r}')]\mathscr{J}\rangle_n & : \pi = \{123\} \\ -(-)^{J+j_{\pi(p')}+j_{\pi(q')}} |[(\pi(\bar{p}')\pi(\bar{q}'))J, \pi(\bar{r}')]\mathscr{J}\rangle_n & : \pi = \{213\} \\ (-)^{J+j_{\pi(p')}+j_{\pi(r')}} |[(\pi(\bar{p}')\pi(\bar{r}'))_{13}J, \pi(\bar{q}')]\mathscr{J}\rangle_n & : \pi = \{231\} \\ -(-)^{\mathscr{J}+j_{\pi(r')}+j_{\pi(q')}-j_{\pi(p')}} |[\pi(\bar{p}'), (\pi(\bar{q}')\pi(\bar{r}'))J]\mathscr{J}\rangle_n & : \pi = \{321\} \\ (-)^{\mathscr{J}-J-j_{\pi(p')}} |[\pi(\bar{p}'), (\pi(\bar{q}')\pi(\bar{r}'))J]\mathscr{J}\rangle_n & : \pi = \{312\} \\ - |[(\pi(\bar{p}')\pi(\bar{r}'))_{13}J, \pi(\bar{q}')]\mathscr{J}\rangle_n & : \pi = \{132\} \end{cases}$$

$$= \sum_{J'_{ab}} \hat{J} C(j'_p j'_q j'_r J, J'_{ab}\mathscr{J}, \pi) |[(\pi(\bar{p}')\pi(\bar{q}'))J'_{ab}, \pi(\bar{r}')]\mathscr{J}\rangle_n \tag{E.18}$$

with

$$C(j'_p j'_q j'_r J, J'_{ab}\mathscr{J}, \pi) = \begin{cases} \hat{J}^{-1} \delta_J^{J'_{ab}} & : \pi = \{123\} \\ -(-)^{J-j_{\pi(p')}-j_{\pi(q')}} \hat{J}^{-1} \delta_J^{J'_{ab}} & : \pi = \{213\} \\ (-)^{2J+J'_{ab}-j_{\pi(p')}+j_{\pi(q')}} \hat{J}'_{ab} \begin{Bmatrix} j_{\pi(q')} & j_{\pi(p')} & J'_{ab} \\ j_{\pi(r')} & \mathscr{J} & J \end{Bmatrix} & : \pi = \{231\} \\ -(-)^{2\mathscr{J}} \hat{J}'_{ab} \begin{Bmatrix} j_{\pi(p')} & j_{\pi(q')} & J'_{ab} \\ j_{\pi(r')} & \mathscr{J} & J \end{Bmatrix} & : \pi = \{321\} \\ (-)^{2\mathscr{J}-J+j_{\pi(q')}+j_{\pi(r')}} \hat{J}'_{ab} \begin{Bmatrix} j_{\pi(p')} & j_{\pi(q')} & J'_{ab} \\ j_{\pi(r')} & \mathscr{J} & J \end{Bmatrix} & : \pi = \{312\} \\ -(-)^{J'_{ab}+J+j_{\pi(q')}+j_{\pi(r')}} \hat{J}'_{ab} \begin{Bmatrix} j_{\pi(q')} & j_{\pi(p')} & J'_{ab} \\ j_{\pi(r')} & \mathscr{J} & J \end{Bmatrix} & : \pi = \{132\}. \end{cases} \tag{E.19}$$

The phase factors are presented without any assumptions on the spins being integers or half-integers. For fermionic total angular momenta, they become

$$C(j_p'j_q'j_r'J, J_{ab}'\mathscr{J}, \pi) = \begin{cases} \hat{J}^{-1}\delta_J^{J_{ab}'} & : \pi = \{123\} \\ -(-)^{J+j_{\pi(p')}+j_{\pi(q')}}\hat{J}^{-1}\delta_J^{J_{ab}'} & : \pi = \{213\} \\ -(-)^{J_{ab}'+j_{\pi(p')}+j_{\pi(q')}}\hat{J}_{ab}' \begin{Bmatrix} j_{\pi(q')} & j_{\pi(p')} & J_{ab}' \\ j_{\pi(r')} & \mathscr{J} & J \end{Bmatrix} & : \pi = \{231\} \\ +\hat{J}_{ab}' \begin{Bmatrix} j_{\pi(p')} & j_{\pi(q')} & J_{ab}' \\ j_{\pi(r')} & \mathscr{J} & J \end{Bmatrix} & : \pi = \{321\} \\ -(-)^{J+j_{\pi(q')}+j_{\pi(r')}}\hat{J}_{ab}' \begin{Bmatrix} j_{\pi(p')} & j_{\pi(q')} & J_{ab}' \\ j_{\pi(r')} & \mathscr{J} & J \end{Bmatrix} & : \pi = \{312\} \\ -(-)^{J_{ab}'+J+j_{\pi(q')}+j_{\pi(r')}}\hat{J}_{ab}' \begin{Bmatrix} j_{\pi(q')} & j_{\pi(p')} & J_{ab}' \\ j_{\pi(r')} & \mathscr{J} & J \end{Bmatrix} & : \pi = \{132\}. \end{cases} \quad \text{(E.20)}$$

Inserting this result into (E.17), we get

$$\sum_{\substack{m_p m_q m_r \\ m_p' m_q'}} \begin{pmatrix} j_p & j_q \\ m_p & m_q \end{pmatrix} \begin{pmatrix} j_p' & j_q' \\ m_p' & m_q' \end{pmatrix} \langle pqr|H^{[3]}|p'q'r'\rangle$$

$$= \delta_{JM}^{J'M'} \sum_{\mathscr{J}J_{ab}'J_{ab}} \hat{\mathscr{J}}^2 C(j_pj_qj_rJ, J_{ab}\mathscr{J}, \sigma)C(j_p'j_q'j_r'J, J_{ab}'\mathscr{J}, \pi)$$

$$\times \langle[(\sigma(\bar{p})\sigma(\bar{q}))J_{ab}, \sigma(\bar{r})]\mathscr{J}|H^{[3]}|[(\pi(\bar{p}')\pi(\bar{q}'))J_{ab}', \pi(\bar{r}')]\mathscr{J}\rangle, \quad \text{(E.21)}$$

and we can interpret the sum on the right-hand side as a matrix-bilinear $C^T M C'$ if we take the Cs as vectors over a combined index $(J_{ab}, \mathscr{J})$:

$$= \sum_{\substack{\mathscr{J}'\mathscr{J} \\ J_{ab}'J_{ab}}} C_{(J_{ab},\mathscr{J})}(j_pj_qj_rJ, \sigma)M_{(J_{ab},\mathscr{J}),(J_{ab}',\mathscr{J}')}(\bar{p}\bar{q}\bar{r}\sigma; \bar{p}'\bar{q}'\bar{r}'\pi)C_{(J_{ab}',\mathscr{J}')}(j_p'j_q'j_r'J, \pi) \quad \text{(E.22)}$$

with

$$M_{(J_{ab},\mathscr{J}),(J_{ab}',\mathscr{J}')}(\bar{p}\bar{q}\bar{r}\sigma; \bar{p}'\bar{q}'\bar{r}'\pi) =$$

$$\hat{\mathscr{J}}^2 \langle[(\sigma(\bar{p})\sigma(\bar{q}))J_{ab}, \sigma(\bar{r})]\mathscr{J}|H^{[3]}|[(\pi(\bar{p}')\pi(\bar{q}'))J_{ab}', \pi(\bar{r}')]\mathscr{J}\rangle \delta_{\mathscr{J}}^{\mathscr{J}'}. \quad \text{(E.23)}$$

Bibliography

[AAA+17] B. P. Abbott, R. Abbott, T. D. Abbott, et al., Phys. Rev. Lett. **119**, 161101 (2017), `10.1103/PhysRevLett.119.161101`, arXiv:`1710.05836`.

[AAC+02] H. Akikawa, S. Ajimura, R. Chrien, et al., Phys. Rev. Lett. **88**, 082501 (2002), `10.1103/PhysRevLett.88.082501`.

[AFW+13] J. Antoniadis, P. C. C. Freire, N. Wex, et al., Science **340**, 1233232 (2013), `10.1126/science.1233232`.

[Ajz90] F. Ajzenberg-Selove, Nucl. Phys. A **506**, 1–158 (1990), `10.1016/0375-9474(90)90271-M`.

[Ban81] H. Bando, Prog. Theor. Phys. **66**, 1349–1360 (1981), `10.1143/PTP.66.1349`.

[BBL+07] S. R. Beane, P. F. Bedaque, T. C. Luu, et al., Nucl. Phys. A **794**, 62–72 (2007), `10.1016/j.nuclphysa.2007.07.006`.

[BBP63] H. A. Bethe, B. H. Brandow, and A. G. Petschek, Phys. Rev. **129**, 225–264 (1963), `10.1103/PhysRev.129.225`.

[Bet65] H. A. Bethe, Phys. Rev. **138**, B804 (1965), `10.1103/PhysRev.138.B804`.

[BFP07] S. Bogner, R. J. Furnstahl, and R. Perry, Phys. Rev. C **75**, 061001 (2007), `10.1103/PhysRevC.75.061001`.

[BG60] K. A. Brueckner and D. T. Goldman, Phys. Rev. **117**, 207–213 (1960), `10.1103/PhysRev.117.207`.

[BG97] S. Balberg and A. Gal, Nucl. Phys. A **625**, 435–472 (1997), `10.1016/S0375-9474(97)81465-0`.

[Bin10] S. Binder, "Angular Momentum Projection and Three-Body Forces in the No-Core Shell Model", master's thesis (TU Darmstadt, 2010).

[BKS03] S. Bogner, T. Kuo, and A. Schwenk, Phys. Rep. **386**, 1–27 (2003), `10.1016/j.physrep.2003.07.001`.

[BLC+14] S. Binder, J. Langhammer, A. Calci, and R. Roth, Phys. Lett. B **736**, 119–123 (2014), `10.1016/j.physletb.2014.07.010`, arXiv:`1312.5685`.

[BNQ13] S. Baroni, P. Navrátil, and S. Quaglioni, Phys. Rev. Lett. **110**, 022505 (2013), `10.1103/PhysRevLett.110.022505`, arXiv:`1210.1897`; Phys. Rev. C **87**, 034326 (2013), `10.1103/PhysRevC.87.034326`, arXiv:`1301.3450`.

[BNV13]   B. R. Barrett, P. Navrátil, and J. P. Vary, Prog. Part. Nucl. Phys. **69**, 131–181 (2013), `10.1016/j.ppnp.2012.10.003`.

[BPC⁺13]   S. Binder, P. Piecuch, A. Calci, et al., Phys. Rev. C **88**, 054319 (2013), `10.1103/PhysRevC.88.054319`, arXiv:`1309.1123`.

[Cal10]   A. Calci, "Ab initio nuclear structure with SRG-transformed chiral NN plus NNN interactions", master's thesis (TU Darmstadt, 2010).

[Cal14]   A. Calci, "Evolved Chiral Hamiltonians at the Three-Body Level and Beyond", doctoral thesis (TU Darmstadt, 2014).

[CLS00]   J. Cugnon, A. Lejeune, and H.-J. Schulze, Phys. Rev. C **62**, 064308 (2000), `10.1103/PhysRevC.62.064308`.

[CNR⁺16]   A. Calci, P. Navrátil, R. Roth, et al., Phys. Rev. Lett. **117**, 242501 (2016), `10.1103/PhysRevLett.117.242501`, arXiv:`1608.03318`.

[Coe58]   F. Coester, Nucl. Phys. **7**, 421–424 (1958), `10.1016/0029-5582(58)90280-3`.

[CUA⁺09]   F. Cusanno, G. M. Urciuoli, A. Acha, et al., Phys. Rev. Lett. **103**, 202501 (2009), `10.1103/PhysRevLett.103.202501`, arXiv:`0810.3853`.

[Dav05]   D. H. Davis, Nucl. Phys. A **754**, 3–13 (2005), `10.1016/j.nuclphysa.2005.01.002`.

[Day67]   B. D. Day, Rev. Mod. Phys. **39**, 719–744 (1967), `10.1103/RevModPhys.39.719`.

[DLMF]   F. W. J. Olver, A. B. Olde Daalhuis, D. W. Lozier, et al., eds., *NIST Digital Library of Mathematical Functions*, `http://dlmf.nist.gov/`.

[DP53]   M. Danysz and J. Pniewski, Phil. Mag. **44**, 348–350 (1953), `10.1080/14786440308520318`.

[DPR⁺10]   P. B. Demorest, T. Pennucci, S. M. Ransom, et al., Nature **467**, 1081–1083 (2010), `10.1038/nature09466`, arXiv:`1010.5788`.

[EHM09]   E. Epelbaum, H.-W. Hammer, and U.-G. Meißner, Rev. Mod. Phys. **81**, 1773–1825 (2009), `10.1103/RevModPhys.81.1773`, arXiv:`0811.1338`.

[EKM15]   E. Epelbaum, H. Krebs, and U.-G. Meißner, Phys. Rev. Lett. **115**, 122301 (2015), `10.1103/PhysRevLett.115.122301`, arXiv:`1412.4623`.

[EM03]   D. R. Entem and R. Machleidt, Phys. Rev. C **68**, 041001 (2003), `10.1103/PhysRevC.68.041001`, arXiv:`0304018 [nucl-th]`.

[EMN17]   D. R. Entem, R. Machleidt, and Y. Nosyk, Phys. Rev. C **96**, 024004 (2017), `10.1103/PhysRevC.96.024004`, arXiv:`1703.05454`.

[ENS⁺15]   A. Esser, S. Nagao, F. Schulz, et al., Phys. Rev. Lett. **114**, 232501 (2015), `10.1103/PhysRevLett.114.232501`, arXiv:`1501.06823`.

[FNR⁺98]   H. Feldmeier, T. Neff, R. Roth, and J. Schnack, Nucl. Phys. A **632**, 61–95 (1998), `10.1016/S0375-9474(97)00805-1`, arXiv:`9709038 [nucl-th]`.

[GAC+94]   B. F. Gibson, I. R. Afnan, J. A. Carlson, and D. R. Lehman, Prog. Theor. Phys. Suppl. **117**, 339–350 (1994), `10.1143/PTPS.117.339`, arXiv:9411027 `[nucl-th]`.

[Gau60]   M. Gaudin, Nucl. Phys. **15**, 89–91 (1960), `10.1016/0029-5582(60)90285-6`.

[GCR+14]   S. Gandolfi, J. Carlson, S. Reddy, et al., Eur. Phys. J. A **50**, 1–11 (2014), `10.1140/epja/i2014-14010-5`, arXiv:1307.5815.

[GCR12]   S. Gandolfi, J. Carlson, and S. Reddy, Phys. Rev. C **85**, 032801 (2012), `10.1103/PhysRevC.85.032801`, arXiv:1101.1921.

[GDS12]   N. Guleria, S. K. Dhiman, and R. Shyam, Nucl. Phys. A **886**, 71–91 (2012), `10.1016/j.nuclphysa.2012.05.005`, arXiv:1108.0787.

[Gel56]   M. Gell-Mann, Nuovo Cim. **4**, 848–866 (1956), `10.1007/BF02748000`.

[GH95]   B. Gibson and E. Hungerford, Phys. Rep. **257**, 349–388 (1995), `10.1016/0370-1573(94)00114-I`.

[GHM16]   A. Gal, E. V. Hungerford, and D. J. Millener, Rev. Mod. Phys. **88**, 035004 (2016), `10.1103/RevModPhys.88.035004`, arXiv:1605.00557.

[GM11]   A. Gal and D. Millener, Phys. Lett. B **701**, 342–345 (2011), `10.1016/j.physletb.2011.05.069`, arXiv:1104.3429.

[GSD71]   A. Gal, J. Soper, and R. Dalitz, Ann. Phys. (NY) **63**, 53–126 (1971), `10.1016/0003-4916(71)90297-1`; ibid. **72**, 445–488 (1972), `10.1016/0003-4916(72)90222-9`; ibid. **113**, 79–97 (1978), `10.1016/0003-4916(78)90250-6`.

[GVH+93]   N. K. Glendenning, D. Von-Eiff, M. Haft, et al., Phys. Rev. C **48**, 889–895 (1993), `10.1103/PhysRevC.48.889`, arXiv:9211012 `[nucl-th]`.

[GW93]   S. Głazek and K. Wilson, Phys. Rev. D **48**, 5863–5872 (1993), `10.1103/PhysRevD.48.5863`.

[Hal93]   D. Halderson, Phys. Rev. C **48**, 581–587 (1993), `10.1103/PhysRevC.48.581`.

[Has17]   K. S. A. Hassaneen, Eur. Phys. J. A **53**, 9 (2017), `10.1140/epja/i2017-12196-6`.

[HBM+16]   H. Hergert, S. Bogner, T. Morris, et al., Phys. Rep. **621**, 165–222 (2016), `10.1016/j.physrep.2015.12.007`, arXiv:1512.06956.

[HH00]   H. Heiselberg and M. Hjorth-Jensen, Phys. Rep. **328**, 237–327 (2000), `10.1016/S0370-1573(99)00110-6`, arXiv:9902033 `[nucl-th]`.

[Hiy12]   E. Hiyama, Few-Body Syst. **53**, 189–236 (2012), `10.1007/s00601-011-0296-8`.

[HKM+01]   E. Hiyama, M. Kamimura, T. Motoba, et al., Phys. Rev. C **65**, 011301 (2001), `10.1103/PhysRevC.65.011301`, arXiv:0106070 `[nucl-th]`.

Bibliography

[HLK17]   M. Hjorth-Jensen, M. P. Lombardo, and U. van Kolck, eds., *An Advanced Course in Computational Nuclear Physics*, Vol. 936, Lecture Notes in Physics (Springer International Publishing, Cham, 2017), `10.1007/978-3-319-53336-0`.

[HM05]   J. Haidenbauer and U.-G. Meißner, Phys. Rev. C **72**, 044005 (2005), `10.1103/PhysRevC.72.044005`, arXiv:`0506019 [nucl-th]`.

[HMN+07]   J. Haidenbauer, U.-G. Meißner, A. Nogga, and H. Polinder, Lect. Notes Phys. **724**, edited by P. Bydžovský, J. Mareš, and A. Gal, 113–140 (2007), `10.1007/978-3-540-72039-3`, arXiv:`0702015 [nucl-th]`.

[HMP16]   J. Haidenbauer, U.-G. Meißner, and S. Petschauer, Nucl. Phys. A **954**, 273–293 (2016), `10.1016/j.nuclphysa.2016.01.006`, arXiv:`1511.05859`.

[HPK+13]   J. Haidenbauer, S. Petschauer, N. Kaiser, et al., Nucl. Phys. A **915**, 24–58 (2013), `10.1016/j.nuclphysa.2013.06.008`, arXiv:`1304.5339`.

[HT06]   O. Hashimoto and H. Tamura, Prog. Part. Nucl. Phys. **57**, 564–653 (2006), `10.1016/j.ppnp.2005.07.001`.

[HXW+17]   B. S. Hu, F. R. Xu, Q. Wu, et al., Phys. Rev. C **95**, 1–10 (2017), `10.1103/PhysRevC.95.034321`.

[Jül16]   Jülich Supercomputing Centre, J. Large-Scale Res. Facil. **2**, A62 (2016), `10.17815/jlsrf-2-121`.

[KKB+01]   G. Kamuntavičius, R. Kalinauskas, B. R. Barrett, et al., Nucl. Phys. A **695**, 191–201 (2001), `10.1016/S0375-9474(01)01101-0`, arXiv:`0105009 [nucl-th]`.

[KKP+12]   J. Kelley, E. Kwan, J. Purcell, et al., Nucl. Phys. A **880**, 88–195 (2012), `10.1016/j.nuclphysa.2012.01.010`.

[KM97]   W. Kutzelnigg and D. Mukherjee, J. Chem. Phys. **107**, 432–449 (1997), `10.1063/1.474405`.

[Lan50]   C. Lanczos, J. Res. Natl. Bur. Stand. **45**, 255 (1950), `10.6028/jres.045.026`.

[Lat12]   J. M. Lattimer, Annu. Rev. Nucl. Part. Sci. **62**, 485–515 (2012), `10.1146/annurev-nucl-102711-095018`, arXiv:`1305.3510`.

[LGP13]   D. Lonardoni, S. Gandolfi, and F. Pederiva, Phys. Rev. C **87**, 041303(R) (2013), `10.1103/PhysRevC.87.041303`, arXiv:`1301.7472`.

[LHS+16]   A. Li, J. N. Hu, X. L. Shang, and W. Zuo, Phys. Rev. C **93**, 015803 (2016), `10.1103/PhysRevC.93.015803`, arXiv:`1511.07979`.

[LLC+17]   J.-J. Lu, Z.-H. Li, C.-Y. Chen, et al., Phys. Rev. C **96**, 044309 (2017), `10.1103/PhysRevC.96.044309`.

[LLG+15]   D. Lonardoni, A. Lovato, S. Gandolfi, and F. Pederiva, Phys. Rev. Lett. **114**, 092301 (2015), `10.1103/PhysRevLett.114.092301`, arXiv:`1407.4448`.

[LMN16]   S. Liebig, U.-G. Meißner, and A. Nogga, Eur. Phys. J. A **52**, 103 (2016), `10.1140/epja/i2016-16103-5`.

[LNQ⁺15]   J. Langhammer, P. Navrátil, S. Quaglioni, et al., Phys. Rev. C **91**, 021301(R) (2015), `10.1103/PhysRevC.91.021301`, arXiv:`1411.2541`.

[LPG14]   D. Lonardoni, F. Pederiva, and S. Gandolfi, Phys. Rev. C **89**, 014314 (2014), `10.1103/PhysRevC.89.014314`, arXiv:`1312.3844`.

[LS80]   S. Lee and K. Suzuki, Phys. Lett. B **91**, 173–176 (1980), `10.1016/0370-2693(80)90423-2`.

[LSY97]   R. B. Lehoucq, D. C. Sorensen, and C. Yang, *ARPACK Library*, 1997.

[Mac01]   R. Machleidt, Phys. Rev. C **63**, 024001 (2001), `10.1103/PhysRevC.63.024001`, arXiv:`0006014 [nucl-th]`.

[MBI⁺85]   T. Motoba, H. Bandō, K. Ikeda, and T. Yamada, Prog. Theor. Phys. Suppl. **81**, 42–103 (1985), `10.1143/PTPS.81.42`.

[ME11]   R. Machleidt and D. Entem, Phys. Rep. **503**, 1–75 (2011), `10.1016/j.physrep.2011.02.001`, arXiv:`1105.2919`.

[Mil07]   D. J. Millener, "Hypernuclear Gamma-Ray Spectroscopy and the Structure of p-shell Nuclei and Hypernuclei", in *Top. strangeness nucl. phys.* Vol. 724, edited by P. Bydžovský, J. Mareš, and A. Gal, Lecture Notes in Physics (Springer Berlin Heidelberg, Berlin, Heidelberg, 2007), pp. 31–79, `10.1007/978-3-540-72039-3_2`.

[MRS89]   P. M. M. Maessen, T. A. Rijken, and J. J. de Swart, Phys. Rev. C **40**, 2226 (1989), `10.1103/PhysRevC.40.2226`.

[NAD⁺17]   H. Nemura, S. Aoki, T. Doi, et al., in 34th annu. int. symp. lattice f. theory (Feb. 2017), PoS(LATTICE2016)101, arXiv:`1702.00734`.

[Nak⁺10]   K. Nakamura et al., J. Phys. G **37**, 075021 (2010), `10.1088/0954-3899/37/7A/075021`.

[Nak10]   K. Nakazawa, Nucl. Phys. A **835**, 207–214 (2010), `10.1016/j.nuclphysa.2010.01.195`.

[NAS02]   H. Nemura, Y. Akaishi, and Y. Suzuki, Phys. Rev. Lett. **89**, 142504 (2002), `10.1103/PhysRevLett.89.142504`, arXiv:`0203013 [nucl-th]`.

[Nav07]   P. Navrátil, Few-Body Syst. **41**, 117–140 (2007), `10.1007/s00601-007-0193-3`, arXiv:`0707.4680`.

[Nem09]   H. Nemura, Phys. Lett. B **673**, 136–141 (2009), `10.1016/j.physletb.2009.02.003`, arXiv:`0806.1094`.

[NKB00]   P. Navrátil, G. P. Kamuntavičius, and B. R. Barrett, Phys. Rev. C **61**, 044001 (2000), `10.1103/PhysRevC.61.044001`, arXiv:`9907054 [nucl-th]`.

[NKG02]   A. Nogga, H. Kamada, and W. Glöckle, Phys. Rev. Lett. **88**, 172501 (2002), `10.1103/PhysRevLett.88.172501`, arXiv:`0112060 [nucl-th]`.

Bibliography

[NMO⁺13]   S. N. Nakamura, A. Matsumura, Y. Okayasu, et al., Phys. Rev. Lett. **110**, 012502 (2013), `10.1103/PhysRevLett.110.012502`, arXiv:`1207.0571`.

[Nog05]   A. Nogga, Nucl. Phys. A **754**, 36–42 (2005), `10.1016/j.nuclphysa.2005.01.013`.

[Nog13]   A. Nogga, Nucl. Phys. A **914**, 140–150 (2013), `10.1016/j.nuclphysa.2013.02.053`.

[OHK⁺17]   M. Oertel, M. Hempel, T. Klähn, and S. Typel, Rev. Mod. Phys. **89**, 015007 (2017), `10.1103/RevModPhys.89.015007`, arXiv:`1610.03361`.

[Ôku54]   S. Ôkubo, Prog. Theor. Phys. **12**, 603–622 (1954), `10.1143/PTP.12.603`.

[OV39]   J. R. Oppenheimer and G. M. Volkoff, Phys. Rev. **55**, 374–381 (1939), `10.1103/PhysRev.55.374`.

[PHK⁺16]   S. Petschauer, J. Haidenbauer, N. Kaiser, et al., Eur. Phys. J. A **52**, 15 (2016), `10.1140/epja/i2016-16015-4`, arXiv:`1507.08808`.

[PHM06]   H. Polinder, J. Haidenbauer, and U.-G. Meißner, Nucl. Phys. A **779**, 244–266 (2006), `10.1016/j.nuclphysa.2006.09.006`, arXiv:`0605050 [nucl-th]`.

[PR08]   S. Perez-Martin and L. M. Robledo, Phys. Rev. C **78**, 014304 (2008), `10.1103/PhysRevC.78.014304`, arXiv:`0805.4318`.

[PW05]   P. Piecuch and M. Włoch, J. Chem. Phys. **123**, 224105 (2005), `10.1063/1.2137318`.

[RB67]   R. Rajaraman and H. A. Bethe, Rev. Mod. Phys. **39**, 745–770 (1967), `10.1103/RevModPhys.39.745`.

[RBV⁺12]   R. Roth, S. Binder, K. Vobig, et al., Phys. Rev. Lett. **109**, 052501 (2012), `10.1103/PhysRevLett.109.052501`, arXiv:`1112.0287`.

[RCL⁺14]   R. Roth, A. Calci, J. Langhammer, and S. Binder, Phys. Rev. C **90**, 024325 (2014), `10.1103/PhysRevC.90.024325`, arXiv:`1311.3563`.

[RGP09]   R. Roth, J. R. Gour, and P. Piecuch, Phys. Rev. C **79**, 054325 (2009), `10.1103/PhysRevC.79.054325`, arXiv:`0806.0333`.

[RHK⁺96]   A. Reuber, K. Holinde, H.-C. Kim, and J. Speth, Nucl. Phys. A **608**, 243–304 (1996), `10.1016/0375-9474(96)00256-4`, arXiv:`9511011 [nucl-th]`.

[RLC⁺11]   R. Roth, J. Langhammer, A. Calci, et al., Phys. Rev. Lett. **107**, 072501 (2011), `10.1103/PhysRevLett.107.072501`, arXiv:`1105.3173`.

[Rot09]   R. Roth, Phys. Rev. C **79**, 064324 (2009), `10.1103/PhysRevC.79.064324`, arXiv:`0903.4605`.

[RPP⁺06]   R. Roth, P. Papakonstantinou, N. Paar, et al., Phys. Rev. C **73**, 044312 (2006), `10.1103/PhysRevC.73.044312`, arXiv:`0510036 [nucl-th]`.

[RSY99]   T. A. Rijken, V. Stoks, and Y. Yamamoto, Phys. Rev. C **59**, 21–40 (1999), `10.1103/PhysRevC.59.21`, arXiv:`9807082 [nucl-th]`.

[RY06]   T. A. Rijken and Y. Yamamoto, Phys. Rev. C **73**, 66 (2006), `10.1103/PhysRevC.73.044008`, arXiv:`0603042 [nucl-th]`.

[SB09]   I. Shavitt and R. J. Bartlett, *Many-Body Methods in Chemistry and Physics* (Cambridge University Press, Cambridge, 2009), `10.1017/CBO9780511596834`.

[SCB06]   C. Samanta, P. R. Chowdhury, and D. N. Basu, J. Phys. G **32**, 363–373 (2006), `10.1088/0954-3899/32/3/010`, arXiv:`0504085 [nucl-th]`.

[Sch18]   S. Schulz, "Four-Nucleon Forces in Ab-Initio Nuclear Structure", in preparation, doctoral thesis (TU Darmstadt, 2018).

[SFI⁺05]   P. K. Saha, T. Fukuda, W. Imoto, et al., Phys. Rev. Lett. **94**, 052502 (2005), `10.1103/PhysRevLett.94.052502`.

[SNY⁺08]   P. Sternberg, E. G. Ng, C. Yang, et al., in Proc. 2008 acm/ieee conf. supercomput. (2008), 15:1–15:12.

[SO96]   A. Szabo and N. S. Ostlund, *Modern Quantum Chemistry* (Dover Publications, New York, 1996).

[TAA⁺01]   H. Takahashi, J. K. Ahn, H. Akikawa, et al., Phys. Rev. Lett. **87**, 212502 (2001), `10.1103/PhysRevLett.87.212502`.

[TAA⁺05]   H. Tamura, S. Ajimura, H. Akikawa, et al., Nucl. Phys. A **754**, 58–69 (2005), `10.1016/j.nuclphysa.2005.01.034`, arXiv:`0411028 [nucl-ex]`.

[TCG⁺02]   D. Tilley, C. Cheves, J. Godwin, et al., Nucl. Phys. A **708**, 3–163 (2002), `10.1016/S0375-9474(02)00597-3`.

[TKG⁺04]   D. Tilley, J. Kelley, J. Godwin, et al., Nucl. Phys. A **745**, 155–362 (2004), `10.1016/j.nuclphysa.2004.09.059`.

[TLB⁺16]   A. Tichai, J. Langhammer, S. Binder, and R. Roth, Phys. Lett. B **756**, 283–288 (2016), `10.1016/j.physletb.2016.03.029`, arXiv:`1601.03703`.

[TTA⁺00]   H. Tamura, K. Tanida, D. Abe, et al., Phys. Rev. Lett. **84**, 5963–5966 (2000), `10.1103/PhysRevLett.84.5963`.

[TTA⁺01]   K. Tanida, H. Tamura, D. Abe, et al., Phys. Rev. Lett. **86**, 1982–1985 (2001), `10.1103/PhysRevLett.86.1982`.

[VLP⁺11]   I. Vidaña, D. Logoteta, C. Providência, et al., Europhys. Lett. **94**, 11002 (2011), `10.1209/0295-5075/94/11002`, arXiv:`1006.5660`.

[VMK88]   D. A. Varshalovich, A. N. Moskalev, and V. K. Khersonskii, *Quantum Theory of Angular Momentum* (World Scientific, Oct. 1988), `10.1142/0270`.

[VP08]   I. Vidaña and A. Polls, Phys. Lett. B **666**, 232–238 (2008), `10.1016/j.physletb.2008.07.066`, arXiv:`0805.1999`.

Bibliography

[VPR+01]   I. Vidaña, A. Polls, A. Ramos, and H.-J. Schulze, Phys. Rev. C **64**, 044301 (2001), `10.1103/PhysRevC.64.044301`.

[WAW+12]   M. Wang, G. Audi, A. Wapstra, et al., Chin. Phys. C **36**, 1603–2014 (2012), `10.1088/1674-1137/36/12/003`.

[Weg94]   F. J. Wegner, Ann. Phys. (Leipzig) **506**, 77–91 (1994), `10.1002/andp.19945060203`.

[Wei79]   S. Weinberg, Physica A **96**, 327–340 (1979), `10.1016/0378-4371(79)90223-1`.

[Wei91]   S. Weinberg, Nucl. Phys. B **363**, 3–18 (1991), `10.1016/0550-3213(91)90231-L`.

[WGN+14]   R. Wirth, D. Gazda, P. Navrátil, et al., Phys. Rev. Lett. **113**, 192502 (2014), `10.1103/PhysRevLett.113.192502`, arXiv:`1403.3067`.

[WGN+18]   R. Wirth, D. Gazda, P. Navrátil, and R. Roth, *The Hypernuclear No-Core Shell Model*, submitted to Phys. Rev. C, 2018, arXiv:`1712.05694`.

[Whi02]   S. R. White, J. Chem. Phys. **117**, 7472 (2002), `10.1063/1.1508370`, arXiv:`0201346 [cond-mat]`.

[Wic50]   G. C. Wick, Phys. Rev. **80**, 268–272 (1950), `10.1103/PhysRev.80.268`.

[Wir13]   R. Wirth, "Ab-initio Structure of Hypernuclei", master's thesis (TU Darmstadt, 2013).

[WR16]   R. Wirth and R. Roth, Phys. Rev. Lett. **117**, 182501 (2016), `10.1103/PhysRevLett.117.182501`, arXiv:`1605.08677`.

[WR18]   R. Wirth and R. Roth, Phys. Lett. B **779**, 336 (2018), `10.1016/j.physletb.2018.02.021`, arXiv:`1710.04880`.

[WSS95]   R. B. Wiringa, V. G. J. Stoks, and R. Schiavilla, Phys. Rev. C **51**, 38–51 (1995), `10.1103/PhysRevC.51.38`, arXiv:`9408016 [nucl-th]`.

Acknowledgments

"The other two are still lost on the infinite plane of uniform density."
xkcd.com #669 "Experiment" by Randall Munroe, CC BY NC 2.5

154

Academic CV

Education

1994–1998   **Elementary School**, Käthe-Kollwitz-Schule, Darmstadt
1998–2007   **Secondary School**, Lichtenbergschule Gymnasium, Darmstadt
2007–2011   **Bachelor of Science, Physics**, Technische Universität Darmstadt
2011–2013   **Master of Science, Physics**, Technische Universität Darmstadt
2013–2018   **Doctoral Studies, Physics**, Technische Universität Darmstadt

Peer-Reviewed Publications

[GMN$^+$14]   D. Gazda, J. Mareš, P. Navrátil, et al., Few-Body Syst. **55**, 857–860 (2014), `10.1007/s00601-014-0848-9`.

[WFL$^+$13]   R. Wirth, E. Fiori, B. Löher, et al., Nucl. Inst. & Meth. A **717**, 77–82 (2013), `10.1016/j.nima.2013.04.006`, arXiv:`1304.1651`.

[WGN$^+$14]   R. Wirth, D. Gazda, P. Navrátil, et al., Phys. Rev. Lett. **113**, 192502 (2014), `10.1103/PhysRevLett.113.192502`, arXiv:`1403.3067`.

[WGN$^+$18]   R. Wirth, D. Gazda, P. Navrátil, and R. Roth, *The Hypernuclear No-Core Shell Model*, submitted to Phys. Rev. C, 2018, arXiv:`1712.05694`.

[WR16]   R. Wirth and R. Roth, Phys. Rev. Lett. **117**, 182501 (2016), `10.1103/PhysRevLett.117.182501`, arXiv:`1605.08677`.

[WR18]   R. Wirth and R. Roth, Phys. Lett. B **779**, 336 (2018), `10.1016/j.physletb.2018.02.021`, arXiv:`1710.04880`.

Conference Proceedings

[SFI$^+$13]   J. Silva, E. Fiori, J. Isaak, et al., in 2013 3rd int. conf. adv. nucl. instrumentation, meas. methods their appl. (June 2013), pp. 1–7, `10.1109/ANIMMA.2013.6727967`.

Declaration of Originality

I hereby declare that all shown results, except from explicitly cited passages, are original by myself and I have commenced no earlier attempt to achieve a doctoral degree with the handed-in results.

Roland Wirth

Roland Wirth